International Young Physicists' Tournament Proceedings 2010-2011

Edited by

Dina Izadi, Ariaian Young Innovative Minds Institute

and

Ilya Martchenko, University of Fribourg and Lund University

IYPT Proceedings Book 2010—2011

[*] Team of Iran, IYPT 2010
[1]*Sharif University of Technology, Iran*
[2]*Amirkabir University of Technology, Iran*
Corresponding authors: saba.zargham@gmail.com (S. Z.),
ghaednia.hamid@gmail.com (H. G.)

ŁukaszGładczuk[1]
[*] Team of Poland, IYPT 2010
[1]*StanisławStaszic XIV High School, Warsaw, Poland*
Corresponding author: lukaszgladczuk@gmail.com (Ł. G.)

Una Pale [1]
[*] Team of Croatia, IYPT 2010
[1]*University of Zagreb, Croatia*
Corresponding author: una.pale@gmail.com (U. P.)

Alexander Barnaveli[1]
[*] Team of Georgia, IYPT 2010
[1]*Ilia Vekua Physical and Mathematical School 42, Tbilisi, Georgia*
Corresponding author: s.barnaveli@gmail.com (A. B.)

StanislavKrasulin[1]
[*] Team of Belarus, AYPT 2010
[1]*Belarusian State University, Belarus*
Corresponding author: s.krasulin@gmail.com (S. K.)

Una Pale [1]
[*] Team of Croatia, IYPT 2010
[1]*University of Zagreb, Croatia*
Corresponding author: una.pale@gmail.com (U. P.)

Alexander Barnaveli[1]
[*] Team of Georgia, IYPT 2010
[1]*Ilia Vekua Physical and Mathematical School 42, Tbilisi, Georgia*
Corresponding author: s.barnaveli@gmail.com (A. B.)

Zahra Karimi[1]
[*] Team of Iran, IYPT 2010

NivesBohačić[1]
* Team of Croatia, IYPT 2011
[1]*University of Zagreb, Croatia*
Corresponding author: nives.bonacic@hotmail.com (N. B.)

Hossein Azizinaghsh[1] and Hamid Ghaednia[2]
* Team of Iran, IYPT 2011
[1]*Sharif University of Technology, Iran*
[2]*Amirkabir University of Technology, Iran*
Corresponding authors: hossein.azizi@gmail.com (H. A.),
ghaednia.hamid@gmail.com (H. G.)

Rojin Anbarafshan, [1]Hossein Azizinaghsh, [2] and Reza MontazeriNamin[2]
* Team of Iran, IYPT 2011
[1]*RaheRoshd High School, Tehran, Iran*
[2]*Sharif University of Technology, Iran*
Corresponding authors: rojin.anbarafshan@gmail.com (R. A.),
hossein.azizi@gmail.com (H. A.), namin@mech.sharif.edu (R. M. N.)

YuliaPeregud[1]
* Team of Belarus, AYPT 2011
[1]*Belarusian State University Lyceum, Minsk, Belarus*
Corresponding author: svann11@mail.ru (Yu. P.)

StanislavKrasulin[1]
* Team of Belarus, IYPT 2011
[1]*Belarusian State University, Belarus*
Corresponding author: s.krasulin@gmail.com (S. K.)

Hamid Ghaednia[1] and HosseinAzizinaghsh[2]
* Team of Iran, IYPT 2011
[1]*Amirkabir University of Technology, Iran*
[2]*Sharif University of Technology, Iran*
Corresponding authors: ghaednia.hamid@gmail.com (H. G.),
hossein.azizi@gmail.com (H. A.)

Matej Večerík, [1]Tomáš Kulich, [2] and Michal Hledík[3]
* Team of Slovakia, IYPT 2011 and Team of Slovakia, AYPT 2011
[1]*School for Exceptionally Gifted Children and Grammar School, Bratislava, Slovakia*
[2]*Comenius University, Slovakia*

[2]*Sharif University of Technology, Iran*
Corresponding authors: info@tami-co.com (A. T. Z.),
namin@mech.sharif.edu (R. M. N.)

KatjaKustura[1]
[*] Team of Croatia, IYPT 2011
[1]*University of Zagreb, Croatia*
Corresponding author: katja_kustura@hotmail.com (K. K.)

Reza MontazeriNamin[1] and AlirezaTahmasebZadeh[2]
[*] Team of Iran, IYPT 2011
[1]*Sharif University of Technology, Iran*
[2]*University of Tehran, Iran*
Corresponding authors: namin@mech.sharif.edu (R. M. N.),
info@tami-co.com (A. T. Z.)

Alexey Krotov[1]
[*] Team of Russia, IYPT 2011
[1]*Lyceum 130, Ekaterinburg, Russia*
Corresponding author: bronze.eye@gmail.com (A. K.)

HosseinAzizinaghsh[1] and Reza MontazeriNamin[1]
[*] Team of Iran, IYPT 2011
[1]*Sharif University of Technology, Iran*
Corresponding authors: hossein.azizi@gmail.com (H. A.),
namin@mech.sharif.edu (R. M. N.)

Acknowledgement

Dear national and international participants in one of the greatest projects in Physics Education I am so happy that this book was inspired by a collaborative project between Ariaian Young Innovative Minds Institute (AYIMI) and Ilya Martchenko which has provided IYPT Archive.

AYIMI as an international institute is going to develop more educational programs between Iran and other countries which help to bring the young talents even closer together.A major goal is to accelerate progress and advancement toward the learning natural sciences such as physics, practically and by team work. The IYPT 2010 and 2011 proceeding book shows the breadth of the researches explored by participants. All the Papers from different countries attended in IYPT 2010 and 2011 have been reviewed by several referees. They have commented on papers to be prepared scientifically. Our thanks go to all participants as students and teamleaders. Our special recognitions go to all the referees who made their great efforts and amazing job.

Dina Izadi
Ariaian Young Innovative Minds Institute (AYIMI), President
Spring 1391 (Iranian Year) / 2012

International Board of Reviewers

Introductory Words

EDITORIAL: ON ATTRACTING AND REVIEWING SUBMISSIONS

Ilya Martchenko [1, 2]
[1] *University of Fribourg, Switzerland*
[2] *Lund University, Sweden*
Email: ilya.martchenko@unifr.ch (I. M.)

The International Young Physicists' Tournament has always been a meeting place for discoveries, creativity, and vibrant ideas.

This book touches on the highlights of the projects that were prepared for the IYPTs 2010 and 2011.

It is not for the first time that some of the bright IYPT projects have been selected to and published in a stand-alone international proceedings book. Such books have been previously published in 1998, 2005, and 2006.

In a next step, we are building further on what has made the IYPT proceedings successful: nearness and openness of the pre-university research reflecting the spirit and the level of the present day IYPTs.

For the first time we have implemented a full-scale professional review of all submissions to select the best and to rigorously check and improve those that are selected.

We opened our formal public call for papers on August 29, 2011.

36 manuscripts from 9 nations have been attracted, most of them in the short time interval before the final deadline of November 24.

The social dynamics of the submissions, quite typical for such projects as conference proceedings, is illustrated by Figure 1.
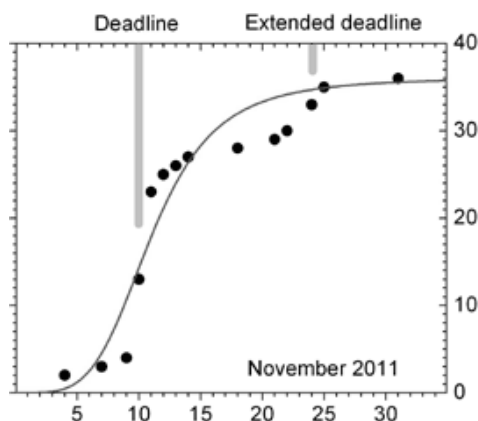
Figure 1. A logistic sigmoid function is used to fit the total number of received manuscripts as a function of time. The inflection point and the maximum daily submission rate coincide well with the first formal deadline

The information hub for the project was set within the IYPT Archive: *http://archive.iypt.org/iypt_book*.

Here all submissions were indexed and all further details and status updates were collected. The original reviews, authors' letters to the reviewers, and online supplementary materials stay indexed online at this webpage.

We set a standard of 2 or 3 reviews per each submission, and the authors had to address and resolve the reviewers' concerns and revise the manuscripts before any further action or decision was taken.

The key aim of the review was to ensure that the manuscripts were appropriately scoped, written clearly, did not contain any visible mistakes or misconceptions, and stayed at a good level of depth and originality.

We focused on checking the consistency of results and conclusions. As a guideline, we assumed that the articles in the book should be usable by the intended audience (future participants, teachers, researchers in physics education, and people outside of the IYPT.)

We equally believed that each paper must present only independent experimental and theoretical results. All ideas or approaches that were not of own work, were requested to be referenced rigorously, without exception.

The written reviews took form of corrections or suggestions for students, questions, commentaries, evaluations, and recommendations.

Many reviewers requested re-writing or clarifying some parts of the text, questioned the conclusions and the data interpretation, and signaled issues that the authors should have promptly resolved.

Not all of the manuscripts passed through the reviewing stage, and we had 3 manuscripts rejected and 4 more manuscripts rejected but invited for possible re-submission.

The reviewing team comprised 25 reviewers from 12 nations. The total number of the first stage reviews was 91.

The performance of reviewers and authors, but also are own operational performance, may be illustrated by the distribution of waiting times to collect feedback and corrections (Figure 2.)
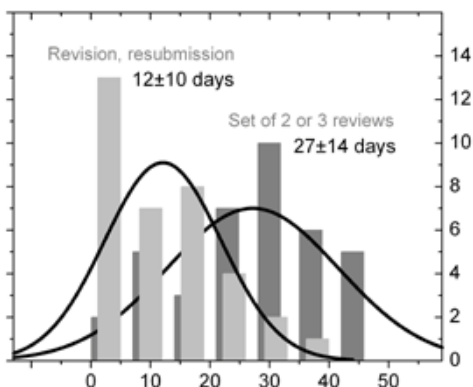
Figure 2. The histogram shows the distribution of waiting times to collect feedback from the reviewers and corrected manuscripts from the authors. In average, it was taking 27±14 days to collect a necessary and sufficient package of 2 or 3 reviews and deliver a decision. In a next step, it was taking 12±10 days to receive a revised manuscript. Note that Gaussian fits are only rough approximations of the data, where a peak of *immediate revisions* is for example seen

After collecting all revisions, re-submissions, and extra 7 reviews, the following final decision was delivered by January 17, 2012: 32 manuscripts selected and accepted, with the yeilded acceptance ratio of 89% (Figure 3.)
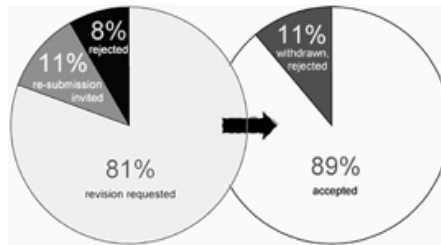
Figure 3. The pie chart shows the interim and final decisions for each of the 36 submitted manuscripts

We offer a special thanks to authors who demonstrated a deep interest, self-determined motivation, and attention to detail as their papers underwent reviewing.

When looking through their feedback and informal commentaries, we may sum up that the review was a successful learning experience for each and every author. They learned to revise own narrative and data representation; satisfy the necessary standards of style, clarity and consistency; respond point by point to several pages of critical remarks; and meet tight deadlines.

We extend our deep and sincere gratitude to the reviewing community who handled their difficult and important mission with utmost speed and professionalism.

This book could not have become a reality without a commitment of Dr Dina Izadi who initiated the idea to publish the proceedings, and provided a warm and productive setting for the preparatory efforts.

We hope that the book will bring back good remembrances of these two IYPTs, and serve as a helpful asset to promote the IYPT to a broader readership.

With grateful thanks for the pleasure of cooperating on the project.

Ilya Martchenko

IYPT Archive

Invited Papers

THE INTERNATIONAL YOUNG PHYSICISTS' TOURNAMENT (IYPT)

Gunnar Tibell[1]
[1]Division of Nuclear and Particle Physics
Department of Physics and Astronomy
Uppsala University, Sweden
Email: gunnar.tibell@physics.uu.se (G. T.)

History and administration

In this paper a team competition called the International Young Physicists' Tournament (IYPT) will be described, in particular with respect to the skills one hopes to develop among participating students. The history of IYPT dates back to 1988 but in the beginning the event was always organized inside the Soviet Union or, from 1992, in Russia. However, already from the year 1979 there was a precursor organized at Moscow State University for secondary school students from the Moscow region. In 1994, for the first time, it was arranged in a different country, namely The Netherlands. Since then sixteen countries have organized IYPT with a fluctuating number of countries participating. In 2004, for the 17th IYPT, Brisbane, Australia, was the host for 26 teams from 24 countries, representing six continents; in 2005 Winterthur, Switzerland, in 2006 Bratislava, Slovakia, in 2007 Seoul, Korea, in 2008 Trogir, Croatia, in 2009 Tian Jin, China, and in 2010, Vienna, Austria hosted the IYPT event. Austria became the first country to arrange an IYPT event for the second time

The details of the competition structure are strictly prescribed in Regulations, whereas the organization itself is ruled by Statutes, adopted in June 2004. The governing body is an International Organizing Committee (IOC) which meets at least once annually, during an IYPT event. The event itself is arranged by a Local Organizing Committee (LOC). Between IOC meetings an Executive Committee handles the issues as decided by IOC. It consists of eight members: President, Secretary General, Treasurer, two members elected by the IOC and the three LOC chairpersons from "last year, this year and next year". The fiscal year of IYPT runs from November 1 to October 31.

IYPT structure

The structure of the competition has been developed through the years from the start, but the changes introduced have normally been slight. In each of the five qualifying rounds, called Physics Fights, three, or sometimes four, teams meet and present their solutions to one of the 17 problems on the list. A team consists of five members, representing one country. However, up to the year 2007 the host country could have two teams participating. As a remnant from history the Russian language was allowed in the discussion; today everything is conducted in English.

Which problem a certain team has to tackle is decided by a so called challenge from one of the other teams present in the qualifying round. There are three roles possible in a round: reporter, opponent and reviewer. The opponent challenges the reporter for one of the problems. The reporter can refuse to accept the challenge, but after a total of three refusals during the five rounds the grading of the jury will be lowered. After the report of the solution the opponent will scrutinize the solution and point out merits as well as possible weaknesses. The reviewer comments both the solution of the reporter and the remarks of the opponent. All items on the agenda are strictly

timed. The report, for instance, can take no more than 12 minutes, whereas the opposition and the following discussion with the reporting team are allowed a maximum of 15 minutes.

After this first part of a particular qualifying round the roles are changed, and at the end of a full round all teams have had each of the three roles. If four teams are present the members of the fourth are called observers, and they remain passive. Also this role is adopted by each of the four teams in turn.

The performance of the teams is graded by an international jury, composed of normally 5 to 8 members who are either independent or connected to a team not participating in that particular round. In most cases jury members come from different countries and none of them comes from the same country as a participating team. The grading of the jury is recorded and forms the basis for a decision, after the five qualifying rounds, to select the best three teams who compete in the final round. The rules are different in the final in the sense that the three teams choose themselves which problem they want to handle. The choice is made according to the ranking after the first five rounds, the team with the highest ranking chooses first, etc.

IYPT problems, selection and examples

The 17 problems to be solved by participating teams are decided by IOC on suggestions from an international group of physicists, consisting of both school teachers and researchers from various institutions, mostly universities. They are nowadays published on the Internet, typically ten months before the competition takes place. The IOC normally has well over 100 problems to choose from. Care is taken to spread the problems over as many subfields of physics as possible. Additional criteria involve the need for problems which require some experimental research and which are by their nature "open", i.e., they should not have a unique solution but rather be possible to handle from different aspects and thus to give alternative solutions. Physics subfields which are quite frequent among the selected problems are mechanics, electricity/magnetism and optics. In these cases it is relatively easy for the students to find equipment, to construct models and develop strategies for discussing their solutions.

However, it has been shown difficult to list problems from certain areas like "modern" physics. Partly this is due to the assumption that many school curricula do not include this subfield, partly also to restrictions in handling radioactive substances, for instance. In general it could be added that the selected problems often favour schools with modern laboratory equipment. However, in judging the presented solutions the jury can take into account the ingenuity and creativity of the participants and thus compensate for the lack of equipment.

Some examples of problems will be given below, in order to show the character of typical IYPT problems.

The city of Odessa in Ukraine hosted the 15th IYPT in 2002. In that event the following problem was chosen in the final by the winning Polish team:

Spinning ball

A steel ball of diameter 2-3 cm is put on a horizontal plate. Invent and construct a device, which allows you to spin the ball at high angular velocity around a vertical axis. The device should have no mechanical contact with the ball.

In 2003 IYPT was organized in Uppsala, Sweden. The winning German team had chosen the following problem:

Heat engine

Construct a heat engine from a U-tube partially filled with water (or another liquid), where one arm of the tube is connected to a heated gas reservoir by a length of tubing, and the other arm is left open. Subsequently bringing the liquid out of equilibrium may cause it to oscillate. On what does the frequency of the oscillation depend? Determine the pV diagram of he working gas.

The following problem was given in Brisbane in 2004:

Didgeridoo

The 'didgeridoo' is a simple wind instrument traditionally made by the Australian aborigines from a hollowed-out log. It is, however, a remarkable instrument because of the wide variety of timbres that it produces. Investigate the nature of the sounds that can be produced and how they are formed.

It was chosen by the Polish team in the final and the solution presented live performances as well as theoretical descriptions of how the sound was produced. The solution of this problem made the Polish team winners.

The winning Croatian team in Bratislava in 2006 chose a problem with the following wording:

Electrostatics

Propose and make a device for measuring the charge density on a plastic ruler after it has been rubbed with a cloth.

A final example is taken from Vienna in 2010. There the winning team from Singapore had chosen the following problem:

Magnetic spring

Two magnets are arranged on top of each other such that one of them is fixed and the other one can move vertically. Investigate oscillations of the magnet.

What skills are developed?

For participants in the IYPT competition it is evident that certain skills are needed for success. Some of these are essential also for success later in life, especially if a student chooses to continue to a career in physics research or in teaching.

In the preparation for the competition some experimental research as well as a study of the theoretical basis for a solution to the problem are needed. This work would normally be done in a team, sometimes inside the team that appears in the competition. In addition, search in the literature is normally performed, and the participants have the liberty to quote suggestions from elsewhere, also from teachers or professional researchers. Already it is clear that to be prepared for the event itself the following skills have to be developed:

> *Experimental research,*
> *Theoretical study,*

*Correct references to other results quoted, and
Team work.*

The reports are given in English and the time assigned is quite limited. For the vast majority of teams English is a foreign language; some years back no team in fact had English as their mother tongue. It is thus essential to learn to present a solution in a clear, convincing and logical way and to be disciplined regarding the time to be used. In addition, the use of modern visual means of presenting a report becomes increasingly important for the outcome. The corresponding skills would be:

*To present as clearly as possible the solution suggested,
Using modern means of communication, and
To plan the report within the time given.*

In the discussion periods, between opponent and reporter as well as when the reviewer makes comments, great emphasis has traditionally been put on the way possible criticism is formulated. Unnecessarily aggressive behaviour will be punished by the jury. Remarks like "Obviously you have not understood the physics behind your reported solution" do not open for an efficient discussion and must be excluded. Adding the fact that an IYPT event, when hundreds of young students from all over the world meet and associate for a week, calls for some behavioural attitudes, one might add to the list the need for and development of

Social skills in a broad sense.

The selection of national teams

Just as is the case for the better known International Physics Olympiad different countries have adopted quite different strategies for selecting their national teams. Quite a few organize their own national qualifying competitions in order to find the best team for representing their country. In some cases the selected students are also invited to prepare for their performance in IYPT at a university. Other countries depend on a few enthusiastic physics teachers who trim and encourage pupils from their own classes.

The school curricula in different countries also differ substantially, making it more or less difficult to fit in the rather extensive preparation needed for students of the final year in upper secondary schools.

It is clear that if only the resulting ranking would be important for participating teams such different preparation possibilities could appear unjust. However, like in most other instances it is only fair that those who have the best preparation also reach the best ranking. In addition there are certainly many other positive features of participating which compensate for a less successful ranking.

Since in many countries girl students show less interest in physics than boys it is encouraging that a considerable number of girls do participate in IYPT. Recent years have even seen teams of only girls among the competitors, once from Poland and once from Australia. It is possible that the cross-disciplinary nature of some of the problems is a contributing cause.

The future of IYPT

After a period of difficulties to find willing hosts for the next IYPT events the situation is now encouraging in the sense that we seem to have a "line" of candidates for the next few years. In 2011 Iran will be the host and the Czech Republic is already committed for 2012.

An international organization, the World Federation of Physics Competitions ((WFPC) was recently set up. It held its fourth Congress in Baske Ostarije, Croatia, in July 2010. In the first issue of Vol. 12, their journal Physics Competitions gives a full account of the agenda of this meeting. Both national and international competitions are presented. In previous issues of their journal the impact of events like IYPT on the physics curriculum is discussed by experienced teachers who have also been organizers of different competitions.

In closing I should like to express my gratitude to the IYPT organizers and participants for providing an outstanding platform for social and professional contacts. In particular my period of presidency between 1998 and 2008 will be vividly remembered as a source of constant encouragement in the mission of transferring to colleagues and young people the enthusiasm for the cause of physics education in its broad sense.

I should like to thank A. Nadolny, former Secretary General of IYPT, for providing important details, especially concerning the history of IYPT

Computer on-line systems for innovative Labs in Secondary School

Mario Gervasio[1], Marisa Michelini[2], Alberto Stefanel[3]
Research Unit in Physics Education of the University of Udine, Italy
Corresponding authors: gervasio@fisica.uniud.it, marisa.michelini@uniud.it,
alberto.stefanel@uniud.it

Abstract

The researches on the role of laboratory in teaching/learning physics point out the validity and opportunity of introducing the use of on-line measurements in didactic laboratories also at low level (12-16 years old), It emerges the need for systems easy to be carried out with cheap materials, directly connected to the computer via USB, so that requires brief time of setting up and few knowledge of electronics, for a good use and eventual modifications. In this prospective on-line measurements with sensors are thought as a first extension of senses in a laboratory that aims to a study of phenomena to reach a formalization based on an interpretative examination of experimental analysis. In this perspectivea cluster of very simple tools consisting on sensor connected via USB to computer was created to perform specific measurements: temperature in time with 4 probes; light intensity vs space displacement; resistivity vs. temperature for metal, semiconductor and superconductor. The technical characteristics of the tools and examples of measurements that can be carried out are here presented, referring to previous papers for students learning and experimentations in school.

1. Value of using on-line sensors in didactic laboratory

Social, methodological-disciplinary and practical reasons lead to the using of computer in school
Laboratory (Michelini 1992¸ Hofstein, Lunetta 2004, Zacharia 2003, Bernhard 2003, Lunetta et al. 2007):
- Our everyday life is full of computerized objects and it is important, on social level, to prepare young students to this continue evolution, with information, adequate experiences,methodologies and critical instruments to understand and use such apparatuses.(Swan, Miltrani 1998; Riel 1998)
- In research laboratories computers manage data and are integral part of the investigation. Soon-line experiments may allow students to understand contents and methods characterizingphysics.
- On practical level, on-line experiments offer efficiency, time-saving, reliability, precision,reproducibility of data, all with quite cheap instruments. Moreover they allow an immediate anddirect contact with the phenomenon, advancing a laboratory open to the personal construction ofideas and new occasion of learning, thanks to the following potentialities (see also Giugliarelli et al 1994)
- Extension of the possibility of
  - observation of events too much quick or slow as regards manual measures
  - measures in rather inaccessible places
  - collecting data easily, favoring in this way the comparison of diagrams and graphs, thesearch of characteristics and boundary/ initial conditions, various considerations about theanalyzed system (e.g. energetic)
  - study of nonlinear processes, like the transitory in several types of phenomena, thanks to thequick data acquisition (not possible in traditional laboratory, where measures regard thevariation of quantities in initial and final

equilibrium states). This allows familiarity withexperimental situations and theoretical closely examination based on experimental evidence (see also Hirata 1986 and Mascellani et al 1989)

These possibilities make the experimentation in school closer to the reality and, thus, moreinteresting and stimulating, so that phenomena may be analyzed in their completeness andinterpretative models easily understood.

- Improving quality of the measurement, its reliability and sensitivity that allows both advancedand base experiments, these latter in several deeper ways, to encounter the interests of students, sothat the laboratory becomes culturally stimulating.

- Time-saving (collecting quickly data on-line) and good reproducibility, that favors theconceptualization and the focusing of the attention on data, on planning and manual aspects (chooseof the experiment and its assembly), on physical problems, on the description of the characteristicsof phenomena, on the comparison between different experimental situations.

- Collecting many data, that limits the introduction of hypothesis and allows the use of statisticalmethods

- Attention to conceptual aspects of procedure of measurement: setting and calibration of thesystem, choice of the measure interval, sensitivity, resolution, time of data acquisition.

- Real time graphs of time depending (or not) phenomena, whose understanding (of role andmeaning) may help in overcoming some cognitive problems (e.g. lacking in capability of executionand use of graphs) thanks to the following potentialities:

• Visual impact favors the analysis of the phenomenon

• the possibility to follow, in real time, the evolution of the phenomenon and/or thecharacteristics of collected data stimulates the search of interpretations, common discussion, the comparison of ideas, analysis and selection of meaningful parts, the determination ofquestions and problems to test.

• in explorative activities, in which student compares sensorial information with signalscollected by the sensors, the graph favors the rationalization of sensations and the nucleationof interpretative hypothesis.

• collecting several graphs for each event makes graph a familiar representative tool (see also Thornton, Sokoloffet 1999, 2004).

- Developing of planning capability, comparison between data collected in different times andconditions, comparison between phenomena describable through similar formal relations. (see also Lunetta, Hofstein, 2004)

- Applications in system of control that allow to understand the concepts of feedback, stability, notlinearity, and to develop plans for automation.

- Possibility of integration with other software: a) of calculus, for data processing, b) of simulation,for the comparison with the theory, c) of modelling, for a process of interpretation that starts fromthe hypothesis of the students. The software is a set of tools for data processing. It has to be open,flexible, and multifunctional and it represents a powerful tool to analyze conceptual meaning of data, todevelop analytic thought, investigative interest, intuition and theoretical thought.

It is clear that on-line experimentation cannot and mustn't be the only way to carry out a laboratoryactivity. But a correct management of the activity avoids the reduction of active participation ofstudents and capability of analysis of the experiment. It may stimulate a deeper study of treatedargument: in fact it often happens that the graphs given by computer suggest other graphs.(Van den Berg E. et al. 2007).

2. Sensors as proposals of extension of senses

Thinking to the validity and opportunity of introducing the use of on-line measurements in didacticlaboratories also at low level (12-16 years old), It emerges the need for systems

easy to be carriedout with cheap materials, directly connected to the computer via USB, so that requires brief time ofsetting up and few knowledge of electronics, for a good use and eventual modifications.

In this prospective on-line measurements with sensors are thought as a first extension of senses in a laboratory that aims to a study of phenomena to reach a formalization based on an interpretativeexamination of experimental analysis.

A continue and active intervention of the user is required, both for the choice of the parts to utilizeand for the way to utilize them. Moreover, several activities are possible: common or in groupphenomenological exploration, experimentation to individuate relations between variables, measureof physic quantities, proof of theoretical hypothesis, experimental examination of phenomena. Theuser has to plan the way to carry out the experiment too, so that planning and manipulative aspects,the analysis and the interpretation of data, are choices in an experimental activity in which each onemay organize the construction of his knowledge.

The hardware is simply made of sensors, connected directly to the computer via USB.The software usually offers several options for each phase and the user may choose the procedure(e.g. setting up, calibration, measure, management of files) and assign few operations andparameters (e.g. sampling interval, number of sensors to use, variables and scale for real-timegraphs). Here we present three examples of hw-sw systems on thermal, optical and electricalphenomena.(Michelini, Pighin 2005; Michelini 2005).

3. Real-time Temperature vs Time measurement with Termocrono

Termocrono is a system based on on-line sensors to make four contemporary real-time measures oftemperature that allows to follow thermodynamic processes, that is the evolution of a previous system named Termografo. (Mazzega, Michelini 1990, 1996) The connection to the computer is viaUSB. The system consists of a hardware and a software part.The hardware has a circuit for data acquisition and analogical-digital conversion. The temperaturemeasure is based on the measurement of the inverse saturation current of germanium inverselypolarized diodes. The conversion is of current-time type to utilize the precision of quartz oscillatorof computer to do the measure. With the same supply of computer and though each diode acapacitor is charged, at ends of which a tension comparator is inserted, with predefined minimumand maximum values of intervention. A monostable vibrator generates a square wave that startswhen that minimum value is detected, and ends when that maximum value is measured. So theduration of the square wave depends on the time (t) of charge of each capacitor, that depends ondynamic resistance R of the diode (t=RC), that depends on the temperature of germanium diodes, inwhich the saturation inverse current is a constant strongly dependent by the temperature.The duration of square wave is measured, utilizing a quartz oscillator (16 MHz). With the frequencycounting set off by the oscillator you detect the number of impulse generated in the period of activation of the square wave, so that the temperature measure depends on the number of generatedimpulses. The utilized impulses meter is at 32 bit, with a time-out value at 22nd bit (4.194.303 counting):above that value the sensor is supposed bad working.An interface card, implemented with a microcontroller PIC 18F252 by Microchip Technology, isused to read in the same time the four counting of the four independent sensors. The counting issent to the computer via USB connection, realized using a decoding module FT245BM.(Gervasio, Michelini 2006)
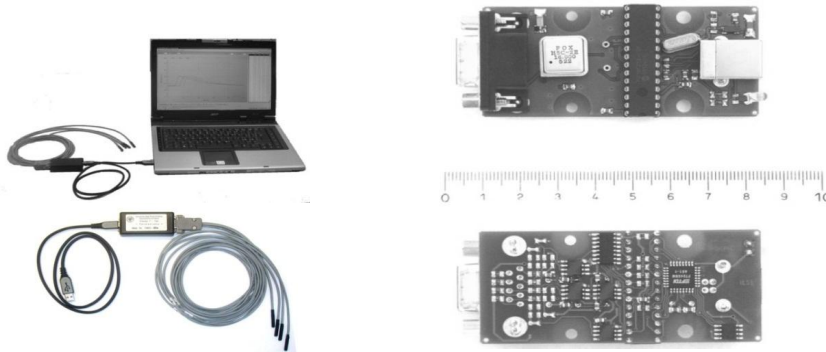
Fig. 1 To the left: The Termocrono interfaced via USB to the computer. To the right, the circuit for signals acquisition and analogic-digital conversion of data acquired by Termocrono

In fig 1,the Termocronois connected to the Laptop via USB port. Ile black box (cm 9 x cm 4 x cm 1,5) containsthe circuit for signals acquisition and analogic-digital conversion of data acquired by Termocrono. The temperature diode-sensors are connected to four bipolar cables (2m) that are connected to the box through only oneconnector. The four sensors may be used independently too.Fig 2 shows the user interface: It is possible to visualize at the same time the graph and the data ofone or all the sensors. Graphic scale may be at dynamic or fixed optimization.A specific function of the system allows the calibration using the comparison with anotherthermometer in a minimum of 2 and a maximum of 15 thermal equilibrium states. The values oftemperature are determined by the system through a fitting between the calibration points, utilizingthe function of transfer of the system.

The measure interval is [-10°C,+100°C], the sensibility is 0,1°C, the measure accuracy is ±0,3 °C.Each group of sensors requires calibration before using. The calibration is stable for the same hardware group. The function "Real Time Plot" of the program activates the measure. Dataacquisition consists of a measure per second and a real-time graph that evolves in time is carriedout on the video.

Graphs and tables may be saved in archives, so that they may be recalled for examination and/orprinting. Recording format of tables of data is directly compatible with any calculus sheet.The system may be used with any computer via USB connection.
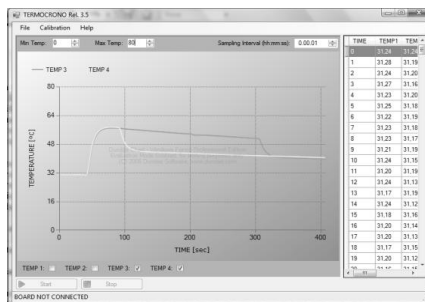
Fig. 2. User interface of the software of the system Termocrono

3.1. Examples of measures

Termocrono is proposed as extension of senses for experimental explorations at low school level,

thanks to Its semplicity and flexibility [Michelini e Stefanel, 2004; Michelini e Pighin, 2005; Binda et al 2005; Michelini, Santi, Stefanel 2010].

Thanks to the sensibility, accuracy and quick data acquisition, It allows experimental study of statesof thermodynamic transformations. So it allows the study of transitory states too, as impulses andthermal waves, possible with difficulty with other systems in didactic laboratories [Mazzega, Michelini 1990, 1996a,b; Girardini et al 1991]. Here some examples of measures are presented, relevant for different aspects, to understandthe meaning of measure of temperature and the zero principle of thermodynamic.

A) Two sensors are on a table; a student takes in his hands a sensor first, then both and at the endputs one sensor on the table again.

This experience makes students aware that:

- the table and the hands are two systems with different constant temperature
- during the transitory the sensors measure their own temperature
- only when sensor and system are in thermal equilibrium the given information about thetemperature regards the system
- the different length of the phases of warming and cooling of sensors is caused by the differentefficiency of the systems during thermal interaction.

B) In Fig. 3 the evolution in time of the temperature of two masses of water (m1= 300 g at T1=10,2°C and m2= 150 g at T= 49,8 °C) is shown. The system is so set: the box with the massm2 is putted inside the other. The two systems evolve towards a common equilibrium temperature, weighted average over the masses (Fourier law of thermal equilibrium). Resulting equilibrium temperature is 24,1°C and allow the calculation the mass 11,9 g , as equivalent in water of the box.
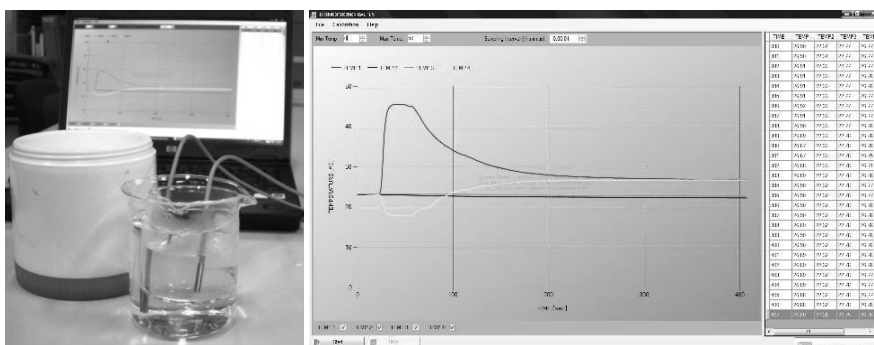
Fig.3 – Evolution in time of two masses of water of 300g and 150g at the temperature of 16,2°C and 46,8°C

C) The sensors are covered with sheets of different materials and are at home temperature on atable; a student takes sensors in his hands, waits thermal equilibrium, then put sensors on the table again. This experience makes students aware that the sensors reach the same temperature but indifferent time intervals, dependent on materials, and introduces the idea of thermal conductivity.

Response time of the sensors
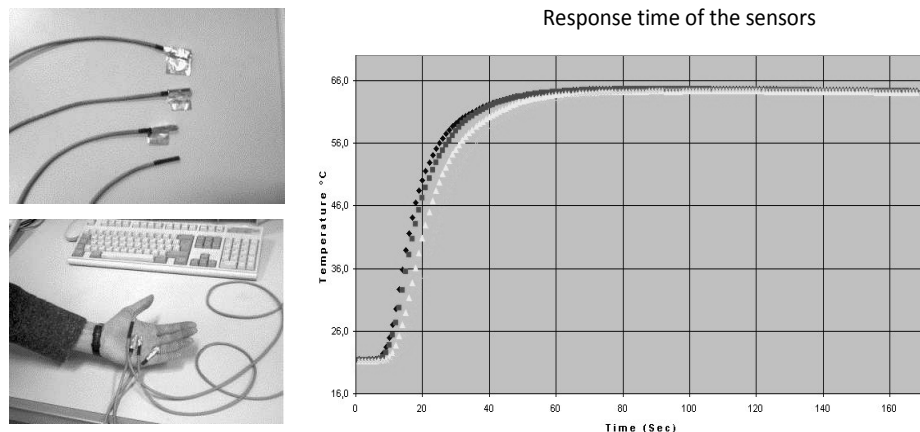
Fig. 4 – Evolution in time of the temperature of 4 sensors of different masses in a big mass of warmer water

D) Fig. 4 shows data obtained when the four sensors are covered with different masses ofaluminum (0, 2, 4 and 10g) and putted in a big mass of warmer water (isothermic).
The dependence of the time to reach equilibrium on the mass of aluminum allows to understand themeaning of time of response of a system and to calculate It.It is possible to study the exponential low to reach equilibrium.

4. A simple system for diffraction experiments: Lucegrafo

Here are presented the hardware and the software characteristics of a simple home-made system foron-line data acquisition of light intensity according to its position (Gervasio, Michelini 2010a).Hardware:The equipment is elementary: a commercial linear cursor potentiometer, a phototransistor, anassembly box, USB cable.
Fig 5 shows that the phototransistor is inserted in a housing made an aluminum block solid with thecursor of the potentiometer, so that the optic signal is correlated with the position by means of theresistance of the potentiometer. A small rectangular screen (12 cm x 2 cm), solid with to the opticsensor support, has the function of allowing overall qualitative observation of the distribution oflight intensity. At the center of the screen there is a hole (section area 1 mm2) functioning as adiaphragm for the optic sensor. A screw guide for fine movements of the cursor is eventuallyavailable. Both the sensors (potentiometer and phototransistor) are connected to the processor viaUSB. The calibration of the system is made measuring the light intensity as a function of the distance from a point-like source. The experimental dependence of the light intensity on the squareof distance is both a confirm of the current transfer function assumed and the way to find theunknown parameters.
There are 3 ranges of sensibility, to acquire the 12th maximum and the central maximum, at adistance of 2 m, with a single slit of 0,1 mm and a laser with λ~650Å.
Software: During the measure the system acquires and represents on the screen, both in graphical and numerical way, couples (I,x) (intensity, position), one per second, so that, moving linearly thecursor, the space distribution of light intensity for a length of 60 cm is acquired.The measure is represented in linear response: the intensity, in the graph, is represented in arbitrary units, proportional to the light intensity incident the sensor.
Here some examples of didactical activities are presented, those impossible to carry out with traditional systems without sensors in didactic laboratories, referring to previous work

for a more detailed presentation (Mascellani et al 1989, 1992, Corni et al. 1993; Frisina, Michelini 1996).
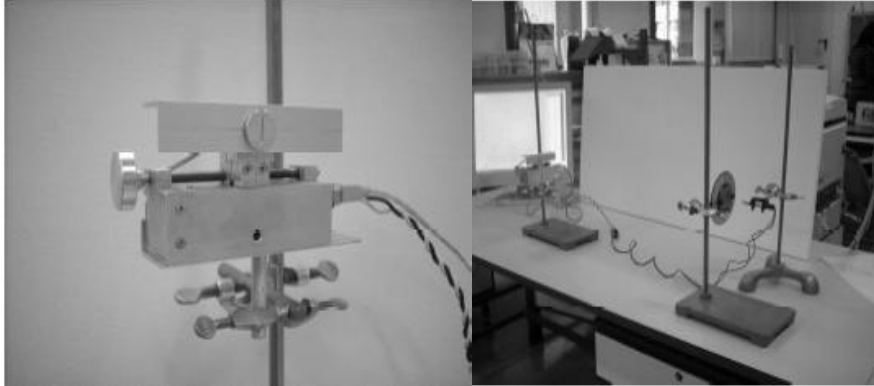
Fig 5 To the left, the Lucegrafo systemmounted on a vertical support; To the right, the apparatus set upfor the measurements

A) Exploration of light intensity distribution of a diffraction pattern:Qualitative inspection of the diffraction pattern on a screen, changing the distance D between theslit and the screen: the screen intercepts constant angular distribution of light intensity; in fact, thedistances of minima and maxima from the central maximum increase proportionally to the distanceD.The system cannot reveal in the same scale both the intensity of the central maximum and those ofthe nearby ones, unless the incident intensity is reduced(see Fig 6 and Fig 7). This gives theopportunity for adiscussion both of the characteristics of the diffraction pattern and those of opticalsensors.

B) Analysis of peak intensity. The Fraunhofer approximate law for light intensity $I_M$of the maxima of order M>0 relative to that of the central maximum I_o: $\dfrac{I_M}{I_o} = \dfrac{4}{\pi^2(2M+1)^2}$

expresses the proportionality between peak high and the inverse of the square distance from the central maximum on the screen.

In fact, by substituting the approximate relationship for the maxima position:

$$\frac{X_M - X_o}{D} = (2M+1)\frac{\lambda}{2a},$$

this equation can be written more simply:

$$\frac{I_M}{I_o} = \left(\frac{D\lambda}{\chi a}\right)^2 \frac{1}{(X_M - X_o)^2} \text{ or } \frac{I}{\sqrt{I_M}} = \left(\frac{\pi a}{D\lambda}\right)\frac{1}{\sqrt{I_o}}(X_M - X_o).$$
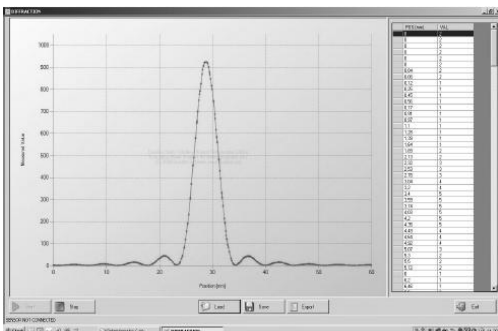
Plotting $\dfrac{1}{\sqrt{I_M}}$ versus $(X_M - X_o)$ we obtain a straight line (Fig 8).

The central maximum intensity can be calculated from the slope of the straight line through theorigin, starting from the other involved parameters.

Fig 6. Diffraction pattern with the system in the low range of sensibility
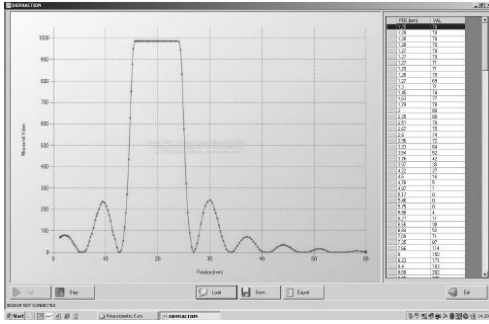
Fig 7. Diffraction pattern with the system in the high range of sensibility
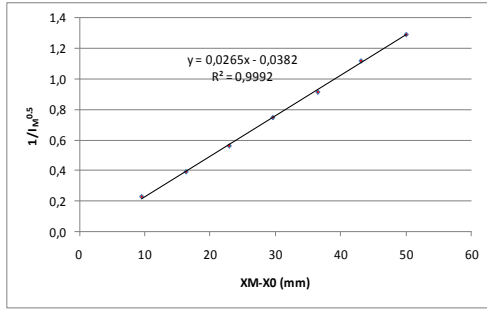
Fig 8. Inverse of the square root of he intensity of the maxima as a function of their distance fromthe central one. The case of a slit of 12 μm and screen distance D=1,4m

5. Resistivity vs Temperature measurement in superconductors

A USB probe for the measurement of resistivity versus temperature in metal, superconductor and semiconductor solids and a combined room temperature Hall coefficient measurement for metals and semiconductors has been developed and patent by Mario Gervasio and Marisa Michelini (Gervasio, Michelini, 2010b). The resistivity measure can be carried out in the 78-400K temperature range selecting different controlling heating rate. Current and magnetic field are parameters to selected by the user in Hall coefficient measurement. The system to measure the resistivity versus temperature has been designed so as to implement measures in a four-terminal configuration, the two external contacts are used for the injected current of 100 mA and the two internals to measure the voltage, proportional to the electrical resistance of the sample.

The software interface is designed to be user friendly, giving to the user the opportunity to set up the relevant parameters of the measurements and to have a direct vision of the real time graph during the experiments. High quality measurements give to opportunity to fit data with curves based on theoretical models.

Measurement procedure can be chosen by the user:
- thermal inertia, from the temperature of nitrogen liquid at room temperature
- ramp with continuous heating
- temperature of thermal inversion. Is chosen, via software, the gap in temperature between a measure and the next.

Each measurement is made by detecting the voltage, on the two internal contacts, first time with the injected current and then subtracting the voltage corresponding to zero current. Under these conditions it is obvious that there is no need for manual adjustment of the offset because the correct measure of the voltage will be that obtained from the difference of the two readings (measure "quasi ac").

Electronic solution for the measurements:To perform the resistivity measurements, three hardware modules have been designed: 1. constant current source; 2. voltage measurement; 3. heater.

5.1 The system

The **generating current circuit.** The current value remains strictly constant during a change of resistance of the sample. This current can be varied from 1 to 150 mA through VREF1 tension generated by software. A constant fixed current value is obtained by producing a constant reference tension with a Zehner diode in a circuit where two

operational amplifier are located to provide to the tension measurement on the sample (between the two internal point contacts) for he resistivity measure (milliohm). The problem of bias tension of the contacts is overcome, because the output reference tension can be fixed via hardware, minimizing the input current in the operational amplifier. The amplification rate ranges from 5 (open circuit) and 1000. The second amplifier guarantee measured values of the order of mV.
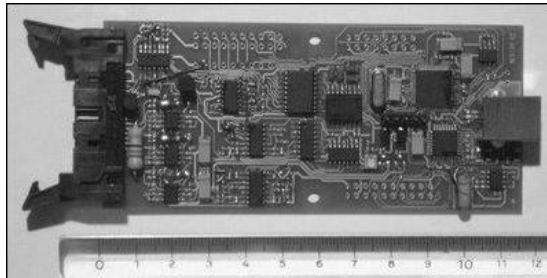
Figure 9. The picture shows the interface card for connection (via USB) to your computer

The **reading circuit** of the input voltage. The potential difference between the two internal contacts is obviously proportional to the electrical resistance of the sample and is withdrawn into the operational amplifier AD627, electrically powered with dual VCC (+10 V) and VEE (-10V), as it provides the ability to measure positive and negative tensions. The card includes 6 (six) different circuits of reading (use one at a time) the voltage on the two internal terminals on the sample, each with its own gain to handle the broadest range of measures without the need for manualadjustment.

The **module of the heater** can provide a maximum current of 250 mA, directly accessible from the USB port of your computer. For stronger heating it is necessary to use a small external power supply. The command for the injection of the heating current is run by software based on the measurement procedure chosen. The heater is realized by two resistance of 100 Ohm (1 watt) are inserted in a parallel circuit on the base of the Al box.The increasing of the temperature is realized by acting via software on an analogic heliportpotentiometer connected with a power transistor given the requested corrent to the heater. The resistivity measurements are carried out in rampa .

To **measure the temperature** is used as sensor a PT100 platinum resistance (R = 100 ohms at 0 ° C), with a variation of 0.4 ohm per ° C. This allows, with a 12-bit analog converter, to obtain, in the temperature range that interests us, a sensitivity of 0.05 ° C. Measures of temperature and resistivity are decoded with two 12-bit analog-digital and multiplexed by a ACD converter PIC 18F6527 microcontroller from Microchip Technology

programmed for the purpose required. The data is sent to the computer through a USB connection, achieved through the use of decoding module FT245BM. The interface (Fig 10) is very simple and familiar. Real time graphs are produced on the screen.

5.2 Resistance of superconductors measurement.

For measurement we used a YBCO (Yttrium Barium Copper Oxide) "Colorado." On the contacts side we have glued the temperature sensor, on the other side we have positioned
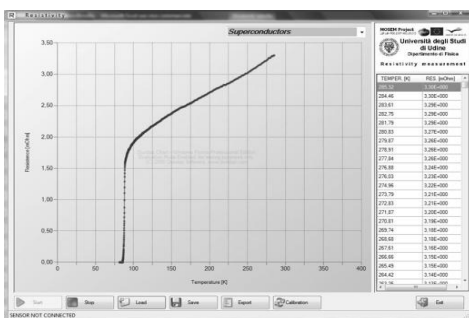
Fig 10. The user interface for the measurement of the resistivity vs temperature of a solid sample (superconductors in the case of the figure)

the heater, made of an aluminium plate of thickness 4 mm, inside of which are housing two 10 ohm resistors in series (heating current of 220 mA, taken directly from the USB connection). Everything was placed inside a aluminium container, closed at the top with a screw cap, used for immersion in liquid nitrogen. The top of the container is made with a tube, suitable for the passage of the cable connection and size that do not seal the container (Fig. 11).
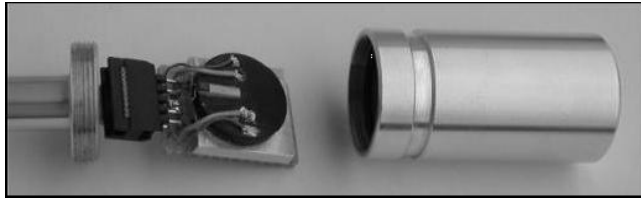
Fig. 11 – YBCO sample with aluminium container

The testing system: The temperature sensor is putted in contact with the sample in the Al box and connection wires are collected on the cover of a thermos containing the liquid nitrogen (Gervasio, Michelini 2010b).
Testing data are reported in fig. 10, 12 and13. In figure 12 a commercial testing sample is used, obtained data in rampa heating at 0,02 °C per second.
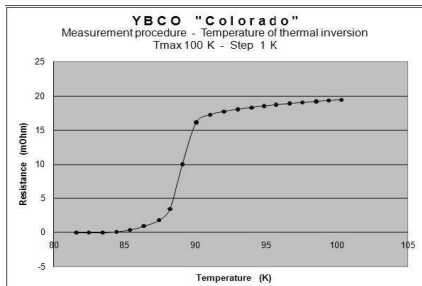
Fig.12 – Data obtained with commercial sample at heating rate of 0,02 °C/s
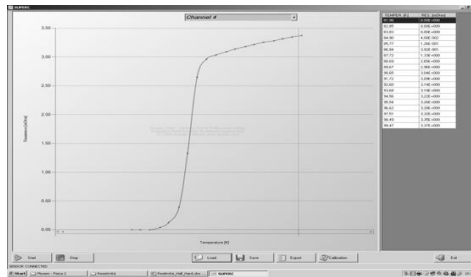
Fig.13- Example of measurement. The duration of measure is about 15 minutes

5.3 Resistance of semiconductors measurement

Even in this case the heater is formed by a plate of aluminium of dimensions 22 x 22 x 4 mm, within which are housed four 1.2 ohm resistors connected in series to provide a total value of 4.8 Ω (Fig. 14). The power supply for the heater is given by a small external power supply (typical power adapter to charge cell phone or similar) from 5 V to provide a suitable heat output of 5 watts, required to bring the sample from nitrogen liquid temperature to 400 K .
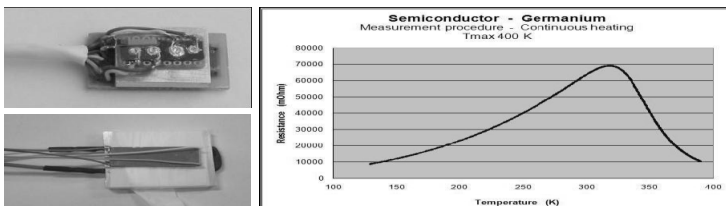
Fig. 14. To the left. A semiconductor sample assembled and insulated before inserting it in the aluminium box. To the right example of measurement of resistivity versus temperature, where is evident the first increasing part related to the extrinsic behaviour of the doped sample, and the last intrinsic part, related to the intrinsic behaviour of the resistivity of a semiconductor

The sample of semiconductor has been packaged as in the previous case and everything was placed inside a aluminium container (the bottom of the container used for superconductors) partially immersed in nitrogen liquid for cooling. Once at the desired temperature, the container is extracted from the nitrogen liquid, maintained in the environment of the Dewar, and begins continuous heating. In Figure 15 we see that in a first zone behaviour resembles that of metals (extrinsic behaviour due to the doped impurities and the second part of the curve the concentration of free carriers increases exponentially with increasing temperatures, producing the decreasing of the resistivity of the sample (intrinsic behaviour for a semiconductor).

5.4 Resistance of metals measurement

The sample is made with a piece of insulated copper wire wrapped as shown in fig. 15. The insulation between heater, sample and thermal probe is realized with multiple Teflon wrappings. The measurement procedure is the same already described for semiconductors. Sample data reported here (Fig. 15) with the relative fitting are representative of the sensitivity and reliability of the system.
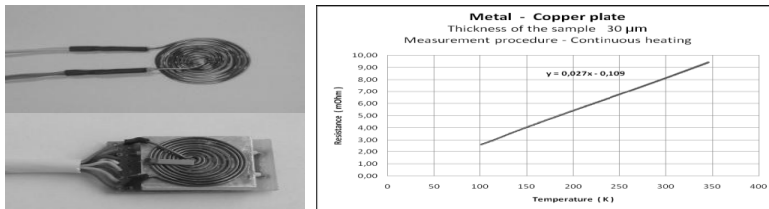
Fig.15 - The copper sample and resistance measurements and fitting

5. 5 Software

The software interface for the measurement of resistivity is quite simple and only takes a few tricks to its proper use.
You first need to select the channel associated with the measure (superconductor; semiconductor, metal - Fig. 16). This is done according to the value of the resistance of the sample and the injected current, so as not to bring the operational amplifier saturation.
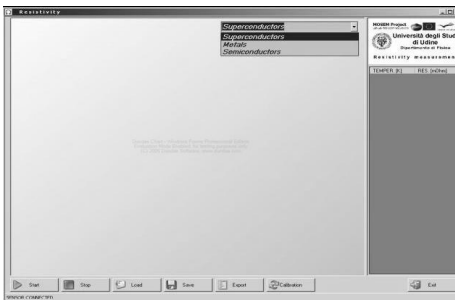
Fig.16 – Resistance measurement Software: windows to select the channel (measurement of superconductors, semiconductors, metals)

continuous heating (Fig. 17).

Once you press the button "Start" the system asks if you want to continue with the simple measure, without heating, or if you want to set the heating controls. To measure free, just press "OK" (Fig. 17).
To make the measurement with the heating is required to tick the corresponding application. The screen that appears as a consequence of this choice, you can set the value of the maximum temperature at which it wants to bring the sample (starting from the current temperature), the step that will be used in temperature controlled by heating or set the
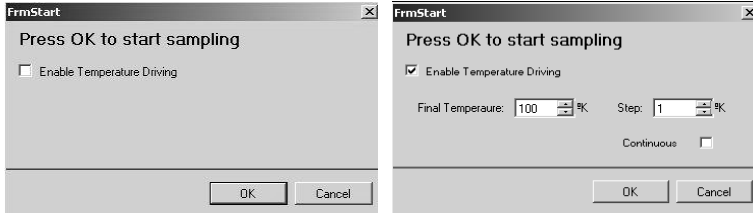
Fig.17 – The start windows, before and after enabling temperature Driving

6. Hall effect measurement

The Hall effect measurement system is managed with a very simple software, suitable for both samples metals and semiconductors (Fig. 18).
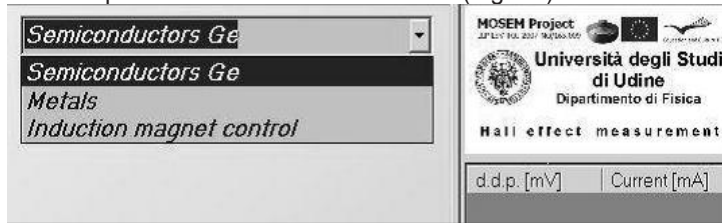
Fig.18 – The window to select the channel for the measurement of the Hall coefficient

Another opportunity is to be able to review the law of variation of the magnetic field of permanent magnet system used for measurement, depending on the distance between them (Induction magnet control). The Fig. 19 shows the permanent magnet system used to measure Hall effect for the metal and semiconductor samples.

Fig.19 – The permanent magnet system used to measure Hall effect for the metal and semiconductor samples. The distance between two neodymium magnets can be easily changed obtaining magnetic field strength of about 1 T

To measure Hall effect on semiconductor and metal samples, it works simply by choosing the desired option on the menu to scroll up on the right of the screen. After choosing the option to measure, the first thing to do is that of calibration. You start this process by taking on the "Calibration", with the sample completely outside the magnetic field. This screen shows the window like in Fig. 20 (left), showing the voltage measured on the active channel.
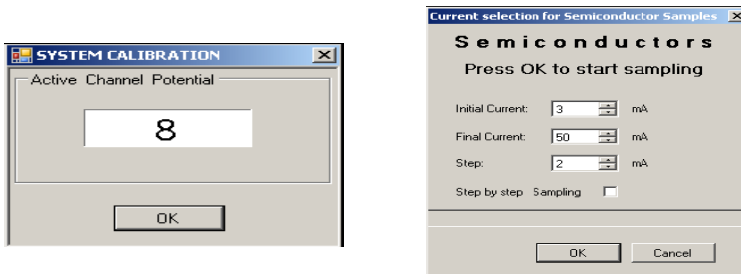
Fig. 20.The dialogue windows of the Hall coefficient measurement system, to set up the measurement parameters
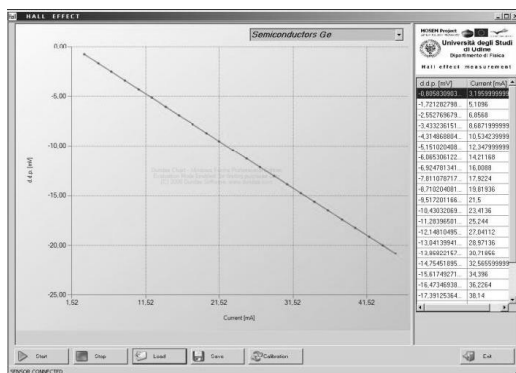
Fig. 21 – Hall measurement on a sample of germanium doped

It acts on this multi-turn potentiometer on the sample in order to read a potential equal to 0 (zero). This procedure is necessary to eliminate the potential difference that inevitably is created for the not perfect alignment of the terminals for the measure of the d.d.p. Hall. After finishing this procedure begins by acting on the measure button "Start". The system asks you to set the initial value of current injected into the sample, the final value and the step current you want (Fig. 20-right). At this point the measurement can be performed automatically or step by step at the request of the operator. To do this you must tick the appropriate option. Depending on the type of sample chosen for measurement, metals or semiconductors, vary the range of current accepted. For metallic samples is requested the same external power supply used for heating in the measurement of resistivity.

Conclusion

The cluster of tools for physics didactic laboratory here presented is constituted of sensors connected via USB to the computer for dedicated measurements of: temperature in time with 4 probes; light intensity vs space displacement; resistivity vs temperature for metal, semiconductor and superconductor. The connection to the computer via USB provides brief time of setting up and few knowledge of electronics, for a good use and eventual modifications. The hardware/software solutions ensure higher sensitivity than those typical of commercial apparatuses, allowing measures of high quality and reliability. The solid and compact assembly of the apparatuses allows easy transport and use. The software usually offers several options for each phase and the user may choose the procedure(e.g. setting up, calibration, measure, management of files) and assign few operations and parameters (e.g. sampling interval, number of sensors to use, variables and scale for real-timegraphs). In this prospective on-line measurements with sensors are thought as a first extension of senses in a laboratory that aims to a study of phenomena to reach a formalization based on an interpretativeexamination of experimental analysis. The active participations of learners in the projects of the experiments that can be done is stimulated by the opportunity to set up easy the procedure of measurements, both for the choice of the parts to utilizeand for the way to utilize them. The users plan the way to carry out the experiment, so that planning and manipulative aspects, the analysis and the interpretation of data, are choices in an experimental activity in which each one may organize the construction of his knowledge.

References

Bernhard J. (2003) Physics Learning and Microcomputer Based Laboratory (MBL) — Learning effects of using MBL as a technological and as a cognitive tool, in D. Psillos, P. Kariotoglou, V. Tselfes, G. Fassoulopoulos, E. Hatzikraniotis& M. Kallery (Eds.), Science education research in the knowledge based society (pp. 313-321) Kluwer Academic Press

Binda M G, Fanutti M, Stefanel A (2005) Sensori on-line nella scuola dell'infanzia e nella scuola primaria, in M Michelini, M. Pighin eds, Comunità Virtuale dalla Ricerca all'Impresa dalla Formazione a Cittadino, contributi selezionati al XLIII Congresso Annuale AICA, Udine: AICA - Università di Udine, ISBN: 88-8420-287-6, pp. 969-973

Corni F, Mascellani V, Mazzega E, Michelini M, Ottaviani G, (1993) A simple on-line system employed in action experiments, in Light and Information, Girep Book, L C Pereira, J A Ferreira, H A Lopes Editors, Univ. do Minho, Braga.

Frisina A, Michelini M, (1996) Physical optics with on-line measurements oflight intensity, in Teaching the Science of Condensed Matter and New Materials, GIREP-ICPE Book, Forum, p.I62

Gervasio M, Michelini M, (2006) TERMOCRONO. Un semplice sistema economico eflessibile per misure di temperatura in tempo reale, in Didamatica 2006- Atti, Andronico A, Aymerich F, Fenu G eds., AICA, Cagliari, p.522-529

Gervasio M, Michelini M (2010a) Lucegrafo. a simple USB Data Acquisition System for Diffraction Experiments, in Michelini M. ed, Prooc. *Multimedia in Physics Teaching and Learning, selected paper from the 14th MPTL Workshop, Udine 2009,* Università di Udine, http://www.fisica.uniud.it/URDF/mptl14/contents.htm

Gervasio M, Michelini M (2010b)A USB probe for resistivity versus temperature and Hall coefficient,in Michelini M. ed, Prooc. *Multimedia in Physics Teaching and Learning, selected paper from the 14th MPTL Workshop, Udine 2009,* Università di Udine, http://www.fisica.uniud.it/URDF/mptl14/contents.htm

Girardini D., Sconza A., Mazzega E.. Michelini M. (1991) Studio della conduzione del calore con l'utilizzo del computer on-line, La Fisica nella Scuola, XXIV, 2, 1991, p.7I

Giugliarelli G., Michelini M., Michelutti G. L., Santi L., (1994) *Tecnologie moderne e progettualità nell'attività sperimentale per favorire i processi di apprendimento*, in Strategie di insegnamento della fisica: il ruolo del problema e il ruolo del laboratorio, La Fisica nella Scuola, XXVII, 4 Suppl. Spec., p.113-135

Hirata K. (1986) *How can we use microcomputers effectively in teaching and learning physics*?, Communicating Physics, ICPE (IUPAP), pag.132

Hofstein A., Lunetta V.N. (2004) The Laboratory in Science Education: Foundations for the Twenty-First Century, *Science Education, vol. 88, Issue 1, pp.28-54*

Lunetta V,N., Hofstein A. and Clough M., (2007), Learning and teaching in the school science laboratory: an analysis of research, theory, and practice, In N, Lederman. and S. Abel (Eds,), Handbook of research on science education. (pp. 393-441),

Mascellani V.,. Mazzega E.. Michelini M.. (1989) Nuove opportunità di apprendimento in ottica mediante l'uso dell'elaboratore, La Fisica nella Scuola, XXII, suppl.4, 4, p.4S.

Mascellani V., Mazzega E., Miche!ini M. (1992) Un sistema per esperienze di ottica on-line e indicazioni per attività didattiche nello studio della diffrazione ottica, La Fisica nella Scuola, XXV, Speciale congiunto AIF-SIF),p.l32

Mazzega E., Michelini M. (1990) Termografo: un sistema per misure di temperatura on-line nel laboratorio didattico, La Fisica nella Scuola, XXII, 4,p.38

Mazzega E, Michelini M, (1996a) On-line measurements of thermal conduction in solids: an experiments for high school and undergraduate students. Teaching the Science of Condensed Matter and New Materials, GIREPICPE Book, Forum Udine.

Mazzega E, Michelini M, (1996b) Termografo: a computer on-line acquisition system for physics education, in Teaching the Science of Condensed Matter and New Materials, GIREP-ICPE Book, Forum, p.239

Michelini M (1992) L'elaboratore nel laboratorio didattico di fisica: nuove opportunità per l'apprendimento, Giornale di Fisica, XXXIII, 4, p.269

Michelini M. (2005) *The Learning Challenge*, in Planinsic, G., and Mohoric, A. (Eds.), *Informai Learning And Public Understanding Of Physics*, (Girep-University of Ljubijana, Ljubijana, 2006), pp. 18-39.

Michelini M, Pighin M. eds (2005) Comunità Virtuale dalla Ricerca all'Impresa dalla Formazione a Cittadino, contributi selezionati al XLIII Congresso Annuale AICA, Udine: AICA - Università di Udine, ISBN: 88-8420-287-6.

Michelini M., Santi L., Stefanel A. (2010)Thermal sensors interfaced with computer as extension of sense in primary school, Il NuovoCimento C, Vol. 33, 3, pp. 171-179

Michelini M, Stefanel A. (2004) Una collana di esperimenti realizzati con materiale povero e sensori collegati in linea con il computer per esplorare Stati e processi termici, Università di Udine, Udine

Riel M.,(1998) *Educational Change in a technology-rich environment*, Journal of Res. In Computering in Education, 26, pp. 31-39

Swan K., Miltrani M., (1998)*The changing nature of teaching and learning in computer-based classrooms*, Journal of Res. In Computering in Education, 25, pp. 121-127

Sokoloff , D.R.., Lawson, P.W., Thornton, R.K. (2004) *Real Time Physics*, Wiley, New York.

Thornton, RK., and Sokoloff DR. (1999) Learning motion concepts using real-time microcomputer-based laboratory tools, *Am. J. Phys.* 58 (9), pp. 858-867

Van den Berg E., Ellermeijer T., Slooten O. (2007) Proc. GIREP conf. 2006, *Modelling in Physics and Physics Education,* GIREP -Conference, Amstel, Univ. of Amsterdam , Amsterdam, ISBN/ISSN: 978-90-5776-177-5

Zacharia Z (2003) Beliefs, Attitudes, and Intentions of Science Teachers Regarding the Educational Use of Computer Simulations and Inquiry-Based Experiments in Physics, JOURNAL OF RESEARCH IN SCIENCE TEACHING VOL. 40, NO. 8, PP. 792–823.

Experiments in a research based path on superconductivity for secondary school

Marisa Michelini[1], Rossana Viola[2]
Physics Education Research Unit of the University of Udine, Italy
Corresponding authors: marisa.michelini@uniud.it , rossviola@yahoo.it

Introduction

In the framework of Mosem EU project on superconductivity, we developed a curricular proposal based on a set of experiments on electromagnetism and superconductivity. It consists of a series of low tech and high tech experiments, useful both for students learning and teacher training. The experiments on electromagnetism play the role of a sort of introduction to understand the contribution of electromagnetic induction in some phenomena linked to magnetic levitation of a magnet on a superconductor.

The value of these experiments is incremented by the teaching/learning path we developed and in which are integrated.

In the framework of a research for a curricular teaching/learning path in vertical perspective, according to MRE model (Duit R., 2006), a study dedicated to the specific knot of magnetic levitation – Meissner effect and pinning effect - to students (17 – 18 years old) of 4th and 5th year of Secondary School has been carried out. The context was those of the Summer School on Modern Physics, organized by Physics Department of University of Udine in the Project of the Lauree Scientifiche Project - *Innovazione didattica in Fisica e Orientamento* (IDIFO2). It took place in July 2009. The class group we worked with consists of 42 students, selected on the base of their school curricula.

An experimental explorative learning path has been carried out: the situation path is offered with CLOE conceptual labs approach (Michelini, 2005) in which an explorative hands-on situation path is proposed using stimuli worksheets (Martongelli, 2001; Michelini, 2003) and a strategy based on SPPEA cycles (Situation, Prevision, Planning, Experiment, Analysis). These worksheets were organized in a path for students, done in previous researches (Fedele, 2005; Bradamante, 2005; Michelini, 2006). Rogersian interview followed the activity to clarify interpretative spontaneous ideas and type of reasoning.

Learning paths for low secondary school students (14 – 15 years old) have been carried out too.

In this work main experiments on superconductivity are presented, underlining aims, equipment, what to do, observed results and explanation of phenomena.

At the end of the work the learning path is presented in detail, through the sequence of experiments It is based on. The rationale is shown through the detailed research questions to study the learning processes: for each situation (Sx) research questions (Ry) are shown.

Experiments

We reported here some of the simple experiments integrated into the educational path designed and experimented.

Magnetic levitation: Meissner effect

Aim: to study magnetic properties of superconductors

Equipment:

- a sample of YBCO (II type low pinning superconductor)
- a strong magnet
- a plastic pliers
- a Petri cup
- liquid nitrogen
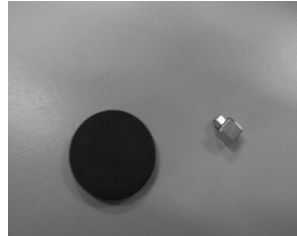
What to do:
1. put the magnet near the sample of YBCO to individuate eventually magnetic properties of YBCO.
At the room temperature there is too low or null interaction.

2. put the sample of YBCO into the cup, put the magnet on the sample, pour liquid nitrogen on the system; pay attention to leave the magnet in its position (if it moves, take it with pliers and never with your fingers), let the nitrogen finishes to boil: now YBCO is at the temperature of 77K.
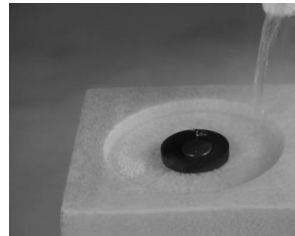
When temperature decreases, the magnet goes up and levitates on the superconductor. This happens because, under critical temperature Tc (92K for YBCO), the sample becomes a superconductor, It behaves as a perfect diamagnetic material and expel the magnetic field of the magnet (Meissner Effect) and this causes repulsion.
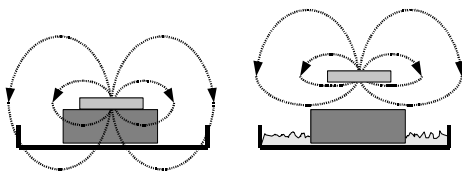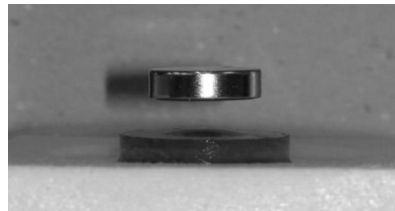
On the left, a sample of YBCO(grey coloured) and a magnet (blue coloured) at the room temperature: the sample of YBCO behaves as a normal metal and magnetic field crosses It.

On the right, the system under critical temperature: the superconductor expels the magnetic field of the magnet (Meissner Effect).
Meissner Effect: the force acted by the superconductor on the magnet (on the right) is the same force that a virtual magnet, symmetric with respect superconductor surface (on the right), would act. Superconductor behaves as a "magnetic mirror".
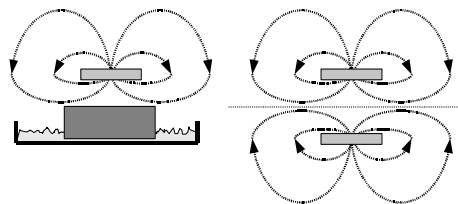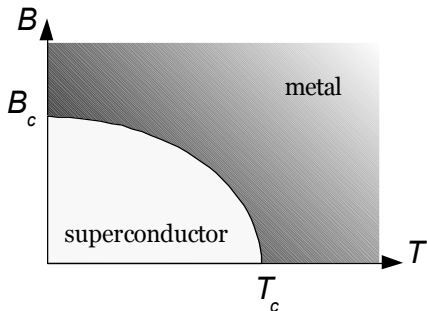
Phase diagram, illustrating the conditions of existence of superconductivity in a metal: superconductivity exists only below a given temperature (Tc), and magnetic field (Bc).

When the pellet temperature increases and goes up critical value, superconductive properties are lost and the magnet falls down.

This experiment is known as "field cooled experiment": at the room temperature the sample of YBCO is in magnetic field of the magnet and It crosses It, than is cooled and we observe described Meissner effect.

Take the magnet with pliers and move It, putting It far and than, near again. We observe that levitation comes back.

3. "zero field cooled experiment": cool the sample of YBCO (with low pinning) without a magnetic field and only after cooling, below the critical temperature, is the magnetic field introduced by bringing the magnet near. Observed effect is the same of the case 2 and we observe levitation of the magnet but in this case there is no Meissner effect because there is no expulsion of magnetic field by the superconductor.

The reason of this link between superconductors and magnet is due to a partial pinning of magnetic flux.

Magnetic levitation: Meissner Effect and pinning Effect

Aim:
to study the effects of a strong pinning

Equipment
- sample of YBCO (strong pinning II Type superconductor)
- a strong magnet
- a plastic tin spacer
- plastic pliers
- a Petri cup
- liquid nitrogen

What to do
1. put the magnet near the sample of YBCO to individuate eventually magnetic properties of YBCO.

At the room temperature there is too low or null interaction.

2. Place the sample of YBCO in the cup, place the spacer on the sample and the magnet on the spacer, pour liquid nitrogen on the system, let the nitrogen finishes to boil: now YBCO is at the temperature of 77K. Take away the spacer. We observe that the magnet levitates on the superconductor. Try to move the magnet using pliers: you
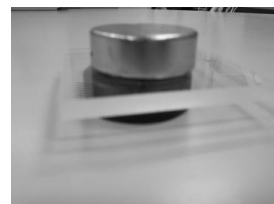
can feel that It is too difficult.

3. Repeat the experiment without spacer. After the transition they are attached and It is very difficult to separate them.
A strong magnetic link between magnet and superconductors is observed.
This link exists with both used samples, but with a strong pinning pellet It is so strong to "hide" Meissner effect.
Actually, there are two types of superconductors:
- type I superconductor, where superconductivity can only exists in the Meissner state, under critical values of temperature Tc and magnetic field Bc, with no magnetic field present in the bulk of the pellet. There is perfect diamagnetism and pinning effect is no observed. So, after the transition, we can observe levitation only in particular situations, like the following
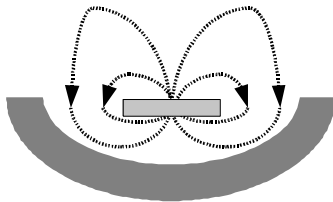
A bowl made of lead, cooled down below 7.4 K, becomes a type I superconductor. A magnet in this bowl will levitate and will not fall. To cool down the lead bowl, liquid helium, instead of liquid nitrogen, is used. Liquid helium is cooler (4.2 K under ambient pressure), but is more expensive and is more difficult to manipulate.

- Type II superconductor that have a behaviour that is more complex. This behaviour is responsible for the existence of the observed magnetic "link".

A USB PROBE FOR RESISTIVITY VERSUS TEMPERATURE AND HALL COEFFICIENT

A USB probe for the measurement of resistivity versus temperature in metal, superconductor and semiconductor solids and a combined room temperature Hall coefficient measurement for metals and semiconductors has been developed and patent by Mario Gervasio and Marisa Michelini. The resistivity measure can be carried out in the 78-400K temperature range selecting different controlling heating rate. Current and magnetic field are parameters to select by the user in Hall coefficient measurement. The software interface is designed to be user friendly, giving to the user the opportunity to set up the relevant parameters of the measurements and to have a direct vision of the real time graph during the experiments. High quality measurements give to opportunity to fit data with curves based on theoretical models.
The system to measure the resistivity versus temperature has been designed so as to implement measures in a four-terminal configuration, the two external contacts are used for the injection current and the two internals to measure the voltage, proportional to the electrical resistance of the sample.
Measurement procedure can be chosen by the user:
- thermal inertia, from the temperature of nitrogen liquid at room temperature
- ramp with continuous heating
- temperature of thermal inversion. Is chosen, via software, the gap in temperature between a measure and the next.

Each measurement is made by detecting the voltage, on the two internal contacts, first time with the injected current and then subtracting the voltage corresponding to zero current.

Under these conditions it is obvious that there is no need for manual adjustment of the offset because the correct measure of the voltage will be that obtained from the difference of the two readings (measure "quasi ac").
To make the resistivity measurements have been designed in three hardware modules:
1. constant current source;
2. voltage measurement;
3. heater.
This current through VREF1 tension generated by software.
The injected current in the samples can be varied from 1 to 150 mA.
To measure the temperature is used as sensor a PT100 platinum resistance.
Measures of temperature and resistivity are decoded with two 12-bit ADC and multiplexed by a PIC 18F6527 microcontroller from Microchip Technology programmed for the purpose required.
The data are sent to the computer through a USB connection. The duration of measure is about 15 minutes
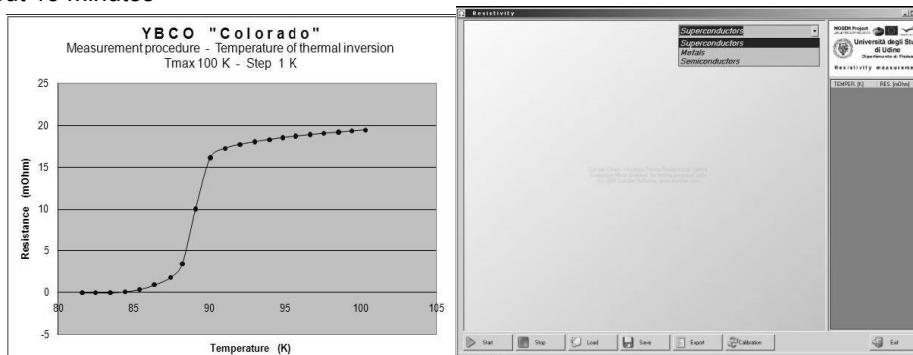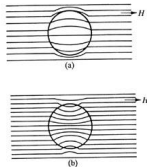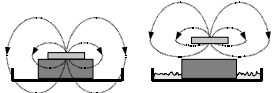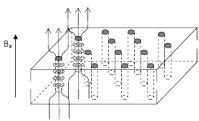
Curricular path and its research questions

In Table 1 the research question (RQ) are split according with the main situations (S) of the learning path and the relative written questions posed to students (Qx).

Table1. The detailed research questions of the path

Situation (S, in the worksheet)	Research questions (RQ)
1. INTERACTION BETWEEN DIPOLES	
S1. Put a magnet near an other magnet: interaction between dipoles	1- Is the planning proposal based on explicit/implicit hypothesis?
S2. Representations of a magnetic dipole: Using vectors, scheme of all the situations found and relative effects. $\rightarrow \leftarrow \quad \leftarrow \rightarrow$ $\rightarrow \rightarrow \quad \leftarrow \leftarrow$	2- Do students recognize the different types of interactions between two magnets according to faced poles (attraction or rotation + attraction) 3- Do students use a description in terms of dipole?
S3. Examining the attraction at a distance with different explorers in the space around a magnet, magnetic field lines are recognized.	4- Do students recognize that magnetic field lines are closed?
S4. Magnetic field lines pattern in two cases - equal poles facing - different poles facing Representation, for each situation, in terms of vectors of	5- Does the idea of superposition of field emerge? 6- Do students describe lines and/or compare them in the various situations?

dipole and in terms of field lines.	Do they recognize that field lines pattern allows a prevision about the type of interaction that will be between the dipoles?
S5. Analysis of the possibility of suspension of a magnet on an other one. Representation in terms of vectors of dipoles and in terms of field lines. .	7- Do students recognize the impossibility of suspension of a magnet on an other one without a constraints? 8- Are students reasoning on a descriptive level or on an interpretative one too? 9- Is a description in terms of dipoles used? 10- Are magnetic field lines used to explain phenomenology?
2. INTERACTIONS OF A MAGNET WITH OBJECTS MADE OF DIFFERENT MATERIALS: FERRO – PARA – DIA MAGNETISM	
S6. Interactions between a magnet and objects made of different materials, putting the magnet near: S6.1. a paper clip or a little sphere: ferromagnetism S6.2. a torsion balance with [copper sulphate and water] or [aluminium dust and water] or [copper sulphate and oil]: para and diamagnetism S6.3. a thin pyrolytic graphite lead: diamagnetism Representation, for each of the three situations, in terms of vectors of dipoles and in terms of field lines.	11- Do students represent experimented situations using a description in terms of dipoles and field lines? 12- Are students reasoning on a descriptive level or on an interpretative one too? Which interpretative models emerge for observed phenomenology? 13- Are the analogies and differences between observed situations recognized? 14- Do students recognize considered objects behaviour as dipoles, induced by external magnetic field? 15- Do students explore phenomena studying only one or both the poles of the magnet?
S7. Analysis of the possibility of suspension of a thin pyrolytic graphite leaf on a magnet.	16- Are the analogies and differences with the case of the suspension of a magnet on an other one recognized? 17- Do students recognize the need of a constraint to have suspension?
S8. Exploration of interactions between a magnet and a sample of YBCO (YBa2Cu3O7 – a II type low pinning superconductors) to determine the type of material.	18- Is the planning proposal based on explicit/implicit hypothesis?
3. FIELD LINES	
S9. Analysis of magnetic field lines inside and outside materials: S9.1. Analysis of the possibility that the presence of a material in a uniform and constant magnetic field may modify total magnetic field. S9.2. Analysis of how total magnetic field is modified if a ferromagnetic, paramagnetic, diamagnetic material is inserted in a uniform magnetic field, according to the representation with field lines, to the representation with vectors of dipoles and to observed behaviour in experimental exploration.	19- Do students take into account the principle of superposition of fields? Both inside and outside the material? 20- Do students give a description/interpretation in terms of dipoles and/or field lines?

S9.3. Field lines pattern for the system magnet + YBCO (at the room temperature)

S10. Exploration of the behaviour of the system magnet + YBCO (a II type low pining superconductors) when temperature decreases (using liquid nitrogen): Meissner effect and pinning effect	21- Is the transition recognized? Are descriptions in terms of process? 22- Are students on a descriptive level or on an interpretative one? 23- Is a description in terms of field lines used?
S11. Comparison and description in terms of dipoles for each one of following cases: 1) two magnets 2) magnet and pirolythic graphite 3) superconductor and magnet While in the case of the diamagnetism of the pyrolytic graphite a not equilibrium suspension is shown, the superconductor seems to be in equilibrium. Pinning effect.	24- Do students use a description in terms of dipoles? 25- Which interpretative models emerge to explain pinning effect?

4. THE ROLE OF FARADAY-NEUMANN-LENZ LOW

S12. A magnet levitating on a sample of YBCO (a II type low pinning superconductors) – the role of Faraday-Neumann-Lenz Low in some phenomena linked to magnetic levitation: S12.1. the magnet levitates and It does not fallow on the superconductor S12.2. for levitating magnet there is only one permitted rotating axis, that is the magnetic N-S axis of the magnet S12.3. magnet levitates with any orientation of Its magnetic axis and, in spite of the fact that there is only the friction with air, It does not orientate following Earth	26- Do students interpret observed phenomena in terms of magnetic flux variation using Faraday Low? How?

magnetic axis	
5. THE EFFECTS OF HIGH PINNING	
S13. Exploration of interactions between a magnet and a sample of YBCO (YBa2Cu3O7 – a II type high pinning superconductors) to determine the type of material. Field lines of the system magnet + YBCO (at he room temperature)	
S14. [Cooling with a magnetic field] Exploration of the behaviour of the system magnet + YBCO (II type high pinning superconductors) when temperature decreases in the two following cases: S14.1. magnet on the sample of YBCO S14.2. with a spacer between Field lines pattern of the systems after the transition. Description and comparison of situations S 10, S14.1. and S14.2 before and after the transition, in terms of vectors of dipole, in terms of field lines and in terms of flux variation.	27- Do students recognize the birth, between magnet and superconductor, of a link of the same type of last exploration? 28- Which interpretative models emerge to justify the different strength of that link as regards last case?
S15. [Cooling without a magnetic field] To cool the sample of YBCO and then try to put near the magnet.	29- Which interpretative model is used to explain observed behaviours?
6. STABILITY OF LEVITATION	
S16. A thin pyrolytic graphite leaf and 4 magnets (parallelepiped shaped): possibility to obtain levitation of the graphite on the magnets 	30- Is the planning proposal based on explicit/implicit hypothesis?
S17. A sample of II type high pinning superconductors (with a spacer) on: 1) a magnet 2) a quadrupole The system is cooled. Exploration of behaviour and stability in both the situations. Description and comparison of the two situations, before and after the transition, in terms of vectors of dipole, in terms of field lines and in terms of flux variation.	31- For each the cases 1) and 2), do students give a description/interpretation in terms of dipoles, field lines, flux variation? 32- Which interpretative models emerge to justify the differences in stability of levitation in the two situations?

7. LEVITATING MAGLEV TRAIN	
S18. Problem solving. Prototype of MAGLEV train based on magnetic levitation. Students are asked to: 1) describe the train 2) describe Its functioning 3) explain Its functioning	33- Which descriptive elements of the system and of Its functioning emerge as important from the descriptions given by students? 34- Which interpretative models are used to explain the functioning of MAGLEV train?

Conclusions

A series of simple low tech and high tech experiments on superconductivity is integrated in a research based educational path for secondary school students. The proposal is studied into the framework of design based research and the EU project Mosem. According with MRE research line the proposal were experimented with talent secondary school students participating to the IDIFO2 Italian Summer School.

The proposal here presented has been described through detailed research questions done in the study of the learning processes: for each situation (Sx) research questions (Qy) have been indicated.

Dividing each step in research questions is very useful also for the teacher who is interested in knowing ways of reasoning and conceptual organization of knowledge of the students.

Data analysis carried out on the experimentation is based on the classification of the answers to the research questions, to underline associated conceptual developing.

The path of research questions is a useful guide also for the teacher who wants to plan an analysis of the reasoning of the students according a coherent framework and organized paths.

REFERENCES
[1] Bagno, E. and Eylon, B. S., Am. J. Phys. 65 (8) 726-736 (1997).
[2] Bartolini Bussi, M., Lyn D Englis, Graham A. Jones, Richard A. Lesh, Dina Tirash, Handbook of International Research in Mathematics Education. Publisher Lawrence Erlbaum Associates, Place of publication Mahwah, NJ, 2002 , chapter 28
[3] Bradamante, F., Michelini, M., Childrens' ideas about gravitation: investigating a model of gravitationalfiel, in Teaching and learningphysics in new contexs, Girep book of selected papers, Ostrava Czech Republic, 2004, p.I 80-182 [ISBN 80-7042-378-1]
[4] Bradamante, F., Fedele, B., Michelini, M., (2005), Children 's spontaneous ideas ofmagnetic and gravitationalfields, ESERA, selected paper, Cresils, Barcellona [ISBN: 689-i 1-29-1]
[5] Borges, A. T. and Gilbert, J. K., Int. Journal of Sci. Ed. 20 (3) 361-378 (1998).
[6] Duit, R., ESERA Summer School, Braga, 2006, at http://www.naturfagsenteret.no/esera/summerschool2006.html
[7] Faraday, M., Experimental Researches in Electricity, London: Taylor and Francis (1955), Vol I, II, III.
[8] Fedele, B., Michelini, M., Stefanel, A. (2005) A. Five-ten years old pupils explore magnetic phenomena in Cognitive Laboratory (CLOE), ESERA, selected paper, Cresils, Barcellona [ISBN: 689-1 1-29-1]
[9] Galili, I. and Kaplan, D., Am. J. Phys. 65 (7) 657-668 (1997).
[10] Guisasola, J., Almudi, J. M. and Ceberio, M., Science Education, 8 (3) 443-464 (2004).
[11] Guisasola, J., Almudi, J. M. and Ceberio, M., Students ideas about source of magnetic field, II int. Esera Conf., pp. 89-91(1999).
[12] Guisasola, J., Almudi, J. M. and Ceberio, M., Enseñanza de las Ciencias, 21 (2) 281-293(2003).
[13] IDIFO2 is a national Italian project on Modern Physics in secondary school. Responsible: Marisa Michelini. Participants: 15 Italian university research unit in Physics Education
[14] IPN Kiel, Die elektromagnetische Induktion (IPN Curriculum Physik) Stuttgard, (1985).
[15] Maloney, D. P., O'Kuma, T. L., Hieggelke, C.J. and Van Heuvelen, A., Phys. Educ. Res., Am. J. Phys. Suppl. 69 (7), pp S12-S23(2001).
[16] Maxwell, J. C., A Treatise on Electricity and Magnetism,Dover Publications, INC (1954)
[17] Michelini M, The Learning Challenge: A Bridge Between Everyday Experience And Scientfic Knowledge, in Informai Learning And Public Understanding Of Physics, G Planinsic and A Mohoric eds., Girep book of selected contributions, Ljubijana (SLO), 2006, p. 18-39 [ISBN 961-6619-00-4]
[18] Peters, P. C., Am. J. Phys. 52(3) 208–211(1984).
[19] Rainson, S. and Viennot, L., Int. J. Sci. Educ. 14(4), 475-487(1992).
[20] Salverberg, E. R., De Jong, T., Ferguson-Hassler, M. G., Am. J. Phys. 39 (10) 928-951 (2002).

[21] Stefanel, A. (2008) Disciplinary knots and learning problems in electromagnetism, in Sidharth B.G., Honsell F., Sreenivasan K., De Angelis A. eds, Frontiers of Fundamental and Computational Physics, 9th International Symposium, American Institute of Physics, Melville, New York, .231-235

[22] Tornkwist, S., Pettersson, K. A. and Transtromer, G., Am. J. Phys. 61(4) 335-338(1993).

[23] Thong, W. M. and Gunstone, R., Res. Sci. Educ. 38, 31-44 (2008).

PHYSICS EDUCATION BY RESEARCH PROJECTS

Dina Izadi[1] and Hamidreza SeifanAhari[2]
[1]Ariaian Young Innovative Minds Institute (AYIMI),Iran
Email: info@ayimi.org

Abstract

In many countries there is much discussion about the role of problems solving in the curriculum. Educationalists often say that we should concentrate on learning instead of teaching in our classrooms and that the problem solving classroom will encourage good learning because problem solving is a doing activity instead of watching activity. Physics is a strategically important subject that underpins much of engineering and other science subjects. If we cannot introduce this subject to youngsters enormous potential will be wasted. To prepare the secondary school's students for further education at universities and colleges we should provide them with the opportunities to engage in an active learning by research. The traditional teaching methods (including textbooks, lectures, and pages of homework problems) are becoming increasingly less attractive to today's students so observation and in situ experiments which are related to the real life should be modified with learning activity in helping students overcome the identified difficulties in physics education.

Introduction

We should come to notice that there is no border among different sciences and students can learn chemistry, physics, biology,… simultaneously but a key factor in successful learning is a learner's motivation. How can we motivate our students with different abilities and interests? Like all other sciences, physics is based on experimental observations and quantitative measurements which mathematics is a tool that makes connection between theory and experiment. There are fundamental laws that govern natural phenomena and they are used to develop theories that can predict the results of future experiments. But in many countries there is much discussions about the role of problem solving in the curriculum. Educationalists often say that we should concentrate on learning instead of teaching in our classrooms and that the problem solving classroom will encourage good learning because problem solving is a doing activity instead of watching activity. But why some students do not engage in this activity. Are these problems difficult and boring? Don't they understand the problems completely? Do they need to compare these problems with natural phenomena happen around them? Do they need more experiments to solve these problems? These are some questions should be considered by teachers to motivate their students with different abilities and interests. Students should be notified about the importance of what they are taught. Some of the students have no interest in learning as they think these lessons are useless and they will not need them in the future. They should be given some examples of what they are learning in their daily life in order to aware them about the role of their knowledge in their life. This fact that they will be able to improve their life and even make more money with their studies can lead them to comprehend their lessons more enthusiastically.

Solving Problems in Physics by Research

Combination of the knowledge and experiments to motivate students is an important factor in active learning but to improve it in a high level we need a debating and

asking in a cooperative atmosphere. Physics, the most fundamental physical science, is concerned with the basic principles of the Universe. It is the foundation upon which the other sciences—astronomy, biology, chemistry, and geology—are based. Even though the beauty of physics lies in the simplicity of the fundamental physical theories and in the manner in which just a small number of fundamental concepts, equations, and assumptions can alter and expand our view of the world around us but it is too hard for some of the students to learn it. By research students can get idea from other works and perform statistical measurements. In a quantitative research they need some variables to be measured sometimes by experiment and sometimes by questionnaire. The description of these variables in terms of the other variables can be shown in tables and graphs too.

The relation between education and industry is one of the most important parameters can affect learning program. Involving students, teachers and sometimes parents in solving physics problems by research and finding relationship between learning new skills and what industry needs enables us to enrich physics education at schools. During the sequences which are carried out, the following kinds of activities cause students and teachers motivation in physics:

a) **Selected problems which are attractive, practical and related to everyday life,** will encourage students more to solve the problems and find the solutions practically

b) **Involving students by teachers to find a new method in solving the problems,** this makes students think more and try to invent something new and extend their abilities

c) **Qualitative and quantitative approaches and deductions,** which enable students to learn how evaluate their data statistically and compare by plotting graphs

d) **Report the results in a competition individually or in a team work,** makes them self-confidence and enables them to defend their projects

Different Processes in research projects

Sometimes students might require guidance in research projects. Research helps us to see the world with fresh eyes so we can find our place in this world. Re-SEARCH implies two aspects focus on: 1- what and how can we search for in enough details 2- how and what we think about it and its affection in the real world and we should think about both these aspects. Teachers can give an idea about a phenomenon which occurs around us without notification and ask their students to think and find the different processes to investigate it. A team work is very useful because different ideas can be added to help each other. As an example teachers can talk with students about the motion of honey being drizzled (Fig. 1).

Fig. 1. honey being drizzled
http://en.wikipedia.org/wiki/Viscosity
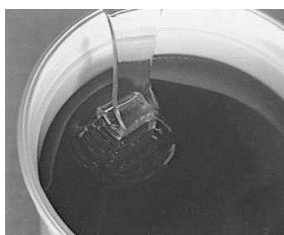
Students who are interested in this subject can start with:

1- Doing experiments with fun

Making physics interesting for students plays a prominent role in learning. Students should have fun during their classes and they should enjoy while doing an experiment or even some calculations, as if they are in a playground. They should eagerly find a way to solve their problems and learn how to cooperate with each other. Although some specialists believe that teachers should be very strict and do not let their students move during the class, they should be invited to work in pairs or groups to discuss. Also as a matter of memorizing, they can remember what they were taught much more easily if they learned it in a different way. By pouring honey they will see its amazing shape which comes done like a spring. Students should do more experiments to get the best results.

2- Investigating the phenomenon by research

Physics is the science of nature. It is nonsensical to say that it can be learned by reading some books and memorizing mathematical formulas. It should be touched by the students and it is not possible unless they do some research projects. Some problems should be designed by the teachers and ask the students to find a solution for that in a specified period of time. To find the most important parameters which affect the spring shape of honey when it pours down, students should search in different fluid mechanics references, make their research by internet and so on.

3- Comparing quantitative and qualitative measurements

Some of these questions (but not essentially all of them) need some experimental setups. In this case students can compare their quantitative and qualitative results and find out their accuracy by calculating the errors in their observations. To find the shearing stress between the layers of honey; the dependency of either dynamic or kinematic viscosity of honey to temperature; calculating the Reynolds number are some of the quantitative measurements. Moreover, the results can be compared with other groups to discuss about the qualitative measurements too. Students can also notice the other possible solutions for their problem or guide their fellow mates.

4- using programming software

Nowadays, using programming software is very popular and young people are also really keen on them. There are a lot of projects in physics that can be simulated, calculated or modeled by these computer programs. As writing these programs need a very accurate mind and are a time consuming process, it can enhance the ability of learners by defining some appropriate projects. Not only can they produce a program than could be developed as the time goes by, but they also dominate every details of the subject which they were asked about.

Conclusions

Research projects are the bases of learning at university and school. The advantage of making students familiar with research projects is preparing them for their future understanding. Regardless of their major at university, the more they get used to "Research Method", they better can tackle their problems afterwards. They may also find their interest in a particular major while doing a project. For example, while doing a project regarding motion and dynamic they may get interested in mechanics engineering or while doing an experiment about printed board circuits they may feel they would like to carry on in electrical engineering. By implementing some basic and simple research projects, in fact students can get ready to analyze some more complicated effects. This highlights the significance of research projects in the future.

References

[1] Berry J. &Sahlberg P., Investigating Pupils' Ideas of Learning, learning and instruction , Vol. 6, No.1, pp. 19-36, 1996.

[2] William M.K. , Qualitative Approaches, http://www.socialresearchmethods.net/kb/

[3] How to Attract More Students to Science and Engineering Using Video Games, http://mvpmodelingsolutions.com/mvpblog/2010/10/how-to-attract-more-students-to-science-and-engineering-using-video-games

IYPT- 2010

No. 1, Electromagnetic cannon: Measurements and simulations of the terminal velocity of a projectile

Saba Zargham[1] and Hamid Ghaednia[2]
[*] Team of Iran, IYPT 2010
[1]*Sharif University of Technology, Iran*
[2]*Amirkabir University of Technology, Iran*
Corresponding authors: saba.zargham@gmail.com, ghaednia.hamid@gmail.com

Abstract: Kicking a ball by means of an RLC circuit can be done using various systems. The explanation of one such design is the main goal of this paper. When a capacitor is discharged into the solenoid, it forces the ferromagnetic plunger to slide through the solenoid and eventually kick the ball. Terminal speed of the ball is proportional to the velocity of the plunger which itself is only determined by the force applied to the plunger by the solenoid. Therefore calculating this force and studying the related factors are necessary which has been done both theoretically and experimentally. Numerical results were compared with experiments in order to prove and examine theoretical conclusions.

Keywords:plunger,solenoid

Introduction

Building shooting device that usesa solenoid and a capacitor (asvoltagesource), is the goal of this article. Such systems are also used in Robocup soccer robots.Whenacapacitor is discharged into a solenoid, the solenoid generates a magnetic field, whichcanexert force on ferromagnetic material, (ex. ferromagnetic plunger).In order to provide the system with the necessary force required to kick a ball,a "plunger" was used which was consisted of two parts, a ferromagnetic part and a non-ferromagnetic shooter, that could slide through the solenoid with the minimum amount of friction possible. (See picture) Experiments were done with a golf ball of 45 grams mass.
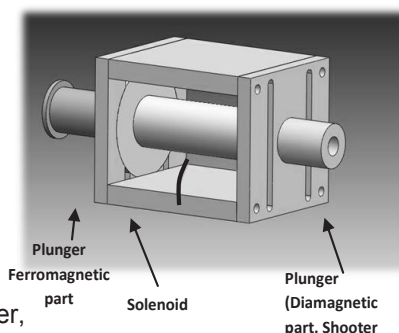
Figure 1:Solenoid and Plunger

Terminal velocity of the ball is dependent on the factors listed below: 1-Initial voltage 2-Capacitance, 3-Diameter of the solenoid's wires, 4-Solenoid's inner diameter, 5-Solenoid's body material, 6-Plunger's diameter, 7-Plunger's length 8-Plunger's mass, 9- Initial position of the plunger, 10-Initial distance between the plunger and the ball, 11-Number of wire turns.

The problem can be classified into three chief sections;we will first discuss the capacitor's discharge procedure. In the second section, the motion of the plunger is studied. And finally, in section three, we present the equations governing the collision between the plunger and the ball. In order to reach a quantitative theory and

investigate all three sections together , a MATLAB program was developed to simulate the design and solve the resulting differential equations (by Runge-Kutta method). Various effective factors mentioned above, are studied both theoretically and experimentally in order to find the optimized solenoid, which results in the maximum velocity at all times.
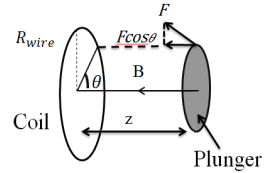
Figure 2:Exerted force to each element from each wire

Theory (Mathematical model)

Section 1

Interactions between the capacitor and the solenoid are simulated (The solenoid being an inductor:

$$+\frac{q}{c} + IR + L\frac{di}{dt} = 0 (1)$$

Figure 3:Total force exerted to each element

$$L = \mu_0 n^2 A\, l_s (2), R = \frac{\rho}{A_w}\left(\frac{l_s}{d_{wire}}\right) = \sum_{i=0}^{\left[\frac{d_{out} - d_{in}}{d_{wire}}\right]n} 2\pi\left(R_p + \frac{2i+1}{2}\right) (3)$$

Where A is the surface area of the solenoid, A_w is the cross section of the wire, d_{wire} is the diameter of the wire, and l_s is the length of the solenoid.

Section 2

There are two general methods for simulating magnetic materials- the dipole method and the current ring method,with the secondmethod having a higher accuracy, which we have chosen to use. Thus, we have consideredthe ferromagnetic part of the plunger to be made up of afinite number of disks (or current rings) with the same radius as the plunger and acurrent, which depends on the thickness of the disk,magnetic field of the solenoid and the plunger's magnetic properties.

$$\mu_0\vec{M} = (k_m - 1)\vec{B} (4)$$

The magnitude of $\vec{M}$ is defined as the magnetic moment per unit volume of a substance. As you might expect, the total magnetic field B at a point within a substance depends on both the applied (external) field B0, and the magnetization of the substance.

Considering the properties of the solenoid results in equation number 5; which simulates the rings current intensity.

$$i = \frac{dv}{\pi R_p^2}(1 - k_m)\frac{N}{l_s}I (5)$$

Where dv isthevolume of each element, $k_m$is a constant dependent onthemagnetic properties of the ferromagnetic plunger, R_p is the radius of the plunger, $l_s$is length of the solenoid, N is the number of current rings and I is the solenoid's current.Substituting for i, (equation number 5), the force exerted on each element of the plunger:

$$f_x = \frac{\mu_0 iI}{2} R_{wire} R_{plunger} \; z \int_0^{2\pi} \frac{d\theta}{(z^2 + R^2 \cos^2\theta + (R\sin\theta - R_{plunger}))^2)^{5/2}} \quad (6)$$

When the capacitor is discharged into the solenoid, the plunger tends to slide through it, in response to the force it feels from the magnetic field. But, we must take into account that each current ring of the solenoid tends to attract the plunger, therefore, as the plunger moves forward it will start to feel a force opposite the direction of it's velocity. (Hence the minus term in the formula below)

Thus, the net force exerted on the plunger can be calculated by integration:

$$
\begin{aligned}
F_x = \lambda &\sum_{j=0}^{(\frac{l_s - y + x}{d_w})} \sum_{n=0}^{(\frac{d_{out} - d_{in}}{d_{wire}})} \int_0^{2\pi} \frac{z \, d\theta}{\left(\left(\frac{2j+1}{2} d_w\right)^2 + \left(R_p + \frac{2n+1}{2} d_{wire}\right)^2 \cos^2\theta + \left(\left(R_p + \frac{2n+1}{2} d_{wire}\right) \sin\theta - R_p\right)^2\right)^{\frac{3}{2}}} \\
- \lambda &\sum_{j=0}^{(\frac{y - x}{d_w})} \sum_{n=0}^{(\frac{d_{out} - d_{in}}{d_{wire}})} \int_0^{2\pi} \frac{z \, d\theta}{\left(\left(\frac{2j+1}{2} d_w\right)^2 + \left(R_p + \frac{2n+1}{2} d_{wire}\right)^2 \cos^2\theta + \left(\left(R_p + \frac{2n+1}{2} d_{wire}\right) \sin\theta - R_p\right)^2\right)^{\frac{3}{2}}}
\end{aligned}
$$

$$\lambda = \frac{\mu_0 iI}{2} R_{wire} R_{plunger} \quad (7)$$

Section 3:

After solving energy and momentum equations, the terminal velocity of the ball is determined: [1],[2]

$$v_b = \frac{2\mu k \, v_{p1} + \sqrt{(2\mu k \, v_{p1})^2 + 4(1-\mu)(\mu k^2 + \mu k)}}{2(\mu k^2 + \mu k)} \quad (8)$$

Where $k = \frac{M}{m}$ (M is mass of the ball and m is the plunger's mass), v_{p1} is the velocity of the plunger before collision and μ is the contact coefficient.

Figure 4: Calculating Terminal Velocity

Experimental Setup

The entire system consists of a solenoid, a plunger and a ball. Both Aluminum and Teflon have been used for the solenoid's body material. The plunger, as mentioned before, has two parts; the ferromagnetic part is made of iron and the diamagnetic part, aluminum.

Figure 5: experimental setup

Figure 6: solenoids used in experiments

A "speedometer" was designed to determine the speed of the ball. This device is consistent of four sensors in order to reach the most accurate result. Experiments were done with solenoids of 5 cm length, 3 cm outer diameter, and three different inner diameters of 10, 8, 6 mm. (Fig.5)

Experimental Analysis

The concurrence between the theory and experiments enables us to use thismethodin finding the optimum dimensions of the system for any given initial conditions. The theory shows that the velocity would alter linearly in respect to the increase of voltage. Experimental results are also in good agreement with this(Fig.7). A capacitor with higher capacity, stores a greater amount of energy, but since it also has an extended discharge time, the plunger won't absorb all the energy before the collision. Therefore increasing the capacitance, more than a certain amount will not result in any changes in the velocity of the ball (Fig.8 & Fig 9).
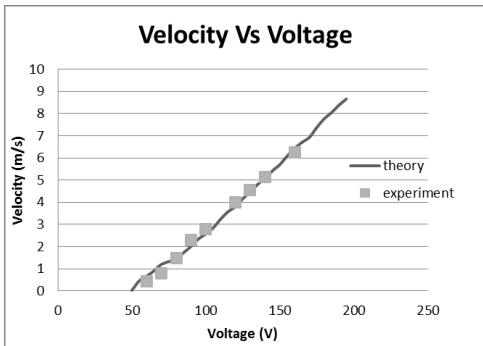
Figure 7: Velocity vs Voltage
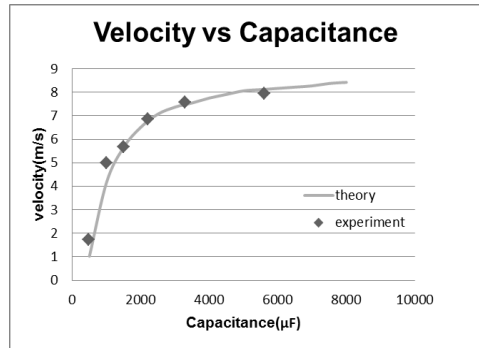
Fig.8 Velocity vs Capacitance

This is why the initial position of the plunger is an important factor;since the energy absorption of the plunger is altered also by the discharge time of the capacitor. The plunger must beinside the solenoid when the current intensity reaches its maximum, in order to hit the ball with maximum velocity . Therefore, as u can see in Fig.10, this factor has an optimum.
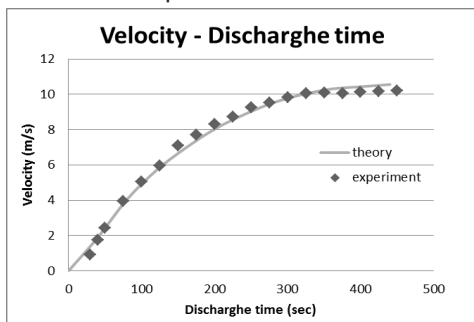
Figure 9: Velocity vs discharge time
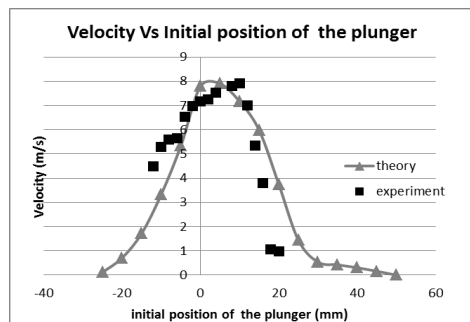
Figure 10: Velocity vs initial position of the plunger

Increasing the number of layers has two different effects on the ball's terminal speed.As the number of layers increase, the resistance of the circuit will also increase. As a result the current intensity inside the solenoid will decrease. Ergo, velocity reduces escalation of the number of layers also increases the inductance of the RLC circuit, so a greater force is exerted on the plunger. Consequently, there should be an optimum number for both of these factors. This point is where the inductor acquires the maximum quality factor, which can be calculated by our numerical method (Fig.11 & Fig.12)
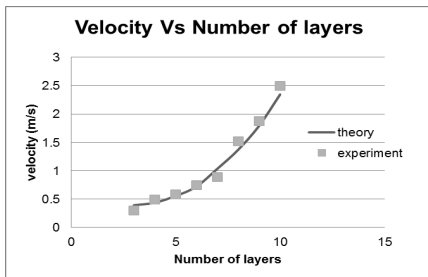
Figure 11: Velocity vs number of layers
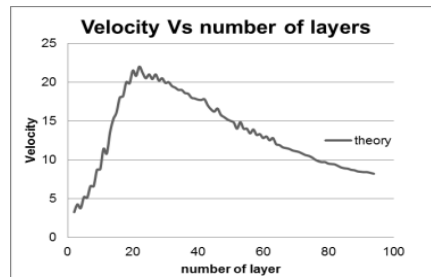
Figure 12: Velocity vs number of layers

The material of the solenoid can significantly affect the strength of the magnetic field inside the solenoid. The solenoid's body is usually made of either diamagnetic or paramagnetic material.

In broad terms, diamagnetism and paramagnetism are different types of responses to an externally applied magnetic field. *Diamagnetism* is a natural consequence of Lenz's law, according to which the electric current resulting from an applied field will be in the direction that opposes the applied field. In other words, the induced current will flow in the direction that creates a field opposite to the applied field. In other words, diamagnetic material can weaken an external applied magnetic field.

Paramagnetism occurs in materials whose atoms lack permanent magnetic dipole moments, whether they are spin types or orbital moments. Thus these materials won't affect the inner magnetic field. Since they tend to align with any external magnetic field.

Fig.13 shows the velocity vs voltage for two different materials used as the solenoid's body, Teflon as a diamagnetic material and aluminum as a paramagnetic one.
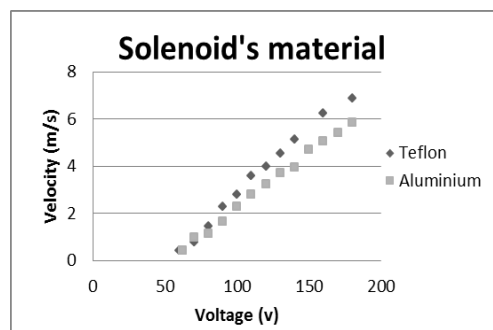
Figure 13: Velocity vsVoltage for different materials

Conclusion

Comparisons between theoretical and experimental results prove our numerical model, hence the numerical solution, has the proper accuracy to predict the outcome of further experiments and can be used to find the optimum system, of any desirable size; One that creates the strongest magnetic field, so that the plunger can absorb maximum energy from the solenoid in the minimum time interval.

For each solenoid of certain dimensions, length of the ferromagnetic plunger, diameter of the wire and the number of layers should be optimized. e.g. for a solenoid with 5cm length, 3cm outer diameter and 1.4cm inner diameter, the outer diameter is proportional to number of wire layers which is 20 for a wire of 0.6mm diameter. (Fig. 14 & Fig. 15)
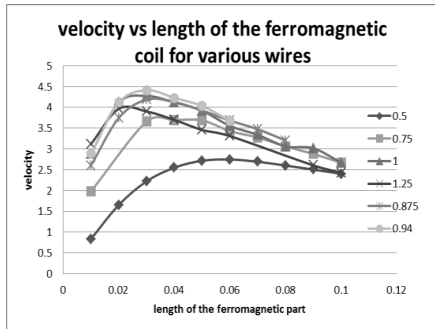
Figure 14: Velocity vs length of the ferromagnetic coil for various wires
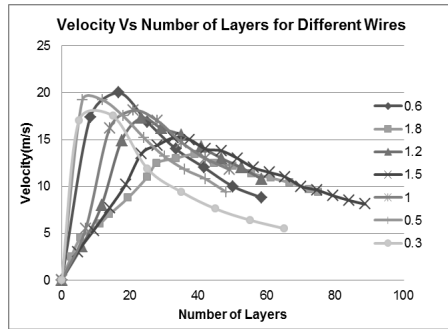
Figure 15: Velocity vs number of layers for different wires

For instance,to find the maximum possible velocity for a certain system with the 45 mm outer diameter, 10 mm inner diameter, 2mm thickness of the Teflon solenoid' body,2000 μF capacitor charged with a voltage of 220 volts, (using Fig.15) the maximum possible velocity for different wire's diameter can be found theoretically.

In Fig.16 the black line shows the maximum possible theoretical velocity, and the gray line shows the maximum possible velocity after applying geometrical limitations.
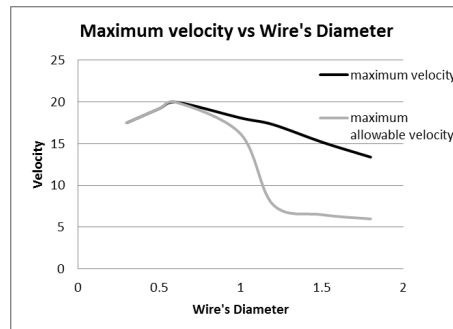
Figure 16: Maximum possible velocity

References

[1]Mechanics by KenithR.Symon, Addison Wesley,Third edition, 1971

[2]Analytical mechanics by Grant R. Fowles, Fourth edition CBS international editions, 1987

[3]physics by Robert Resnik, David Hallidayand Kenneth S. Krane, Fifth edition, 2002

[4]NayfehM.Hasan, Electricity and Magnetism by Monir H. Nayfh, Morton K. Brussel, university of Illinois at Urbana-Champaign, first edition, 1985

[5]Introduction to Electrodynamics,DavidJ.Griffiths, Third edition, Prentice Hall, 1999

[6]Numerical Methods for Scientists and Engineers,K.SankaraRao,, Third edition, Prentice-Hall of India 2007

[7]B.P.T.vangoch, Optimizing a Solenoid for a Robocup kicker, DCT-number: 2006.051

No. 2, Brilliant pattern: Caustics and optical catastrophes in an illuminated water droplet

Łukasz Gładczuk [1]

[*] Team of Poland, IYPT 2010

[1] *Stanisław Staszic XIV High School, Warsaw, Poland*

Corresponding author: lukaszgladczuk@gmail.com (Ł. G.)

Abstract

Laser beam illuminating a drop of water is reflected and refracted at the air-water boundary. As a result various patterns forming around the drop are observed on the screen. Patterns were captured using a digital camera and phenomenon is described in terms of catastrophe theory.

Introduction

A drop of water has been an interest of studies of many scientists, mostly because of its specific aerodynamic and optical properties. Problem of investigation of patterns that can be observed when suspended drop of water is illuminated with laser light was one of the problems for 23rd IYPT. Here the approach of the Polish team to this task is presented.

If one wants to guess what patterns will be seen after the drop of water is illuminated with light beam, the first idea that comes to his mind is the rainbow. This is a commonly known optical phenomenon. Nevertheless, it can be shown, that rainbow is only one of numerous optical patterns that can be observed during the study under laboratory conditions. Suspended drop of water has a complicated shape and it is hard to describe how it affects light paths. In some cases it can be approximated by a ball, but most of interesting patters are created due to drop's specific tear like shape. Because of complex structure of observed patters and complicated shape of the drop, it is hard to describe the phenomena in means of mathematical formulations. However, there are several clues suggesting that observed patters are examples of optical catastrophes. Similar patterns created by a drop of water placed on the microscopic glass and illuminated from below were earlier investigated and described as optical catastrophes [1, 2].

In this article, we present an experimental setup used to recover light patterns coming out of a suspended drop of water. Out of wide range of observed patterns, the most common were chosen and discussed. Images were analyzed in terms of catastrophe theory and compared with elementary catastrophes.

Experimental investigation

Used in the study experimental setup is shown in figure 1. The drop of water was created by a needle attached to a laboratory stand and connected to a syringe with deionized water. Because the laser light pointed at a
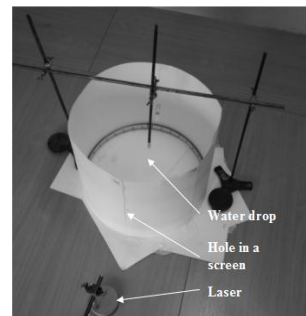
Figure 1: Experimental setup

drop of water can be reflected and refracted in any direction, a cylindrical paper screen, 1 m in diameter, with a paper bottom was built around the drop. The water drop was illuminated by green laser beam through a small hole in a side of the screen. All experiments were conducted in a dark room. Light patterns appeared on the screen depended on the place of illumination and the shape of the drop. Diameter of the drop was adjusted from 1 to 7 mm using a syringe, larger drops could not be hold on a needle and felled down. The different parts of the drop were illuminated, by changing laser's beam direction. Some patters appeared only in dynamic condition, i.e. when the drop's size was continuously changed. Observed patterns were captured and recorded with a digital camera. For some specific experiments, instead of the water drop a fine optical glass ball of 5 mm in diameter was used. In this way significance of drop's shape to the phenomenon was determined.
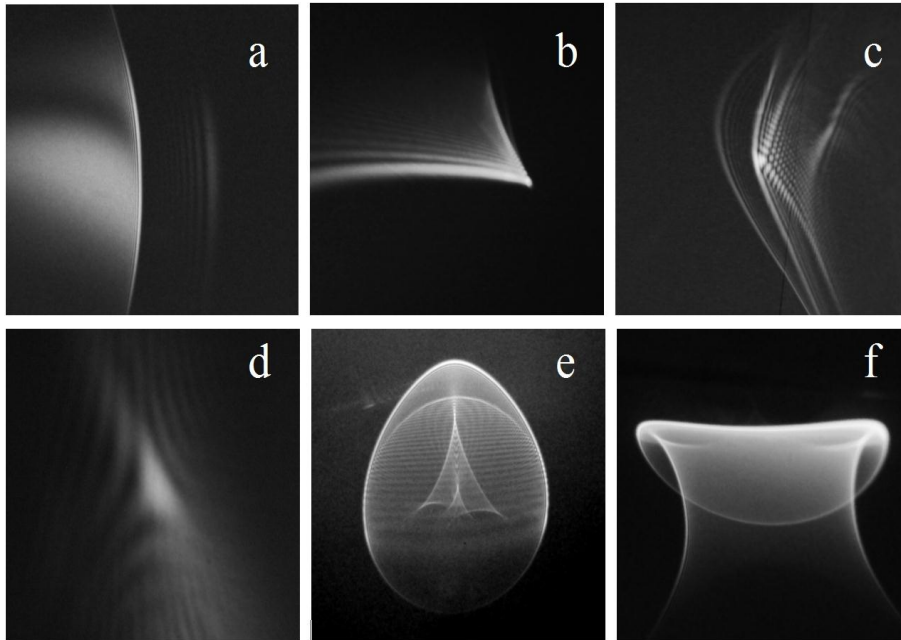
Figure 2: Pictures of patterns observed when a drop of water was illuminated with green laser light

Pictures of the most interesting and characteristic patterns are shown in figure 2. Figure 3 illustrates place where drop of water was illuminated and the figure 4 place on the screen where a given pattern appeared. All of these light patterns consist of very bright curves, called caustics, which divide brighter parts of the screen from darker parts (see figure 2a). Pattern in figure 2a is a caustic being approximately a straight-vertical line. It appeared when the drop was illuminated at the middle of the height (figure 3). This pattern was the easiest one to observe and appeared in places on the screen marked as **a**, see figure 4.

Pattern presented in figure 2b was a caustic similar to a cusp. Again one can notice that brighter parts of the screen are separated from darker one by a bright curve. Pattern 2c has more complex structure than ones presented above. It consists of curves whose shapes are similar to parabola or cusp. Pattern 2d has shape similar to a triangle with interferential pattern around it.
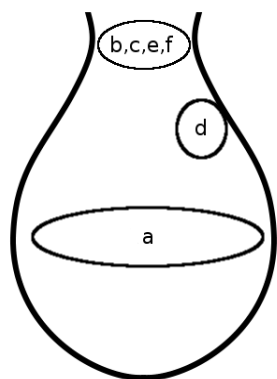
Figure 3: Drawing presenting where laser beam was directed to create patterns a, b, c, d, e, and f seen in figure 2
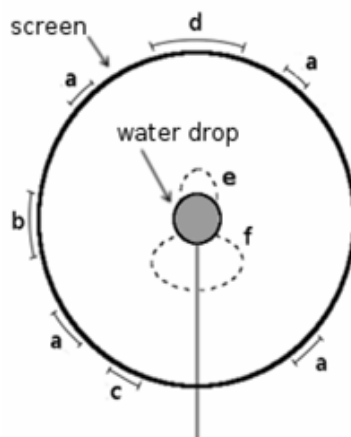
Figure 4: Drawing presenting places where patterns a, b, c, d, e, and f appeared on the screen. Patterns e and f appeared on the bottom of the screen

This pattern was hard to capture as it was very sensitive to the place of drop's illumination (see place **d** in figure 3); a slight vibration (created by traffic on the street) interrupted the image. Pattern 2e appeared only when drop's size was changed, never in stationary conditions. Image in figure 2e consists of egg shaped caustic with additional patterns inside, forming a shape similar to an arrow. Pattern 2f had different shape for small and big drops. When drop was small it had a parabolic shape with its arms facet outward the drop. When drop was bigger it began to form shape seen in figure 2f. Photo seen in figure 2f was taken right before drop detached from a needle.

When drop of water was replaced with a fine glass optical ball, pattern seen in figure 2a was the only one caustic observed. This shows that the specific drop's shape is relevant to disused patterns.

Theoretical Description

Parallel light rays of the same wavelength, directed onto a spherical drop of water are reflected and refracted at water-air boundary (figure 5). It seems obvious, that the interferential phenomena occur in the observed images, but the studies presented in this paper are focused on the geometrical aspects of the phenomenon. Rays that are only once reflected inside the drop form a first order rainbow, which is the most familiar caustic.

Applying law of reflection and Snell's law, formula describing final direction of each ray can be found [3]:

$$\theta = \pi + 2\alpha - 4\arcsin\left(\frac{\sin(\alpha)}{n}\right);$$

(1)

where: n – relative refractive index between water and air, α – angle of incidence of initial ray on a drop, θ – angle between incidence light ray and one coming out of a drop.

This function is plotted in figure 6 (for case of water drop in air). One can see that for values of θ larger than critical ($\theta_{cr} \approx 137.5°$) there are two values of α satisfying the equation (1). A bifurcation occurs at value of θ equal to critical angle (two solutions merge into one) and there is no solution of equation (1) when the $\theta < \theta_{cr}$. Rays that travel near the bifurcation create a caustic which appears on a screen as a bright line. The value of critical angle depends on the wave length; therefore if drop is illuminated with white light, each colour forms a caustic at a slightly different angle, together observed as a colourful rainbow.

If multiple reflections inside the drop are considered, second and higher order rainbows can be described [3]. In conducted experiments we were able to observe several rainbows up to a very dim 6-th order rainbow. In figure 2a the first and fifth (on the dark, right side of first) order rainbow is seen.

The rainbow is the only pattern that can be described using spherical drop model. Description of patterns presented in figure 2b, c, d, e, f requires more advance theory. As it was shown in case of a rainbow, bright curves called caustics appear in places where many rays intersect the screen. In mathematical formulation those are critical points of functions illustrating rays direction. Several researchers, notably J. F. Nye [2] and M. V. Berry [4], investigated such light patterns and came to a conclusion that those patterns can be explained in terms of catastrophe theory.

Figure 5: Drawing illustrating trajectories of light rays illuminating spherical drop of water
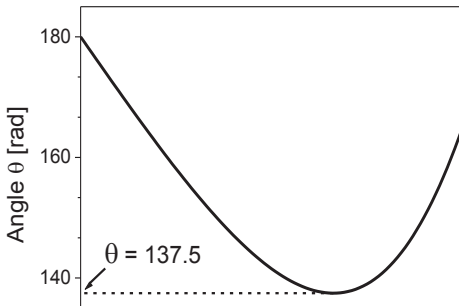
Figure 6: Dependency of θ angle vs. incidence angle α for n = 1.33

Catastrophe theory

Catastrophe in physical system is defined as a sudden, qualitative change of the system's behavior with a smooth change in external conditions [5] (for example water begins to boil with a smooth change of temperature). Catastrophe theory analyses degenerated critical

points. For one variable function those are points for which not only first but also second or more of higher-order derivatives become zero. Those points correspond to formation of caustics.

Caustics form at bifurcations which divide areas where number of rays crossing each point differs by two. In order to determine number of rays passing through each point; all light rays are taken under consideration. Their optical path length depends on initial and end position of a light ray. Initial position of the ray (out of a parallel bunch of parallel rays) can be described by two coordinates (X, Y), and the end position (position on the screen) by three coordinates (p, q, r). On the basis of Fermat's principle, the path of light between two points is extreme (a minimum, maximum, or other type of critical point) with respect to time. Using this principle it is possible to find the number of light rays, coming from (X, Y), reaching a given by (p, q, r) point in space.

In most cases, the function describing optical paths is complicated, and usually its expansion in Taylor series around interesting points - critical points - is investigated. Details of this procedure are presented in reference [6]. Catastrophe theory states that all such functions with 4 or less control parameters can be transformed around critical points, to a one of seven forms called elementary catastrophes, using only smooth transformations. Five elementary catastrophes of our interest are listed below:

1. Fold $A_2(x) = \dfrac{1}{3}x^3 + ax$

2. Cusp $A_3(x) = \dfrac{1}{4}x^4 + \dfrac{1}{2}ax^2 + bx$

3. Swallowtail $A_4(x) = \dfrac{1}{5}x^5 + \dfrac{1}{3}ax^3 + \dfrac{1}{2}bx^2 + cx$

4. Hyperbolic umbilic $D_4^+(x, y) = x^3 + y^3 + axy + bx + cy$

5. Elliptic umbilic $D_4^-(x, y) = x^3 - 3xy^2 + a(x^2 + y^2) + bx + cy$
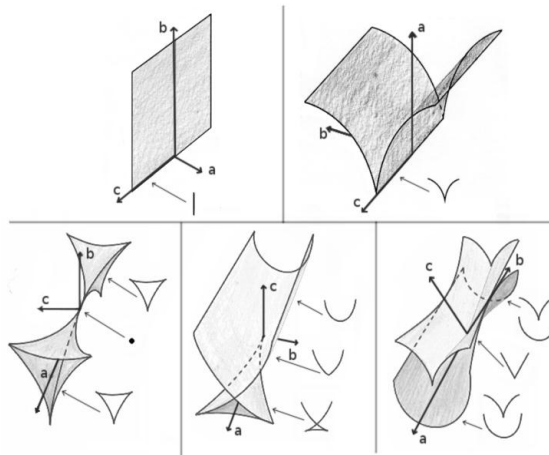
Figure 7: Bifurcation sets of elementary catastrophes: fold, cups, elliptic umbilic, swallowtail, hyperbolic umbilic. Exemplary cross-sections are shown next to each structure

Variables x, y and parameters a, b, c are connected with coordinates X, Y and p, q, r by smooth transformations.

The number of extremes of catastrophes depends on value of parameters a, b, c. (In discussed case - how many light rays cross given point of space.) In (a, b, c)-parameter space, boundaries between regions where the number of extremes differs by two - are surfaces, and define a bifurcation set of a given catastrophe. In figure 7 bifurcation sets associated with elementary catastrophes (listed above) are shown in (a, b, c)-parameter space. For example of elliptic umbilic, if a point (a, b, c) is inside "triangular pyramid" there are two critical points (two light rays), if outside there are four (four light rays).

Comparison of observed patterns with elementary catastrophes

A pictures presented in Figure 2 are the most characteristic representatives of images captured during experiments. In performed investigation, used screen was a two dimensional object, so patterns observed on the screen were cross-sections of three dimensional structures. For explanation of obtained images in terms of catastrophe theory, they have to be compared with the cross-sections of the bifurcation sets of catastrophes. As one can see, cross sections of the bifurcation sets (see figure 7) and patterns seen in the figure 2 reveal several similarities. While discussing first-order rainbow (figure 2a) it was shown that caustic appears at the boundary between region where there are two rays and no ray leaving a drop. This is an example of the fold catastrophe where a cross section is a line. It is a boundary between values of parameter **a** with two extremes and with none. Pattern seen in figure 2b is an example of cup's catastrophe. Its caustic is similar to a cross-section taken through a cups catastrophe (figure 7b). By analogy to fold catastrophe one may expect that observed caustic is boundary between regions where number of rays crossing the screen through each point differs by two (bright-dark side). However it is not possible to proof experimentally how many rays cross the screen. Analogously patter 2c was found to be example of hyperbolic umbilic, 2d - elliptic umbilic catastrophe. Patterns seen in figure 2e and 2f, could not be characterized as one of elementary catastrophe. They appear to be more complex structures, which are composed of simpler forms described above such as fold and cups catastrophes.

In mathematic formulation caustics correspond to critical points of functions describing light rays contributing to observed patterns. Such critical points in optics were investigated, and several scientists came to conclusion that they are well explained by catastrophe theory [2, 4]. In investigated case function describing light paths can not be found easily due to complicated shape of a drop. However, it seems that this function has several critical points that appear on the screen as caustics, similar to patterns obtained from catastrophe theory.

Conclusions

We constructed an experimental setup and recover optical patterns created by laser beam scattered on a drop of water suspended on a needle. Several light patterns were captured. It was concluded that bright curves in observed patterns are caustics. The simplest caustic appearing on the screen as a straight line pattern was labeled as rainbow and described in terms of spherical drop model. Obtained patterns were analyzed by means of catastrophe

theory. It can be concluded that observed light patterns are elementary catastrophes or composition of those elementary forms.

Dedication

The author would like to dedicate this paper to the memory of his teacher Mr. Stanisław Lipiński (the team leader of the Polish team to the IYPT 2010).

References
1. J.D. Walker „A Drop of Water Becomes a Gateway into the World of Catastrophe Optics", Sci. Am. 261 (1989) 176.
2. J.K. Nye, „Natural Focusing and Fine Structure of Light: Caustics and Wave Dislocations", Institute of Physics Publishing 1999.
3. J.D. Walker "multiple rainbows from a single drop of water and other liquids" Am. J. Phys. 44 (1976) 422.
4. M. V. Berry. Elliptic umbilic diffraction catastrophe. Phil. Trans. Royal Soc. London A 291 (1979) 453
5. V.I. Arnold, "Catastrophe Theory", Springer Verlag Berlin Heidelberg 1984.
6. T. Poston, I. Steward, „Catastrophe Theory and its Applications", Pitman Publishing Limited 1978

No. 4, Soap film: Deflection in uniform and radial electric fields

Una Pale[1]
Team of Croatia, IYPT 2010
[1] *University of Zagreb, Croatia*
Corresponding author: una.pale@gmail.com (U. P.)

1. Introduction

When a soap film is created and placed into the electrical field it deforms. Aim of this paper is to explore and explain why the electrical field affects the soap film. It will also investigate how the parameters: electrical field, distance from charge and radius of soap film determine the shape of soap film.

2. Theory

2.1. Soap film

Soap is a molecule that consists of two parts: long hydrocarbon chain and ionic end. Long hydrocarbon chain is non polar and therefore hydrophobic, while ionic end on the other side is polar and creates ion-dipole bond with water [Figure 1] It means that it is hydrophilic and soluble in water. Hydrophilic part of molecule orientates towards water molecules, while hydrophobic tends to be the furthest form water and goes to surface. This helps to visualize how the soap film looks in microscopic scale. It consists of two layers of soap separated with water layer. [Figure 2] If there is too high concentration of soap soluted in water soap molecules start to form clusters. While soap molecules are pretty compact on the surface, water molecules, ions and charges in water layer are free to move.
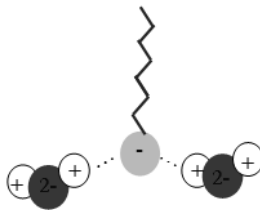
Figure 1: Soap molecule   **Figure 2:** Soap film
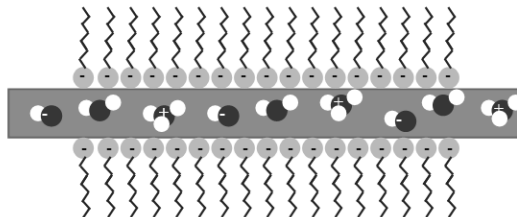
Since there are attractive Van der Waals forces between molecules, soap film as liquid in general, tends to have the smallest surface area. Because of the $E = \gamma S$ where E is energy and γ is surface tension, the liquid, or in this case soap film has a resistance to change of shape because it would mean greater energy.

2.2. Soap film in an electrical field

When we put soap film in an electrical field there are few possibilities: soap can be isolated in air, or can be grounded through the framework it is stretched on.

When it is isolated it means that it is neutral as a whole, and when it is put near charge the charged particles in water move and the charge redistributes. Opposite charges of the one creating field come in the middle and others go to the edge.

Charges in the middle are attracted to the charge creating field and soap film extends, as seen in the [Fig. 3.a]. In another case, when it is grounded and put near a charge, free charges come from or go into the ground. Now the number of positive and negative charges in soap film is not equal and film is charged as a whole. The soap film also deforms. Due to the radial electrical field the forces are not the same on all parts of the film. They are the strongest in the middle because there is the smallest distance. Since, in an electrical field electric force is additional force to soap film except of surface tension, now the net force is not zero until the film elongates.

While the value of extension depends on the grounded or not grounded and many other parameters, the direction of extension doesn't depend on these cases. Polarity of charge doesn't effect the direction of elongation of the film either. In one case positive charge in film comes in the middle of the film and in another negative comes in the middle but it always elongates towards the charge causing the electric field.
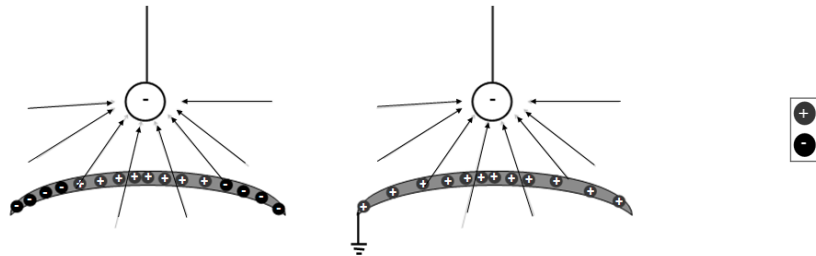
Figure 3: a)isolated soap film b)grounded soap film near charge (in radial electric field)

If soap film is in homogenous electric field e.g. between two oppositely charged plates a different behaviour occur. If the soap film is isolated nothing happens [Figure 4a]; there is no deformation because the force on positive and negative charges are equal but in opposite directions. If the soap film is grounded additional charges come to soap and they tend to be far from each other. The surface is stretching until achieving the equilibrium when electrical force is the same as the surface tension force. [Figure 4b] Instead of putting soap inside two metal charged plates (huge capacitor) soap was stretched on one of these two plates. Now if the plate with soap was isolated the 20kV wasn't enough to notice the deformation that could be measured, and if the plates were too close sparks appeared. If the soap was grounded nice deformations were noticed and for this case theory will be presented later. This situation is almost the same as when grounded soap is between plates.
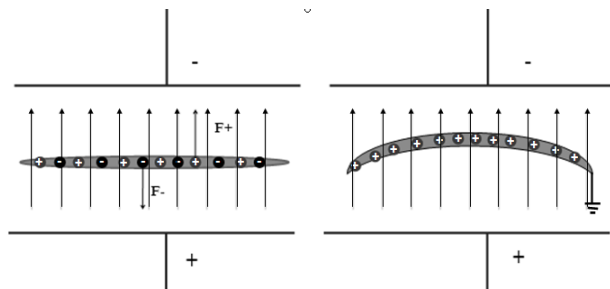
Figure 4: a) isolated b) grounded soap between two oppositely sharged plates

48

2.3. Homogenous field

When the effect is achieved, it can be noticed that the deviation is small (less than 4 cm) and later when the shape was more precisely observed that it could be described as a parabola. Since the deformation was small two assumptions were made: the surface charge density is homogenous; $\sigma = E\varepsilon_0$ and secondly that parabola could be approximated as a part of the circle. From [Figure 4a] the equation of the parabola describing the shape of elongated film can be written: $p(r) = ar^2 - p_0$ and $p_0 = aD^2$, where *a* is coefficient of parabola, *(r,p)* are (x,y) coordinates of some point on the soap film curvature, p_0 is elongation and *D* is radius of the hole in plate. If it is approximated with a part of circle of large radius compared with radius of hole it can also be written $p_0 = R - \sqrt{R^2 - D^2} \approx \frac{1}{2}\frac{D^2}{R}$, where *R* is radius of imaginary circle the soap is part of. From last three equations a relation between radius of imaginary circle and coefficient of parabola can be found: $R = \frac{1}{2a}$. It can be noticed that parabola coefficient a shouldn't depend on the radius of hole.
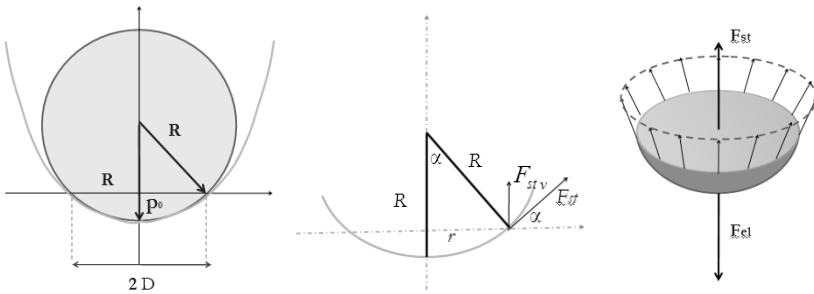
Figure 5: a)geometry of soap film   b)surface tension   c) net force is zero

When the film is elongated it means that resultant force is 0. It means that the surface tension force and electrical force are equal but in opposite directions. [Figure 5c] Surface tension acts in tangential direction [Figure 5b] but for the stabilisation (when film stop with stretching) only the vertical component matters. Total surface tension force is $F_{st} = \gamma L = 2r\pi\gamma$ where γ is surface tension and *r* can be seen on [Figure 5b]. Using the geometry [Figure 5b] $\alpha \sim \sin\alpha = \frac{F_{st.v.}}{F_{st}} = \frac{r}{R}$ a vertical component is $F_{st.v.} = \frac{2r^2\pi\gamma}{R}$. At the same time the electrical force is $F_{el} = \sigma SE = \varepsilon_0 E^2 r^2 \pi$. Net force is zero; $F_{el} = F_{stv}$. From that equation $R = \frac{2\gamma}{\varepsilon_0 E^2}$ and $a = \frac{\varepsilon_0}{4\gamma}\left(\frac{U}{d}\right)^2$ is get; where *U* is voltage between soap film (plate on which soap was stretched) and plate and *d* is distance between those two plates.

2.4. Radial field

In this case the shape of the film is more complex and the surface charge density is no more homogenous. Moreover here is possible to observe case when soap film is grounded and when it isn't. All these parameters affect the shape which was too hard to predict and explain theoretically because everything starts with the distribution of charges on surface which wasn't possible to observe or determine. But the measurements were made.

In all cases the effect of gravity was neglected because preresearches showed that the effect is too small to be measurable.

3. Apparatus

A voltage source from 1-25kV was necessary to create electrical field strong enough to deform film enough to be able to recognize it. The soap film was stretched on one metal plate with a hole. Plates with three different diameters of holes were used; 13, 26, 39 cm. And there was one without a hole. Between those plates was always isolator so there wouldn't be arcing. [Figure 6a] A steel sphere was used to create a radial electrical field. It was put above the plate with soap film [Figure 6b].

A plate with hole was used instead of wire loop because of few reasons; it was shown that film is more stable and lasts longer when it was stretched on plate since on the surface of plate around hole could be some amount of soap to prevent soap film from bursting very fast.
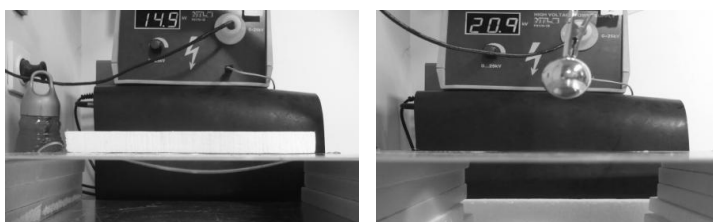
Figure 6:   a) soap in homogenous field   b) soap in radial field

4. Methods

The shape was described with coefficient of parabola and the elongation. These two values were measured and determined from pictures made from side view. They were processed the program "ImageJ". This way the dots of the shape were chosen and then a mathematical function could be fitted. The equation that determines shape was determined [Figure 7a,b].
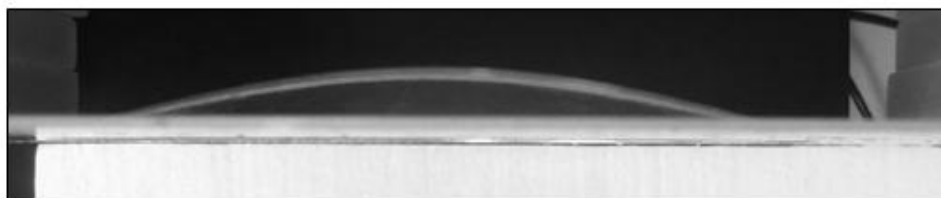
Figure 7: a) soap film photographed from side view, ready to process
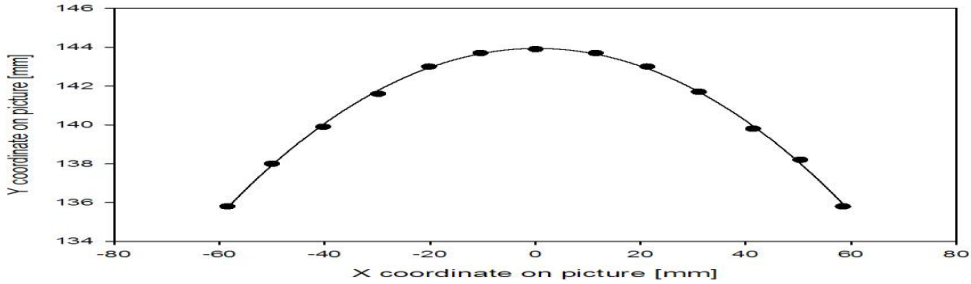
Figure 7: b) the picture processed, mathematical function fitted

The extension of soap film and coefficient of parabola shape were determined for different diameters of soap film, different voltage and different distance from charged body or distance of plates. First soap film was stretched on a plate with a hole which was above another plate. These plates were at certain distance and voltage. Second case was with a radial electric field where a spherical metal ball was hold above soap film. A distance and voltage between plate and sphere was changed. Also the measurements for isolated and grounded soap film were conducted.

5. Results

5.1. Homogenous field
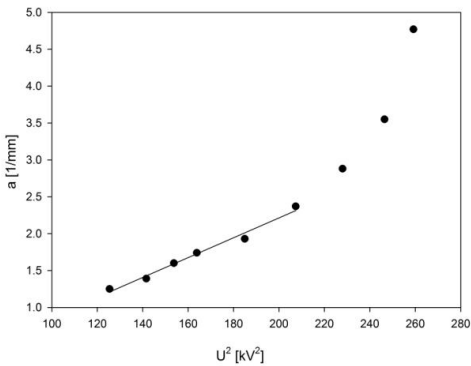
Graph 1: Parabola coefficient dependance on voltage

On [Graph 1] it can be seen that coefficient of parabola is proportional to the square of voltage which agrees with

$$a = \frac{\varepsilon_0}{4\gamma}\left(\frac{U}{d}\right)^2$$. The coefficient of line is

free parameter, because too many parameters affect it which couldn't be precisely measured. It can also be seen that after certain voltage dependence is
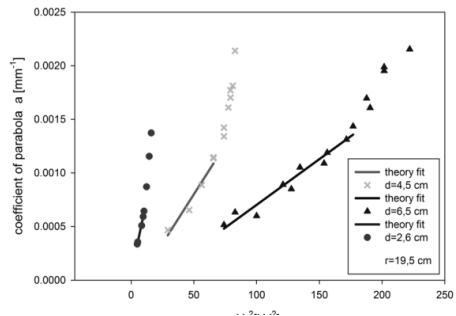
Graph 2: Parabola coefficient dependance on voltage for different distanced from plate

not linear any more. It's because above that voltage the deformations become bigger and shape is more complicated. Moreover, assumption that the surface charge density uniform wouldn't be appropriate any more. Also, it was observed that the soap film becomes very unstable because of the water that seeps inside of soap film and starts to
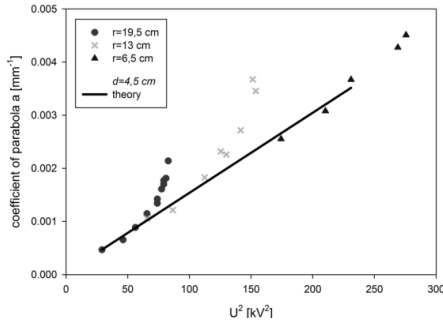
Graph3: Coefficient of lines from previous graph b; in dependance on distanced from plate

of $b = \dfrac{\varepsilon_0}{4\gamma}\dfrac{1}{d^2}$. [Graph 4] shows that coefficient of parabola *a* doesn't depend on the radius of plate D. It is because for this linear part, extension is very small compared with radius of hole, which withdraws that radius of imaginary circle is much bigger than radius of hole. This was derived in theoretical part and now it can be seen from measurements. Due to that it is considered that for small deformations this theory is justified.

form a droplet at the bottom. When a droplet drops soap film goes up and start to vibrate. Then again, it takes time for droplet to form, and after several iterations soap film burst. From [Graph 2] coefficient dependence on square of voltage for different distances of plates is noticed. These lines have different slopes. The coefficient *b* is slope of lines which is shown on [Graph 3]. Here is clearly seen that they depend linearly on $1/d^2$ because
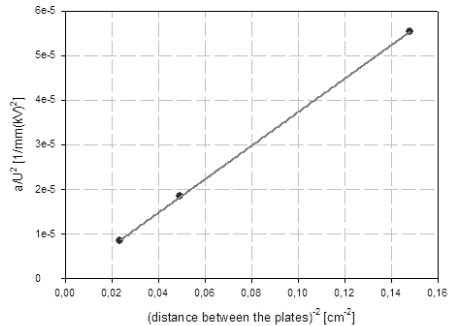
Graph 4: Parabola coefficient dependance on the radius of soap film

5.2. Radial field
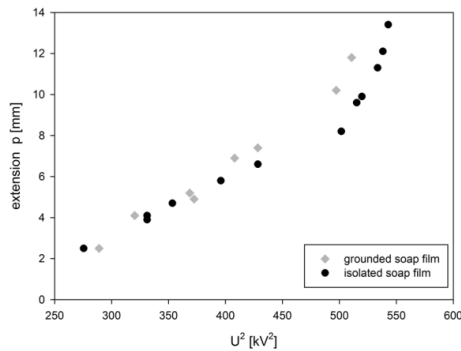
Graph 5: Extension *p* for grounded and isolated soap film

In this case the shape of film was too complex so only the elongation was measured. In [Graph 5] extension *p* for different voltage is shown for both grounded and isolated soap film. It can be seen that there is a difference, but it's hard to say how important the difference is. It is logical that for isolated film greater voltage is necessary than for grounded because in grounded there are additional charges that came from ground and affect the electrical force. From [Graph 6] and [Graph 7] it's seen that the diameter of soap film and distance from charged ball also affect the extension. For smaller radius the surface tension force is greater so bigger voltage is necessary for the same extension. Also if the steel ball is closer the electrical forces are greater so smaller voltage is needed for same extension. In case of radial field there is qualitative explanation but unfortunately quantitative conformation of measurements with theory is missing.
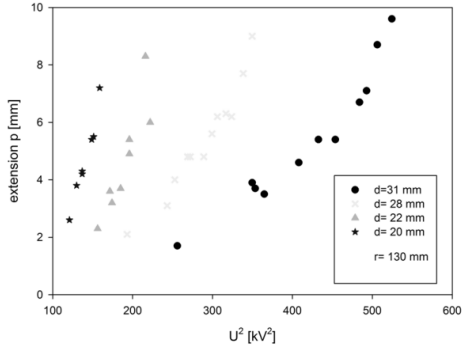
Graph 6: Extension dependence on voltage for different distance from steel ball
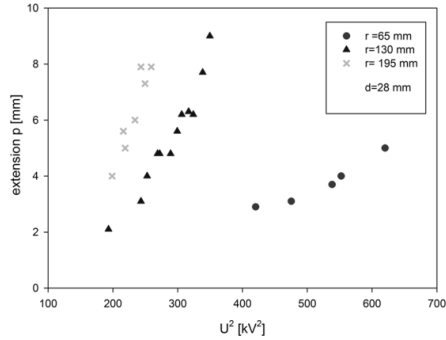
Graph 7: Extension dependence on voltage for different radius of soap film

6. Conclusion

The effect of shape deformation of a soap film in different electrical fields was observed. Two cases were studied; when a charged body is a sphere which creates a radial electrical field and if a charged body is a plate which creates homogenous field. If the soap film is between two oppositely charged plates there is no deformation because the forces on positive and negative charges inside of film are the same. That's why soap film was stretched on a hole in one of these parallel plates. Also two cases were studied, with isolated soap film and with grounded. If it was isolated the 20kV was not enough for film to elongate more than few millimetres and measurements couldn't be done. That's why the paper is orientated to grounded soap film. For small deformations the distribution of charges on film is uniform, and shape was represented as parabola, part of the circle and the quantitative predictions were made. Parabola coefficient which describes a shape is proportional to the square of voltage, and inversely proportional to the distance. It doesn't depend on the radius of soap film. This was confirmed with the measurements and excellent agreement was achieved. In the case of radial field the shape was to complex and charge distribution wasn't possible to determine so there is no quantitative theory but qualitatively the dependence of extension on voltage, distance and radius of film was explained.

References

[1] Halliday, Resnick, Walker (2000) Fundamentals of Physics: Wiley
[2] Cyril Isenberg (1992) The science of soap films and soap bubbles. New York: Dover Publications

No. 4, Soap film: Interactions with charged bodies of various shapes and the discharge asymmetry with respect to the polarity change

Alexander Barnaveli[1]

* Team of Georgia, IYPT 2010

[1]*Ilia Vekua Physical and Mathematical School 42, Tbilisi, Georgia*

Corresponding author: s.barnaveli@gmail.com (A. B.)

Problem: ***Create a soap film in a circular wire loop. The soap film deforms when a charged body is placed next to it. Investigate how the shape of the soap film depends on the position and nature of the charge***.

1. The Soap Film Structure

Let's start investigation of this problem by considering the soap film structure[1]briefly.

Figure 1. Soap film structure
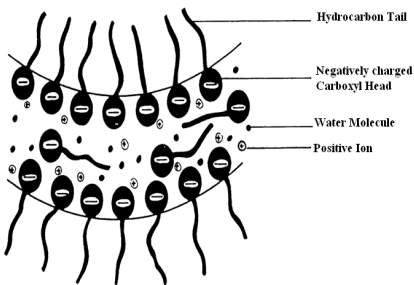
Soap film is formed by surface active agents (Surfactants). There are two layers of soap molecules, between which there is water (see Figure 1[1,2]).

A soap molecule is divided into positive $Na^+$and negative$C_{17}H_{35}COO^-$ions.

Negative ions collect on the surface of film and they **formsurface structure**.

Between two layers of film are water and Na^+ ions.

Soap molecules play the important role in the film formation[1,2]:

✓ Negative ions $C_{17}H_{35}COO^-$formthe surface structure of soap film;
✓ Soap molecules decrease the evaporation of water;
✓ They also decrease the surface tension.

Here we want to note that this difference in the positive and the negative ion distribution in a soap film leads toa very interesting phenomenon, which will bediscussed below.

In some of our experiments we added a small amount of glycerinto soap, because the glycerin decreases the water evaporation from the surface and alsostabilizesthe soapfilm[1,2]. So, due to the glycerin a soap film gets an "extra duration of life" and becomes more elastic.

2. The experimental Setup

Now let us describe our experimental setup(for better quality color photos please see our presentation [3]). We used:

• A voltage source - an old CRT monitor, which provides $27\ 000\ V$;
• Electrodes of different forms;
• Different distances between the electrodes and the soap film;

Figure 2. Experimental setup

- A metal loop (frame) for the soap film - grounded one and also not grounded;
- A dielectric loop (frame);
- Different sign of body charge (and this gavedifferent results!!!).

3. A spherical charged body

We began experiments with an interaction betweena spherical charged body and a soap film.In our experiments we used the frame for soap film of radius$a$~*5 cm*.Too small frames were not convenient for making observations and measurements, while too large – to get stable films and to avoid influence of even small air flows.

It was observed, that:

– As larger the distance $d$between sphere and film - the less the influence (deformation);

– In the case of d~*5 cm*, the height h of the film deformation in the center was about*1 cm*and the film remained stable;

– For the small d~h, the stable state did not occur. Film continued to stretch, discharge developed and film exploded.

3 cm
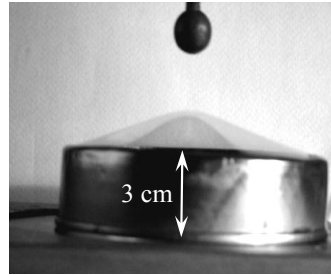
Figure 3

Let us explain this theoretically.When the charged body approaches the film, the charges on the latter will be redistributed (since the film is a conductor) in the way to make the film equal-potential. Electric field on the film will be compensated by these redistributed (Induced) charges. On the film, near the external charge, the opposite-signed chargeswill gather(they are attracted by this external charge and thus the film will stretchtowards it – see Figure 3), while far from it – the same-signed charges are gathered. Generally, the distribution of charges on the film will be quite complicated, but approximately the problem of "soap film-external charge interaction" can be solved by using the "Electrostatic Image Method".We will assume the external charge as a point charge and the film shape as a spherical segment.

In such interaction the electrostatic force is balanced by the surface tension force. The lattercan be calculated by means of Laplace equation whilethe electrostatic force between the charge and the film we calculated using an "electrostatic image method". Equating the Coulomb and the surface tension forces we can calculate the dependence of h on theexternal sphere charge$Q$ and on$d$. We will use the approximation, when the deformation is much less than the loop radius and the distance to the charged sphere.

Electric force.

Thus our assumptions are the following:

- The external field redistributes the charges on the film;
- The film surface is equal-potential;
- The interaction between the charge and the grounded sphere film can be "effectively" presented as the interaction between the two point charges;
- The value and the place of "effective" charge mustgive equal-potential film surface;
- We assume that the film is a sphere segmentABC of the height h;
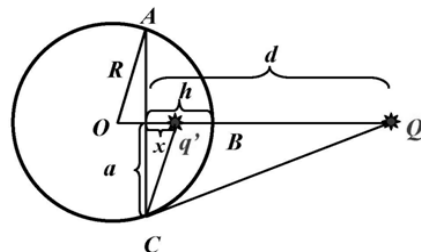
Figure 4. The method of electrostatic image

- AC – the loop (frame) of a radius a;
- Q – the external charge, at the distance $d \gg h$;
- q' – the "effective" charge at the distance x from the loop.

From the Figure 4 the condition of $\varphi_B = \varphi_C = 0$ (a grounded film) leads to the following values:

$$x = \frac{2a^2 h - a^2 d + h^2 d}{a^2 + 2dh - h^2}; \quad q' = -Q\frac{a^2 + h^2}{a^2 + 2dh - h^2} \quad , \tag{1}$$

and the effective electrostatic interaction force will be:

$$F_k = kQ^2 \frac{(a^2 + h^2)(a^2 + 2dh - h^2)}{4(d-h)^2(a^2 + dh)^2} \quad . \tag{2}$$

This force must be balanced by the surface tension force.

Surface tension force.
Using the Laplace formula $P_l = 4\sigma_0 / R$ and taking into account, that

$$R = \frac{a^2 + h^2}{2h}$$

we obtain

$$p = \frac{4\sigma_0}{R} = 4\sigma_0 \left(\frac{2h}{a^2 + h^2}\right) .$$

If we write down $F_l = pS$, we will get that the force of the surface tension is

$$F_l = 8\pi\sigma_0 h. \tag{3}$$

Balance of Electrostatic and Surface tension forces.
Using the force equilibrium condition $F_k = F_l$ for (2) and (3) we get:

$$kQ^2 = \frac{32\pi\sigma_0 h (d-h)^2 (a^2 + dh)^2}{(a^2 + h^2)(a^2 + 2dh - h^2)} . \tag{4}$$

It is quite a complicated formula, so to make it clearer, let us use the approximation, when $h \ll a; \; h \ll d$. We can do it in our case, since the film stretch in our experiments was small compared to the frame radius. In this approximation the equations (1),(2),(4) get the form:
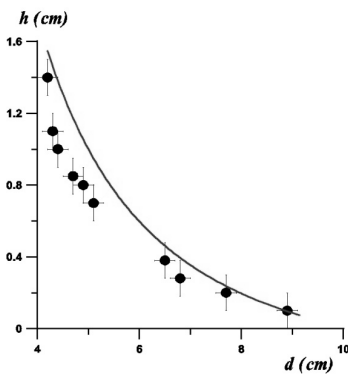
Figure 5. The dependence $h(d)$ for the stable states:
(experiment - points;
theory - curve)

$$x \approx 2h - d \; ; \quad q' \approx -Q \quad ;$$
$$F = kQ^2/(4d)^2 \; ; \quad kQ^2 = 32\pi\sigma_0 hd^2 , \tag{5}$$

where from we get the dependence of h on Q and d:

$$h = \frac{k}{32\pi} \cdot \frac{Q^2}{\sigma_0 d^2} = \frac{1}{128\,\pi^2\varepsilon_0} \cdot \frac{Q^2}{\sigma_0 d^2} . \tag{6}$$

Let's calculate h for our experiment. This dependence is given on the graph. For a $1cm$ radius charged

sphere, at the potential $\varphi = 27\,000\ V$, we get:

$$Q = C\varphi = 4\pi\varepsilon_0 r \cdot \varphi \approx 3 \cdot 10^{-8}\ Coulomb.$$

Noting that $\sigma_0 \approx 25 \cdot 10^{-3}\ N/m$, for the distance $d = 5\ cm$ from (6) we get $h \approx 1\ cm$, that is quite near to our experimental results.

Let us make some notes. From (3) and (2): $F_l \sim h$; $F_k \sim 1/(d-h)^2$. If $h \ll d$, the F_l increases with h faster than F_k. So the stable equilibriums reached. If $h \sim d$, situation is opposite - F_k increases with h faster than F_l, so the film stretches and explodes.

4. A flat charged body

By the flat charged body the film deformation was larger (see Figure 6) because the field was stronger.
However without grounding the stretch of the film was significantly less because in that case the ions could not "leave" the film.

6. An approximately uniform field

To obtain the uniform field we used two parallel large lids. The bottom lid was grounded while to the top lid the high voltage was applied.
The film was formed on a plastic (dielectric) loop. In the uniform field the film did not stretch, due to the force symmetry.
In the strong field the film simply was torn by the forces acting on the positive and negative charges.

7. Interaction of film with charged nail

In this case the soap film did not stretch out, but the dip was formed, as if there blew the wind from above (see Figure 7). The observed dip (instead of a "hill") was caused by so called "electric wind", which blew rather strong and this strength was greater than the strength of attraction. Electric wind takes place when the density of charge on the electrode is very high (like the case of nail-type sharp electrode) and electric field near it is very strong. The field at the bottom of the nail polarizes the air molecules and strongly repels the electrons. They hit the film and form the above-mentioned dip. The fact that this wind was caused by charged particles we proved by the following experiment. Instead of soap film we placed the detector of charged particles and it fixed a large amount of accelerated particles.

3 cm
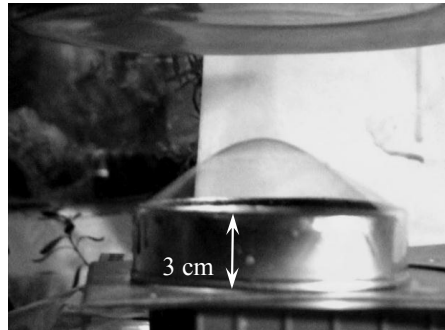
Figure 6. Flat charged body
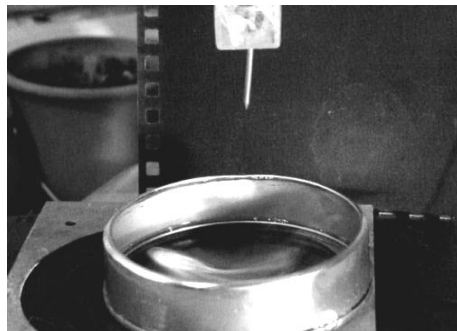
Figure 7. Sharp-ended body

Figure 8. Small-headed charged body

8. Interaction of film with small-headed charged body

In this case the observed behavior reveals both processes -the electric wind and the attraction towards electrode. Both –the "dip" and the "hill" are formed (See Figure 8).

9. The asymmetry with respect to the change of poles

As we mentioned in the beginning of this article, the difference in the positive and the negative ion distribution in soap film causes a very interesting phenomenon. It took place when we changed the poles, i.e. the charge sign of the body. It seems to be the most interesting result and now let's carefully consider it.

3 cm
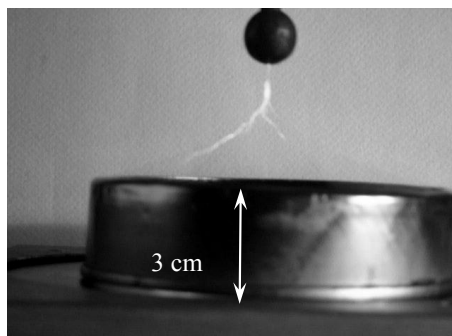
Figure 9. Discharge (yellow),Positively charged body

In our experiments we observed, that change of the poles (i.e. charge sign of the body) affects the shape and the color of discharge on the soap film. Parameters of spark are dependent on the sign of the electrode charge. When electrode was charged **positively**, discharge was **spread and yellow, while** when the electrode was charged **negatively,** discharge was **bluish and straight.**

What is the reason of this?
At high temperatures the atoms emit the electromagnetic waves (photons). Frequency of emitted light depends on the transition energy between two levels in atom: $E_{Photon}=h\nu$, where h – is Planck constant, and ν- frequency of emitted light.
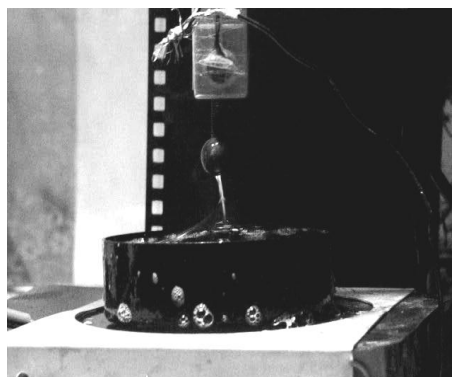
Figure 10. Discharge (blue), Negatively charged body

It is known, that *Sodium (Na)* emits yellow light, while *Nitrogen* - bluish-lilac light. Thus we can conclude that when electrode is charged negatively the light is emitted by the atoms of *Nitrogen* (which are present in air) while in the case of **positively** charged electrode, the light is emitted by *Sodium (Na)* atoms. Why it is so?

The Negative external charge accelerates the electrons toward the film. The accelerated electrons strike the *Nitrogen* atoms of air and cause their **bluish-lilac** emission. Also, in this case the positive Na^+ ions in soap are attracted by the negative external charge, move along the film freely towards the point nearest to this external body, concentrate there and cause the *straight form of discharge*.

In the case of **positive external charge** heavy ions of air accelerate towards the film. These ions hit the film and punch out of it the positive Na^+ ions which form the "cloud" above the film. So the discharge proceeds in this "cloud" of positive Na^+ ions. This gives the **yellow** color of discharge. Besides, in this case the punched out Na^+ ions are attracted by the negative ions of soap (these negative ions form the soap film structure and are more or less "spread-fixed" around the film surface area). Thus

the *discharge becomes more "spread"* (here we see the discharge shape asymmetry with respect to pole sign. It is caused by the soap film ionic structure – different "flaw freedom" degree of the positive and the negative ions).In this case we also saw that most upper part of the spark (which is above the cloud of positive Na^+ ions) is blue, while the main yellow region is within the cloud of the punched out Na^+ ions.

As we observed, the discharge destroys the film.

10.   *Conclusion.*

In this work we studied thesoap film interactions with the charged bodies. The different shapes of the charged bodies were tested and the resulting film deformations were examined
We found out that film deformation strongly depends on:

–   The shape of the charged body
–   The charge value
–   The distance from the film
–   The grounding of the loop on which the film is formed
–   The soap film structure

Also, a very interesting phenomenon of the discharge asymmetry with respect to the change of poles was observed. In the case of Negative external charge the straight bluish-lilac discharge takes place, while in the case of Positive external charge – the "spread" yellow discharge. We explained it by the specific ionic structure properties of a soap film.

Finally I want to thank my grandfather Tengiz Barnaveli for his help in the experiments with the high voltage.

References
[1] Cyril Isenberg. The science of Soap Films and Soap Bubbles.Dover Publications, NY1992.
[2] http://www.soapbubble.dk/en/bubbles/
[3] http://solutions.iypt.org/uploads/2010_GE_Soap_film_Alexander_Barnaveli_1321459517.pptx

No. 6, Ice: Regelation effect revisited

Stanislav Krasulin [1]
[*] Team of Belarus, AYPT 2010
[1]*Belarusian State University, Belarus*
Corresponding author: s.krasulin@gmail.com (S. K.)

Introduction

This task asks us to investigate a very interesting phenomenon, which was first observed over a century ago[1]: if a wire with weights attached to each end is placed across a block of ice, this wire may pass through the ice without cutting it.

In our work, most experiments were held in the room with air temperature 23°C (unless otherwise mentioned); for producing ice blocks we had used usual ice cube tray, which was filled with usual water and placed in the refrigerator at temperature of -11.5°C for at least 12 hours.

It should be noted, that ice blocks, produced such way, have a non-transparent region in their central part. It happens due to the presence of air and other gases, dissolved in water. These gases can't freeze together with water, and when it crystallizes they just leave it. However, when a vessel with water is put in a refrigerator, first the outer parts of water will turn into solid state, and gasses in the still liquid water in the inner part will be captured inside. And when this water finally crystallizes, gases form small bubbles, which make ice non-transparent[2,3]. Certainly, they also change mechanical and thermodynamic properties of the ice, and it's difficult to predict how exactly. Fortunately, the non-transparent region wasn't very big, so it was possible to make a cut through ice without entering it; so, in our experiments we were placing wire so that it would go only through the transparent region.

Experimental setup

Scheme of our experimental setup is presented in fig. 1. A block of ice is placed onto a piece of wood, which is mounted in two supports. Wood is used because due to less efficient heat
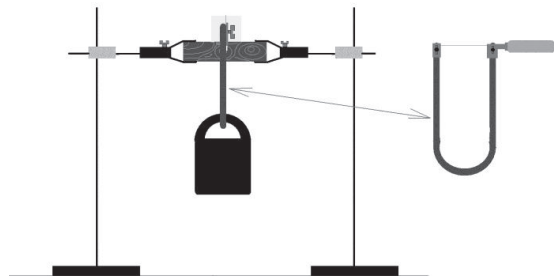
Figure 1. Experimental setup

exchange it reduces melting (compared to the ice, mounted directly into metal supports). There is a slit made in the wooden block, so that wire could continue moving down after exiting ice cube. In all our calculations we have assumed, that wire inside the ice isn't curved. To achieve it in experiment the wire is mounted in a fretsaw, instead of its blade. Load is attached to the fretsaw.

Qualitative explanation

Already first experiments had shown that effect, described in the problem, does take place: ice really remained in one part. But we also had noticed that even two originally separate blocks of ice tend to become one. If environment temperature is positive, there is a thin layer of melted water on the ice; and when twoice cubes are put in contact, heat from this water is "sucked" by ice; thereby, water crystallizes,

connecting two blocks together. However, after it had happened, there is no slit on the surface of the ice in the place, where cubes had connected.And if wire passes through the ice, it lefts a notable slit; it proves that these are two different phenomena.

But what have happened to the ice, which was in the place of the slit? Surely, it had melted. And, for some reason, it was melting faster than all other ice. Thisreason is additional pressure, applied by the wire. This effect is called "regelation", and was first observed by Michael Faraday[4]. The matter is that volume of a portion of ice at the temperature 0°C is bigger than volume of the same portion of water at the same temperature; therefore, if we apply pressure to the ice, we help it to decrease it's volume, correspondingly, assisting in melting. For example, if ice is under pressure of 130 bar, it will melt at the temperature -1°C. And in atmospheric pressure ice melts at 0°C. Approximating, that between these two points dependence of melting temperature on applied pressure is linear, we can write:

$$T(P) = P \cdot \frac{-1°C}{129 \ bar};$$

where P is applied pressure, and T(P) is temperature at which ice will start melting.

So, let's describe what's exactly happening in our experiment. When a wire is placed across an ice cube, pressure is applied to a small portion of ice, so it melts at negative temperature (it certainly requires some heat, but it comes from the surrounding air). Once it is turned into water, pressure pushes it upwards, around the wire. During this movement water heats up almost to 0°C. But when water reaches top side of the wire, there is no more pressure; water now is super-cooled, therefore it instantly crystallizes, releasing heat. This heat is transferred down through the wire and is used to melt a new portion of ice[2]. And the cyclerepeats.

This theory is proven by the fact that wire leaves a turbid trace in the ice. It occurs exactly because of super-cooled liquid crystallization. Liquid starts to crystallize around different dirt particles; so a lot of crystals is growing at the same time. That is why not one solid crystal is formed, but a set of small ones. Borders between these crystals scatter light, making the whole structure less transparent than usual crystal of ice.

Quantitative analysis

Our theory states that all the ice involved in the cycle one time melts into water, and one time heats up. Thereby, total heat required is:

$$Q_1 = cm(0°C - T_0) + \lambda m;$$

where c is ice's heat capacity, λ is specific heat of fusion,T_0 is original temperature of ice, and m is mass of ice under the wire, it can be calculated as m=ρhdl; where ρ is ice's density, h is height of the ice block, d is wire's diameter and l is length of the part of the wire which touches ice. Now, if we approximate our system as closed (no heat enters or leaves the system) than all this heat have to pass through the wire. Heat flux through the wire is:

$$W_1 = \frac{K \cdot (0°C - T(P)) \cdot S}{d};$$

where K is wire material's heat conductivity, S is area of contact of wire with crystallizing water. Thereby, time, required for the wire to pass through the ice, is:

$$t = \frac{Q_1}{W_1} = \frac{\rho h d^2 l (c(-T_0) + \lambda)}{KMg};$$

where M is total mass of the weights attached to the wire.

Experimental analysis

In the last formula time is proportional to the square of wire's diameter and inversely proportional to the mass of load.We had checked correctness of these dependences for the nichrome (heat conductivity 12 W/(m*K)) wires (fig. 2). It can be seen, that dependence of the time of cutting on the load's mass is correct;however, we can't be so sure about dependence on wire's diameter. The matter is that for precise measurements we had needed wires of different diameter, but 100% identical chemical composition; and we found only three such nichrome wires. In the fig. 2 this dependence is fitted by parabola, using the fact that it should go through (0; 0) point. It can be seen, that dependence is close to parabola; but due to the number of experimental points, we can't state that dependence is proven. We can only say that for nichrome increase in wire's diameter increases time, required for cutting; thus, at least qualitatively proving theory.

But these dependences do not work for the copper (heat conductivity 382 W/(m*K)) wires at all. As shown in Table 1, not only cutting time now decreases with increase of wire's diameter, but also there is almost no dependence on the load's mass.
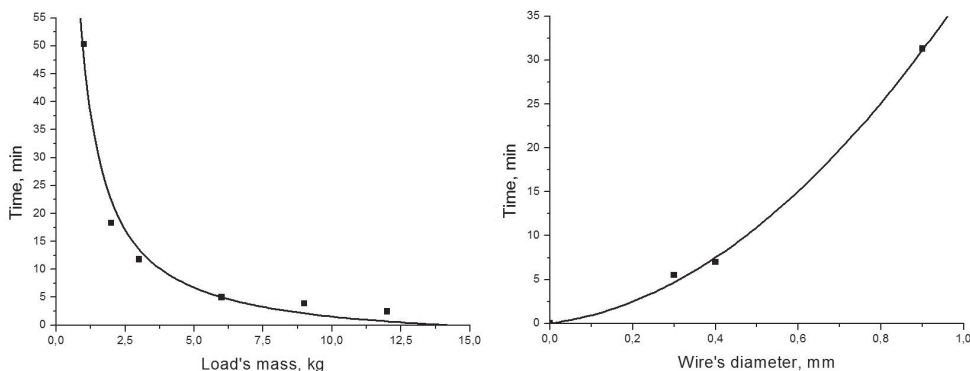
Figure 2.Left plot shows cutting time subject to loads mass for the nichrome wire (d=0.4 mm),fitted by hyperbola; **right** is time of cutting for three nichrome wires with 6 kg weight attached, fitted by parabola

Table 1. Cutting times for copper wires with different parameters

Wire's diameter, mm	Load's mass, kg	Cutting time
0.6	5	18 min 20 s
1.35	5	8 min 50 s
1.45	5	8 min 08 s
1.45	1	9 min 20 s

We had explained the failure of our theory for copper wires by its heat conductivity: copper's heat conductivity is about 8 times higher than nichrome's. For nichrome, we could ignore heat inflow from the environment through the wire; and for copper such inflow is significantly higher, and our approximation of system as closed doesn't work anymore.

This idea successfully describes what we see in Table 1: if we increase wire's diameter we increase heat income from environment; if mass of load is changed, it affects temperature of water melting, which is, in this case, less important.
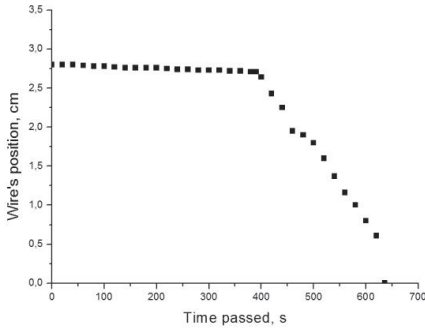
Realization of the closed system for copper
In order to prove correctness of these explanations experimentally, we had run an experiment, where all heat exchanges with surroundings were reduced to minimum. Whole setup had been moved outside (temperature of air was 0.5°C); melting snow had been put around free ends of the copper wire.

Figure 3. Dependence of the wire's position on time passed. Temperature of surrounding air 0.5°C.

Results of the experiment can be seen in fig. 3. At first wire was moving very slow – the heat, required for melting of the first portion of ice, was being accumulated; the fact that it took so much time proves that heat inflow was very small.

It is also interesting to note, that if temperature of surroundings is lower than melting temperature of ice under given pressure, then process won't start. Since even with high load's masses this melting temperature is only slightly smaller than zero, we hadn't observed wire cutting the ice if air temperature was lower than 0°C.

While heat was being accumulated, ice under the wire was melting; finally, enough ice had melted, so that water had covered the upper side of the wire. Once it had crystallized, enough heat was released to melt another portion of ice; the cycle started; velocity of wire significantlyincreased. But after it, velocity remained constant until the end of experiment, proving that not only no heat enters the system, but also that losses of heat during cycle are negligible.

Quantitative analysis of not-closed system
First, it is required to take into account heat income. Since above the wire temperature is 0°C and under it it's T(P), we can approximate, that whole wire has temperature T(P)/2. By measuring temperature of the wire with thermocouple at various distances from the ice cubewe had found, that distance y between the last point of wire, where temperature is equal to air one, and the first point where it is equal T(P)/2, is about 3 cm.Thereby heat flux through the one side of the wire:

$$W_2 = \frac{K \cdot (T_{air} - \frac{T(P)}{2}) \cdot \pi d^2}{4y}; \ y \approx 3 \text{ cm};$$

where T_{air} is air temperature. Since wire has two ends, total income of heat from environment is 2*W_2.

Fig. 3 had shown that amount of heat, spread into ice is negligibly low; however, for full description of the not-closed system we had decided to take these losses into account too. We had frozen a block of ice with several thermocouples in it; then we let the wire cut the ice, while measuring temperature through all thermocouples. It had shownthat on the distance of about 1 cm from the wire ice's temperature hasn't changed during experiment. Assuming that heat escapes from the wire, and from the zone above wire, heat flux into one side can be calculated as:

$$W_3 = \frac{K_{ice} \cdot (\frac{T(P)}{2} - T_0) \cdot 2dl}{x}; \quad x \approx 1 \text{ cm};$$

Total lack of heat will be 2*W_3.

Finally, we had also taken into account that specific heat of fusion also depends on the temperature, at which melting occurs: for water at 0°C λ=330 kJ/kg, and at -7°C it's 317 kJ/kg. Once again, in this part the dependence can be approximated as linear; which means that dependence on the pressure is also linear:

$$\lambda(T) = \lambda(T(P)) = 330 \frac{kJ}{kg} - \frac{13 \frac{kJ}{kg}}{7°C} \cdot T(P)$$

So, now total heat, which is required for melting ice, equals:

$$Q = \rho h dl (c(0°C - T_0) + \lambda(T(P)));$$

and total heat flux, coming to the melting ice, is:

$$W = W_1 + 2 \cdot W_2 - 2 \cdot W_3$$

Combining all this we are now able to write a formula for finding time, required for cutting through the ice, if system can't be approximated as closed:

$$t = \frac{Q}{W} = \frac{\rho h dl(c(0°C - T_0) + \lambda(P))}{(K(0°C - T(P))l - \frac{1}{x} \cdot 4 \cdot K_{ice} \cdot (\frac{T(P)}{2} - T_0) \cdot dl + \frac{1}{2y} K \cdot (T_{air} - \frac{T(P)}{2}) \cdot \pi d^2)}$$

Since it is hard to remember all these symbols, they are listed in the Table 2:

Table 2. List of symbols, used in the formula for finding time, required for cutting through the ice, if system can't be approximated as closed

Symbol	Meaning
ρ	Ice's density
h	Height of ice block
d	Wire's diameter
l	Length of wire's part, which touches the ice
c	Ice's heat capacity
T_0	Original temperature of ice
λ(P)	Ice's specific heat of fusion (linearly depending on pressure, applied by the wire)
K	Wire material's heat conductivity
T(P)	Ice's melting temperature (linearly depending on pressure, applied by the wire)
x	Distance between the wire and point of ice block, where temperature does not change during experiment
K_{ice}	Ice's heat conductivity
y	Distance between the last point of wire, where temperature is equal to air one, and the first point where it equals T(P)/2
T_{air}	Air temperature

Conclusions

Because of the pressure ice under wire melts at negative temperature; in liquid form it goes upwards and freezes back under the wire, creating turbid region. Then cycle continues again and again.

If temperature of surrounding air is close to 0°C (but still positive), then this system can be described as closed; wire cut through the ice with constant speed, proving, that heat losses are negligibly small.

For materials with low heat conductivity this system also can be approximated as closed; however, for materials with high heat conductivity it is necessary to take into account income of heat from the environment through the wire.

To improve mathematical model further, it is possible to calculate heat losses and affect of melting temperature on the specific heat of fusion.

It should be noted that wire must go through the transparent region of the ice block, because properties of the non-transparent region are significantly different.

References
[1] J.T. Bottomley, "Melting and Regelation of Ice", Nature, London, 1872;
[2] E. Hahne, U. Grigull, "Some Experiments on the Regelation of Ice", Physics of Ice, Pienum Press, 1969;
[3] Wikipedia contributors, "Ice cube", Wikipedia, The Free Encyclopedia, 9 January, 2012;
[4]Michael Faraday, "On Regelation, and the Conservation of Force", *Philosophical Magazine,* Vol. 17, 1859.

No. 8, Liquid light guide: Reflections in the Colladon fountain

Una Pale [1]
[*] Team of Croatia, IYPT 2010
[1] *University of Zagreb, Croatia*
Corresponding author: una.pale@gmail.com (U. P.)

1. Introduction

Light guide is a fiber-optic cable which is used to transfer signal (light pulses). This is one of basic ways of information transfer. It is wide spread in computer networks, telecommunications, medicine, fiberoptic ect. Usually is made from glass, quartz or plastic. In this paper, research of the properties of water which enable water jet to serve as a light guide is presented. Colladons' apparatus for so called "light fountain" or "light pipe" from 1840 was constructed. The main goal was to determine how intensity of transferred light and length of jet capable to transfer light depend on the shape of the jet. Experimental results are described and compared with a computer model.

2. Apparatus

The apparatus was very similar to Colladons' apparatus [Figure 1] but with few extra improvements so the measurements could be done. [Figure 4] A large transparent vessel with a horizontal nozzle and a laser (He-Ne laser, 630nm) was set. The nozzle and laser were in the same horizontal level and laser was pointed into the nozzle so it could enter a water jet leaving the nozzle. Nozzle had to have perfectly smooth walls and narrow toward the end so it could prevent turbulences to appear. The plastic end of pens turned better of any other glass of metal tubes.

Figure 1: Colladons' apparatus [4]

3. Materials and methods

In the beginning in vessel was 10 liters of water and the jet was almost horizontal. As water seeped, because of the reducing height of water in the vessel and hydrostatic pressure, the output velocity also reduced so the curvature of water jet became steeper. Every few seconds the intensity of light in jet, always in the same vertical distance form nozzle, was measured. A photo resistor was set so that it could be moved horizontally. It had larger sensor surface than the cross section of jet so that when it was placed inside of jet all light came onto the sensor. At the same time the jet was photographed so measurements could be taken and curvature could be determined mathematically (the coefficient of parabola).
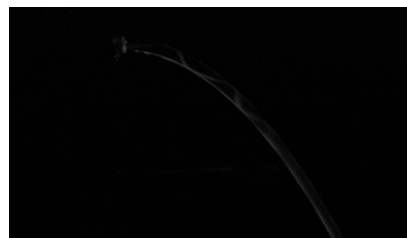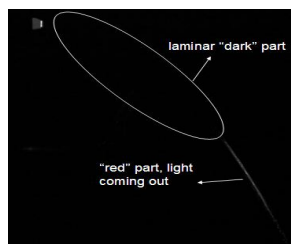
Figure 2: a) the effect („dark" and red part)   b) reflections inside a jet (in opaque water)

3.1. Measuring the length of laminar part of the jet

There were two phases in the jet; "black" and red part (since the laser was red). First part where jet was "dark" and smooth was part where the light was completely inside of the jet and wasn't coming out (in our eye) so it couldn't be seen (in the dark). After some length, the jet wasn't consistent (smooth) any more and started to turn into drops. This part of the jet was always bright and red because light started to come out of the jet. Here it couldn't serve any more as a light guide. Goal was to determine how the length of laminar part of the jet depends on the shape of the jet. Laminar part is important because only this part of jet can conduct the light. It was photographed and pictures were processed with program "ImageJ". The coefficient of parabola which jet described was calculated and the length of the curve of "dark" part of jet was measured. As a reference for dimensions there was a ruler photographed in the picture.

3.2. Measuring the intensity of light

As the shape of jet and parabola coefficient changed; due to the geometry optics, the intensity of light that stays inside of the jet also changed. Also, intensity which came to the place of measurement changed. It was measured always on the same vertical level (about 5 cm below the output level) in "black" part of jet. At this place a photo resistor was put and the resistance was measured since it depends on intensity of light. The dependence of intensity on electrical resistance (of photo resistor) is not linear and it was necessary to calibrate it.

Figure 3: Calibration of the photo resistor

Some materials (e.g. glass plates) absorb the light that passes through them. Changing the number of glass plates the total absorption was changed so the intensity of light on resistor too. The light absorption is proportional to the number of plates. Different number of them was put between laser and photo resistor. [Figure 3] The dependence of resistance on number of glass plate was determined. [Graph 1]

$$R \propto (number.of.plates)^3$$

$$\frac{1}{U} \propto (number.of.plates)^2$$
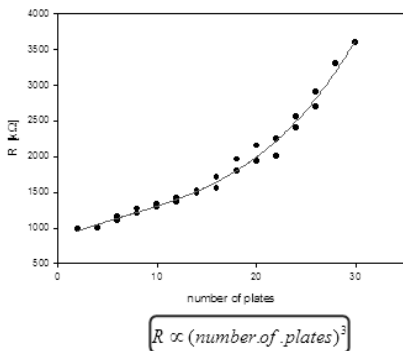
Graph 1: Calibration of the photo resistor **Graph 2:** Calibration of the photo diode
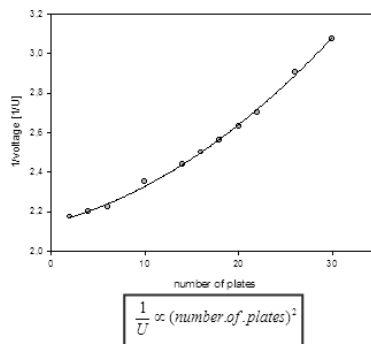
The same procedure was repeated with photo diode instead of resistor and voltage was measured. It was known that the dependence of voltage on light intensity was linear. This way the dependence of voltage on the number of plates N was determined. [Graph 2] Since for the photo diode is $I \propto U$ (I as light intensity) and the previous calibrations gave these relations; $R \propto (N)^3$ and $\frac{1}{U} \propto (N)^2$ it followed that the

dependence of intensity on electrical resistance of photo resistor is: $I \propto \left(\frac{1}{R}\right)^{\frac{2}{3}}$.

The area of photo resistor was larger then the area of cross section of jet for all diameters of nozzle. This way all light inside of the jet was absorbed by the resistor.

Now when it was known how to get the intensity from resistance and when the apparatus was constructed [Figure 4] and the method were developed the measurements could be done.
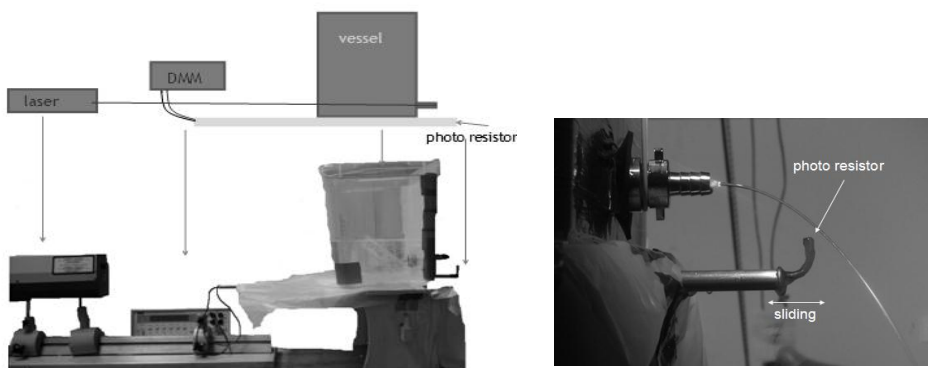
Figure 4: The apparatus

4. Theory

There are two main reasons for the loss of the light: hydrodynamic and optical. Hydrodynamic reason is the decomposition of the jet. Because of the gravity the velocity of water increased and since the flow rate has to be constant, the diameter of the jet decreased. On the surface of the jet there are always small fluctuations called Plateau-Rayleigh fluctuations, no matter how laminar the jet is. If the perturbations are decomposed into sinusoidal components, it can be seen that some components grow with time while others decay with time. Among those that grow with time and increase of velocity, some grow at faster rates than the others. In addition, the jet narrows over the path due to continuity equation, so jet turns into drops. These turbulences are unpredictable and it's very hard to theoretically determine the place at the jet where they will cause leakage of light from the jet. That's why it was photographed.

Second reason is optical. In different mediums light spreads with different velocity and has a different wavelength and that's why it refracts or reflects when it comes to the border between two different mediums. What will happen with light when it comes to border depends on the input angle and refractive index. If input angle is smaller than the boundary angle (for water it is 48.6°) the light passes in second

medium but with different output angle. This angle is determined by the Snell's law. If the input angle is greater than boundary angle, the total internal reflection happens and it means that the light stays in the previous medium, and the 100% of initial intensity is preserved. It is important not to forget that even if the most of the light refracts still some percent of the initial light and it's intensity stays in initial medium. This percentage is determined with the formula:

$$K = \left(\frac{n_1 \cos\alpha - n_2 \cos\alpha}{n_1 \cos\alpha + n_2 \cos\alpha} \right)^2$$

Formula 1: Percentage of light that stays inside of jet in dependance of the input angle

5. Computer simulation

This math model was made to calculate the intensity of the light at the end of the "dark" jet. Simulation required some approximations. Considering jet as a projectile motion of water particles it's shape could be written in perfect conditions as $y = \frac{-g}{2v^2} x^2$. In program, jet was presented with two parabolas. They had same formulas but one was translated above another for the value of the diameter of the nozzle. [Figure 5] It was assumed that the first reflection has the lowest angle of incidence, so if the ray gets reflected first time, it will reflect later as well and the intensity will stay unchanged after first interaction. That's why in the program only the place where laser ray strikes the edge of the jet first time was observed. [Figure 6]
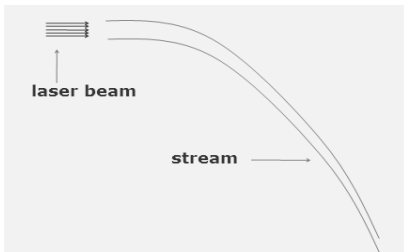
Figure 5: Jet and laser represented in program
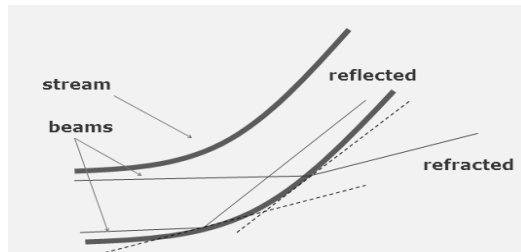
Figure 6: First intersection of laser ray and jet parabola

The laser beams were simulated as a set of parallel lines. [Figure 5] This is how the program worked: 1. for each line the intersection with beam parabola is found 2. angle between laser ray and straight line perpendicular to the parabola is found 3. if the angle is greater than the boundary one the percentage of intensity stays 100, if the angle is smaller the percentage is calculated by the formula [Formula 1] 4. intensities are multiplied with 1/n if there is n observed rays and than summed 5. this procedure is repeated for different parabola coefficients so the measurement with different output velocities are simulated.

6. Results and discussion

6.1. Dependence: Intensity of light - coefficient

The intensity of light that stays in jet after first refraction (until the beginning of the dissipation of the jet) decreases steeply as the coefficient of the parabola starts to increase. Later it becomes almost a constant. [Graph 3] As criteria of a good light guide it was taken a number of 30% of initial intensity that has to be preserved. This number was an arbitrary number that was chosen on basis of measurements. From graph it can be seen that the maximal coefficient of parabola for jet to still be "good" light guide is 0.2.

In graph the line represents the computer model and dots measurements. Theory and measurements agree very well. It confirms theory that only the first intersection is important and that it is satisfactorily to present the jet as two identical parabolas.
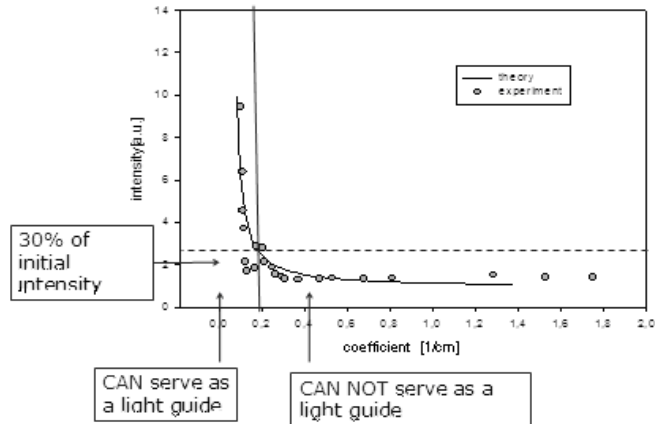
Graph 3: Intensity dependence of parabola coefficient

6.2.Dependence: Length of the laminar part of the jet – coefficient

The length of the laminar part of the jet wasn't possible to predict theoretically because the turbulences appear after only few centimeters from the nozzle, but the question is when they significantly influence on the refraction and reflection. In [Graph 4] the measurements of the length of curve of "black" part of the jet from taken pictures are shown.
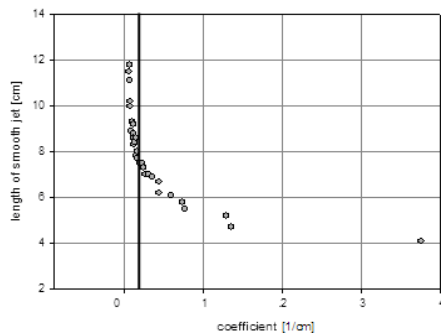
Graph 4: Dependence of length of laminar part of jet on coefficient of parabola

6.3 Influence of the diameter of the nozzle

The diameter affects the coefficient of the parabola. The thicker the jet is for the same height of the water in the vessel, coefficient is smaller which means that the jet is more horizontal. [Graph 5] It may seem contradictory but it's because of the friction with nozzles which can't be neglected. In case of greater diameter the friction with nozzles smaller effect on the outcome velocity. That's also why the velocity couldn't be determined from the height. The diameter was from 1.5mm to 4.5 mm.
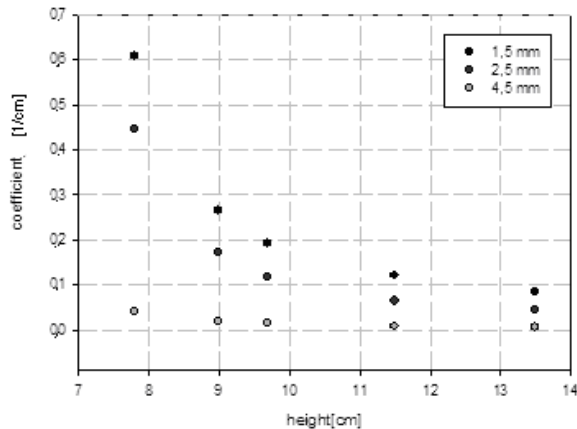
Graph 5: Influence of diameter of the nozzle on the coefficient of parabola

7. Conclusion

The goal of research was accomplished. Conditions under which the jet operates as a light guide were determined. If it has a coefficient of parabola which describes its shape smaller than 0.2, then it preserves more than 30% of initial light. This 30% of intensity that was declared as a boundary for water jet to be a "good" light guide because no matter how steep the curvature of jet is, it always leads some amount of light till the end (where it turns into drops), but after this 30% the intensity decreases really slowly with tendency of becoming a constant as the coefficient is increased. Moreover, for smaller coefficients the length on which this intensity of light can be transported (length of "black" jet) is longer. Diameter of the jet affects the outcome velocity and the coefficient for the same height of water in vessel. The best light guide possible to achieve is with big diameter of the nozzle, and a lot of water in vessel so the coefficient is smaller.

This solution gives intensity dependence on water path parabola coefficient which is not very practical. A more useful solution would be dependence on initial jet velocity. However, it wasn't practically feasible to measure jet velocity for different coefficients. Also it wasn't possible to determine velocity neither theoretically because of the unknown friction with nozzles.

In comparison with industrial light guides composed of glass or plastic this light guide made of water stream guides light at shorter distance due to greater absorption of light and disintegration of water stream.

Refrences

[1] Halliday, Resnick, Walker (2000): Fundamentals of Physics: Wiley

[2] A.Llor (2005): Statistical hydrodynamic models for developed mixing instability flows: Springer

Berlin

[3] S.M. Čantrak (2005): Hydrodinamics: Beograd

[4] http://en.wikipedia.org/wiki/Optical_fiber

[5] http://en.wikipedia.org/wiki/Plateau%E2%80%93Rayleigh_instability

No. 13, Shrieking rod: Compression, bending and torsional waves in a metal rod

Alexander Barnaveli[1]
* Team of Georgia, IYPT 2010
[1]*Ilia Vekua Physical and Mathematical School 42, Tbilisi, Georgia*
Corresponding author: s.barnaveli@gmail.com (A. B.)

Problem: ***A metal rod is held between two fingers and hit. Investigate how the sound produced depends on the position of holding and hitting the rod?***

Abstract
When someone hits the metal rod -compression, bending and torsion waves are excited. We can hear the sound created by these waves. We investigated the types of waves depending on how one hits the rod and the modes of the waves depending on the place one holds the rod. Also damping of these waves was investigated.
We found that the frequency of a standing wave depends on where we hold the rod - if one holds the rod in the place where are nods of several modes, all these modes occur. Touching the rod at the ends will stop the sound. The frequencies of bending waves are lower than of compression waves. Damping of waves depends on the frequency.

1. Wave types in rod

It is clear, that the sound appearing when someone hits the metal rod is created by the waves which originate in the rod due to hit. So let us listdowndifferent types of waves which can be originated in the rod.They are of three types.

A. Quasi-longitudinal *Compression waves*(Fig. 1a). They are *Quasi* longitudinal due to transverse strains– as rod stretches, it grows thinner.

B. *Bending waves* (Fig.1b).These waves involve both compression and share strains. Their velocity depends on frequency so they are dispersive.

C. Transverse *Torsion waves* (Fig. 1c). They represent a lateral displacement χ which varies with x and gives rise to a shear strain. In thin rod torsion shear waves travel at a speed which is always little less than longitudinal wave speed.

The type of waves arising in a thin rod depends on the way one hits the latter.

When one hits a rod along its axis, type (A) waves do arise (Fig 2a).Of course if the hit is ideally central. Such waves arise also if one slide the fingers along the rod. When one hits the rod normally to its axis, two types of waves – (A) and (B) do arise. When one hits the rod tangentialy to its diameter (Fig 2c), all three types of waves are generated because it will strain, bend and compress.

Now let us discuss all these cases. Let us start with longitudinal waves.
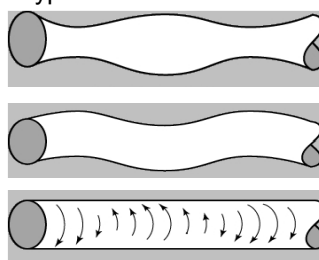
Figure 1.(a,b,c)[1]
Wave types in thin rod

(A) – type **Compression waves** *(in ideal case)*

Also if sliding fingers along the rod

(B) – type **Bending waves**
(A) – type **Compression waves**

(C) – type **Torsion waves**
(B) – type **Bending waves**
(A) – type **Compression waves**
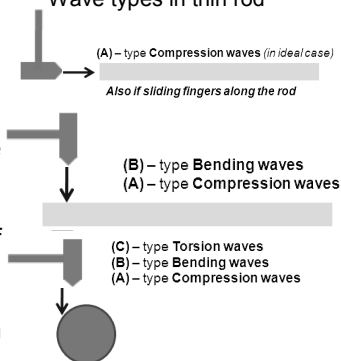
Figure 2 (a,b,c). avesdepending to hit

2. Longitudinal waves

Compression waves in a thin bar or rod are described **w** by a one-dimensional wave equation of the second order[2,3]:

$$\frac{\partial^2 w}{\partial t^2} = \frac{E}{\rho}\frac{\partial^2 w}{\partial x^2} = c_L^2 \frac{\partial^2 w}{\partial x^2}, \tag{1}$$

where $w\,(x,t)$ is an axial displacement of a small volume element, x is coordinate along the rod, E is Young's modulus, ρ is the rod density. From this equation one concludes, that such waves propagate along the rod with the velocity

$$C_L = \sqrt{E/\rho}. \tag{2}$$

(Here the thin rod approximation was used. In a thick rod the longitudinal wave speed decreases slightly at the high frequencies due to the effects of the lateral inertia[1,2]).Harmonic standing wave solution of the wave equation (1) for the boundary condition when the ends of the rod are free has the following form[2]:

$$w = A\,Cos(\frac{\pi n}{l}x)\,\cdot Cos\,(\frac{\pi n c_L}{l}t - \varphi) \tag{3}$$

With the frequency modes

$$\nu_n = \frac{\omega}{2\pi} = n\frac{c_L}{2l} \quad ; n = 1,2,3, \dots \tag{4}$$

and corresponding wave lengths

$$\lambda_n = \frac{c_L}{\nu_n} = \frac{2l}{n} \quad ; n = 1,2,3, \dots \tag{5}$$

For clear understanding we can represent these modes in the following way (Fig. 3). The Abscissa axis is along the rod, while on the Ordinate axis we can show the vibration amplitude. In the places of nodes there is no vibration, while in the places of antinodes the vibration amplitude is the largest [4,5].

Here from, we can conclude, that in order to get some particular frequency modes, one must hold the rod in the node places of these modes. For example let us consider first three harmonics.

The First Harmonic:

From (4) and (5) we can see that wave length$\lambda_1 =$ $2l$;frequency$\nu_1 = \frac{\sqrt{E/\rho}}{2l}$; The nod position can be calculated assuming that the left end of the rod is anti-node and nearest nod to it is at *λ/4* distance, i.e. for the first harmonic nod is at *x=l/2*.

The Second Harmonic:

Similarly wave length$\lambda_2 = l$; frequency$\nu_2 = \frac{\sqrt{E/\rho}}{l} = 2\nu_1$; nod position at *x₁=l/4*; *x₂=3l/4.*

The Third Harmonic:
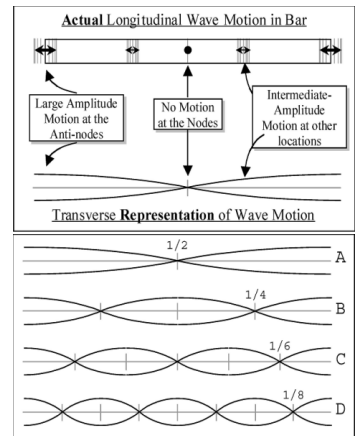
Figure 3[6].
Longitudinal wave modes

Wave length $\lambda_3 = 2l/3$; frequency $v_2 = \frac{3\sqrt{E/\rho}}{2l} = 3v_1$; nod position at $x_1=l/6$; $x_2=l/2$, $x_3=5l/6$.

Using similar calculations we can find the parameters of higher modes. Note, that all these vibration modes (*n = 0, 1, 2, 3, 4, 5,…*) *have the same longitudinal* speed of sound propagation in the rod $c_L=\sqrt{E/\rho} = v_i\lambda_i$.

3. *Experiments with Longitudinal waves.*

Now let us try to exite the quasi-longitudinal waves in the rod and investigate the sound we'll hear.

To make rod sound clearer and louder, we tried to: hit the rod as fast as possible; hit it not very hard, because in other case harmonic form of waves will be violated; hit the rod with thing, that doesn't produce high sound itself (e.g. Ebonite Rod), so it will not mix with the sound of rod; hit it axially or normally, and not intermediate.

Also we excited the longitudinal waves by sliding the hand along the rod axis. We used the *Rosinpowder* to make fingers more sticky.

Figure 4[6].Making Longitudinal waves

In our experiments we observed that the pitch of the sound can be varied by changing the places when we held the rod or by changing the length of the rod itself.

Let us describe the results of our experiments.

At first we took *Aluminum* rod *(ρ_{AL} =2,7·10³kg/m³ ; E_{AL} =70×10⁹ N/m² ; $C_{L(Al)}$= 5082.4 m/s)* of length *l=1,2m*. According our theoretical calculations, for this rod:

Parameters of the first harmonic are: λ_1=2.4m; v_1=2117 Hz; nod is at*: x=0.6m.*

The second harmonic has the following parameters:λ_2=1.2m; v_2=4234 Hz; nodes are at: x_1=0.3m, x_2=0.9m.

The third harmonic has the following parameters:λ_3=0.8m; v_3=6351 Hz; nodes are at:x_1=0.2m, x_2= 0.6m , x_3= 1.0 m.

Figure 5. Spectrum of the *Al* rod (holding in the center)

We recorded the sound of the rod using computer microphone with wide sensibility range and made its analysis by means of "Sound Forge" program. On Figure 5 we represent the spectrum analysis of the frequencies of sound generated by this *Al* rod when we hold it in the center and hit axially or slide the fingers along it. As we see, in such case several modes having nodes in the center are excited. We see clearly modes "1" and "3". Their frequencies match with theoretical calculations quite well. The second mode is damped because it has no node in the center. Higher modes

have lower amplitudes (for given energy the amplitude of oscillation is inversely proportional to its frequency) so they are more difficult to detect. Thus we can see that if one holds the rod in the place where are the nods of several modes, all these modes will occur. Touching the rod at the ends will stop the sound.

We made experiments with rods of different lengths and different materials. For example here we present also the sound generated by the *Brass* rod (ρ_{Br}=8,5·10^3kg/m^3 ; E_{Br} =95×10^9 N/m^2 ; $C_{L(Br)}$= 3480 m/s)of length *l= 0.4m*. According our theoretical calculations, for this rod:

Parameters of the first harmonic are:λ_1=0.8m; v_1=4350 Hz; nod is at: *x= 0.2m*.

The second harmonic has the following parameters:λ_2=0.4m; v_2=8700 Hz; nodes are at: x_1=0.1m,x_2=0.3m.

The third harmonic has the following parameters:λ_3=0.27m; v_3=13 050Hz;nodes are at:x_1=0.07m, x_2= 0.2m, x_3= 0.33 m.
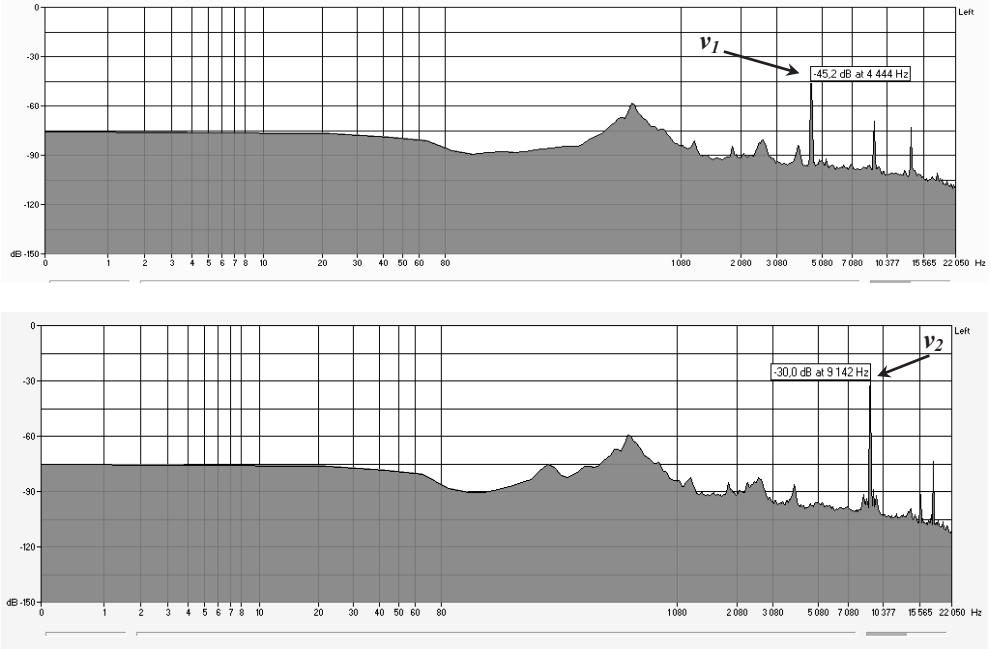
Figure 6 (a,b). Spectrum of the *Brass* rod (a –holding in the center, b holding at -*l/4*)

On Figure 6 we represent the spectrum analysis of the frequencies of sound generated by this *Brass* rod when we hold it in the center (a) and at *l/4* (b). We can see that in the first case first mode is excited and in the second case – the second mode.

Note, that on Figures5 and 6 we see also pikes at lower frequencies. They correspond to other waves – bending waves, which will be discussed below. Of course in our experiments we could not hit the rod ideally, to excite only longitudinal (A)-type waves.

4. **Bending waves**

Now, let's consider the bending waves arising in the rod when we hit it normally to its axis. Bending waves in the thin rod (i.e. using approximation when rod diameter is

much less than the wavelength) are expressed by theEuler-Bernoulli beam theory equation of motion [2,3,5]:

$$\frac{\partial^2 y}{\partial t^2} = -\frac{EK^2}{\rho} \cdot \frac{\partial^4 y}{\partial x^4},\tag{6}$$

Where K is so-called "Gyration Radius" of the rod cross section:

$$K^2 = \frac{1}{S}\int z^2 dS,$$

S– is the cross-section area of the rod, z – is the radial distance from the rod central axis, y- is the displacement in the direction perpendicular to x(average symmetry center axis of the process), that describes the oscillations of the rod segments. For example, for the solid cylinder of radius a:

$$K^2 = \frac{1}{\pi a^2}\int_0^{2\pi}\int_0^a r^2 \cdot \frac{1}{2}rdr \cdot d\theta = \frac{1}{\pi a^2}\cdot\frac{2\pi}{8}a^4 = \frac{a^2}{4}.$$

In (6) the shear deformations and rotary inertia are neglected. This is fourth order differential equation. Thus the velocity of transverse waves is dependent on the frequency. So the dispersion takes place.
Solution of equation (6) has the following form[2,3]:

$$y(x,t) = \cos(\omega t + \varphi)\cdot[A\cosh(kx) + B\sinh(kx) + C\cos(kx) + D\sin(kx)]\tag{7}$$

where $k=\omega/v$ is the wave (propagation) number. As we mentioned above, wave velocity is dependent on frequency:

$$v = \sqrt{2\pi v K c_L}.\tag{8}$$

This Eyler-Bernoulli beam theory gives the solution of bending waves in a thin beam or rod at low frequency. For the thick bars and for high frequencies it does not work.
Now let us consider the transverse vibration modes in thin bar. They depend on the "end conditions". For our task we consider *"both free ends"* condition - no torque and no shearing force. They give the following restrictions on standing wave frequencies [2,3].

$$v_n = \frac{\omega_n}{2\pi} = \frac{\pi K}{8l^2}\sqrt{\frac{E}{\rho}}\cdot[3.011\,^2; 5^2\,;7^2\,;...;(2n+1)^2\,...]\tag{9}$$

and wave lengths:

$$\lambda_n = \frac{4l}{[3.011\,;5\,;7\,;...;(2n+1)...]}\,,\tag{10}$$

Where for $n=1$ we use 3.011 instead of 3.
    The frequencies and nodal points (for which x satisfies equation (7)=0 for all the time t) for the first modes are given in the table 1[2,3]:
The graphs of bending rod are given on the Figure 7.On this figure the numbers are

Table I. Characteristics of transverse vibrations in a bar with free ends.

Frequency (Hz)	Wavelength (m)	Nodal positions (m from end of 1-m bar)
$f_1 = 3.5607\ (K/L^2)\sqrt{E/\rho}$	1.330L	0.224, 0.776
$2.756 f_1$	0.800L	0.132, 0.500, 0.868
$5.404 f_1$	0.572L	0.094, 0.356, 0.644, 0.906
$8.933 f_1$	0.445L	0.073, 0.277, 0.500, 0.723, 0.927

relative frequencies; to obtain actual frequencies one must multiply them by $\frac{\pi K}{l^2}\sqrt{\frac{E}{\rho}}$.

Here we must note that for thin rods the first several modes of the bending waves have frequencies sufficiently lower than those for the longitudinal waves due to extra coefficient $\frac{K}{l}$(compare (9) with (4)). So they are below the hearing range and we can hear only the higher modes of binding waves. However higher modes are vanishing rapidly (we shall discuss it below).

1.133

3.125

6.125

10.125
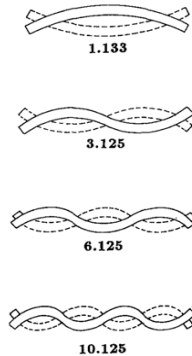
Figure 7. Bending modes [2,3]

Also, if one will consider the different "end conditions", the case with condition (a) "both free ends" begins with modes of higher frequency than case (b) "one clamped end -one free end" and(c) "two supported ends"[2,3], thus the second mode in case (a) is in "hearing frequency range", but in cases (b) and (c)–is not. This is why we considered only *"both free ends"* condition.

Here we must also mention that the effect depends on the point, where the rod is hit. The effect is much stronger, if one hits the rod transversally at the anti-nodes of the mode allowed by holding position. In such case relevant mode will be excited highly. Let us calculate the frequencies for the rods we used in experiment.

5. *Experiments with Bending waves.*
Now Let us describe the results of our experiments when we hit the rod normally to its axis with the Ebonite stick.
For our experiments we took *steel* rod (ρ_{St} =7,8·10³kg/m³;E_{St} =200×10⁹ N/m²;$C_{L(St)}$= 5150 m/s) of length *l*= 0.6m; radius *a*= 0.007m; Gyration radius *K=0.0035m.*
According our theoretical calculations, for this rod:
The first harmonic has the following parameters:λ_{B1}=0,8m;v_1=190Hz; nodes are at:x_1=0.13m, x_2= 0,47m.
The second harmonic has the following parameters:λ_{B2}=0,48m; v_2=525Hz; nodes are at:x_1=0.08m , x_2=0.3m , x_3=0.52m
The third harmonic has the following parameters:λ_{B3}= 0.34m; v_3=1029Hz; nodes are at:x_1=0.056m, x_2=0.21m, x_3=0.39m, x_4=0.544m.
As it was expected, if one holds the rod in the point where nods of several modes are placed all these modes will occur. Touching the rod at the ends damped the sound (because, as we discussed above, in such a case with the one clamped end only the high modes are in the "hearing range" but the high modes are damped very rapidly).
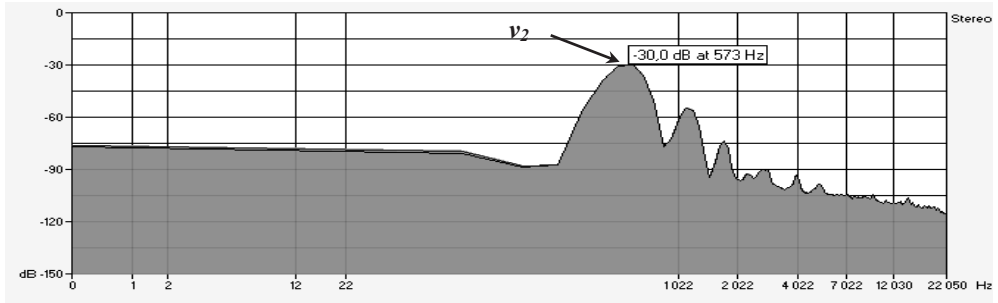
Figure 8. Spectrum of *Steel* rod (holding in the center)

On Figure8 we represent the spectrum analysis of the frequencies of sound generated by this *Steel* rod when we hold it in the center. We can see that in this case the second harmonic mode is excited.

Here it is worth to recall, that the low frequency pikes we saw on Figures 5 and 6, correspond to these bending waves. Of course in those experiments we occasionally excited such waves too.

As to (C)-type **Torsion Waves**, we did not focus on them due to technical difficulties, in particular the exciting of such type of waves without exciting other types of waves of large amplitude.

Beats.

In our Experiments we noticed that sound became sometimes stronger, sometimes weaker (see picture 9). This was because of Beats - an interference between two sounds of slightly different frequencies.
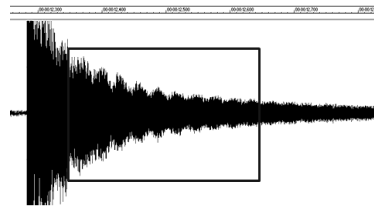
Figure 9. Beats

6. **Sound damping.**

Damping of rod vibrations generally speaking can be caused by the following reasons: 1. Air damping; 2. Internal Damping; 3. Transfer of energy to other systems (e.g. fingers holding the rod).

Sound damping is the exponential function. For vibration amplitude one can write[2,3]:

$$A = A_0 e^{-\frac{t}{\tau}}$$

where τ is the so called "decay time" – the time at which amplitude damps in e-times. This decay time for the mentioned damping reasons has the following form[1,2]:

For the Air dumping: $\tau_a \sim \rho r / \sqrt{v}$ where r is rod radius, ρ its density and v – vibration frequency.

For the Internal damping: $\tau_{int} \sim \frac{1}{\pi v}$

For the case of energy transfer to other systems: $\tau_{sup} \sim \frac{1}{lGv^2}$

As we can see, in all cases dumping is higher for large frequencies. So, we can conclude that higher modes damp sooner, also, longitudinal waves damp faster than bending waves because the latter have the lower frequency modes. This we saw in out experiments – the longest lasting were the low modes of bending waves.

7. *Conclusion.*

We investigated compression, bending and torsion waves which are excited if one hits the thin rod.
We find that:
- There are different types of waves in the rod - compression, bending and torsion waves;
- The type of wave (are they compression, bending and torsion waves, or several type of waves at the same time)depends on how dowe hit the rod;
- The frequency of standing wave depends on where we hold the rod - if one holds the rod in the place where are the nods of several modes, all these modes will occur. Touching the rod at the ends will stop the sound;
- The frequencies of bending waves are lower than of compression waves;
- Damping of the waves depends on frequency.

References
[1] http://encyclopaedia.biga.ru/enc/science_and_technology/ZVUK_I_AKUSTIKA.html

[2] Rossing T.D., Fletcher N.H. "Physics of musical instruments".New York etc., Springer-Verlag 1991.

[3] Rossing T.D., Russell D.A. Am.J.PhysVol 58, No 12. 1990. P.1153.

[4] S. Errede. "The Physics of a Longitudinally Vibrating Metal Rod".University of Illinois, Urbana-Champaign, IL, 2009.

[5] D.R. Lapp. The Physics of Music and Musical Instruments.Wright Center for Innovative Science Education, Tufts University, Medford, Massachusetts, 2003.

[6] www.arborsci.com/Data_Sheets/Files/SingingRods.pdf ; www.arborsci.com/singing-rods-set-of-2

No. 13, Shrieking rod: Investigating the sound produced by hitting a metal rod

Zahra Karimi [1]

[*] Team of Iran, IYPT 2010

[1] *Sharif University of Technology, Iran*

Corresponding author: sh.z.k.93@gmail.com (Z. K.)

Abstract: Working with the sound waves while there are several types of motions and several patterns can be a complicated task. This paper contains the results of investigating the sound waves (based on frequency) caused by hitting metal rods which are held from one point within their length. The investigations are done by analyzing Fourier spectra of the sounds produced by metal rods. It will be proved experimentally that the rods behave similar to tubes open from one end in propagating the sound. In this case there are many different patterns which are caused by longitudinal and transverse waves propagating within the rods.

Keywords: rod, longitudinal waves, transverse waves

Introduction

Many of the interesting effects and phenomena in physics are caused by various behaviors of the waves e.g. sound but unfortunately high school students don't have enough experimental experiences with sound waves. One of the goals of this paper is to figure out different patterns of sound waves which can propagate within a metallic rod both in theory and experiments (the focus is on standing waves).It's been proved that both longitudinal and transverse waves can propagate in solids. In the case of cylindrical metal rod which should be held at a certain position within its length and be hit, for finding the right patterns of propagation paying attention to both holding point and hitting type is necessary.

Hypotheses

Holding point can be considered as a node because approximately there is no motion at this point, the place of this node is really critical in understanding the accurate pattern of longitudinal and transverse waves.

A metal rod can be analyzed theoretically in similar way as a tube opened from both ends. In case of longitudinal oscillations, only the fundamental frequency and harmonics, for which the nodes are at the same place as holding point, can be observed. This means that the longitudinal wave can only be produced by holding the rod at even multiples of the length ($1/2L.1/4L.1/6L,...$).(figure 1)
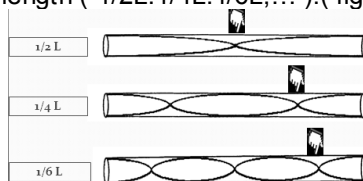
Figure 1

Note that the place of node affects the propagation of the transverse wave as well as longitudinal wave but the fundamental frequency and harmonics of transverse wave are not as simple as longitudinal wave but the second harmonic of the transverse motion and fundamental of longitudinal motion both have nodes at center [2].

Moreover torsion waves can propagate in rods if the rods are hit on the edges [1] but these waves are not investigated in this paper due to their complicated structure and small diameter of the rods which were used for experiments.

There are two general types of hitting the rod one is striking it at the end (figure 2) and the other is hitting it downward (figure 3).
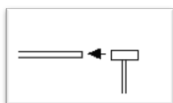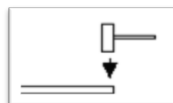
Figure2   **Figure3**

when the rod is been stroke at the end there will be a longitudinal wave (if it's been hold at the points mentioned above e.g. 1/2L,1/4L,…) but if it's been hit downward, both longitudinal and transverse motion can be observed. To go through the details, paying attention to the vibration which is caused by each type of hitting and the direction of propagation of the wave (sound) can be helpful. When the rod is stroke at the end there will be a horizontal vibration at the end while the wave is propagating horizontally within the rod's length as well, this situation is the description for a longitudinal motion (as it is mentioned above, the place of holding is important too), but when the rod is been hit downward both vertical and horizontal vibrations can be produced and these vibrations cause waves which are propagating horizontally , in this case both longitudinal and transverse waves can be produced(again the place of holding is important) .

Experiments

For going through the details of the wave patterns, proving the hypotheses and investigating the effect of different parameters on the sound caused by hitting the rod, experimental observation is indispensable.

Parameters bellow are those which their effect on propagation of sound waves in the rod will be explained in the experiments.

-length of the rods
-material of the rods
-place of holding
-type of hitting
-place of hitting

For understanding the effect of each parameter on the sound waves having the frequency and intensity of the waves and their spectra is essential, the best way to measure these two parameters and achieving to waves' spectra is doing a Fourier transform on the sound caused by hitting the rods.

Experimental setup

The setup which experiments were done with contains a microphone which is placed at a constant distance from the rod (in order to record the sound), a hammer for hitting the rod and a rod (it's been held tight from one point within its length).(figure4) &(figure5)
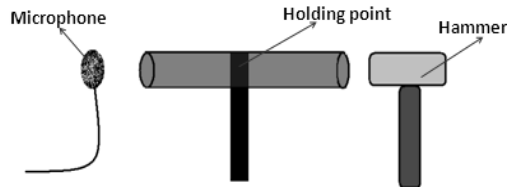
Figure4
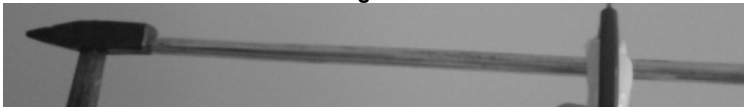
Figure5

The process of each experiment

1-hitting the rod
2-recording the sound with a microphone (Neumann U 87 Ai capable of recording 16 to 18000 Hz) attached to a computer
3-doing the Fourier transform on the sound with a software(Cool Edit Pro 2.0)
4-analayzing the spectrum(amplitude verses frequency)

-Effect of the length and holding position
Harmonic longitudinal motion

In this part the experiments were done with aluminum and steel rods in different lengths and each of them were held from three different positions (center, 1/4 of the length,1/6 of the length) and been hit, in each case the longitudinal frequency is measured from the spectrum of the sound recorded from the experiment (e.g. figure 6)

Green=60cm aluminum rod
red-=50cm aluminum rod
Purple=40cm aluminum rod

Frequency

Aluminum rods
Diameter=8mm
Holding point=center
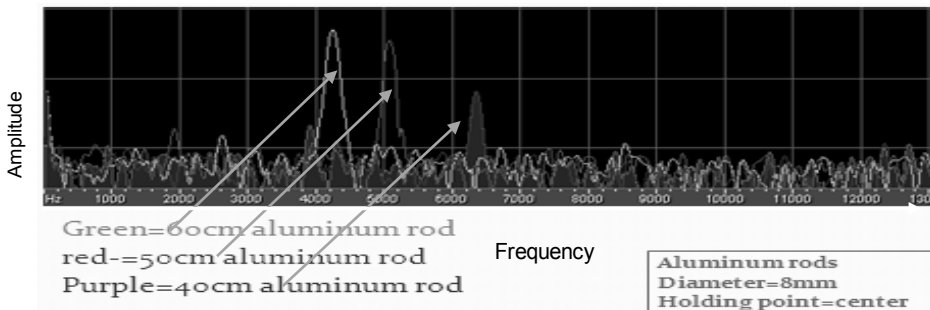
Figure6

For doing a comparison between the numbers came from the experiments and the theory, expected frequency for each rod has been measured due to its holding position

and material, there is an example of measurements done for achieving to the expected number of frequencies:

L=60cm	a =12mm	V=4963 m/s *	Holding point=1/2 L

*the speed of the sound in aluminum is measurable by knowing its Young's modulus and density following the formula: $v = \sqrt{\frac{Y}{\rho}}$

$$f_n = n\left(\frac{V}{2L}\right) \quad n = 1, 2, 3... \qquad f = \frac{v}{\lambda}$$

$$\lambda = 2L$$

$$f_L = \frac{4963.3}{1.2} = 4136.08 Hz$$

[3]

To visualize these comparisons there are graphs which were drawn by the numbers came from experiments and the numbers measured by the theory.
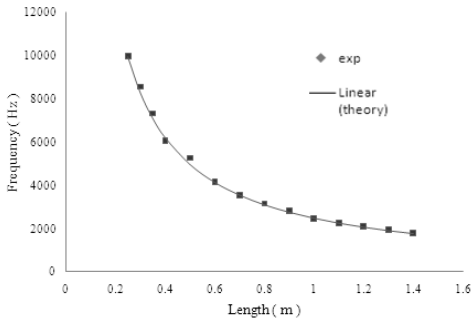
holding point: center
material: aluminum diameter:12mm
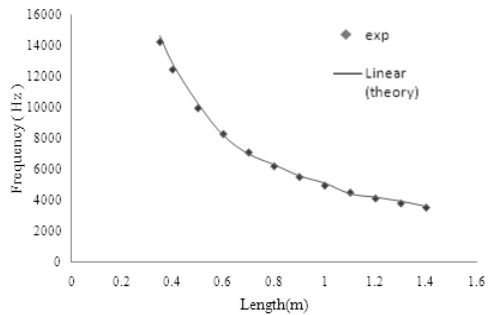
holding point: 1/4of the length
material: aluminum diameter:12mm
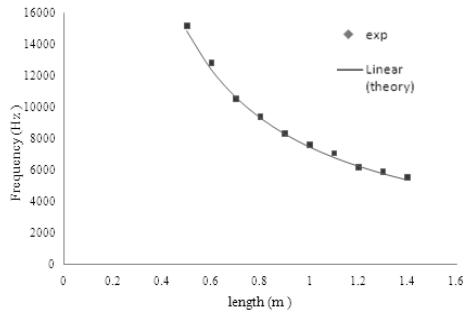
holding point: 1/6of the length
material: aluminum diameter:12mm
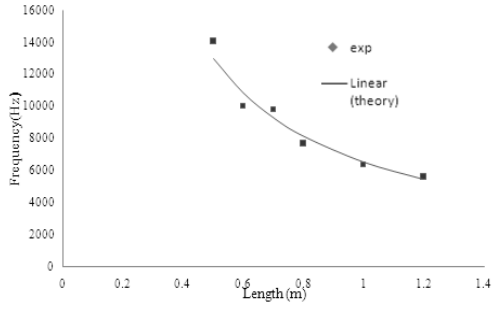
holding point:center
material: aluminum diameter:12mm

As it is obvious in each case theory line fits the experiment data, but there are some other longitudinal waves which can be observed in the spectra of the sounds, these longitudinal waves appear in the form of a fundamental frequency and its odd harmonics (exactly like a tube which is closed from one end). For example for a rod described in the table below

Aluminum rod	Length=140cm	Diameter=12mm	Holding point=1/2 L

These frequencies can be observed in the spectrum

Fundamental	3rd harmonic	5th harmonic	7th harmonic
1756 Hz	5297Hz	8828Hz	12360Hz
-	1756*3.001	1756*5.001	1756*7.002

From the data above it can be concluded that 1756Hz frequency is the fundamental and other frequencies are the odd harmonics. From the formula of longitudinal waves the length of the rod which is producing these frequencies can be measured.

$$f = \frac{v}{\lambda}$$
$$\lambda = 4L$$
$$f = 1756 Hz$$
$$1756 \times 4L = 4963.3$$
$$L = 0.70m$$

For the example above 70cm is exactly the distance between the holding point and hitting position, this means that the part of the rod which is between the holding point and hitting position is acting like a tube which is closed from one end.

These phenomenon was repeated for other places of holding (1/4 length and 1/6 length) as well. For example for the rod described in the table bellow

Aluminum rod	Length=140cm	Diameter=12mm	Holding point=1/4 L

These frequencies can be observed in the spectrum:

Fundamental	3rd harmonic	5th harmonic
3576 Hz	10720Hz	17522Hz
-	3576*2.99	3576*4.9

And again measurements show: $\longrightarrow$

$$f = \frac{v}{\lambda}$$
$$\lambda = 4L$$
$$f = 3576 Hz$$
$$3576 \times 4L = 4963.3$$
$$L = 0.346m$$

This number is approximately equal to ¼ of the length: 0.346≈0.35
These waves can be observed in the rods with shorter or longer lengths as well.

Harmonic transverse motion

Unlike the longitudinal harmonics detecting the transverse harmonics is not easy, this is because of quick damping and small frequency of these waves, but still in some cases these waves are detectable.
For example in steel rod (length=0.5m, radius=1mm) if it is held from center the second and forth harmonics which have same nodal positions are expected to be produced.[1]
Frequencies of these waves are measured as bellow:[1,2]
v=6100 m/s (v=velocity K=radius of gyration for cross section L=length)

$$f1T = 3.5607 \frac{K}{L^2} V \quad f4T = 8.933\,f1T$$
$$f1T = 43.44\,Hz \quad f2T = 388\,Hz$$

The frequency detected in the experiments for this case was 405 Hz

Transverse and longitudinal waves
-type of hitting

Type of hitting won't cause any change in longitudinal motion but it will affect the existence of the transverse motion.(figure 7)&(figure8)

Aluminum rod	Length=60cm	Diameter=8mm	Holding point=1/2 L
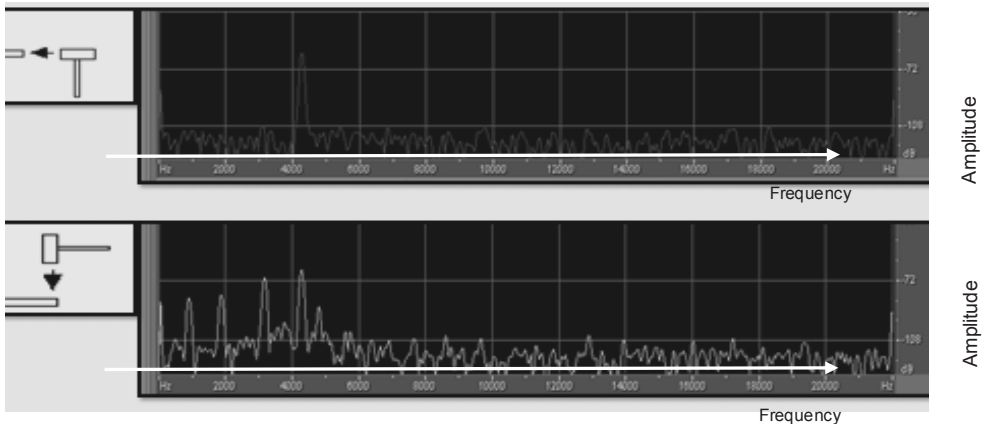
Figure 7
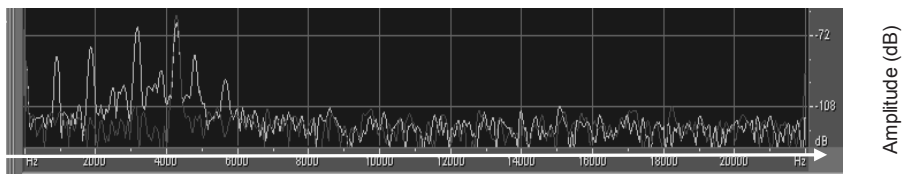
Frequency (Hz)
Figure8

The longitudinal fundamental in both cases=4306Hz

Note that by hitting the rods downward some transverse waves will occur but they will damp quickly and they are not the expected transverse harmonics unless the rod is held from a transverse harmonic nodal point, the term transverse motion is referred to these waves due to their structure but they shouldn't be misunderstood with harmonic transverse motion.

For going through the details about this fact that longitudinal waves won't change by changing the type of hitting again using a graph can be helpful.

Material=aluminum	Diameter=12mm	Holding point=1/2 L
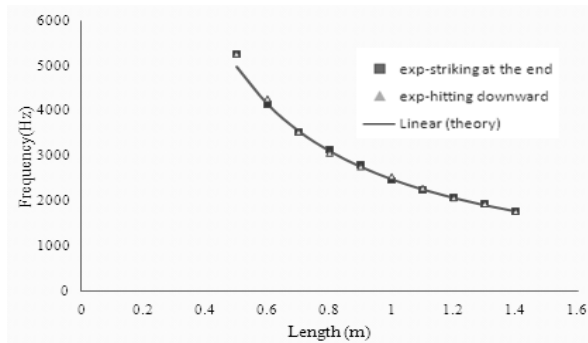
For longitudinal waves these three data series fit on each other, this means that the longitudinal motion is independent of hitting type.

Effect of hitting place: although both transverse and longitudinal motions in the rod are dependent to the holding place (which is considered as a node) but both of this waves are independent of place of hitting.(figure9)

Material=aluminum	Length=60cm	diameter=12mm	Holding point=1/2 L
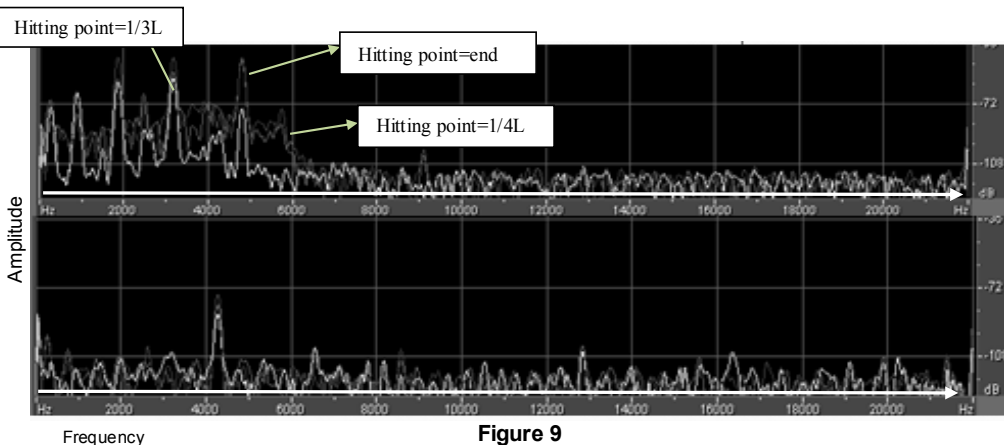
Figure 9

Figure 9 shows the spectra of the sound caused by hitting the same rod at different positions in different colors. Frame one is in the first second after hitting and frame two is milliseconds after frame one, in frame two only the longitudinal motion can be observed, this is because of the longer sustainability of the longitudinal waves in compare to transverse waves due to their less energy loss.

Note that if a rod is held from one of it nodes and hit on the other node the harmonic frequency which have the same node place might be produced but will be damped quickly due to the strike on the other node.

Effect of diameter: although the longitudinal waves are independent to the rod's diameter but transverse motion can change by changing the rod diameter, this is simply because of the structure of transverse waves.
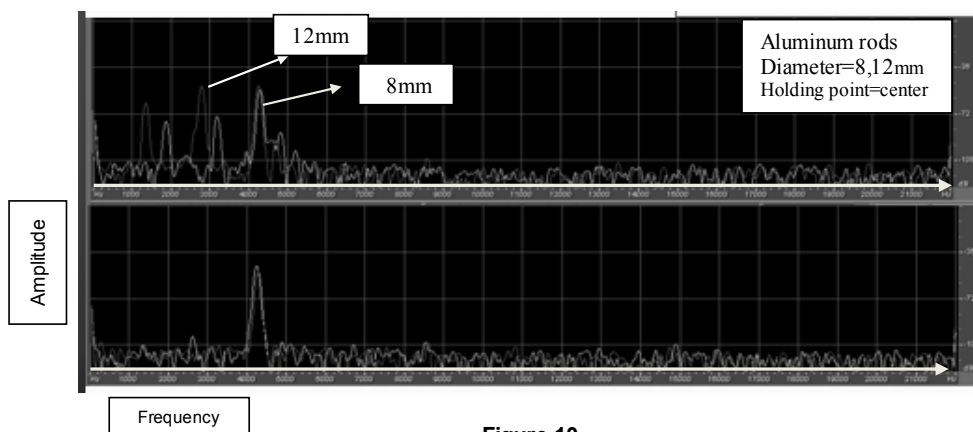
Figure 10

In the first frame of figure10 it is observable that two spectra (belonging to two rods with different diameters but same materials) don't fit on each other in the first two frequencies but they fit on each other in the third frequency (third frequencies are the longitudinal frequencies due to the measurements and their longer sustainability).in frame two which shows the situation of the waves a few milliseconds after the first frame (after disappearance of transverse motion) it is clearly obvious that the longitudinal waves of the both rods fit on each other and have the same frequency.

Summary of the results:

-Both longitudinal and transverse motion can occur in the rods.

-Hitting the rod downward in any place within its length will cause a transverse motion.

-There is a node at holding point.

-Standing longitudinal waves can only occur when the holding point is at an even multiple of the length (measurable nodes)

-The place of hitting won't affect the longitudinal waves.

-The transverse waves are dependent to the rod diameter.

-Rod material won't change the behavior of the transverse and longitudinal waves propagating in it.

-Some of the longitudinal waves in the rod are produced by certain parts of the length not all of it.

References

[1]Rossing T D Russell D A 1990 Laboratory observation of elastic waves in solids Am. J. Phys. 58 (12), 1153-1162
[2]   Paul   Doherty,   Ringing   aluminum   rods,2-8.   (1997)
http://www.exo.net/~pauld/summer_institute/summer_day11sound/ringing%20_Al_rod.html
 [3] Halliday D Resnick R Walker J 2010 Principles of Physics Wiley

No. 14, Magnetic spring: Vertical oscillations in a system of two magnets

Igor Marković [1]

[*] Team of Croatia, IYPT 2010
[1] *University of Zagreb, Croatia*
Corresponding author: imarkov@dominis.phy.hr (I. M.)

1. Introduction

This is the original solution of team Croatia for the Problem 14, Magnetic Spring for the IYPT in Vienna, 2010. I was then a senior high school student and in charge for this problem but never got to report it. Here are given: a theoretical model based on conservation of energy, description of the experimental apparatus and a discussion of the results.

2. Problem

Two magnets are arranged on top of each other such that one of them is fixed and the other one can move vertically. Investigate oscillations of the magnet.

3. Theoretical model

3.1. Oscillation period

There are two physically important aspects in this setup that cause the oscillations; gravitational force (attraction) and magnetic force (repulsion). For the theoretical model a simple dipole approximation was used for the magnets and friction was neglected. The problem was approached using the law of conservation of energy. The total energy of the system is given with:

Figure 1: Qualitative graph of potential energy. Total energy is determined from the initial hight, z_{max}

$$E_{tot} = \frac{mv_z^2}{2} + mgz + \frac{\mu_0\mu^2}{2\pi z^3} = E_p(z_{max}) \quad (1)^{1,2}$$

m being the mass of the magnet, z position on the vertical axis, v_z the corresponding velocity, and $\mu = B_r V_m/\mu_0$ its magnetic dipole moment[1] (B_r is the remanent field and V_m the volume of the magnet). This expression, upon extracting the time differential from the vertical velocity, putting $E_{tot} = E_p(z_{max})$ and integrating from z_{min} to z_{max} (from the lowest to initial height of the magnet), yields, after rearrangement:

$$T = \sqrt{\frac{2z_{max}}{g}} \int_\gamma^1 \frac{d\zeta}{\sqrt{1-\zeta}\sqrt{1 - \frac{\gamma^3}{\zeta^3}\frac{\zeta^2+\zeta+1}{\gamma^2+\gamma+1}}} \tag{2}$$

with T the period of oscillations and $\gamma = z_{min}/z_{max}$, $\zeta = z/z_{max}$ substitutions made to simplify of the formula. The integral can be thought of as a correction of the free fall due to magnetic repulsion. The substitutions make the integral dimensionless and store all the parameters of the magnet in a single parameter of the formula, γ:

$$\frac{\gamma^3}{\gamma^2+\gamma+1} = \frac{B_r^2 V_m^2}{2\pi\mu_0 mgz_{max}^4} \tag{3}$$

The theoretical predictions thus come from solving the expression (2) with given parameters of the system whereby we have a quantitative theoretical model of the first oscillation period with no free parameters.

3.2. Oscillation trajectory

In the trajectory prediction two extremes are analyzed: the magnet moving far from the equilibrium and oscillations near the equilibrium. In both cases approximations are used on the potential energy (Figure 1). In the first case, we can approximate the potential with two straight lines. The gravitational part gives a linear dependence (as in (1)) while the magnetic part gives a vertical potential barrier. Behaviour of the magnet is then similar to a bouncing ball (the energy here being drained by, along with air resistance, the eddy currents[1] instead of deformations). The trajectory for each period in that case is a parabola[2]. In the second case, near the equilibrium, the potential energy can be approximated with a parabola, thus making the magnet behave as a harmonic oscillator[3] (damped because of air resistance, eddy currents and friction with the tube). This means that the trajectory near the equilibrium is a damped sine[3].

4. Apparatus and measurements

For any measurement, what is needed first is a setup that enables the magnets to behave as the problem states. That was achieved using the apparatus shown in Figure 2. The tube enables only vertical motion of the mobile magnet and is lifted form the housing so that the airflow through the tube would be unobstructed and cause less damping. The magnets used were long and cylindrical to improve the dipole approximation. They were NdFeB, with the remanent field of B_r=1.4T.

4.1. Period measurements
A hand made copper coil, made of 50μm thick wire, was placed around the tube for period
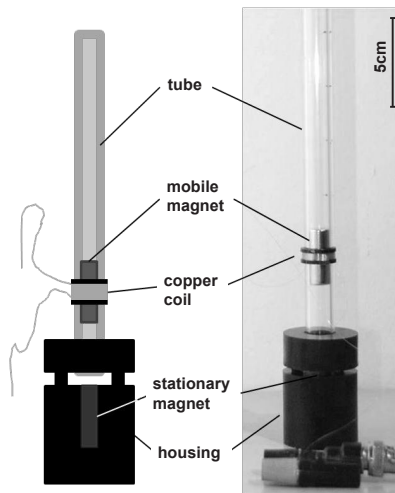
Figure 2: Magnets housing with the coil to measure the period

measurements. It was attached by a sliding plastic ring at the equilibrium position (Figure 2). Moving through the coil, the magnet induces a voltage proportional to its speed[1]. The voltage is measured by a high internal resistance voltmeter, and the signal from it is than stored on a computer via an AD converter. A typical measurement is shown in Figure 4a.

Mass was changed by stacking M4 nuts upon a threaded rod attached to the magnet. The bottom nut was made of steel so that is 'sticks' to the magnet while the other nuts and the rod were brass so as not to change the geometry and the parameters of the magnet. Period and equilibrium position were measured in dependence of mass of the magnet. Period was also measured in dependence of initial height, $z_{max.}$

4.2. Trajectory measurements

To find the trajectory of the mobile magnet the housing was placed upon a small wheelcart pulled by an electromotor at a constant velocity. This provided an x axis in space that is linear with time. A luminescent fluid (from fishing gear) was attached on top of the mobile magnet in a capsule (Figure 3) and the magnet was set to oscillate on the moving cart. A photo with a 6 second exposition was taken in complete darkness giving the position z of the magnet in time, an oscillogram of the magnet (Figure 4b). Also, using this method, the z_{min} vs. z_{max} dependence was determined.

The period measurements give the behaviour of the first period for the corresponding initial height while the trajectory (position) measurements explain the way the system evolves from there. That means that, if it proves that our theoretical model can predict both of those with satisfying accuracy, we can predict the magnets oscillations entirely.
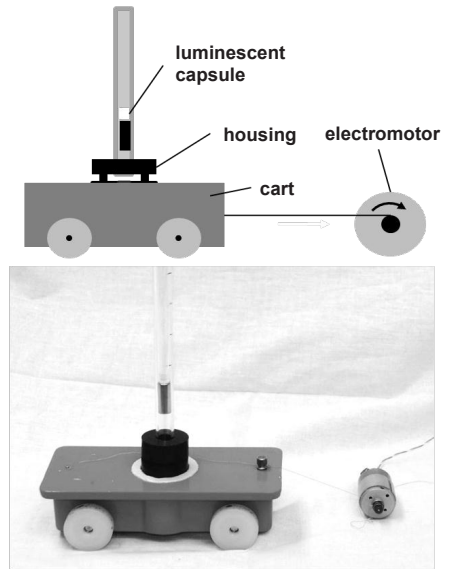
Figure 3: Trajectory measurement apparatus
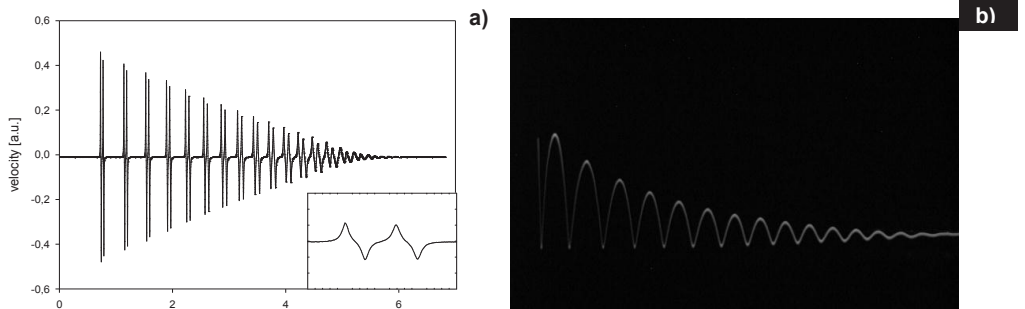
Figure 4: typical measurements of
a) period (insert is a closeup of one period)   b) trajectory (oscillogram**)**

5. Results
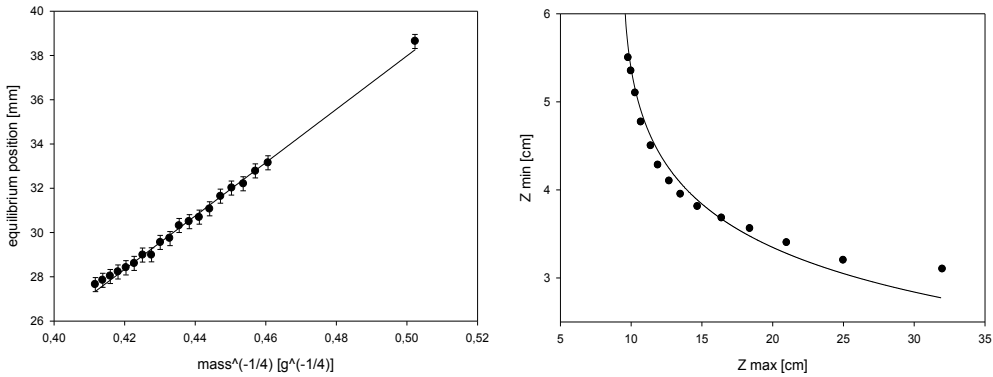
Figure 5:
a) graph of the dependence of the equilibrium position on mass to the -1/4. The line is a linear fit to verify the dipole approximation
b) graph of minimal to maximal height dependence. The line is the theoretical prediction from (2). Estimated error is given with the point size

Some measurements were made to verify the validity of the dipole approximation and the consistency of the theoretical approach (Figure 5). To verify the dipole approximation, static case when the magnet is motionless in the equilibrium position is examined. The sum of forces that act on the magnet in that case is zero (differentiating E_p at $z=z_{eqilibrium})^2$. The dipole approximation is in the magnetic repulsion force. In the expression obtained that way equilibrium position is proportionate to mass to the power of -0.25 ($z_{eq} \sim m^{-1/4}$). Figure 5a is a graph of that dependence with a linear fit which shows that the approximation is valid in this experimental range. To connect the „period" and „trajectory" aspects as well as to check the consistency, the z_{min} vs. z_{max} (within one period) dependence is crucial. In the theoretical model it is given with γ, which is the ratio of the two but also connects to all parameters of the magnet as given in (3). Good agreement of experimental
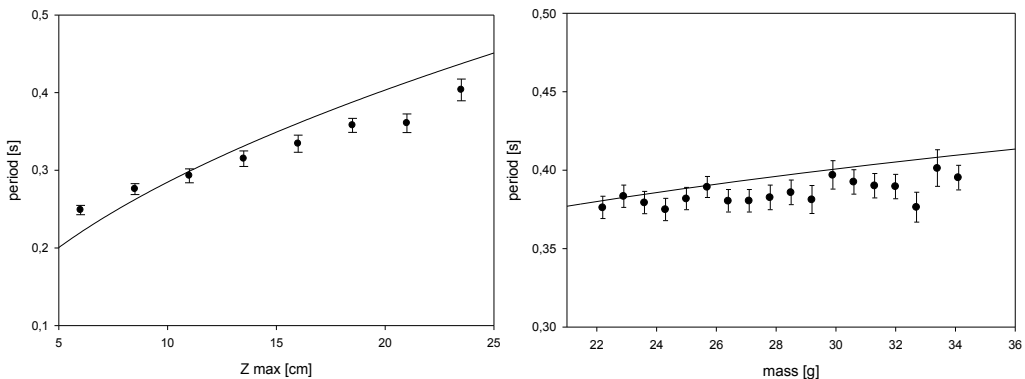
Figure 6: a) dependence of period on initial height, b) dependence of period on mass
The lines are theoretical prediction from (2)

data with the theoretical prediction (Figure 5b) truly gives strength to the proposed theoretical model. It only begins to disagree for large initial heights, where obviously friction needs to come into account.

In Figure 6a is given the graph of the dependence of period on initial height. Each local trajectory maximum can be seen as an initial height point; the graph than shows that the period is not constant during the oscillations but decreases. The experimental mass dependence of the period (Figure 6b) follows the theoretical line well with only a small offset and shows the expected behaviour of slight period increase for bigger masses.

The trajectory measurements (Figure 7) consist of analyzing pictures such as the one in Figure 4b. Two regimes are separated by a vertical line in Figure 7. In the first regime the magnet goes far from the equilibrium and is in a free fall scenario. Thus,

Figure 7: analyzed oscillogram with fitted parabolas, damped sine and the parabola envelope. The vertical line is the boundry between regimes

parabolas were fitted to the experimental curve. The second regime is when the magnet is near the equilibrium position and behaves as a damped harmonic oscillator. There, a damped sine is fitted to the curve. The envelope fit over the peaks is parabolic. That is consistent with the fact that the speed of the magnet was decreasing linearly with time (Figure 4a).

6. Conclusion

The solution to this problem was based on two approaches, the period and the trajectory. The first one includes a quantitative theoretical model with no free parameters that gives good agreement with the experiment even in spite of its simple approximations. The dipole approximation is shown to be valid by the dependence of equilibrium position on mass. The period was observed to increase both with the increasing mass and the initial height (not constant during oscillations). Deviations from the experimental data were observed for large initial heights. That is contributed to the lack of friction in the model. The mutual consistency of the two approaches is tested twice. First, the dependence of the lowest on the highest point of oscillations within a period is determined experimentally from the trajectory and agrees well with the prediction from the period theory. Second, from period measurements we see that the speed drops linearly whereas the maximal hight drops parabolically in the trajectory measurements.

A quantitative theoretical model was given with (2) that has no free parameters, experiments were developed and the obtained results were in good agreement with the theoretical prediction. The oscillations of the magnet were thus thoroughly explained.

7. References

[1] Purcell 1965 Electricity and magnetism: Berkeley physics course, vol.2
[2] Kittel 1965 Mechanics: Berkeley physics course, vol.1
[3] Crawford 1968 Waves: Berkeley physics course, vol.3

No. 15, Paper anemometer: Autocorrelation analysis of the noise from a fluttering paper strip

Igor Marković [1]
[*] Team of Croatia, IYPT 2010
[1]*University of Zagreb, Croatia*
Corresponding author: imarkov@dominis.phy.hr (I. M.)

1. Introduction

Here is presented the original solution of team Croatia for the Problem 15, Paper Anemometer for the IYPT in Vienna, 2010. The problem was often presented that year, even at the finals, and each time with a different interpretation. Here is yet another one, conceptually different then any we saw presented at the IYPT. We deem this interpretation to be the one that follows the text of the problem the best.

2. Problem

„When thin strips of paper are placed in an air-flow, a noise may be heard. Investigate how the velocity of the air-flow can be deduced from this noise."

3. Apparatus

The idea was to create controlable air-flow conditions in which to put the strips of paper, record the sound and determine the velocity vs. noise intensity dependence depending on the parameters of the strips (number, material, dimension…). Thus it would be enough to record the noise for a strip configuration on an unknown velocity and from the noise intensity thus obtained we get the air-flow velocity. The apparatus was set up in a special air-tunnel for better control and precision of air-flow characteristics and velocity. Inside it, a paper strip holder is fixed. A microphone was placed beneath the holder outside the tunnel so as not to disturb the air-flow.

3.1. Air tunnel

This air-tunnel was made by the Croatian IYPT team some years ago to help solve IYPT problems. It was made reffering to a public-accessable NASA's Baals Wind Tunnel design[1] but using many original soutions as well[2]. It is designed to provide maximal laminarity of the air-flow. This is achieved by applying a special-geometry tubes on both the entrance and the exit of the tunnel with grids covering them (Figure 1). The square to circle cross-section transition at the ventilator exit is very important for minimization of air-flow disturbance. For the same reason the ventilator, that is the source of the air-flow, is placed at the exit of the tunnel; it sucks the air in. In the small central part that is the operational part of the tunnel, the air-flow is very laminar which was verified with a smoke and thread experiment. The air-flow velocity can be accurately changed by a voltage power source connected to the ventilator. The voltage was calibrated to the air velocity using a small anemometer. Maximum air-flow velocity achievable in this air-tunnel is 15 m/s. That corresponds to large wind velocities, and is enough to make an operable anemometer.
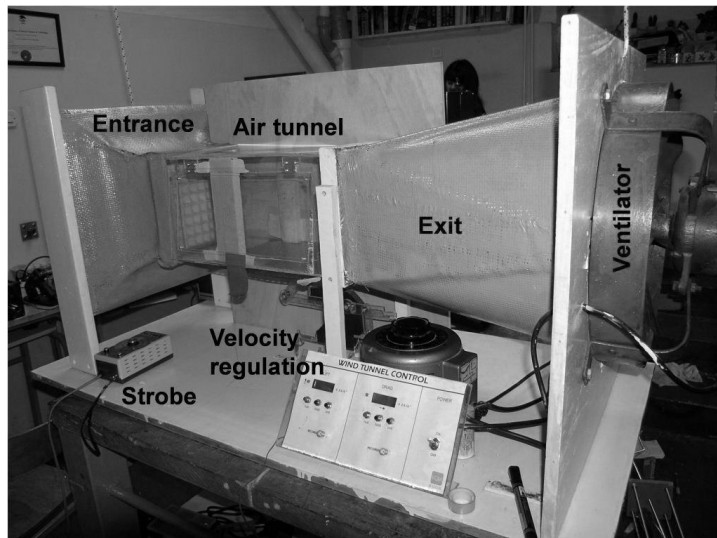
Figure 1: Air tunnel, home made for the purposes of the Croatian IYPT team

3.2. Paper holder

The paper hoder design had two main tasks: to hold various number of paper strips in the middle of the tunnel and to keep it's influence on the flow minimal. For this purpose two polystyrene poles were made and fixed to the sides of the tunnel. Threads were spread between them on which the papers were hung one above the other (Figure 2). The poles were shaped aerodynamically to minimize the disturbance in the air-flow. Two kinds of strips were used to vary the material. One was plain 80 g/m^3 paper and the other was a plastic foil. All the strips used were 15 cm long and 2 cm wide. By changing the size of the strips the principle of how the anemometer works doesn't change so this anemometer was made in reference to this size of strips.
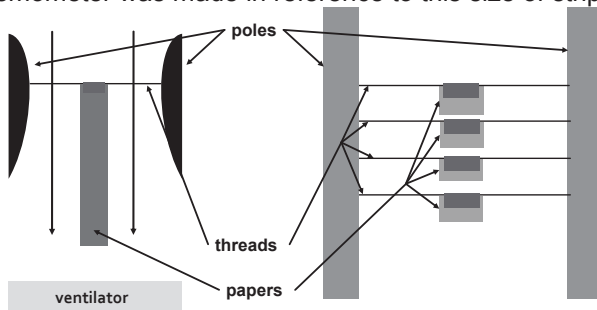
Figure 2: Scheme of the paper holder
Left: top view, red arrows represent the air-flow
Right: front view

Underneath the holder there was a hole in the tunnel. The microphone was placed below the hole so the sound recorded would be as clear and loud as possible.

4. Measurement

We believe that the noise to which the text of the problem referes to is the loud flapping noise made by the strips hitting each other as opposed to the clear sound produced by blowing on the edge of a single paper . Thus our measurements were designed to investigate when this hitting occures and how it can be related to the air-flow velocitiy.

4.1. Strobe measurements

When a strip of paper is put in a moderate air-flow it will oscillate in a wave-like motion. In order to see how this happens and to determine the frequencies of the oscillations a strobe was used. The strobe provides periodic flashes at a set frequency and thus, when it shines on the paper in motion, provides a picture of the paper at time intervals set by the strobe frequency. By setting the strobe to the exact same frequency as the oscillations of the paper the image of the paper is frozen (Figure 3). This is a very accurate method of determining the paper frequency. If the strobe is set near the paper's frequency, the entire trajectory of the paper is seen in slow motion. Using this method three regimes were observed up to 15 m/s. In the first regime, low velocities, the papers all oscillate together, in phase, without even touching so no noise is heared. In the second regime, the oscillations are still regular, but the papers are in counter-phase. They touch but gently so still no noise is heard. The third regime is chaotic, there is no set frequecy at which the strips oscillate and they even bend and hit each othersideways (Figure 3c). The noise from the papers hitting is now heard but the papers are also destroyed from that same hitting (Figure 4). This demands an investigation of how the intensity of the noise deteriorates in time due to the strip edge destruction.
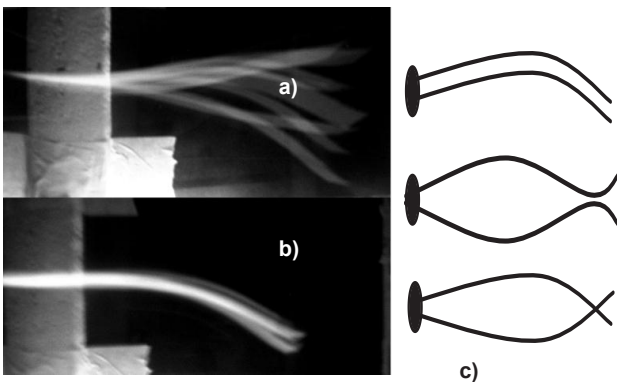
Figure 3: Strobe measurements
a) wrong frequency b) correct
frequency c) regimes sketches
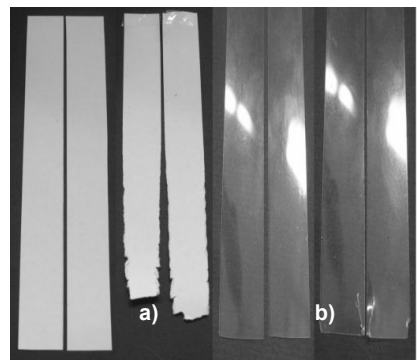
Figure 4: Strip destruction for: a)
paper b) plastic foil
left is before, and right is after being
used

The regimes of oscillations can qulaitatively be explained by the Reynols number of the flow around the paper which is proportional to the flow velocity[3]. The larger the Reynolds number, the smaller the boudry layer on the papers. When the flow is slow, the boundry layers are thick and they merge between the papers causing joint movement of the strips. As the flow gets faster, it makes the boundry layers thinner and the correlation of the strips movements decreases. This causes the strips to first go into the counter-phase regime and finally to the chaotic regime as the flow arond them becomes too turbulent, the boundry layers too thin to keep them correlated.

4.2. Noise analysis

The sound recorded by the microphone was analysed by a specialized computer program. The interval chosen for the analysis was always the same length and it began when the ventilator reached its final velocity. This was done to minimize the effect of intensity reduction due to paper destruction. In the obtained recording the signal (i.e. paper noise), is indistinguishable form the ventilator noise. This was solved by applying the autocorrelation on the sound interval. Autocorrelation is a mathematical method that seaches for periodical events in a signal, it is a much used tool for time domain signal analysis. It has a peak at a time value if similar event occur within the signal with that time as the period. Such an autocorrelation graph for the time interval from this measurement is shown in Figure 5. Once identified as the strips hitting signal, the peak can be seen as a direct picture of the intensity in time of an average strip hit. It is very sharp due to the small duration of the sound of the hit while the height, the intensity, is proportional to the occurence frequency and to the square of the sound amplitude. The intensity of this peak is what is here interpreted as the parameter of the sound by which the air-flow velocity should be determined.
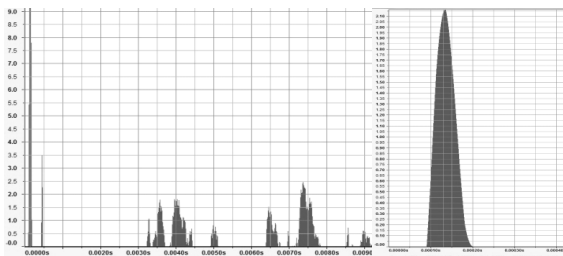
Figure 5: a) autocorrelation graph b) isolated peak that represents the signal (the highest, leftmoast peak from the graph in a)

5. Results

To shed light on the strip motion itself first measurements are those of the frequency to air-flow velocity dependence. This was measured for 1 up to 4 strips of paper. The measurement for 1 paper is shown in Figure 6a. It starts making the noise at about 8 m/s where the graph has a jump. The dependence at the noise regime is approximately

linear. The same dependence for 2 to 4 sprips is shown in Figure 6b but only the silent regimes. A discrete jump can here be seen at the same velocities regardless of the strip number, at the same moment when the strips go form oscillating in phase to counter-phase. It can also be seen that the more papers we have, the lower the velocity at which they begin to oscillate, but also the lower the velocity at which they
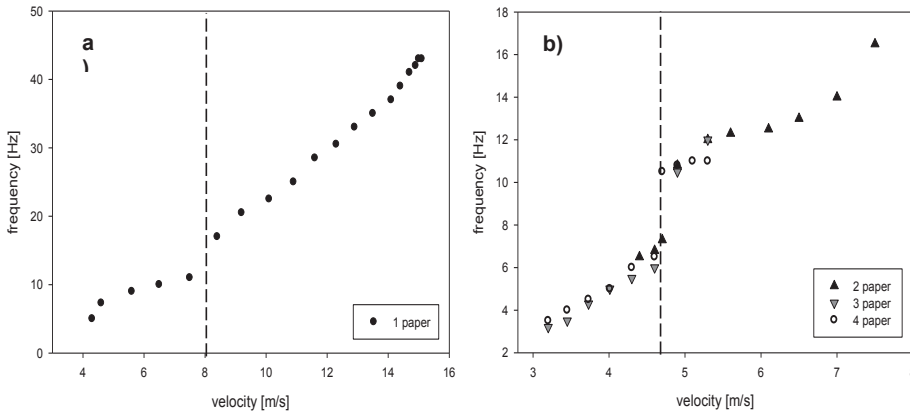
Figure 6: graph of frequency to air-flow velocity dependence for:
a) one paper. The vertical line is the border between the silent regime and the noise regime
b) two, three and four papers. The vertical line is the border of the first and second regime. The data shows the full first and second regime of the paper oscillations.

go to the chaotic regime (Figure 6). The air-flow velocity for the silent regimes can thus be determined by measuring the frequency of the strip oscillations. The problem of paper destruction with time was also investigated to ensure reproducibility oft he measurements. The graph (Figure 7) clearly shows that the intensity of the noise from paper strips drops with time while being relatively constant for plastic foil strips. Similar graphs at different air-flow velocities show that the destruction of the paper strips gets more intense the faster the air-flow. The intensity for plastic strips remains relatively constant at all velocities.
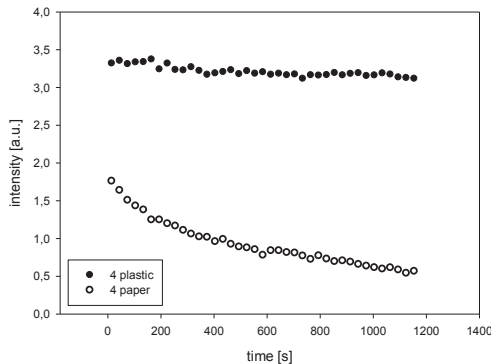
Figure 7: noise intensity in time for plastic and paper strips

The main idea was to obtain a relation that would be in a good agreement with the measured dependence of air-flow velocity on the noise intensity. Thus the velocity to noise intesity dependences were plotted for four strips, both paper and plastic. The graphs obtained (Figure 8) are seen to be approximately linear so the linear fits are set
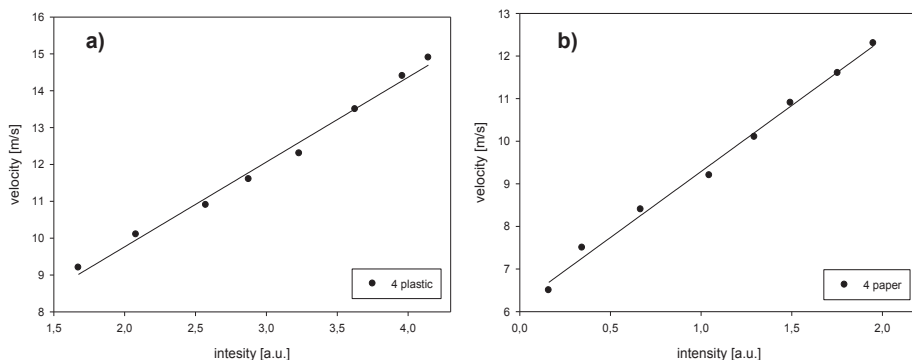
Figure 8: graphs of dependences of air-flow velocities on noise intensity for:
a) 4 plastic foil strips b) 4 paper strips

to be calibration curve for this anemometer. For the four paper strips the fit is y=3.13x+6.19, and for the plastic strips y=2.33x+5.12, with y being the air-flow velocity and x the noise intensity. The measurement can be done with paper for somewhat lower velocities (6 m/s instead of 9 m/s).

6. Conclusion

In order to solve this problem a special apparatus was designed and used to achieve results as precise as possible. The basic characteristics of strip movement was explained through strobe measurements. Two essential regimes were registered, the silet and the noise regime. The silent regime divides into two in the case of more then one strip, the in-phase and counter-phase oscillation regimes. The transition between these regimes was allways at the same air-flow velocity. The destruction of strips was observed and quantified as shown in Figure 6 showing that plastic foil strips provide more accurate velocity measurements.At the noise regime sound autocorrelation was used as a known method to extract the necessary, signal data from all other noise recorded. Thus strip noise intensity was obtained, and the most important part, the formulae, the calibration curves, by which to calculate the air-flow velocity. They were shown for four strip paper and plastic foil measurements. The plastic strips can undergo higher velocities without relevant destruction, but the paper strips can mesure at lower velocities than plastic. The margin of error of this method is estimated from linear regression and intensity deterioration to be 3-5%. The measurable range is 9 to 15 m/s for plastic strips and 6.5 to 12 m/s for paper strips but can be further widened by changing the number of strips or their dimensions. Our interpretation of the problem was based on the fact that the problem uses the term noise which is by definition different to the tone (it doesn't have a frequency, pitch). That was the reason why this type of

measurements and methods were used. By finding acceptable formulae for determination of air-flow velocity from the noise we deem the problem solved.

References

[1]http://www.grc.nasa.gov/WWW/k-12/WindTunnel/build.html

[2http://eskola.hfd.hr/icm/index.php?option=com_content&view=article&id=26:zrani-tunel&catid=31:projekti&Itemid=5]

 [3] Landau L D , Lifshitz E M 1959 "Fluid Mechanics", Addison-Wesley, Reading, MA

No. 16, Rotating spring: A numerical and experimental analysis on the expansion of horizontally rotating helical springs

Reza MontazeriNamin[1]
* Team of Iran, IYPT 2010
[1]*Sharif University of Technology, Iran*
Corresponding author: namin@mech.sharif.edu (R. M. N.)

Abstract

The present paper is a solution to IYPT 2010 problem no. 16, "Rotating Spring". The main objective is to investigate the expansion of a helical spring rotated about one of its ends around a vertical axis. The effect of an additional mass attached to its free end is also a subject of investigation. This investigation is done in means of approximations leading to an analytical solution, as well as a developed numerical solution solving the differential equations assumingequilibriumof the forces in the rotating coordinate system. Both the analytical and numerical solutions are compared to physical experiments made by the author to examine the theoretical achievements.

Introduction

"A helical spring is rotated about one of its ends around a vertical axis. Investigate the expansion of the spring with and without an additional mass attached to its free end."

Assuming the equilibrium condition in the rotating coordinate system, three forces would be exerted to every differential mass.The gravitational force, the spring force caused by its deformation, and the figurative centrifugal force that must be considered since an accelerated coordinate system is being used. The spring tension force will be calculated assuming the Hooke's law. This law is applicable in a limited range of strain in the spring; the range in which it remains elastic. So the spring tension force will be a function of the spring modulus (μ), the spring initial length (l) and the change of length (Δl).

$$F_{Spring} = -\mu \frac{\Delta l}{l} \qquad (1)$$

Note that the modulus was used instead of the spring constant because of being independent on the spring dimensions. For the same reason, the spring linear density (λ) will be used as the parameter instead of the spring mass.

The solution of this problem in the case where the mass of the spring causes extra tension and strain is complicated to solve. To solve this general case, we will later present a numerical solution. However, initially an approximation will be given to describe the case when the mass of the spring is negligible compared to the additional mass attached. In this case, the spring could be considered as a whole, absolutely linear and weightless. So the three forces acting on the additional mass must be in equilibrium.

Equilibrium in the x direction states:
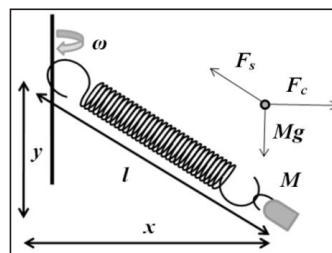
Figure 1: The free body diagram for the additional mass in equilibrium

$$m x \omega^2 - (l - l_0)k \frac{x}{l} = 0 \tag{2}$$

Which can be satisfied by x=0, or:

$$l = \frac{\mu l_0}{\mu + m l_0 \omega^2} \tag{3}$$

Equilibrium in the y direction states:

$$l = l_0(1 + \frac{mg}{\mu \cos(\theta)}) \tag{4}$$

Here θ is the angle between the spring and the rotation axis. If x = 0 then $\cos(\theta)$=1, so:

$$l = l_0(1 + \frac{mg}{\mu}) \tag{5}$$

Note that according to (4) the length cannot be smaller than this value. It can be shown that in the case where equation (3) predicts a larger length than equation (5), the one predicted by (3) is stable and the one predicted by (5) is unstable. Otherwise the prediction of (5) is impossible. So the spring length is:

$$l = \max(l = \frac{\mu l_0}{\mu + m l_0 \omega^2} , l_0\left(1 + \frac{mg}{\mu}\right)) \tag{6}$$

This result will be addressed as the analytical solution and will be compared to the physical experiments in the discussion.

Governing Equations

Because of the mass distribution of the spring along its length, the force needed to hold and rotate the free part of the spring differs in different points along its length. Thus the tension in the spring is not constant, making the linear density also a function of position. So the mass distribution of the spring itself is a function of the tension along the spring.

The equilibrium condition states that for each differential segment of length on the spring, the sum of the forces must be zero. Thus:

$$(\lambda x \omega^2)\hat{x} - (\lambda g)\hat{y} - \frac{d\vec{T}}{dl} = 0 \tag{7}$$

Here T is spring tension, as a function of position, ω is the angular velocity, λ is the linear density, a function of position as well, $\hat{x}$ and $\hat{y}$ are horizontal and vertical unit vectors. T in one point may be assumed to be parallel to the spring in that point, i.e. the spring does not stand any tension normal to its length. Thus:

$$\frac{T_y}{T_x} = \frac{dy}{dx} \tag{8}$$

Derived from the Hooke's law, the linear density of the spring as a function of T is:

$$\lambda = \frac{\mu \cdot \lambda_0}{\mu + T} \tag{9}$$

And the limitation of the boundary is the total mass of the spring:

$$\int_0^L \lambda(l)dl = \lambda_0 l_0 \tag{10}$$

L is the length of the spring after expansion, which is supposed to be the main unknown parameter to solve.

Numerical Solution

To solve the equation, the continuous medium of the spring is converted to a discreet medium. The spring is divided to *n* parts with the same initial length and mass. These are represented as *n* mass points which are connected with differentially small springs. Each point is being pulled by two springs. The position of equilibrium for each point is to be found. Transient method was used by to solve the problem; releasing the spring from an unstable position and iterating towards equilibrium. During iteration, every point will move towards the direction of the sum of the forces exerted to the point. The repetition of the iterations goes on until the movement of the points approaches to zero, i.e. the stable equilibrium condition is achieved.
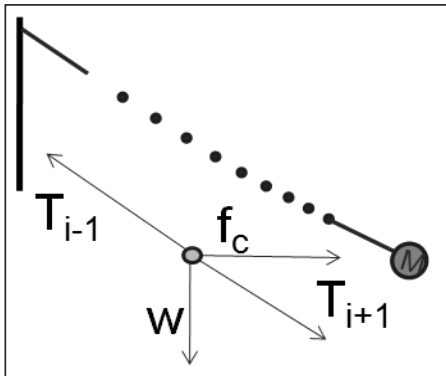
Figure 2: Discretization Assumption: to each point four forces are exerted
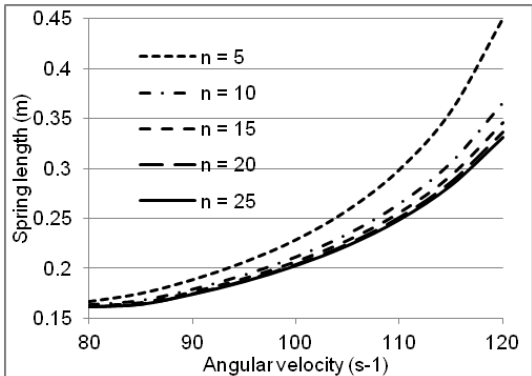
Figure 3: Mesh Independency Check. *n*: Number of mesh points

The numerical solution was developed in QBasic programming language. It takes about 10'000 iterations for each test case to reach convergence. The convergence was assumed to be achieved when the displacement of each of the points during iteration would be less than 1/100000 of the spring length. To make sure about the independency of the results to the mesh size and the discretization number, this number was changed in a test case. The result (Figure 3) shows that the program's result approaches to a constant value when *n* increases. *n* = 20 was used in the rest of the test cases.

Physical Experiments

The relation between the spring length and angular velocity was investigated in physical experiments in several cases, to be compared with the numerical and analytical results.
The spring was rotated using a DC 12V motor, covering the spin range of 100 to 400 RPM. The spin was variable by changing the input voltage to the motor. The connection between the motor and the spring was designed so that the end of the spring would be precisely in the axis of rotation; by putting the spring end inside a hole in the middle of the axis instead of sticking it to the side. Otherwise, standing wave motions could have been observed, especially in

Figure 4: Connection of the Motor and the spring

cases with high angular velocities. The standing waves would make the spring a fully curved shape, with different parts of the spring in different sides of the axis.

The angular velocity of the motor was measured by means of a tachometer. To measure the length of the spring, long exposure time photos were captured from the rotation, so that the entire motion of the spring in one round would be visible. The length of the spring would be measured by scaling the picture, measuring the distance between the two ends of the spring.

The modulus of the spring was measured by suspending masses with a spring of a known length, finding the spring constant and modulus. The mass of the spring was directly measured, used to find the linear density. These parameters were used as numerical input to the program and to the analytic solution to be compared with the experiments.

Figure 5: Long Exposure Time Photos Used to Measure Spring Length. Lower pictures have higher angular velocity

Discussion

The numerical theory showed perfect match with the physical experiments in several test cases. The length of the spring was measured while changing the angular velocity in one test case (Figure 6), in different initial lengths (Figure 7) and in different additional masses (figure 9).

It was not possible to make an experiment with the exact same angular velocity more than once; because the Motor would slightly change the angular velocity over time. Thus, exact error measurements were not quite possible. However, as we see in Figure 6, in the case where there are many measurements in a small region of angular velocity, the differences between the

Figure 6: Comparison of the numerical results and physical experiments

experimental data are small compared to the discrepancy to the numerical results. This fact suggests that the discrepancy between the experimental and the numerical results is not because of direct errors in the measurements. But it may be caused by the uncertain values given as the input of the numerical solution, e.g. initial spring length, which has a precision of about 1mm, and the results are very sensitive to it.

Figure 7: Comparison of the numerical results and experiments in different initial lengths of the spring. Units are in Centimeters
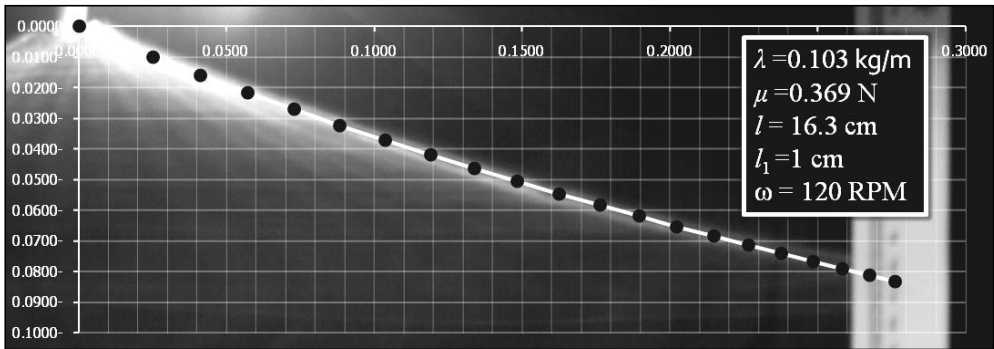
Figure 8: The results of the numerical theory and experiments regarding the spring shape. Axis units are in meters
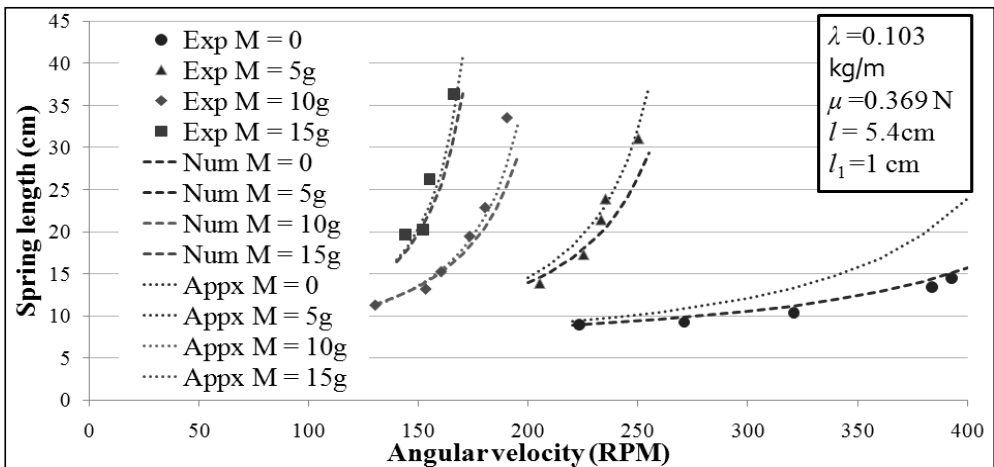
Figure 9: Comparing Analytical and numerical theories with physical experiments in different additional masses

The shape of the spring was also calculated numerically and compared with the experiments. Figure 8 shows this comparison. The Background image is an experiment, and the black points connected with white lines are the predicted positions of the points on the spring outputted from the numerical solution. The shape of the spring is not fully linear; it has a slight curve upwards. The results all show an agreement between the numerical theory and the experiments.

Investigating different additional masses, the analytical theory was also compared with the experiments and the numerical method. As we see in (Figure 9), the analytical solution does not provide the accuracy of the numerical solution especially in small additional masses compared to the spring mass. However it is clear that the errors decrease as the additional mass increases.

As a result, the method of the numerical approach used was fully proved experimentally in the experiment range; and the analytic solution was shown to have an increasing accuracy with the increasing of the additional mass.

References

[1] Beer F, Johnson E R, Dewolf J, 2005, Mechanics of Materials, 4th Edition, *McGraw-Hill.*
[2] Atkinson K E 1989 An Introduction to Numerical Analysis 2nd Edition, *Wiley.*
[3] IYPT 2010 Problems, Official IYPT Website:http://iypt.org/Tournaments/Vienna

No. 17, Kelvin's dropper: Water-dropping electrostatic generator revisited

Alexander Barnaveli[1]
* Team of Georgia, IYPT 2010
[1]*Ilia Vekua Physical and Mathematical School 42, Tbilisi, Georgia*
Corresponding author: s.barnaveli@gmail.com (A. B.)

Problem: ***Construct Kelvin's dropper. Measure the highest voltage it can produce. Investigate its dependence on relevant parameters.***.

1. Kelvin's dropper working principles

In XIX century 60-ies William Thomson, later to be known as Lord Kelvin, invented a very interesting device and showed it on special occasions (see Fig.1)[1].It was a water-drop electrostatic generator, which he called the "water-dropping condenser". It was sometimes referred to as "Kelvin's Thunderstorm". The device uses falling water drops to accumulate charges and generate a high difference in the voltage [1-4].

Figure 1.
"Kelvin's Thunderstorm"

Let us describe the working principle of this device. It consists of a bowl to which two droppers are attached (see Fig. 2)[2]. Under these droppers two metal rings are placed (so-called "inductors") which are cross-wise connected to the two metal jars (so-called "collectors").When one fills the upper bowl with water, jets begin to flow through droppers. The water jets J_{left}, and J_{right} are adjusted so that they break up into droplets near the induction rings R_{left}, and R_{right}, which (as we said) in turn are connected cross-wise fashion to two metal containers C_{left}, and C_{right}.

At first, when the water starts to flow out from the droppers, nothing happens, but as soon as occasionally, due to some fluctuation a negatively charged drop falls e.g. from the left dropper, it passes through the inductor R_{left} and falling into the collector C_{left} charges it (and connected to him right inductor R_{right}) negatively. This negatively charged right inductor attracts the positive ions from the bowl and accumulates them in

Figure 2.
Dropper's scheme

the right collector C_{right}. Respectively the right collector and connected to him the left inductor R_{left} get positive charge and start to attract negative ions from the bowl (increasing this way the negative charge flow through the left dropper) and so on... Thus more and more similarly charged droplets fall in each collector and they become more and more charged. Such process is called ***"Positive feedback"*** (we often witness such positive feedback when we put the microphone attached to PC near the speaker – noise becomes stronger and stronger).

Here we have to mention, that though water in the bowl is electro-neutral, it always contains at least positive H^+(or H_3O^+)and negative $(OH)^-$ions[5]. Due to some ***fluctuation*** it can happen that in one or several drops falling through the one of

droppers there are more ions of one sign, so drop becomes charged, the **symmetry violates** and the above-described avalanche-like process starts.

Here are several more important moments:

- The jets must split into drops in the vicinity of collectors not to let the system discharge. In other case the difference of potentials between two collectors will cause current flow through the water in the opposite direction and the system will not be able to gather the charges.
- Water conductivity ensures the charge flow in the bowl so that ions can flow to the droppers under the influence of inductor's field. Within the bowl the other ions which are repelled by the inductors compensate each-other so the water in the bowl in total is electrically neutral.
- The energy source in Kelvin's dropper is gravitation, which enforces the charged drops to fall through the inductors towards collectors. If not gravity, the charged drops attracted by oppositely charged inductors would fall on them and would not reach the collectors. So the work on the charge separation is done by the gravity forces.

Thus to summarize, the main factors responsible for working of Kelvin's water generator are:

- ✓ The existence of *H+* and *(OH)-* ions in water;
- ✓ The violation of symmetry as a result of fluctuation;
- ✓ The separation of ions under the influence of charged inductors;
- ✓ A "Positive feedback";
- ✓ Electric conductivity of water;
- ✓ Water jets splitting into drops in the very vicinity of the inductor's center;
- ✓ Accumulation of charged drops in collectors due to gravitation force.

2. The experimental Setup

Here is our experimental setup (see figure 3).

In our experiments we evaluated the voltage between collectors with the help of the gap between the electrodes attached to the collectors. The spark jumped when the gap was 1 cm that at ordinary conditions corresponds to *U = 10 000 – 30 000 V*. For our measurements we also used the electrostatic Voltmeter. We also tried different conditions and different parameters of the setup. The results of the experiment strongly depend on the environment conditions – humidity etc.

Figure 3. Experimental setup

3. Evaluations of voltage growth rate

Let's evaluate the parameters which will help us to optimize the experiment, starting with calculation of the voltage growth velocity.

Due to the positive feedback the speed of the voltage growth is proportional to the voltage itself:

$$\frac{dU}{dt} = \alpha U;$$

Where from

$U = U_0 e^{\alpha t},$ (1)

i.e. both the voltage and correspondingly the charge are increasing exponentially.

Let's discuss a coefficient α. One can assume that

$$\alpha \sim \frac{1}{C + C_{Load}} \cdot \left(nC_{Drop} - \frac{a}{R_{Ground}} - \frac{b}{R_{(1 \leftrightarrow 2)}} \right) \tag{2}$$

Where:

C – is the joint capacity of the collectors and inductors;

C_{Load}–is the capacity of voltmeter and other "loads";

C_{Drop}–is the capacity of water drop;

n – is the number of drops, falling into collector in unit of time;

R_{Ground}– is the Resistance between the generator and ground, through which the parasite current flows;

$R_{(1 \leftrightarrow 2)}$–is the resistance between the collectors. Through it the parasite current will

flow as well.

a, b – are the coefficients.

This expression was obtained via following considerations:

- Higher is the capacity of the system - slower is the increase of the voltage (for given speed of charge delivery); so capacity is in denominator.
- There is the "competition" between the accumulation of charge in collectors (the first term in brackets) and its leek through the parasite currents (the last two terms in brackets);
- Charge accumulation rate is proportional to the number of drops per second and to the charge of each drop (The form of the first term in brackets).
- Parasite currents are back-proportional to the Resistance (insulation) of the system (the form of the last two terms in brackets).

From (2) it is clear that if

$$nC_{Drop} < \frac{a}{R_{Ground}} + \frac{b}{R_{(1 \leftrightarrow 2)}} \tag{3}$$

charge accumulation will not take place.

Now let's derive the voltage growth formula using other considerations. Let's draw the electrical scheme equivalent to the Kelvin's dropper (Fig. 4).
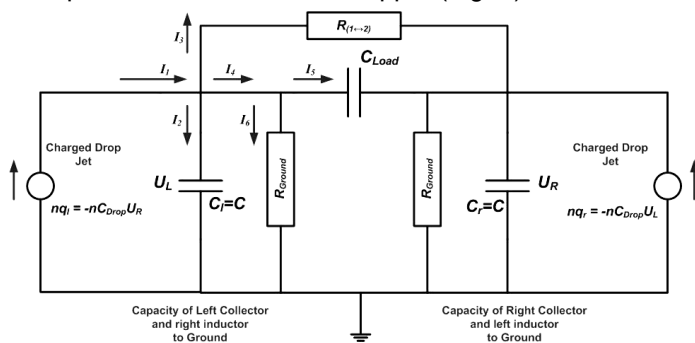
Kelvin Dropper equivalent scheme

Figure 4.

Here:

U_L–is the potential of "Left Collector and Right Inductor" to Ground;

U_R–is the potential of "Right Collector and Left Inductor" to Ground;

$C_l=C_r=C$, where C_l is joint Capacitance of "Left Collector and Right Inductor" with respect to Ground and C_r–is the same for "Right" side;

Charge of drops $q_r = -C_{Drop}\, U_L$ and $q_l = -C_{Drop}\, U_R$ where C_{Drop} is the "effective drop capacitance" – coefficient of proportionality.

Writing Kirchhoff's laws for the currents and taking into account that

$$I_1 = -nC_{Drop}U_R; \qquad I_2 = C\frac{dU_L}{dt}; \qquad I_3 = \frac{U_L-U_R}{R_{Load}};$$

$$I_4 = I_5 + I_6 = \frac{C_{Load}\cdot d(U_L-U_R)}{dt} + \frac{U_L}{R_{Ground}}.$$

We can write from the sum of currents for Left side:

$$\left(-nC_{Drop} + \frac{1}{R_{Load}}\right)U_R - \left(\frac{1}{R_{Load}} + \frac{1}{R_{Ground}}\right)U_L = C\frac{dU_L}{dt} + \frac{C_{Load}\cdot d(U_L-U_R)}{dt}.$$

Similarly from the sum of currents for Right side

$$\left(-nC_{Drop} + \frac{1}{R_{Load}}\right)U_L - \left(\frac{1}{R_{Load}} + \frac{1}{R_{Ground}}\right)U_R = C\frac{dU_R}{dt} + \frac{C_{Load}\cdot d(U_R-U_L)}{dt}.$$

From the symmetry considerations $U_L=U_R$ or $U_L= -U_R$. Let's consider these cases.

   A) For $U_L= -U_R$, the voltage growth equation for the left side takes the form

$$(C + 2C_{Load})\frac{dU_L}{dt} - \left(nC_{Drop} - \frac{2}{R_{Load}} - \frac{1}{R_{Ground}}\right)U_L = 0$$

and the similar is for U_R.

   B) For $U_L=U_R$ the voltage growth equation for the left side takes the form

$$C\frac{dU_L}{dt} + \left(nC_{Drop} + \frac{1}{R_{Ground}}\right)U_L = 0$$

and the similar is for U_R.

The complete solution is the sum of solutions (A) and (B)

$$U_L = A \cdot e^{\alpha t} + B \cdot e^{-\beta t}, \tag{4}$$

where

$$\alpha = \frac{1}{(C+2C_{Load})}\left(nC_{Drop} - \frac{2}{R_{Load}} - \frac{1}{R_{Ground}}\right); \tag{5}$$

$$\beta = \frac{1}{C}\left(nC_{Drop} + \frac{1}{R_{Ground}}\right).$$

It is clear, that solution (B) vanishes exponentially, while for the solution (A) for the voltage growth it is necessary, that

$$nC_{Drop} > \frac{2}{R_{Load}} + \frac{1}{R_{Ground}}. \tag{6}$$

Comparing the equations (4),(5),(6) with (1),(2),(3) we can see that $a=2$, $b=1$. Also we can conclude, that to obtain large charges and high voltage we must provide good insulation $R_{load}\to\infty$; $R_{ground}\to\infty$ and also the intensive jets of charged drops nC_{Drop} in the constructed generator.

4. Evaluation of accumulated charge.

Let's evaluate what possible charge can be accumulated in the Kelvin's dropper in ideal conditions.
In normal conditions 1 liter of water contains ~10^{-7} moles of ions, or $N \sim 10^{16}$ ions; the charge of each ion is $e = 1.6 \cdot 10^{-19}$ *Coulomb*. If all of ions will accumulate in collectors, the whole charge will be

$$Q = N \cdot e \sim 10^{-3} Coulomb \qquad (7)$$

though it is obvious, that this charge is huge, and unreal. Here it is worth to note that the electric forces in Kelvin's dropper also polarize water molecules and split them into ions thus increasing the number of ions and making the effect stronger.

5. Evaluation of the accumulated charge.

Now let's evaluate what voltage can be achieved using the Kelvin's dropper.
It is not very difficult to estimate the voltage between the two charged cylinders. After some calculations we get:

$$U = \frac{\sigma}{\pi \varepsilon_0 \varepsilon} \cdot ln \frac{d-R}{R}, \qquad (8)$$

Where $\sigma = Q/h_{cyl}$ is charge per unit of cylinder height, d is the distance between the cylinder's axes of symmetry, R is the radius of each cylinder ; $d > 2R$.From this formula we also can see, that the larger is the distance$d$ between the collectors - the higher voltage can be achieved.
Using parameters of our setup :$d=0.3m, R=0.05m, \varepsilon=1$, the height of collector $h_{cyl}=0.2m$and noting that for this height from (7) one gets$\sigma=5 \cdot 10^{-3} Coulomb/m$ we obtain from (8):

$$U \approx 5 \cdot 10^8 V \qquad (9)$$

(if we assume that all the ions of 1 Liter of water were separated).
It is obvious that, this voltage as well is huge and unreal. In real experiments there are factors that prevent achieving such huge charges and voltages (though several ten thousands of volts we did get).

6. Factors affecting the result.

In the real conditions there are factors that prevent a high charge and voltage growth in Kelvin's dropper and also factors which support obtaining a higher result.
Preventing factors are:
    a) Electrostatic Corona discharge;
    b) Electric forces affecting the water drops;
    c) Humidity of environment;
    d) "Parasite" currents.
Supporting factors are:
    a) Increase of the number of ions in liquid;
    b) Increase of the number of drops per second;
    c) Increasing insulation and distance between collectors.
   Let us discuss these factors.

a) Electrostatic Corona discharge.

Electrostatic discharge in air takes place when the voltage of electric field reaches 10 - 30 kV/cm. Thus it is real to get 30 000 V with our "Kelvin's dropper". Obtaining higher voltage will be possible in the case of covering the parts with good dielectrics (insulators). On the other hand, at high humidity discharge takes place at smaller voltage as well.

b) Forces affecting the water drops.

Let us estimate what forces are acting on charged drops in Kelvin's dropper to see at what conditions drops will not fall into collectors. If 1 Liter of water contains 10^{16} ions, then in 1 mm^3 drop there will be $n \sim 10^{10}$ ions. If in 1 drop there are only ions of the same sign, then the charge of drop will be $q = ne \sim 10^{-9} Coulomb$. The gravitation force acting on 1mm^3 drop $F_{Grav} = 10^{-5} N$. If the distance between the drop and collector (or inductor) is $\sim 0.1m$ then the electric force affecting the drop is

$$F_{El} \sim k \frac{qQ}{10^{-2}} \sim 10^{10} \bullet \frac{10^{-9}Q}{10^{-2}} \sim 10^3 \, Q.$$

Drop will not fall into collector if $F_{Grav} < F_{El}$, i.e. when affecting charge is about $Q \sim 10^{-8} Coulomb$. *This corresponds to voltage* $U \sim 10^4 \, V$. So we again obtain the tens of thousands volts. In course of experiment we have seen the deviation of water streams from vertical, caused by electric fields (Fig.5).

Figure 5.
Deviation of water streams

c) Humidity of environment.

We made our experiments in humid and dry environments. We saw, that the higher was humidity – the less was voltage. It was due to electrostatic discharge at smaller gap for high humidity.

d) "Parasite" currents (bad insulation).

When during the experiment the device was getting wet, there took place the leak of charge from collectors by means of so called "parasite" currents and as a result the voltage decreased as well.

7. Experiments with different parameters.

Taking into account all factors affecting the above mentioned evaluations and results we carried out experiments with changing the following parameters:
1. Adding the salt to water (i.e. adding ions);
2. Increasing the water jets (though providing their decay into drops);
3. Increasing the distance between the collectors;
4. Improving the insulation of system.

Voltage was measured with electrostatic voltmeter.
We observed that:
- Addition of salt to water forces generator to start its action much faster and provides higher voltage. This is due to Na^+ and Cl^- ions in salt which increase the number of ions in bowl. It makes the amplitude and the probability of initial fluctuation higher. Also, additional ions Increase charge accumulation speed as compared with charge leak speed since in this case each drop has
- larger charge.
- Making water jets stronger also increases the charge

Figure 6.
Porcelain collectors

accumulation speed as compared with speed of charge leak. So charge grows faster.

- Increasing the distance between the collectors enlarges the obtained voltage. As we saw from (8), the further are the collectors from each other, the more voltage is achieved.
- Increasing the degree of insulation gives higher final voltage. We also tried to replace the iron collectors with those, made of porcelain plates. The electrodes were directly inserted into water in these plates (See Fig.6). This gave very good results.

Thus Fulfilling these four conditions, improving the insulation (that is very important), we get 30 000V voltage. We measured the voltage with help of electrostatic voltmeter (see Fig. 7).
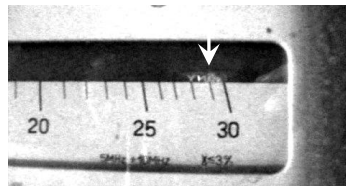
8. Conclusion.

In this work we studied the working principle of Kelvin's water generator and influence of different

Figure 7.
Achieved voltage

parameters on the values of obtained charge and voltage. We constructed our model and observed that by means of the Kelvin dropper it is possible to obtain tens of thousands volts.

The result strongly depends on the surrounding conditions. To obtain a high voltage one must provide:

1. The insulation, as good as possible. May be locating the device upon the two tables, to separate the poles;
2. The less humid environment;
3. The strong jets of drops. May be usage of several droppers;
4. Adding more ions to water. (e.g. adding salt);
5. Increasing the device dimensions.

We managed to obtain 30 000 V.

Finally I want to thank my grandfather Tengiz Barnaveli for his help in the experiments with the high voltage and helpful discussions on the Kelvin dropper equivalent scheme.

References

[1] http://mrgreenbiz.wordpress.com/2008/06/13/
[2] John Vanderkooy. An Electrostatic Experiment of Lord Kelvin with Running Water.Phys 13 news.University of WaterlooCanada January 1984.
http://web.cvcaroyals.org/~rheckathorn/documents/KelvinWaterDropGeneratorPhys13News-Mine.doc
[3] Matthew Trainer. Celebrating the Life of Lord Kelvin.University of Glasgow, Glasgow, UKhttps://dspace.gla.ac.uk/bitstream/1905/701/1/Kelvin+tribute.pdf
[4] Markus Zahn.Self-Excited ac High Voltage Generation Using Water Droplets.AJP Vol 41/ p.196. 1973
[5] http://en.wikipedia.org/wiki/Self-ionization_of_water;
http://www.chemguide.co.uk/physical/acidbaseeqia/kw.html .

IYPT- 2011

No. 1, Adhesive tape: Static and dynamic measurements of the detachment force

Katharina Ehrmann[1]

[*] Team of Austria, IYPT 2011

[1]*University of Innsbruck, Austria*

Corresponding author: k.ehrmann@hotmail.com (K. E.)

Abstract

This paper aims to determine the minimal force to remove adhesive tape from a surface. The total force can be separated into two parts according to the results of this paper: One component to pull off the tape and another one to stretch it. As a result, a minimal force could be found that is depended on the angle of pulling. The main effort thereby was to calculate the surface energy; a value depended on the parameters surface, adhesive and temperature. This achievement could be maintained by conducting a stationary experiment. Furthermore, a second, kinetic experiment was held to point out the surplus of force needed when the tape is being pulled off at a certain velocity.

Introduction

The removal of adhesive tape from a horizontal surface is a multiple layered problem. The force necessary to remove the tape is varying according to the speed and way of pulling at it and may vary at greater velocities. Therefore, this paper concentrates on determining the minimal force necessary to remove a piece of tape from a horizontal surface. The most difficult part thereby was to find the surface energy as it varies from tape to tape and is depended on the surface. In the experimental part it will be described how the surface energy can be found experimentally. The resulting data then will be used to indicate the minimal force of removal by applying the law of energy conservation.

Before turning on finding the minimal force, the nature of adhesive tape as well as the act of pulling needs to be examined more closely.

Adhesive tapes consist of backing material with a thin layer of adhesive on it which may alter in its chemical composition. The chemical substances of which adhesive is made of are polymers. These have viscoelastic properties, which will be of importance later on. The tape's "stickiness", or rather attraction towards a surface, results from the Van der Waals forces existing inbetween adhesive and surface. This so-called surface energy can be described by the following equation (Ciccotti and Giorgini, 2002).

$$\gamma = \gamma_{TA} + \gamma_{SA} - \gamma_{ST} \tag{1}$$

where γ is the adhesion energy per area and γ_x is the surface energy in J/m^2 or N/m. TA stands for the interface between tape and air, SA for the interface surface – air and ST for the interface surface – tape (Figure 1). According to equation [1], adhesion exists if $\gamma < 0$.
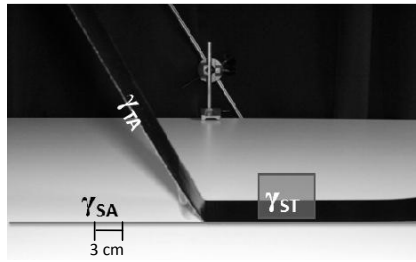
Figure 1: Visualization the different interfaces

The principle of pulling brings along a change in angle. As visible in figure 2, this change results in a shift of the force components which has to be considered: As the horizontal force-component will only result in strain and eventually elongation of the tape, only the vertical force-component can be considered responsible for pulling off the tape.
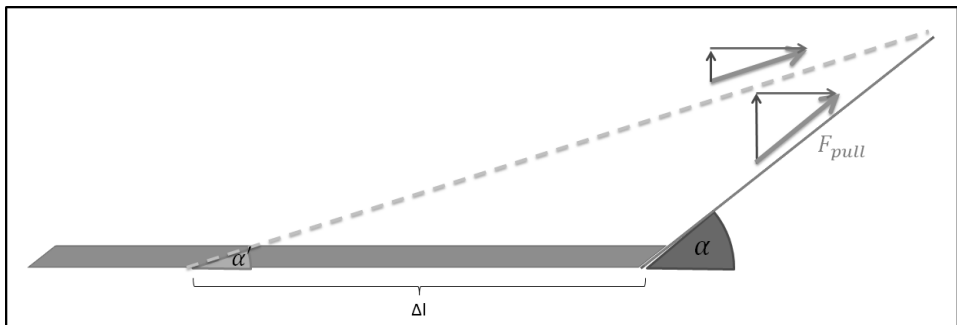
Figure 2: Change of the angle α after a change Δl in length of the sticking tape

Assumptions and Limitations to the Theory

As this is a complex problem where various parameters having enormous effects on the results, it was necessary to cut down the variations in our experimental setups in order to remain straightforward and concentrate on crucial points.

Obviously, the two crucial parameters surface tension and Young's modulus are different for various set ups. Data and results gained through the conducted experiments and presented in this paper have been acchieved for the Nopi® - Tape with a breadth of 5cm and a thickness of 0.04mm ± 0.005mm. Furthermore, the same, alcohol-cleaned surface has been used for all measurements. Various parameters such as surface-roughness, adhesive and temperature that would affect the surface energy have been held constant through the previously described arrangements. Only qualitative analysis of these parameters will be included in this paper.

The velocities used in the kinetic experiments were held low enough in order to assume a constant velocity when pulling. Had higher velocities been used, a phenomenon would have occurred that is commonly referred to as stick-slip – phenomenon in literature and velocities would not have been constant over time. The stick-slip regime describes a periodical change in a tape's detaching velocity despite a constant peeling velocity. (Cortet et al., 2007) This effect would then make pulling-force evaluations pointless.

Two further simplifications were the neglection of the weight of the wires when applying the law of energy conservation and the solely study of angles up to 90°. There may not be a significant difference in the minimal pulling-force if the angle in between the surface and pulled off tape is bigger than 90° according to trigonometric considerations, however, this is not subject of this paper.

Theory

As mentioned above, the total force can be divided into two parts. The vertical component is responsible for pulling off the tape and the horizontal component for elongating the tape due to elasticity:

$$\vec{F}_{Pull} = \vec{F}_{Elasticity} + \vec{F}_{Remove} \tag{2}$$

To remove the tape, the pulling force needs to overcome the adhesion energy inbetween tape and surface. For the minimal force this denotes:

$$\vec{F}_{Adhesion} = \vec{F}_{Pull}$$

As a result, equation [3] can be derived:

$$\vec{F}_{Adhesion} = \vec{F}_{Elasticity} + \vec{F}_{Remove} \tag{3}$$

Thus, to find the minimum of the pulling-force F_{Pull}, the adhesion force $F_{Adhesion}$ (depended on the adhesion energy) and the force $F_{Elasticity}$ used to strain the tape (depended on Young's modulus) need to be found.

In the following, the results of our studies on these two relevant parameters adhesion energy and Young's modulus under the described conditions will be discussed.

A. Young's Modulus

To determine the horizontal fraction of energy needed, the following commonly known equation needs to be considered:

$$\frac{l}{\Delta l} = \frac{1}{E} \cdot \frac{F}{A} \tag{4}$$

where l is the original length, Δl the length-growth when the tape is stressed, E stands for Young's modulus, F for the force applied and A for the affected area. Through the experimentally found stress-strain curve which is shown in figure 5 in the experimental part, we concluded that Young's modulus for the Nopi[®] - Tape is 269 ± 1 MPa.

Surface Energy

As mentioned in the beginning, there are no certain values for the surface energy due to its high dependence on the parameters composition of the tape, temperature and surface. It is obvious that the composition of the tape and surface impacts the strength of the Van der Waals forces and therefore, every tape sticks differently to various surfaces. However, the composition of the tapes' adhesives is unknown and therefore will not be altered in this paper. Furthermore, a row of experiments have shown that the range of temperatures accessible for our setups is too small to make a difference for the planned set of experiments. As for the impact of surface roughness on the surface energy, this paper will only give a short qualitative explanation on how it impacts the sticking-behaviour:

Obviously, a tape will stick best if there is as much interface between the adhesive and the surface as possible. Therefore, rough surfaces with cracks that augment the area contribute to strong adhesion. When these cracks turn too big, however, the adhesive will not be able to fill the gaps anymore. At that point, adhesion energy becomes smaller again. In conclusion it can be said that an even surface can develop stronger as well as weaker adhesion to the tape if compared to a rough surface (figure 3). In the case of the Nopi® - Tape which has a 5 ± 1 μm thick adhesive-layer, cracks with a depth of 4 μm would supposedly present the optimal size. This theoretical evaluation has not been tested further because the aim of this paper is to evaluate the minimal pulling force for the Nopi® - Tape on one certain surface. Changing the parameter surface would only result in a change of measurement results that are inserted in the generally valid formula for γ.
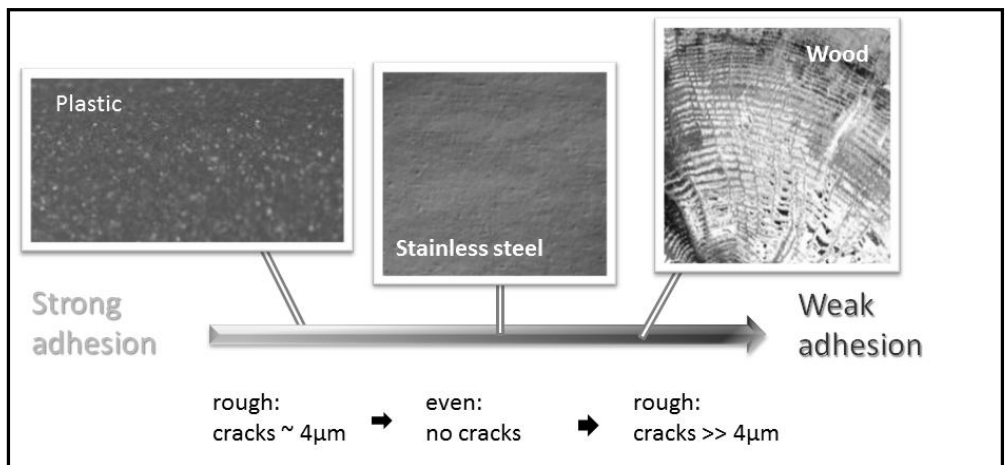
Figure 3: Overview over the development of adhesion energydepending on the size of cracks in the surface

As discussed, the surface energy γ is different for every set up due to its intrinsic nature. Therefore, it had to be found experimentally which appeared to be difficult due to its much dependence. However, through the law of conservation of energy it was possible to be found by conducting a stationary experiment. All involved energies can be summed up through formula [5]:

$$\Delta E_{Pot} = \Delta E_o + \Delta E_D + \Delta E_{Pot2} \tag{5}$$

with

$$\Delta E_{Pot} = m_w \cdot g \cdot h$$

$$\Delta E_o = \gamma \cdot b \cdot x$$

$$\Delta E_{D=} \frac{mg}{bd} \cdot \frac{1}{E} \cdot x \cdot m_w \cdot g$$

$$\Delta E_{Pot2} = \frac{h_h}{2} \cdot \bar{l} \cdot g \cdot h \cdot \rho + h_h \cdot m_s \cdot g$$

In these equations, ΔE_{Pot} as the total energy of the weight attached to the tape to pull it off is described as a sum of ΔE_o , the surface energy, ΔE_D, the energy used for straining the tape and ΔE_{Pot2} , the potential energy resulting from the weight of the construction including weight of the tape, the stick to attach the end of the tape to the string and the string itself. Further used parameters: m_w stands for the mass of the weight that is pulling at the tape, h for the height of the weight, b for the width of the tape, x for the length of the surface being released of the tape, m for the mass of the entire construction as well as the tape, $\bar{l}$ for the peeled length, d for the tape thickness ϱ for the tape density and h_h for the height of the tape's pulled off end. A graphic description of these formulas can be seen in Figure 4.
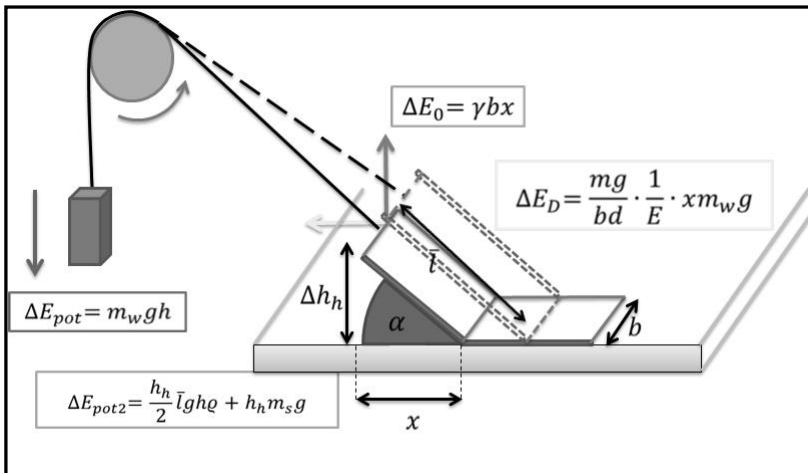
Figure 4: Visualization of Formula [5]

Through inserting values for all these variables except for γ, γ can be calculated with formula [5]:

$$\gamma = \frac{m_w gh - \frac{mg}{bd} \cdot \frac{1}{E} \cdot x m_w g - \frac{h_h}{2} \cdot \bar{l} gh\rho - h_h m_s g}{bx} \ [N/m]$$

Having found the surface energy for the used setup, the minimal force to pull off a tape can now be calculated by this formula:

$$F_{crit} = \frac{\gamma b}{\sin \alpha} \tag{6}$$

In equation [6], F_{crit} depicts the minimal force necessary to pull off the tape at v = 0, v being the speed of pulling. γ is the surface energy in [N/m], b the width of the tape in [m] and α depicts the pulling angle.

Having achieved a result for the minimal force in a stationary case, it was necessary to observe the tape's behaviour when being pulled off at a constant speed rate. Therefore, a new setup was developed. Its schema can be seen in figure 7 in the experimental part of the paper.

The purpose of this new experiment was to find whether or weather not more force would be needed if the tape was pulled off at a certain speed rate. Due to the presumption of the adhesive being a non-Newtonian viscoelastic fluid, a change of the needed force was expected. Neither a change in the ratio of the force components nor a change of the angular dependence but an increase in the total force needed was the anticipation. Through the experiments, this was verified and the adhesive then could be identified as a shear-thickening non-Newtonian fluid. As will be shown in the results, not the shape of the curve, and therefore the angular dependence, or the contingent of the vertical force-component towards the total force changed, but a shift upwards of the equally shaped curve could be seen.

Experimental Setup

The curve in figure 5 shows how the length changes at a certain stress. As expected, it develops linearly in the beginning until the point at which the tape will not go back into its original length at about 13 MPa. This linear section also is the one relevant for the calculation of Young's modulus.
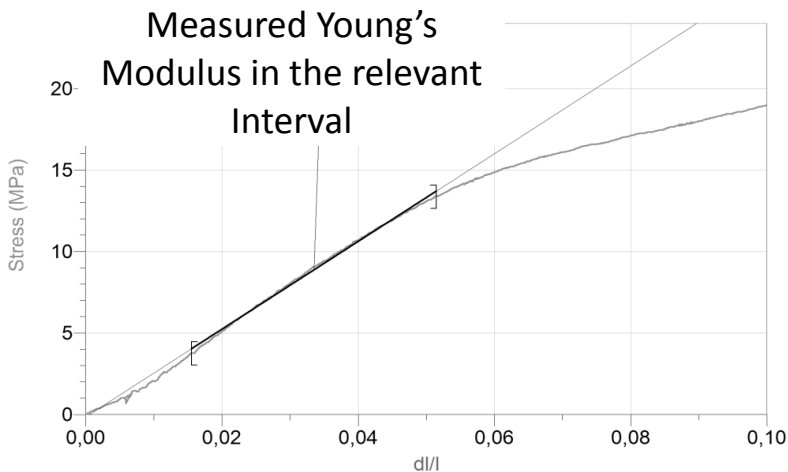
Figure 5: Stress-strain curve of the Nopi® - Tape

The data inserted into formula [5] originates from 10 equal stationary experiments with the Nopi® - Tape as shown in figure 6: Differently heavy weights were attached to the tapes sticking to the standard surface through wires and were left hanging for 5 days to be able to assume the stationary case. The resulting data then was filled in into equation [5]. The mean of these 10 experimental results for the surface energy γ is 14 ± 3 J/m^2 (or also: 14 ± 3 N/m).
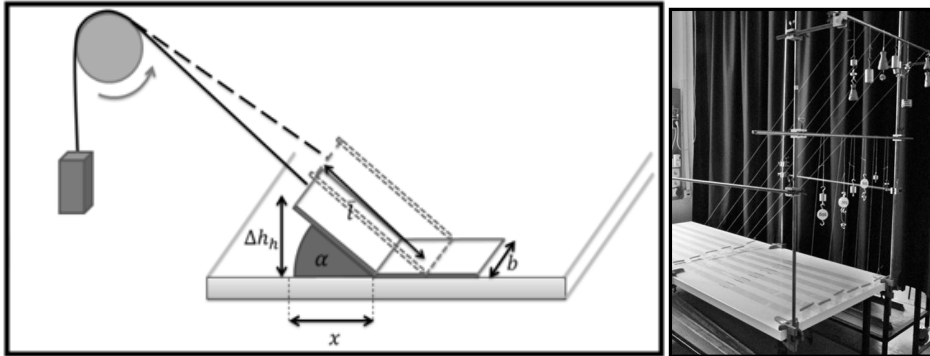
Fig 6: Schema and setup of the stationary experiment
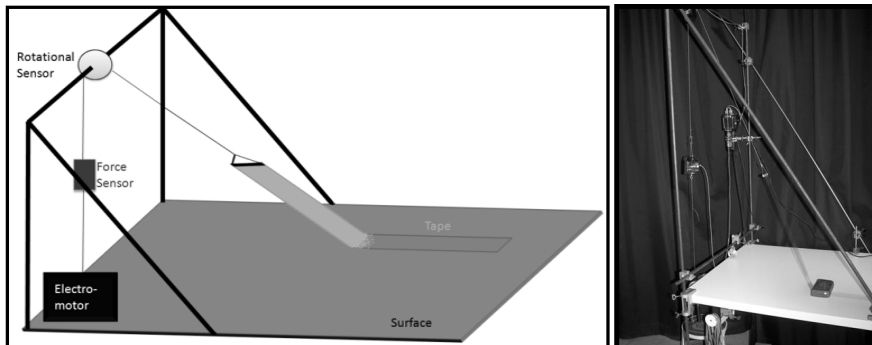
Figure 7: Schema and picture of the setup for pulling the tape at a constant rate

Figure 7 depicts the setup for the kinetic experiments. Through the electromotor, constant velocities could be achieved and altered accurately after each measurement. The sensors measured the force applied, the length of the tape that was pulled off and the angle inbetween tape and surface. This acquired data produced the graphs presented in the paper's Results:

Results

The critical force of the Nopi® - Tape calculated from equation [6] on the used surfaceequals 0.7N ± 0.15 N at 90°. Expressed as a function of the angle F_{crit}, this result can be written as $F_{crit} = \frac{0.7N}{\sin \alpha}$. Figure 8 shows the corresponding plot:
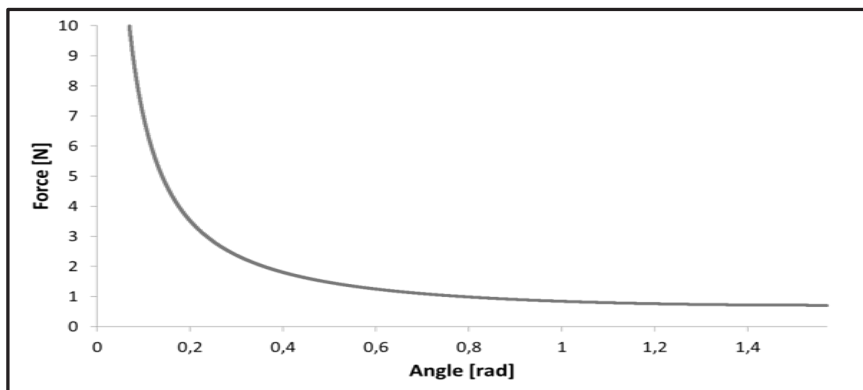
Figure 8: Plot of the critical force to pull of the Nopi® – Tape in dependence on the angle
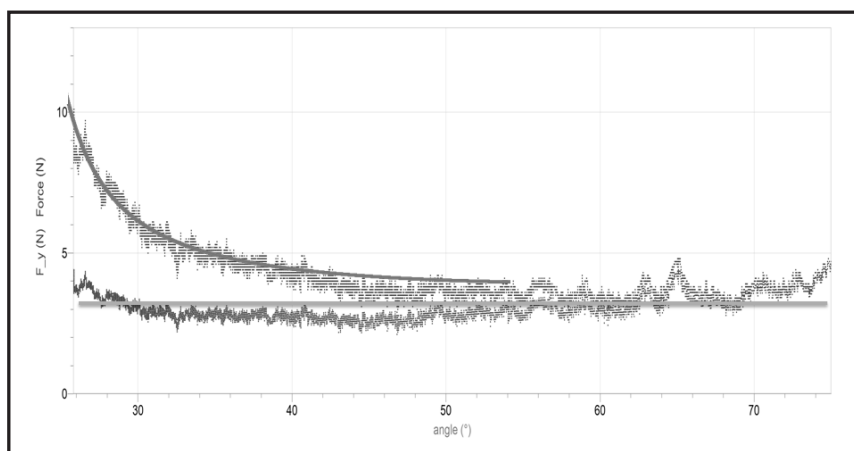
Figure 9: Total force (red graph) and vertical force - component (green graph) in dependence on the angle between tape and surface at 0.16 ± 0.01 m/s (10 measurements per second)

As indicated in figure 9, the graph picturing the vertical force – component F_v can be assumed as linear according to these experimental results, whereas the total force F inclines with the decrease of the angle α in-between tape and surface as stated in [7].

$$F_v = F \cdot \sin \alpha = const. \tag{7}$$

This corroborates the theory applied for and results acchieved from the stationary setup: The smaller the angle α becomes, the more energy has to be dedicated to the strain of the tape. Furthermore, the plotted graph in figure 8 which shows the dependence of the force necessary to pull off the tape on the agle, fits the measurements shown in figure 9.

Figures 10 and 11 show slightly higher velocities than figure 9. Still, the theoretical prediction of how the velocity will develop with changing angle seems to fit. However, the graphs shift upwards: At an angle of 60°, for example, 3 N are needed to pull off a tape at 0.16 m/s (figure 9), whereas 4 and 5 N are needed at 0.25 and   0.3 m/s for the same angle (figures 10 and 11). Additionally, figure 11 includes the horizontal force - component which again appears roughly constant. The mesured data could not be evaluated up to angles of 90° degrees due to initial imperfection of a constant pulling force.

Whenever this paper referred to "fits" of the theoretically predicted graph derived from the stationary experiment, this can only be seen as a fit concerning the graph's shape. As can be seen in figures 9, 10 and 11, the graph experiences a shift upwards whenever velocity is increased. Still, the development of the forces always proceeds in the same way: the vertical component responsible for separating the tape from its surface remains roughly constant whereas the horizontal component increases with decreasing angles due to the elasticity of the tape. Thus, the minimal force necessary to pull off a tape indeed occurs in the stationary case and can be described for any angle of pulling by our model. Furthermore, this paper has shown a qualitative approach on the influence of surfaces on the adhesion energy.
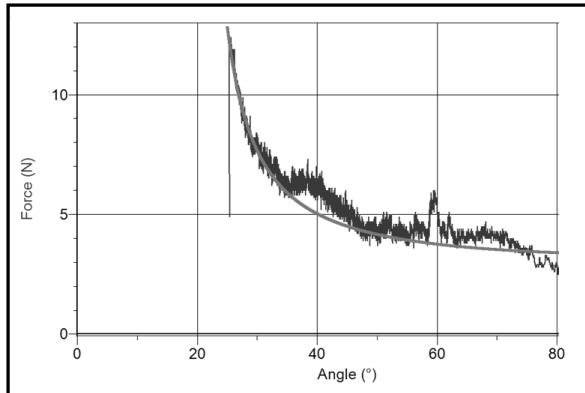
Figure 10: Total force needed to pull off the tape at 0.25 m/s;
red graph: measured, blue graph: theoretical prediction of the velocity development
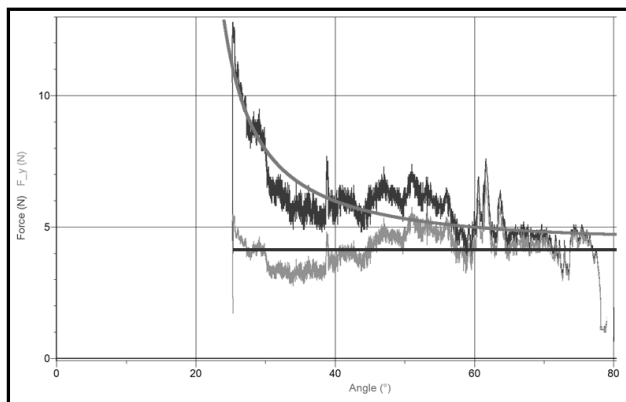
Figure 11: Total force and its vertical component at 0.3 m/s

Discussion

The achieved results presented above show that the force necessary to pull off adhesive tape from a horizontal surface is dominated by two parameters: surface energy and elasticity. This conclusion was drawn from equation [3]. Therefore, this paper set out to characterize these two quantities further.

Through energy conservation, it was possible to calculate γ for the Nopi[®]-Tape within an acceptable range out of the stationary experiment. Furthermore, Young's Modulus was found experimentally and these results then could be used to calculate the critical force for every angle. This is visualized in figure 8. Comparing this result with our experiments, they produced graphs in the exact same manner which verifies the developed formula. Figures 9 to 11 show the described fit of the curves.

As suggested additionally in the theoretical part, it could be proved that the horizontal force component remains roughly constant if there is no change in material or surface whereas the total force inclines with decreasing angles. This can be explained through the additional force that has to be applied due to increasing strain at smaller angles. Figures 9 to 11 anticipate this behaviour.

Another phenomenon observed with the kinetic experiments was the horizontal shift of the curves whenever the velocity of pulling was changed. Therefore, whenever this paper referred to "fits" of the theoretically predicted graph derived from the stationary experiment, this can only be seen as a fit concerning the graph's shape. As can be seen in figures 9,10 and 11, the graph experiences a shift upwards whenever velocity is increased. Still, the development of the forces always proceedsin the same way: the vertical component responsible for separating the tape from its surface remains roughly constant whereas the horizontal component increases with decreasing angles due to the elasticity of the tape. This shift can be explained through the tape's viscoelastic properties: If we assume that the material to be shear-thickening, it can be explained that higher velocities and thus bigger forces contribute to a worse pulling-off behaviour. The more shear forces dominate, the more particles enter a state of flocculation and are no longer held in suspension.

Adding this fact to the theoretical approach, the minimal force necessary to pull off a tape indeed occurs in the stationary case and can be described for any angle of pulling by our model. Furthermore, this paper has shown a qualitative approach on the influence of surfaces on the adhesion energy.

To sum up what has been achieved it could be said that the two experiments have fully proved a novel theory developed in this paper.

Conclusion

In this paper, a theory was developed to predict the force fractions involved in pulling off a tape and their developments when altering pulling-angle or –velocity were observed. The idea was to find the two crucial parameters: the surface energy and Young's modulus. This was accomplished by filling in missing data into equation [5] through the stationary experiment where the conservation of energy is being considered. As a result, a minimal force could be determined in dependence on the angle: 0.7N/sinα. The resulting plot can be seen in figure 8. Through conducting another experiment where the tape is being pulled off at a constant speed-rate, it was possible to observe the development of the total force. As a matter of fact, all curves from the stationary and kinetic experiments fit the theoretical plot. The only difference can be found in the vertical shift upwards that takes place with increasing

velocity for which has also been found an explanation. Through observation of the vertical force-component which was linear in any experiment, the theory again was affirmed.

References

[1] M. Ciccotti, B. Giorgini, "The emergence of complexity in a common scotch roller", in L. Boi (ed.), Symétries, brisures de symétries et complexité en mathématiques, physique et biologie, Bern, Peter Lang, 2006.
[2] Pierre-Philippe Cortet, MatteoCiccotti, LoicVanel; "Imaging the stick-slip peeling of an adhesive tape under a constant load"; Journal of Statistical Mechanics: Theory and Experiment 03, March 2007 (05/03/2007) P03005
[3] K.Kendall; "The adhesion and surface energy of elastic solids"; Journal of Physics D.: Applied Physics; 1971; Vol. 4

No. 1, Adhesive tape: Elastic properties and dynamics of a detaching tape

Stanislav Krasulin [1]
* Team of Belarus, IYPT 2011
[1]*Belarusian State University, Belarus*
Corresponding author: s.krasulin@gmail.com (S. K.)

Introduction

This task asks us to "determine force necessary to remove a piece of adhesive tape from a horizontal surface". Relevant parameters are also to be investigated.

Word "necessary" points that we have to find minimal force required, and, therefore, the most effective way of removing should be used: peeling. It is also said that surface should be "horizontal"; however,there is noaffect of the gravity forces on the interactions between tape and surface. Therefore, our surface should be just flat; not necessarily horizontal.
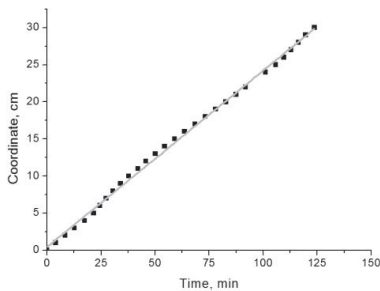
Figure 1. Peeling weight is 0.5 kg, velocity is (2.38±0.02) mm/min.

Experimental setup

Everything will be much easier if tape is peeled with constant force. At the same time, since the tape is peeled, the point of application of force is all the time moving.That is why the best option is to use gravity force: it's constant, it always follows the object. So, experimental setup will be like this: a flat sheet of material (we used acrylic resin), which can be placed at different angles to the horizon in order to change peeling angle – angle between already peeled tape and surface (this is why we replaced word "horizontal" with word "flat"). The tape is placed on the lower side of the sheet, and a weight is attached to tape's end. Then, dependence of coordinate of the border of still attached to thesheet tape on time is measured.

As seen in fig.1, this dependence is linear, therefore force, holding tape, is equal to the gravity force, acting on the weight. However, if attached mass is changed, dependence remains linear. Conclusion: tape "resists" detaching with the force equal to applied. To study this phenomenon, we should take a closer look at the clue behavior and interaction between tape and surface.

Pressure sensitive adhesive

There exist different types of adhesives; however, we had focused our research on the tapes, which used pressure sensitive adhesives (PSAs).This is the type of adhesive, which doesn't require heating, or adding water to start adhesion; that is why it is the most common one. The adhesive itself is generally a viscoelastic non-Newtonian fluid[1,2,3]. It uses van der Waals

Figure 2. Is this pressure sensitive? Peeling weight is 0.5 kg, pressing mass ranges 0.1-30 kg.

interactions between it and other surface's molecules. Most people think that "pressure sensitive" means that the higher pressure is applied when sticking tape to the surface, the better will be interaction between them[1].It is true for most double-sided tapes; however, as shown in fig. 2, it doesn't work for the usual scotch tape (which is probably the most widely-used). In order to explain this fact, we had decided to study the reasons why double-sided tape does respond to the applied pressure.

"Contact area"

Figure 3. Double-sided tape through the microscope

Two-sided tape has rather not flat surface: there are notable "hills" on it (see fig.3). That is why, when putting this tape to some object, first the "hills" meet surface; and to make the lower parts of glue to reach the surface "hills" should be compressed. To describe this effect we had used "contact area" – area of the glue which actually interacts with the surface, in percent of all area of a sample.

Figure 4. Same sample after putting on it just a panel (89 g) and after putting on that panel 6 kg weight

To measure this value another experimental setup was built. With one side tape was attached to a small panel (area of the panel was equal to the area of the sample). The other side of the tape was attached to the upper side of a sheet of glass and weights were placed on the panel. A small LED was attached to the side of the sheet and under the sheet a camera was placed. Then everything is set in the dark place.

The main idea is that the glue, which interacts with surface, is in optical contact with it; and other glue is not. Therefore, light, emitted by diode, is scattered by the interacting glue, causing it to glow. A picture of the sample is taken (fig. 4), and then percentage of bright pixels is calculated using software.

Fig.5 shows dependence of the contact area on the applied pressure. At first it grows very fast: not many hills are touching the surface, and it's not necessary to press hard to deform them. However, when the pressure is increased, the amount of glue which should be squeezed increases too; at the same time, deformation of the already compressed glue also increases. Therefore, 100% contact area is almost unachievable (even after putting over 60 kg on the panel it became only about
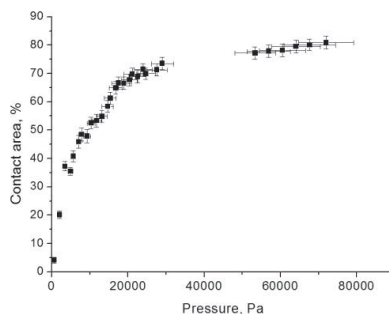
Figure 5. Pressing mass ranges 0.1-10 kg, sample area is 3.7X3.7 cm

96%). It can be noticed that with growth of pressure its error increases significantly. The reason for it is that with bigger weights it is more and more complicated to distribute the pressure uniformly.
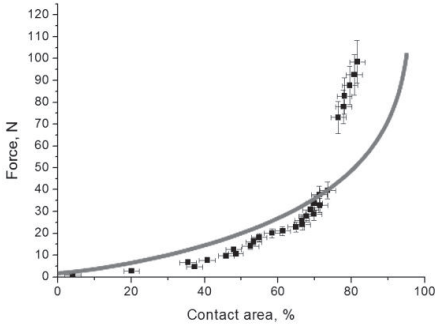
Figure 6. Line shows output of our mathematical model. Dots are, in fact, re-plotted fig.5

Mathematical model

Qualitative explanation can be expanded into quantitative model. Certainly, to create it we need some information about the shape of the glue's surface; or, being more specific, we need to know how big total area of glue, which has some specific thickness is. We can consider, that thickness of glue follows some distribution; and for the simplest mathematical model we will approximate that it is Gauss distribution. Then, if after applying some force distance between the panel and the surface became x, amount of glue, which isn't interacting yet, will be:

$$N(x) = \frac{1}{2\pi\sigma^2} \cdot e^{\frac{-(x-\mu)^2}{2\sigma^2}};$$

where μ is average thickness of glue, and σ is difference between biggest and smallest thickness, divided by 6. Now, if we want to find the force, caused by the deformation of glue (considering, that it behaves according to Hooke's law):

$$F(x) = \int_{x}^{X_{max}} (N(x_n + \Delta x) - N(x_n))S \cdot E \frac{x_n - x}{x_n} \cdot dx_n;$$

where X_{max} is highest thickness of the glue, S is area of the sample, $(N(x_n + \Delta x) - N(x_n))*S$ describes area covered with the glue, which had original thickness between (x_n) and $(x_n + \Delta x)$, and $((x_n - x)/x_n)$ shows relative deformation of such glue. And contact area $C(x)$ will be calculated as $C(x) = (1 - N(x))*100\%$. Now, using software, it is possible to plot $F(x)$ vs. $C(x)$. Comparison between results of the model and actual experimental data can be seen in fig.6. Differences can be explained by the fact, that our approximations with Gauss distribution and Hooke's law are not 100% correct; however, results are rather close: for contact areas less than 70%, difference between theory and experiment doesn't exceed 10%.

Dependence of the detaching velocity on the contact area is linear (fig. 7): the higher is contact area (respectively, the higher was applied pressure) the lower is detaching velocity. So, we have successfully explained why applying pressure to the double-sided tape increases its resistance to peeling. And since we were right with our theory of uneven surface of the glue being the main reason of dependence on applied pressure, we now have an

Figure 7. Peeling weight 0.5 kg. Here we face increased errors, because it is difficult to take a high-quality picture of a long piece of tape

explanation for the lack of such dependence for scotch tape: its glue has rather even surface. That is why, when scotch tape approaches a surface, whole area of the

sample interacts with the surface at once, and all possible bonds are established. And once a bond is established, applying pressure doesn't change anything.

Measurement of Young's modulus
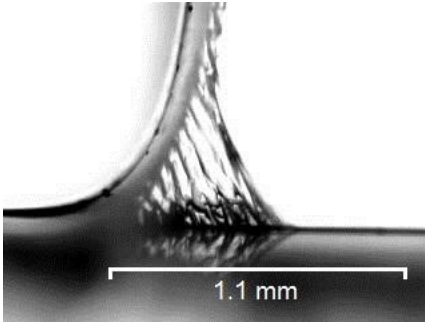
Figure 8. Picture taken when measuring Young's modulus of usual scotch tape, period of oscillations 0.7 s

Calculation of the F(x) in previous chapter required knowing of theYoung's modulus E of the glue.To measure it a thin stripe of the tape was taken, and a very small weight (8.8 g) was attached to it. Then everything was put under the microscope (fig.8). In the very beginning of detaching small oscillations can be observed. Approximating the whole system as a spring pendulum it is possible to find Young's modulus through the period of these oscillations.

However, after several oscillations glue stops following Hooke's law, and finally starts tearing. It should be noticed, that it's exactly glue tearing into two parts – not glue detaching from the surface (fig.9).
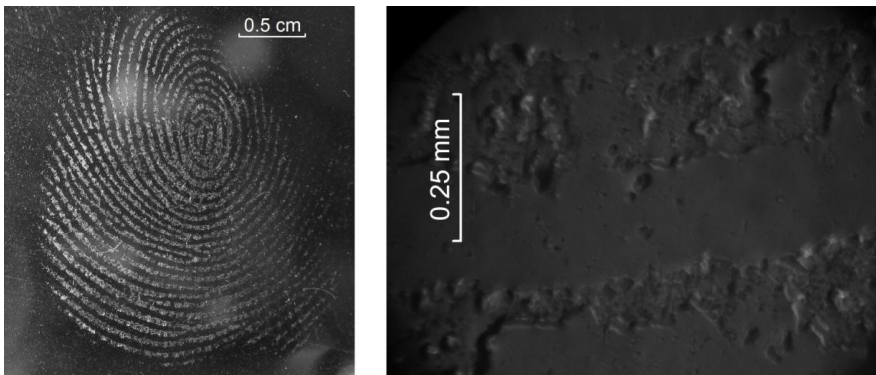
Figure 9. A fingerprint left on the tape, as seen in real life and through the microscope. On the right picture it can be noticed that big part of glue is missing – it had remained on the finger. However, finger doesn't become sticky because glue on it has very uneven surface – contact area effects are applied

Minimal force

Once the glue stopped following Hooke's law it can be described as a viscoelastic non-Newtonian fluid[2,3,4]. While behaving like this, all interactions in glue will depend on the velocity and applied forces. Exactly this behavior explains why tape resists detaching with the force equal to apply.

In fig.10 you can see dependence of the detaching velocity on applied force. Experimentally, we have found that it is a parabola:

$$V_{mm/\min} = (0.40 \pm 0.01)F_N^{\ 2} - (0.43 \pm 0.09)F_N + (0.2 \pm 0.2);$$

It shows that velocity will be zero only if no force is applied. It means that a piece of tape, attached to the lower side of the sheet of material, can be pelt off by its own weight. Experiments show, that it is true: for example, a 3.7X3.7 cm piece of double-sided tape, attached with contact area of 75%, will fell off in 4 days. However, it can happen not because of mechanical processes, but because of chemical: in such a

long periods of time chemical reactions between glue and the surface may occur. There is no way of checking what exactly happens (mechanical destruction of glue or chemical). That is why we decided to reject using term "minimal force" or "force necessary to remove"; we described dependence between applied force and velocity of peeling instead.
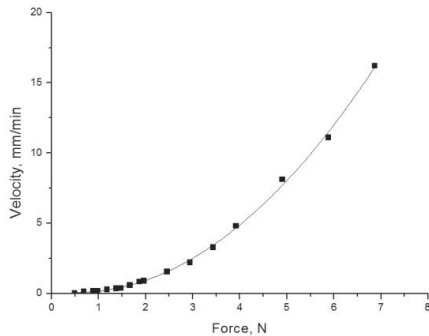
Angle of peeling

Figure 10. Dependence of velocity on force. Line shows fit with parabola. Average error of force is 0.05 N, of velocity 0.02 mm/min.

As shown in fig. 11, angle of peeling (angle between the detached tape, and the side of surface, from which the tape is already removed) significantly influences velocity. It is explained by the fact, that applied force is used for two purposes: its projection, normal to the surface, stretches and tears glue apart; while its projection, parallel to the surface, moves the point of detaching. That is why, if

angle is 180° velocity is low: projection of the force, which should stretch the glue is zero. The same reason for low velocity if angle is 90°: now we don't have projection, which moves point of detaching forward. And the peak of velocity is when projections are equal: when peeling angle is about 135°. If we use peeling angles smaller than 90°, projection of the force, parallel to the surface, is opposite to the peeling direction; therefore, peeling is extremely slow. And, finally, if we try to peel at the 0° angle a slip-stick phenomenon will occur: because of the force applied, tape will slip; but since there is no force projection which can move it away from the surface, new bonds will be established and tape will stick to the surface again. This slip-stick cycle will continue while force is applied; so, in general,

Figure 11. Peeling weight is 0.5 kg

tape will be moving parallel to the surface with very low speed[5].

It is interesting to note, that a small social study had shown that in average, people are peeling tape at the angle of 136.4°, which is really close to the optimal value. However, it can be explained by the fact that person's hand just moves so that resisting force is minimal, therefore choosing optimal angle.

Environment influence

During our work we have noticed, that all long-lasting experiments (especially if they lasted over one day) were giving big errors and sudden jumps of dependences. It is explained by changes in the environment temperature and relative humidity[6].
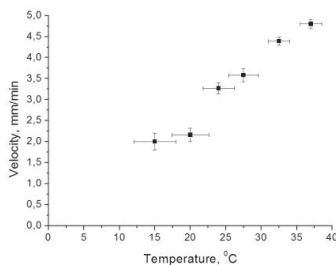
Figure 12. Peeling weight is 0.5 kg. The higher is temperature, the easier it is to detach the tape

Unfortunately, we could not control relative humidity of the air; but we had run an experiment with different temperatures (fig. 12).Still, it was hard to keep temperatures, lower than surrounding temperature, constant during whole experiment; this is why measurements at lower temperatures have higher errors. However, the plot shows quite well that increase in temperature causes increase in peeling velocity: glue behaves as a viscoelastic non-Newtonian fluid, and temperature impacts both its viscosity and elasticity significantly.

Conclusions

Main conclusion of our work is that since tape will detach if any (other than zero) force is applied, there is no such thing as "force necessary to remove"; only dependence between applied force and velocity. This dependence appears to be parabola. The parabola can be affected by the temperature, peeling angle and contact area. Contact area effects are applied if thickness of the glue layer isn't constant (for example, on most double sided tapes). For quantitative analysis we can consider that thickness of glue follows Gauss distribution, and glue behaves according to Hooke's law. Same approximations can be used if measuring Young's modulus of glue through the period of small oscillations. However, if we are describing detaching of the tape, we should take into account, that glue behaves as a viscoelastic non-Newtonian fluid. That is why tape resists detaching with force, equal to the applied.

References

[1] Wikipedia contributors, "Pressure-sensitive Adhesive", Wikipedia, The Free Encyclopedia, 30 December, 2011;
[2]Jeffrey D. Miller, "Surface Chemistry Measurements For Evaluating Coatings Formulations", Pressure Sensitive Tape Council, 2007;
[3] Gareth McKinley's Non-Newtonian Fluid Dynamics Research Group at MIT, "Stretching and Breakup of Polymeric Liquids in a Microfilament Rheometer";
[4] The Adhesive and Sealant Council, Inc website,
http://www.adhesives.org/adhesivessealants/adhesivetechnologies/pressuresensitive.aspx;
[5] Seung-ho Moon, Mark D. Foster, "Scanning Probe Microscopy of PSAs: Recent Developments", Pressure Sensitive Tape Council, 2002.
[6] Christopher C. White, KarTean Tan, Bryan D. Vogt, Donald L. Hunston, "The Origin Of Critical Relative Humidity in Adhesion", Pressure Sensitive Tape Council, 2009.

No. 1, Adhesive tape: Detachment energy, a model and an experimental analysis

Nives Bohačić [1]
[*] Team of Croatia, IYPT 2011
[1] *University of Zagreb, Croatia*
Corresponding author: nives.bonacic@hotmail.com (N. B.)

Abstract

This paper focuses on determining the force necessary to remove a piece of adhesive tape from a horizontal surface and investigating the influence of relevant parameters. It explains a simple and fairly accurate experimental setup which enables changing the angle, width and temperature as well as the surface to which the tape is attached. It gives an insight to both microscopic and macroscopic process of removing the tape and a theoretical model compared with obtained results.

Adhesion, cohesion

Adhesive tape sticks to the surface due to intermolecular interactions between the glue molecules (long polymers) and their interactions to the surface. These forces are adhesion forces (between molecules of glue and the surface) and cohesion forces (between molecules and layers of glue). Thus, there are two easily observed basic fracture types, depending primarily on the velocity of removing the tape from the surface, adhesive and cohesive rupture. A previous study [1] has shown that typically under rupture velocities of ~$10^{-3.5}$ (m/s) cohesive rupture occurs and above ~10^{-3} (m/s) adhesive rupture occurs.More thorough rupture explanations can be found in the Temperature section. While conducting the experiments, the rupture velocity was measured to assure an almost constant peel-off rate (minimum force) and a phenomenon of forming threads between glue layers was observed. During peel-off the stick-slip phenomenon was noticed, but the average velocity was not increasing so no further analysis of it was done.

Model

Assume that the total glue volume is preserved during the thread formation according to$V = Nr^2\pi l$, *N* being the number of formed threads which remains approximately constant over peel-off, *r* the radius and *l* the length of a thread. Critical condition of thread fracture depends on surface tension minimum. At a certain thread length it is more favourable to break into two parts than remain a single very long thread (Rayleigh's instability criteria).

Theadhesive energy per surface area of glue*G*holding the tape needs to be overcome by the peel-off force to remove it.Every tape and surface haveacharacteristical *G* which can be used as a comparison between measurements with different angle, backings and other conditions. This *G* depends on the above mentioned surface tension criteria and therefore on the temperature of the whole system.

The mentioned adhesive energy equals the work done by the peel-off force minus the stretching *S* and dissipation work$Dd(S + D) = bh \int_0^\varepsilon \sigma d\varepsilon \, dx$ where *b* and *h* are tape dimensions (thickness and width respectively),σ is tensile strengthand ε is elongation ($\Delta x/x_0$) of the backing material.

The work of the peel-off force removes the tape from the surfaceas well as elongates it. It is described by the relation $dU = F(1 + \varepsilon)dx$ where F represents the peel-off force. Since the tape does not shear, work done in the plate direction by component F_1(figure 1) is 0. The reduced expression being$dU = F(1 + \varepsilon - cos\theta)dx$.
All above considered,G (adhesive energy per surface) is:

$$G = \frac{F(1 + \frac{\varepsilon}{2} - cos\theta)}{b}$$

Elongation differs between measurements depending on the applied force. Hook's diagram of plastic materials (such as these referred to as backing) shows that there is a small part of strain possible after elastic limit before failure and thus I find the use of Hook's law appropriate. Elongation is calculated using the expression below, E being the Young's modulus, a backing characteristic $\varepsilon = \frac{F}{bhE}$.

Tape properties

Equationspointed out so far help to decide which important tape properties are to be evaluated such as tape width, thickness and Young's modulus. Measurements were done on two types of tape: transparent tape and creped tape (named after backing). Results were compared with factory data.

Experimental setup

A piece of tape (15cm) was attached to an adjustable slope (aluminium and laminate surface)(figure 1) from the bottom side and evenly pressed with a metal cube. It was detached using a weight – various sized pots filled with water/grains. An empty pot hanged on a thin thread. The pot was slowly filled till the peel-off started. To assure that the minimal necessary force was applied a time measurement of the detaching process was done. Time was measured every cm of the peel-off, these intermediate times were compared and only experiments done at a constant peel-off rate were taken into consideration. Peel-off rates were mostly in the interval of both cohesive and adhesive rupture (~$10^{-3.5}$ (m/s) to ~10^{-3} (m/s)).
The pot was afterwards weighed to find its mass and thus the peel-off force $F = mg$.
Angle variations were simple on this slope as it was completely moveable.
Tape width measurements were done using a 5 cm tape cut width a scalpel on a horizontal surface.
Temperature variations required a different setup. A long and wide metal plate (aluminium) was placed horizontally, warmed from one end with an electric stove and cooled down from the other with a constant water stream along the entire edges. This resulted in a linear temperature gradient from one to the other plate side measured with a laser thermometer to mark the same temperature sections.
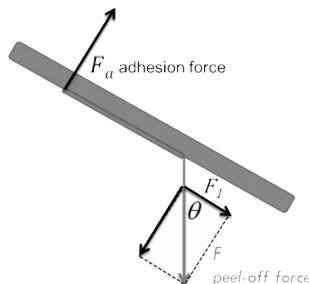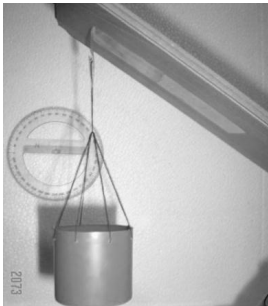
Figure 1: Force analysis on the slope with a marked angle and experimental setup consisting of an adjustable slope and a filling pot.

Relevant parameters

The focus of this study is on angle, width and temperature parameters as these can be evaluated by the presented theory.

A comparison of tapes is included with two tape types (transparent and creped tape). Other tapeswere not taken into consideration. Tape differences could not be considered a true parameter due to variations between glues and backings (on which *G* depends on)and as thesethey areless relevant. Surface dependance is of importanceas it influences peel-rateand is connected with pressure magnitude. Other surfaces besides aluminium and laminate were not investigated because it wasnot simple toexpress surface differences. Presented results just enhance that *G* is a surface-glue not justa glue property.

Angle

A complex relation between angle and the peel-off force requires an indirect representation.The x-axis includes ε, which is dependent on F but changes in a smaller order of magnitude than$\cos\theta$ and thus this is indeed an force/angle relation. All errors are from the progression plot.

$$F = \frac{const(G)}{1 + \dfrac{\varepsilon}{2} - \cos\theta}$$
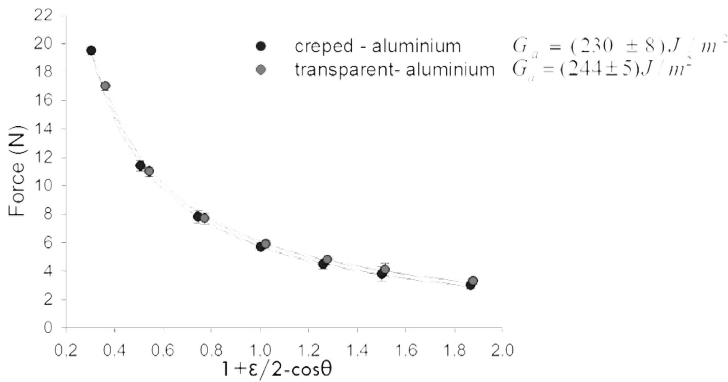
Figure 2: Angle-force dependence on the aluminium surface for tapes, temperature 20°C, first order inverse function plots
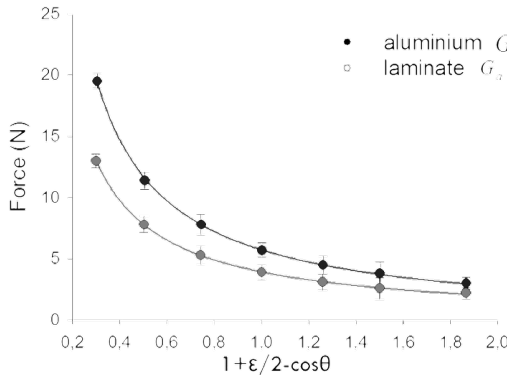
Figure 3: Angle-force dependence on aluminium and laminate surface for creped tape, temperature 20°C, first order inverse function plots

Width

Tape used for this parameter is the same type and manufacturer transparent tape which is initially wider and cut for the purposes of this experiment. This relation is also shown indirectly and follows the equation variation:

$$F\left(1+\frac{\varepsilon}{2}\right)=bG$$

$$G_a = 173 \pm 5\,J/m^2$$
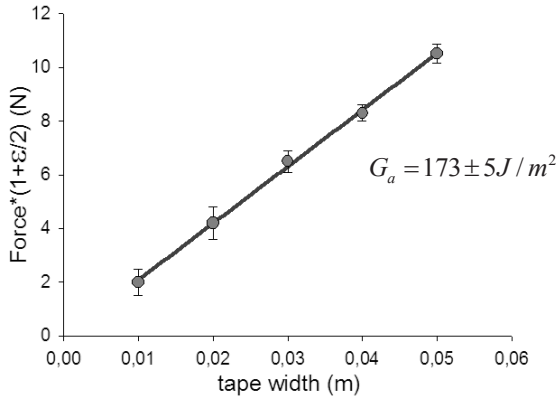
Figure 4: Tape width-force dependence on laminate surface for transparent tape, temperature 20°C, linear regression at a constant angle 90°

Temperature

Observing the tape as a thermodynamic system helps us determine a minimum free energy condition from which the number of forming threads is found. Since surface tension depends on temperature it links the energy condition to temperature dependance.

Thermodynamic free energy F is the amount of work that a thermodynamic system can preform related with $F = U - TS$ where U (the internal energy of the system) is surface energy. U follows the relation $U = N2r\pi l\,\gamma(T)$, $\gamma(T)$ being the surface tension of a surface formed of N threads. S is the system entropy for which a greater number of threads is more favorable and $S \sim kNlnN$ (entropy of an ideal 2D gass).
There is a minimum free energy condition which gives the N_0 number of formed threads

$$U = TS / \frac{d}{dN}$$

.
Energy condition can be related to the force needed to peel-off the tape by surface energy/length derivation $F = \frac{\partial U}{\partial l}, U = N2r\pi l\,\gamma(T)$ resulting in

$$F = \alpha \frac{\gamma(T)^2}{T}$$

This equation is obtained by expressing r by the constant volume relation $V = Nr2\pi l$.

Including surface tension temperature dependence $\gamma(T) = y_0\left(1 - \frac{T}{Tc}\right)^n$, $y_0\left[\frac{J}{m2}\right]$,

where n is an empirical value (11/9 for organic liquids such as glue [2]), the final expression is

$$F = \beta \frac{\left(1 - \frac{T}{Tc}\right)^{22/9}}{T}$$

with Tc being the system critical temperature and β a coefficient.These coefficients were read from the fit and T_c showed agreement with factory data.
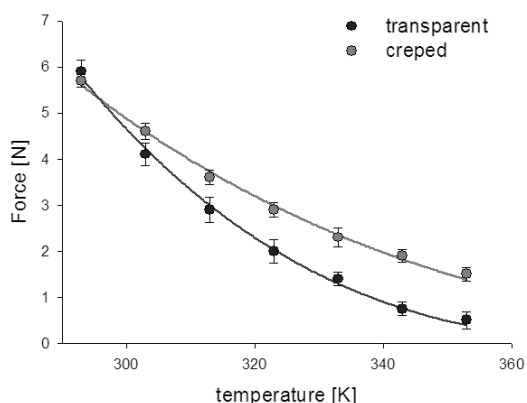
Figure 5: Temperature-force dependence on aluminium surface for both tapes, equation presented regression at a constant angle 90°

Conclusion

In this work a comprehend answer to peel-off force determination and relevant parameters investigation was presented. The peel-conditions were set with fracture energy / surface G property evaluated for:

creped tape on aluminium $G_a = 230 \pm 8 J / m^2$,laminate $G_a = 158 \pm 6 J / m^2$ and

transparent tape on aluminium $G_a = 244 \pm 5 J / m^2$, laminate $G_a = 173 \pm 5 J / m^2$.

This energy determines the necessary force. Conducted experimentsshow the changes ofthis force Fin accordance to predictions - preserving the same $G$for relevant parameters.

Angle (45°-135°), width and temperature (surface tension microscopic view) parameters show an excellent agreement of the experimental results and the theoretical model.

References

[1] A. J. Kinloch, C. C. Lau, J. G. Williams, The peeling of flexible laminates. Int. J. Fracture 1994, Vol:66, Pages:45-70
[2] Wikipedia: surface tension http://en.wikipedia.org/wiki/Surface_tension

No. 1, Adhesive tape: Energy analysis and numerical simulation

HosseinAzizinaghsh[1] and Hamid Ghaednia[2]
[*] Team of Iran, IYPT 2011
[1]*Sharif University of Technology, Iran*
[2]*Amirkabir University of Technology, Iran*
Corresponding authors: hossein.azizi@gmail.com (H. A.), ghaednia.hamid@gmail.com (H. G.)

Abstract

The current article is an investigation on possible methods of determining the force, necessary to remove a piece of adhesive tape from a horizontal surface. Initially, the force was determined based on concepts of surface energy and elastic deformation. In order to increase the accuracy and avoid some simplifications, a numerical simulation was developed.
The force was accurately measured and based on experimental measurements, theoretical predictions were verified.

Introduction

Adhesion occurs due to various types of interactions between the molecules of the adhesive and adherent materials. Depending on the type of the adhesive tape and adherent, different types of interactions are involved e.g. Van der Waals forces, physical interlocking, diffusion of polymers, electrostatic forces, etc.
There are various adhesion theories. None of these theories cover all the different aspects of adhesion. "A promising combination of different adhesion theories does not exist" [1] thus, adhesion is not a well-known phenomenon.
Adhesive tapes are a subject of various measurements [1][2][3][4]. But there is no comprehensive method to model the adhesive tape and predict its behaviour under different conditions. Various types of chemical and mechanical bonds [4] involved in adhesion, seem too complicated to be theoretically modelled. In the present work,a simplified model will be introduced. Despite its simplicity the predictions are quite accurate and are in great agreement with experimental measurements.
It was observed that in some cases (Low peel angle), detaching of the adhesive tape from the adherent material is mainly due to deformation. A significant difference was observed when a paper-backing adhesive tape and a plastic-backing adhesive tape with similar adhesive layers were removed. Thus, aside from adhesive layer and its properties, the properties of the adhesive tape backing are also decisively important.
When the force is applied, stresses propagate along the adhesive tape. These stresses cause the adhesive layer to deform. When the force reaches a critical magnitude, the bonds between adhesive-adhesive or adhesive-adherent or adherent- adherent cannot provide enough force. Therefore they will be removed. In either case, the adhesive tape is removed from the surface.

"The dependence of the peel force on the peel rate is complex. It has been shown that several regimes can be obtained as a function of the peelrate" [2] In order to avoid the

complex behaviour of the adhesive material related to peelrate, all the experiments have been done under a static condition ($v_{peeling} \rightarrow 0$).

Theoretical Analysis

In order to remove a piece of adhesive tape, all the bonds between adhesive-adhesive or adhesive-adherent or adherent- adherent should be removed. Removing each of these bonds requires a certain amount of energy. We define this energy as: $A\gamma$, A is the area of the adhesive tape that has been removed from the surface and γ is the adhesion energy per area. γ is a function of environmental conditions. Aside from this, the deformation of the adhesive tape also consumes energy.

The theory is based upon some assumptions:
- Removing the adhesive bonds consumes energy. This energy is described by γ, surface energy density discussed above.
- Adhesive tape shows considerable strain in respond to stress. This deformation consumes energy and is described by modulus of elasticity, E, which is considered to be constant.
- In the whole process, adhesive tape behaves elastically.
- Wasted energy (energy converted to heat or radiations) is considered negligible
- Small deformations of adhesive layer consume energy. This energy is considered negligible.
- The work done by the peeling force is equal to the change in the energy of the system.

Based on these assumptions, and conservation of energy, the force F can be found. (Fig. 1)
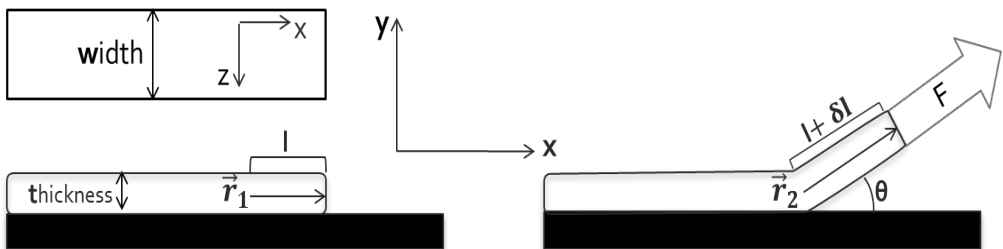
Figure 1: Illustration of parameters

$$W = \vec{F}.\Delta\vec{r} = \gamma A + \frac{1}{2} k \delta l^2 \,(1)$$

$$
\begin{cases}
\Delta\vec{r} = \vec{r}_2 - \vec{r}_1 = l\left[((1 + \frac{\delta l}{l})\cos\theta - 1)\hat{x} + (1 + \frac{\delta l}{l})\sin\theta\hat{y} \right](2) \\[2mm]
\vec{F} = F(\cos\theta\hat{x} + \sin\theta\hat{y})(3) \\[2mm]
A = lw \ (4) \\[2mm]
k = E\frac{wt}{l} \,(5) \\[2mm]
\frac{\delta l}{l} = \frac{1}{E}\frac{F}{wt} \,(6)
\end{cases}
$$

$$(1),(2),(3) \rightarrow W = Fl(1 - \cos\theta + \frac{\delta l}{l})(7)$$

$$(1),(4),(5),(6) \rightarrow W = lw\gamma + l\frac{1}{E}\frac{F^2}{2wt} \,(8)$$

$$(7),(8) \rightarrow F = Etw\left[(\cos\theta - 1) + \sqrt{(1 - \cos\theta)^2 + 2\frac{\gamma}{Et}} \right](9)$$

Numerical Analysis

The simple analysis of the problem using energy concepts is highly effective (as it will be approved in further experiments). In this method some simplifications are inevitable, most importantly, adhesive layer and its deformation and its corresponding energy that are completely neglected. Furthermore, the energy method is highly abstract and it cannot illustrate what really occurs in the process of adhesive tape removal. Thus, in order to avoid several simplifications and also to have a better understating of the phenomenon (which is a really important objective of this paper), a simple numerical model was developed to describe the phenomenon down to the micro level (see online supporting material: Modelled adhesive tape removal video).
The adhesive tape was modelled as series of vertical and horizontal springs (Fig. 2).Vertical springs indicate the adhesive layer and the horizontal springs indicate the adhesive tape backing material. Node is where the vertical and horizontal springs connect to each other, small circles in figure 2. When the force is applied to the first node, the equilibrium state of system (All the nods are in equilibrium state) will be found. At his point, if the length of the first spring is higher than a critical length, the adhesive tape is removed and the necessary force is found. Otherwise the force will gradually increase and the process will repeat (Fig. 3, 4, also see online supporting material: Source code).

The numerical model is based upon some assumptions:
- Wasted energy (energy converted to heat or radiations) is considered negligible.
- In the whole process, both adhesive layer (vertical springs) and adhesive tape backing (horizontal springs)behave elastically.

- The adhesive tape removes because the strain of the adhesive layer (length of the first spring) reaches to its limit.
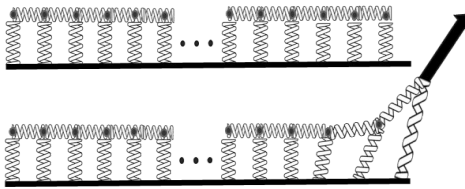
Figure 2: Modeling the adhesive tape as series of vertical and horizontal springs, circles indicate the nodes
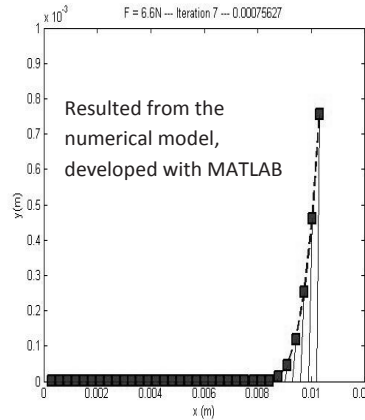
Figure 3: The adhesive tape when removing. Squares indicate the nods, dashed lines the horizontal springs and lines the vertical springs (adhesive layer)

Parameters involved in the numerical model

Four parameters are involved in the numerical model:
- N, Number of the springs. This parameter affects the accuracy of the model and is not a determinant itself. This parameter was set to 100 springs per millimetre.
- K_v, constant of vertical springs. This parameter is proportional to modulus of elasticity of the adhesive layer and its dimensions (thickness and width). These parameters are measured in experiment part.
- K_h, constant of horizontal springs. This parameter is proportional to modulus of elasticity of the adhesive backing and its dimensions (thickness and width). These parameters are measured in experiment part.
- $l_{critical}$, maximum length of the first spring. When the adhesive tape removes, the first spring removes either from the adhesive backing (horizontal springs) or from the surface, because it has reached to its ultimate strain. This ultimate strain is similar to γ parameter discussed in the analytical theory and it is related to chemical and physical properties of both adhesive and adherent materials, their interaction and environmental conditions. This parameter will be calibrated in experiment part.
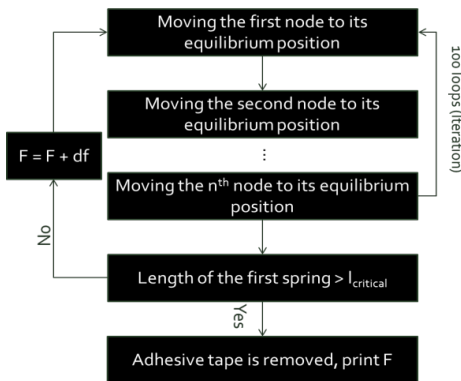
Figure 4: Numerical algorithm
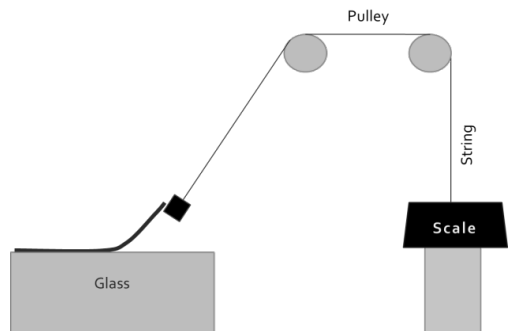
Figure 5: The experimental setup

Experiments:
Measurement of the force

The force necessary to remove a piece of adhesive tape under a static condition was measured. A digital scale with the resolution of 0.1 g is placed on a surface. The height of this surface is adjustable. One end of a string is attached to the scale; the other end is attached to the adhesive tape (Fig. 5).By decreasing the height of the scale, the tension in the string will gradually increase until the adhesive tape starts to peel off from the surface. The number indicated by the scale is the force necessary to remove the adhesive tape. Two types of adhesive tape were experimented, paper-backing and plastic-backing. The comparison between these two demonstrated the significance of the adhesive tape backing material.

Measurement of modulus of elasticity

The applied force was measured when the adhesive tape is deformed (Fig.6).
A scale with the resolution of 0.1 g is placed on a surface. The height of the surface is adjustable. One end of the adhesive tape is attached to the scale. The other end is attached to a fixed point. By decreasing the height of the surface, the adhesive tape will deform and the corresponding force is indicated by the scale. This force was measured as a function of deformation (Changes in the width and length of the adhesive tape). Modulus if elasticity can be found by calculating the slope of force-strain graph (Fig.7). This experiment was repeated three times in order to increase the accuracy.
The measured modulus is equal to $E = E_{layer} + E_{backing}$. By washing the adhesive layer and repeating this experiment, $E_{backing}$ can be found. This way modulus of elasticity of both materials can be measured. In the analytical theory E is required, but the numerical model requires both.
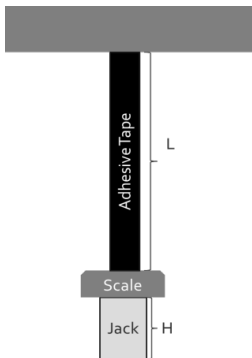
Figure 6: The experimental Setup
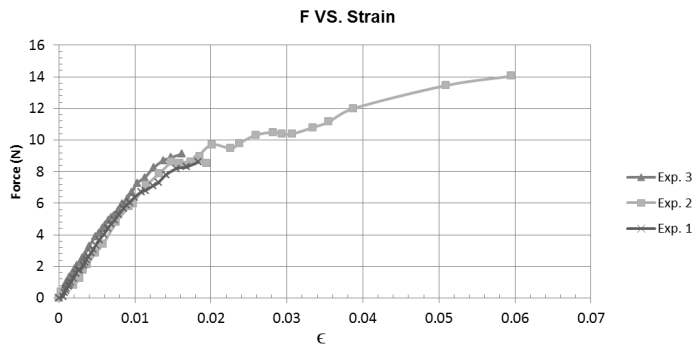
Figure 7: Force vs. Strain, the slope of initial, linear part is proportional to the modulus of elasticity

Measurement of thickness

Internal and external radius of the adhesive tape roll (Fig. 8, r_1 and r_2) and length of the adhesive tape (Fig 8, L) were measured. Based on formula (10) thickness of the adhesive tape can be measured. This thickness is equal to $t = t_{layer} + t_{backing}$. By washing the adhesive layer and repeating the measurements, $t_{backing}$ can be measured. This way both $t_{backing}$ and t_{layer} are found.
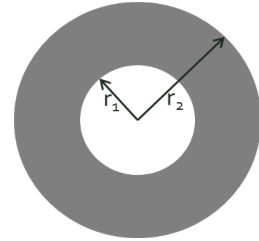
$$\pi(r_2^2 - r_1^2) = Lt \text{ (10)}$$

Figure 8: measurement of thickness
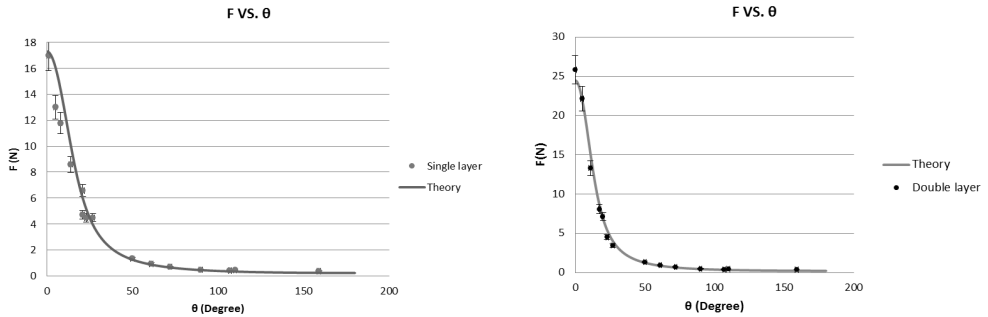
Figure 9: the theory was calibrated (left graph-single layer adhesive tape), and then the calibrated theory was verified in another experiment (right graph-double layer adhesive tape)

Calibration

The theory requires some parameters that are dependent on environmental conditions and chemical properties of adhesive and adherent material, thus, they cannot be directly determined. These free parameters are γ, mentioned in the analytical theory and $l_{critical}$, mentioned in the numerical model. In order to measure these parameters, based on the experimental force vs. peel angle(θ) graph, both theories were calibrated and then another experiment was designed in order to verify the calibrated theory :A double layer adhesive tape was used, and force vs. peel angle (θ) was measured, the result was compared to the prediction of the calibrated theory (Fig. 9).

It is notable that the same type of the adhesive tape was used in both experiments. Therefore, neither γ nor $l_{critical}$ will change. The only parameter that changes in two experiments is thickness of the adhesive tape, which will affect the t parameter in formula (9) and K_h, constant of horizontal springs in the numerical model. Thus, the calibrated parameters will not change in double-layer adhesive tape experiment.

Discussion

Both analytical and numerical methods provide accurate predictions (Fig.10). The prediction of the numerical method is more precise at a low peel angles (θ) while the prediction of the analytical method is more precise at higher peel angles.

In the following, we discuss main sources of difference between theoretical prediction and experimental measurement.
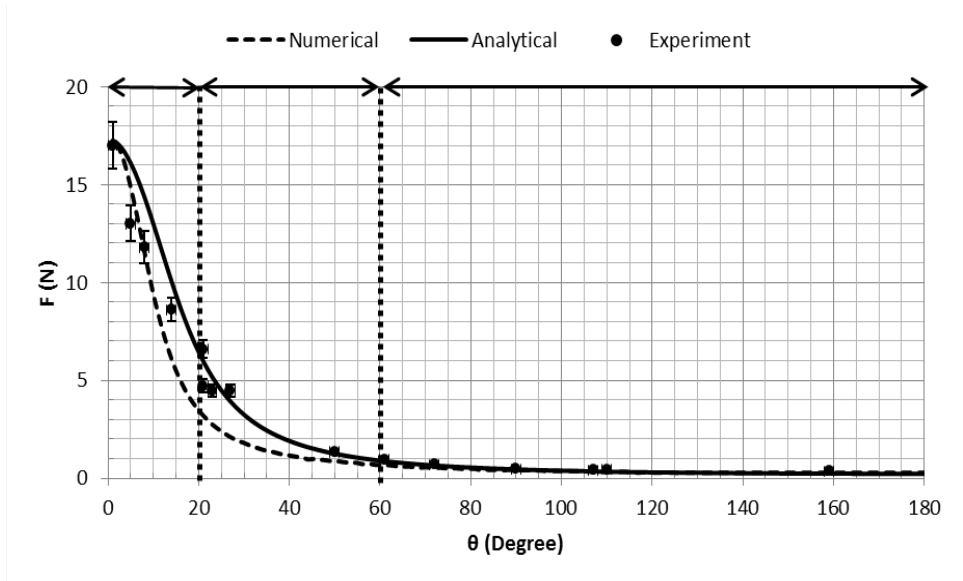
Figure 10: Predictions of numerical and analytical theories and experimental measurements

Experimental error

Error of force measurement was mainly due to the lack of reproducibility in measurements. Especially, in cases when detaching of the adhesive tape requires large force. The error was minimized by repeating the measurements. Furthermore, the static condition of the system and gradual increase of force during the measurements ($v_{peeling} \to 0$), prevents some dynamic and complicated behaviors of adhesive material and enhances the reproducibility of measurement.

Elastic behavior of the adhesive

In both theoretical approaches, it was assumed that adhesive tape behaves elastically during the peeling process. According to Fig. 7 this is only true when the strain of the adhesive tape is lower than 0.02. At low peel angles deformation of the adhesive tape would be more significant, thus it may not behave elastically as it is assumed in the theory. As it is shown is Fig. 10 there is no good agreement between the analytical theory and measurements when $0 < \theta < 20$.

Neglected energy in the theory

According to formula (1), the total energy spent to remove the adhesive tape, will be used to remove the adhesive-adherent bonds and deform the adhesive tape. The deformation of the adhesive layer also consumes energy which is not considered in formula (1).

Neglected parameters in the numerical model

There are two different types of stresses applied to the adhesive layer. Shear stress resulted from horizontal component of the force and normal stress resulted from the vertical component of the force. In the numerical model different nature of these stresses is neglected. The constant of vertical springs is responsible for both shear stress and normal stress applied to the adhesive layer. In reality these two stresses are described by two different modulus, modulus of elasticity (Normal stress) and modulus of rigidity (Shear stress). As it is shown in Fig. 10, when $0 < \theta < 20\ and\ 60 < \theta < 180$, there is good agreement between the numerical theory and measurements. In these ranges only one type of stresses is dominant. While in $20 < \theta < 60$ the prediction is not quite accurate, because two different types of stresses are both effective. Adding another type of spring to the model may improve the accuracy.

Conclusion

According to figure 10 and formula (9), the chief task of this investigation is achieved. However theoretical predictions and experimental measurements are based upon some simplifications (e.g. static condition of the system). The problem has been investigated using two different methods:
- Energy analysis of the system based on concepts of surface energy and elastic deformation of the adhesive tape which leads to accurate results (Formula (9) and Fig. 1, 9).
- Numerical modelling of the system based on the elastic nature of the adhesive tape, which describes the phenomenon down to the micro level and also provides accurate predictions (Fig. 2, 3, 4, also see online supporting material: Modeled adhesive tape removal video).

In the experiment part, the dimensions (Fig. 8) and the modulus of elasticity of the adhesive tape (Fig. 6, 7) have been measured to be used in the theory. One free parameter of the theory, related to chemical properties of adhesive and adherent material, was calibrated (Fig. 9). Finally theoretical predictions were compared to experimental measurements (Fig. 10) and their agreement or lack of agreement in different parts was discussed.

Online supporting material

Modelled adhesive tape removal video
http://archive.iypt.org/iypt_book/2011_1_Adhesive_tape_Iran_HA_HG_Adhesive_Removal.mp4
Numerical model source code
http://archive.iypt.org/iypt_book/2011_1_Adhesive_tape_Iran_HA_HG_Source_Code.txt

References
[1] G.Gierenz, W. Karmann (2001), Adhesives and Adhesive Tapes, Wiley-VCH.
[2] IstvanBenedek (2004), 2[nd]ed, Pressure-Sensitive Adhesives and Applications, Marcel Dekker Inc., New York–Basel.
[3] SinaEbnesajjad (2008), 2[nd]ed,Adhesives Technology Handbook, William Andrew, Norwich - NY- USA
[4] GerdHabenicht (2009), Applied Adhesive Bonding, Wiley-VCH

No. 3, Bouncing flame: Flames in a horizontal electric field, deviation and oscillation

RojinAnbarafshan, [1]HosseinAzizinaghsh, [2] and Reza MontazeriNamin[3]
[*] Team of Iran, IYPT 2011
[1]*RaheRoshd High School, Tehran, Iran*
[2]Sharif University of Technology, School of Computer Engineering, I. R. Iran
[3]Sharif University of Technology, School of Mechanical Engineering, I. R. Iran
Corresponding authors: rojin.anbarafshan@gmail.com (R. A.), hossein.azizi@gmail.com (H. A.), namin@mech.sharif.edu (R. M. N.)

Abstract

The current paper is an investigation on the behaviour and motion of flames in case where the flame is placed between two charged parallel metal plates with different charges. A physical experimental setup has been constructed to make precise experiments. Observations give detailed information about the deviation of the flames towards the negative plate, and in some special cases, the diffusion flames start "oscillating". Theoretical explanation has been proposed for the phenomena and has been proved by the experiments in qualitative predictions. A numerical model has also been developed based on the theory to be compared with the experimental data quantitatively. This paper is based on the original solution of team of Iran on the 3rd problem of IYPT 2011.

Introduction

Flames have been reported to be ionized gases and in some cases to be plasmas [1]. The fact of being plasma or not, depends on the flame temperature and the burning material [1].

Asymmetrical division of the flame in two branches deviating toward different plates, in case where the flame is placed between two charged parallel metal plates, has been observed and investigated in few resources. A suggested explanation is the difference in the mass of the positive and negative ions existing in the flame [2]. In some investigations it is mentioned that the free electrons in the flame existing because of the ionization tend to react with the surrounding air molecules [2].

Other investigations have been made in different experimental situations, e.g. the effect of vertical electric field on flame stability has been investigated numerically by *Belhi* et al. [4] and it has been shown that flame stability increases in the presence of electric fields due to the momentum source which exists because of the electric force exerted to the ions within the flame (ionic wind).

We will discuss the effect of ionic wind on the shape and motion of the flame in horizontal electric field, and will show that the difference of the mass of the positive and negative ions is not a crucial matter in describing the phenomenon. The oscillatory motion of the flame is also a subject of investigation, which has been initially observed by the authors and no other references as we've seen, have reported such a motion.

Theory Base
Chemical analysis

Aside from the combustion process, some other chemical and electro-chemical reactions occur in the flame. In order to determine the electric chargewithin the flame; which is of significant importance in this investigation, these reactions must be well understood.

The first set of chemical reactions in the flame are those related to the main fuel-Oxygen reaction; a highly exothermic reaction. This reaction produces enough heat to raise the temperature to obtain the ionization energy. The second reaction is the heat thermal ionization, decomposing the molecules into positive ions and free electrons in the high temperature zone. This reversible reaction causes free electrons to flow in the boundaries of the ionized zone.

Combustion: $Fuel + O_2 \Rightarrow CO_2 + H_2O + Energy$

Ionization: $Fuel \Leftrightarrow Fuel^+ + e^-$
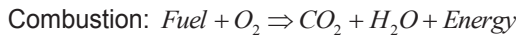
In the presence of the electric field the forces acting on positive ions and electrons are in opposite directions, the charge separation will occur, and the contact of the electrons with oxygen molecules in the boundaries of the flame, increases. Thus,the electrons react with O_2 producing O_2^-.

Electron reaction: $O_2 + e^- \Leftrightarrow O_2^-$

Due to the electron lost in the flame system, positive particles would be dominant, thus the flame will be positively charged. The rate of electron loss, which is equal to the rate of the charge gain, may be a function of several factors such as density, temperature and even the applied voltage. However, we have assumed it to be a constant amount.

Mechanical Analysis

To study the dynamics of the flame, we assume a control volume which's boundary is the visible part of the flame. According to Newton's second law, the derivation of momentum must be equal to the sum of the forces exerted. The derivation of momentum would equal to the changes of momentum inside the control volume plus the sum of the momentum entering the control volume: [4]

Figure 1:
Bouncing motion

$$\Sigma\vec{F} = \frac{\partial}{\partial t}\iiint \vec{V}(\rho dv) + \oiint \vec{V}(\rho\vec{V} \cdot \overrightarrow{dA}) \tag{1}$$

Where $\Sigma\vec{F}$ is the sum of the forces exerted to the control volume, t is time, $\vec{V}$ is the velocity vector of the flow, ρ is the gas density, v is volume, A is area (Figure2).

As an approximation, we assume that gas will be generated somewhere inside the flame and moves with a constant velocity $\vec{V}$ and exits the control volume from the cross-sectional area A. According to this assumption, the above formula changes to:

$$\Sigma\vec{F} = m\frac{d\vec{V}}{dt} + \rho AV\vec{V} \tag{2}$$

Assuming that the gas takes a specific time Δt to exit the mentioned control volume, the position vector ($\vec{r}$) of the flame tip would be $\Delta t \vec{V}$. This leads to equations regarding the position vector:

$$\Sigma \vec{F} = m\Delta t \frac{d\vec{r}}{dt} + \rho A \Delta t^2 r \vec{r} \tag{3}$$

The forces exerted to the control volume are the pressure from the boundary, which will be modeled as the buoyancy force, and the electrical force exerted because the flame is a charged body in an electric field (E).

$$\Sigma \vec{F} = Eq\hat{x} + (\Delta \rho v g)\hat{y} \tag{4}$$

The internal charge of the control volume is needed to find the electric force. Assuming that the combustion process produces charge with a constant rate Q_{in}, for the total charge in the control volume (q) the control volume formulation for the charge would state:

$$Q_{in} = \frac{dq}{dt} + AV\frac{q}{v} = \frac{dq}{dt} + Ar\Delta t \frac{q}{v} \tag{5}$$

The two recent differential equations are the main equations describing the motion of the flame. In the case of steady flow, the changes could be set to zero, and solutions lead to exact constant amounts for the r vector and q.

This equation describes the derivative of charge when no external charge exchange happens. However, the flame is conductive in high voltages [5] this means that electric discharge can occur if the flame electrically touches the plate. We assume a specific distance in which discharge happens, and if the horizontal distance would reach this amount, the total charge of the control volume would be set to zero. This leads to sudden reduction in the electric force and causes the flame to draw back, and again total charge increases, causing to a repetition of the phenomenon and leading to oscillation. The general unsteady case was solved numerically.

Figure 2: Declaration of parameters

Numerical Solution

To solve the general unsteady motion, a numerical solution was used. Equations (3), (4) & (5) lead to the derivations of position and charge as a function of the charge and the constants present in the problem. There is also one more assumption to describe the discharge phenomenon; that is, we assume that if the tip of the flame approaches a specific horizontal distance from a plate, the q will be suddenly set to zero. This assumption or any other assumption describing the discharge phenomenon is crucial in describing the "bouncing" effect (Figure 1), since the discharge is responsible for such a motion. With all these assumptions, this problem is an Ordinary Difference Equation, which we solved numerically using MATLAB ®. We used ODE45 function of MATLAB,

which solves the ODE using an explicit Runge-Kutta formula and the Dormand-Prince pair [6]. Our codes are available as a supplementary material to this paper.

Experimental Method

a) Experimental Setup

The experimental setup consists of several types of flame (candle or Bunsen burner), two parallel aluminum metal plates connected to a high voltage device with the maximum voltage of 14 KV and adjustment resolution of 0.1 KV. Distance between the two plates is precisely adjustable. In order to reach a uniform electric field around the flame, size of the plates is large enough comparing to the size of the flame. The flame is placed exactly in the middle of the two plates.

The corresponding behavior of the flame, under electric field was recorded using a high-speed camera (1000 FPS), placed exactly in front of the flame. Using this video, some precise experimental data was extracted.

b) Video Processing

The recorded video has 1000 frames per second, using MATLAB image processing tool-kit, the relative position of the center of area of the flame (estimated as the center of mass) and the wick of the candle (lower part of the flame) was found. The angle between this vector and vertical line (DA) was measured in each frame (Figure 3). DA as a function of time and voltage was extracted from different experiments.

Figure 3: MATLAB image processing. Left picture: Original picture, Right picture: Processed picture

Experiment

Initially, some qualitative experiments weredesigned to evaluate the basic theory.

Streams of rising smoke were used in order to detect the flow around the flame while it is oscillating. Flows of negative ions toward the positive plate and also positive ions toward the negative plate; were both observed(Figure 4); which verifies the validity of ionic wind theory. These laminar flows also reject the possibility of turbulent flows as the cause of oscillatory motion.

In case of oscillating candle flame, a layer of non-conductive material was placed between the flame and the plates by coating the aluminium plates, avoiding electrical dischargeinteraction

Figure 4: Smoke Experiment

between the flame and plates. As a result, the oscillatory motion of the flame was diminished, verifying the main reason of the oscillation as the electric discharge.

Most of the experiments were done using a candleflame; however the behavior of other flames was also observed. Pre-mixed flames mostly showed no oscillation at all. This is a result of the sufficient ionization degree, which can keep a steady current within the flame in the electrically touching condition with the plate. Some flames; e.g. the diffusion petroleum flame, were highly turbulent; and unsteady motion could be observed even in cases where no external field exists.

Threequantitative experiments were also designed, in order to compare the experimental results with the numerical model predictions. Candle flame was used in all the experiments.
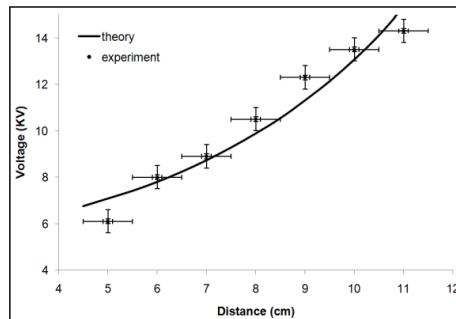
a) Critical Voltage of Oscillation

According to previously proposed theoretical explanation, the "Oscillation" occurs when the flame touches the plate electrically and discharges. For the flame to reach the plate there is a critical deviation angle and its corresponding voltage. This voltage is a function of the distance between the plates. The less the distance is, the lower voltage is required for oscillation to occur. The critical voltage of oscillation was measured by gradually increasing the voltagein different distances between the plates.

b) Deviation Angle(DA)vs. Applied Voltage

Before the flame starts oscillating, it deviates and reaches to a stable condition. DA (Figure 2) is proportional to the applied voltage. By increasing the applied voltage, DA will also increase. A candle flame was placed between the plates; distance between the two plates was fixed, the applied voltage was gradually increased and using image-processing method, the angle of deviation was measured in each voltage.

c) Frequency of oscillation

It was observed that the oscillatory motion of the flamehas a well-defined frequency. In a fixed distance between the plates, this frequency was measured in different voltages using image-processing methods.

Figure 5: Critical Voltage of Oscillation

Discussion

The behaviour of the flame, under different situations has been shown in figures5, 6, 7, 9. These results will be discussed in more details.

1. DA vs. Voltage

Figure7 indicates a linear correlation between the term$\frac{\tan DA}{\sqrt{\cos DA}}$and the applied voltage.

In case of deviation the flame is in equilibrium state. Formulae (3), (4), (5), (6) give:

Figure 6: Deviation Angle

$$\frac{dq}{dt} = 0 , \frac{d\vec{r}}{dt} = 0 \qquad (6)$$

$$\frac{\tan DA}{\sqrt{\cos DA}} = \frac{EQ_{in}}{\Delta\rho g \Delta t}\sqrt{\frac{\rho}{\Delta\rho v g A}} = C \cdot \frac{V}{d} \qquad (7)$$

Where, d is the distance between the plates, V is the voltage. The linear correlation of $\frac{\tan DA}{\sqrt{\cos DA}}$ and voltage indicates that the term $\frac{Q_{in}}{\Delta \rho g \Delta t}\sqrt{\frac{\rho}{\Delta \rho v g A}}$ in formula (7) remains unchanged during deviation. It can be implied that the input electric current (Q_{in}) of the flame and the buoyancy force are not affected in presence of electric field. Equivalently, electric field doesn't affect the combustion process and volume of the flame considerably. This fact was assumed in the theory which is now approved.

Fig 7. Indicates an x-intercept which is not implied by formula (7). When $0 < V < 2$ the flame does not deviate. It can be explained by considering the internal electric field resulted from charge separation, which cancels the external electric field and prevents the flame deviation in this range of voltage.
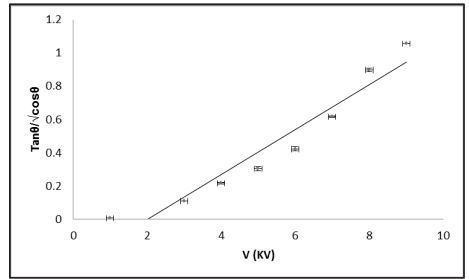
Figure 7: Flame in steady condition (Deviation)

2. Position vs. Time:

Assuming x and y to be the position components of the tip of the flame, plots for x and y vs. time were generated both in theory and experiments (Figure 8). Because of the simplified assumptions in the theory, we see sharp-edge diagrams for the motion which is not observed in experiments. The reason could be that the discharge does not only occur in the touching condition, but also can be possible in other distances. Another
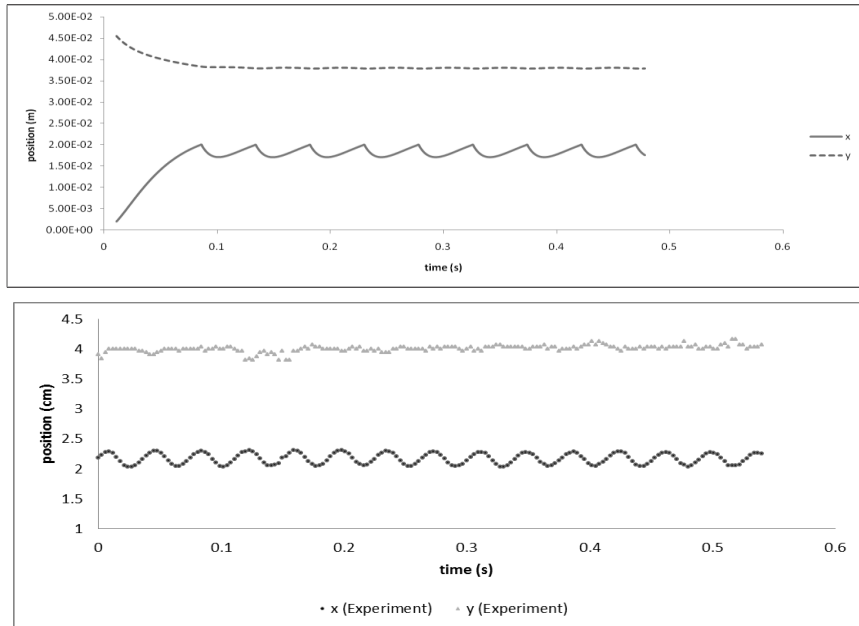
Figure 8: x and y component of position vector of the tip of the flame, resulted from theory and experiments

cause may be the assumption that the position vector and the velocity vectors are the same direction, which is just an approximation and may not be true.

3. Frequency vs. Voltage:

According to Figure 8, the frequency of oscillatory motion of the flame has a well-defined frequency. Electric discharge of the flame triggers the oscillatory motion. The voltage must be high enough to increase the DA and provide this condition. In Figure9 this minimum voltage is 8.5 KV, thus when $0 < V < 8.5$ the flame does not oscillate and the frequency of motion is non-existent (Figure 9). By increasing the voltage, the electric force, which is responsible for the motion, increases. Thus, it speeds up the process and increases the frequency; the theory also predicts an increasing trend for the frequency.When $V > 10.5$, decreasing behaviour is observed. Air drag; which is not considered in the theory, may be responsible for decreasing behaviour in high voltages.
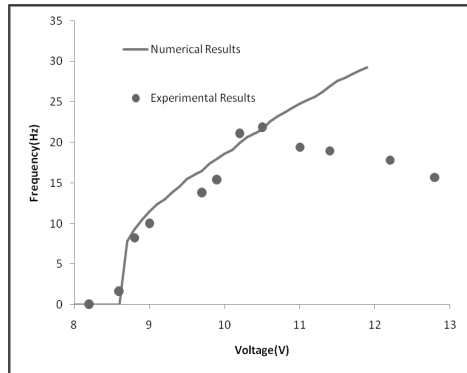
Figure 9: Frequency of Oscillation

References

[1] Gerald R Paul R Plasma and Flames - The Burning Question*Coalition for Plasma Science* 2008
[2] Leh Y K Fei WCW 2010 Visual PelangiKbsm 2010 Physics Spm*Pelangi Publishing Group Bhd*
[3]M. Belhi, P. Domingo, P. Vervisch, "Effect of Electric Field on Flame Stability"
[4] Shames I 2002 Mechanics of Fluids *McGraw-Hill Science*
[5] Wilson H A 1931 Electrical Conductivity of Flames *Rev. Mod. Phys*
[6] Fausett L V Applied Numerical Analysis Using MATLAB *Prentice Hall*
[7] Goodings J M Bohme D K , Chun-Wai N G1979 Detailed ion chemistry in methane-oxygen flames. II. Negative ions *Combustion and Flame* **45** 62

No. 4, Breaking spaghetti: Impact deformation and bending waves

Yulia Peregud [1]
[*] Team of Belarus, AYPT 2011
[1] *Belarusian State University Lyceum, Minsk, Belarus*
Corresponding author: svann11@mail.ru (Yu. P.)

Formulation of the problem

Find the conditions under which dry spaghetti falling on a hard floor does not break.

Introduction

Behavior of dry spaghetti as a brittle rod or behavior of solid bodies during deformations and its mechanical properties was the subject of many researches. But goals of some of these researches ([1], [2], [3], [4], [5]) are investigations of behavior of solid bodies in cases of static deformations. The goal of my research is to describe the processes which occur during dynamic deformation. My research is not the same as the previous researches because: 1) I investigate impact of spaghetti with some surface after free fall of spaghetti (the tips of spaghettis are not fixed). 2) I explain why exactly bending waves are the cause of breaking. 3) I investigate dependences of different important parameters what can change something in our system (but they don't change the cause of breaking).

Dynamic deformation is not the same kind of deformation as static deformation because the causes of breaking of spaghetti during impact with some surface are waves (waves appear in spaghettis during dynamic deformations – [6], [7]). The kind of wave which breaks spaghetti (the kind of wave which dominates in exact case) depends of conditions of an impact of spaghetti with the surface. That's why we must find out what kind of wave occurs in spaghetti to understand the main cause of breaking and, finally find the conditions under which dry spaghetti falling on a floor does not break.

The goal of my research is to determine the most important kind of wave what breaks spaghetti, estimate parameters of this wave, determine the point of maximum curvature and investigate the conditions under what probability of breaking is the least.

Explanation of processes in spaghetti

To begin with, we should consider three different variants for spaghetti to hit the floor: 1) horizontally, 2) vertically, 3) at some angle between 0° and 90°. The cause of breaking in the first case is compressive strain. But we need enormous amount of energy to compress spaghetti so much. Moreover, it is hard to make such experiments and this kind of impact is not very interesting. The third variant of hitting demands very complicated mathematical model. That's why I investigated only vertical falling of spaghetti.

And now let's explain what exactly happens with spaghetti during the impact. It was mentioned before that the cause of breaking of spaghetti is some kind of wave. There are 4 basic kinds of waves: longitudinal, transverse, torsional, bending waves. Torsional waves don't take place during the impact because spaghetti isn't twisted very much. Transverse waves usually occur in continuous

medium, not in rods. Longitudinal waves take place during every impact of solids. Nevertheless, from the point of view of energy necessary for breaking of spaghetti, the energy necessary for breaking with bending is less than without bending. The influence of longitudinal waves is negligible. Therefore, spaghetti is more likely to break because of curving. Thus, deformation of whole spaghetti is a combination of 2 deformations – some layers of spaghetti are stretched, some are compressed. Using a high-speed camera, I have taken videos of impact. I took some frames (Figure 1) of these videos and in that way proved the theory about bending waves: we can see that spaghetti really bends.

Now, understanding the nature of processes what occur in spaghetti, we can determine velocity of bending wave ([8]) in spaghetti (c_b)

$$c_b = \sqrt{\frac{2\sqrt{2}\pi \cdot R}{T}} \cdot \sqrt{\frac{E}{\rho}}$$

Figure 1: bending of spaghetti at the moment of impact

E – Young modulus of spaghetti, T – period of wave, ρ – density of spaghetti, R – section radius of spaghetti.

I approximated the dependence of reaction force of surface on time as sinusoid and estimated period of wave. The shape of bend of the spaghetti is sinusoid too.

$$T \approx 2t \approx 0{,}004s$$

t – time of the impact, found with the help of high-speed camera (1000 frames/s).
Also I found Young modulus of spaghetti: *E ≈ 2,3•10^7 Pa.*
Now it is possible to estimate the velocity of propagation of bending wave: $c_b \approx$ 16,6 *m/s.*
As a consequence of these estimations, I can calculate the wave-length (λ):

$$\lambda \approx c_b \cdot T \approx 6cm$$

Bending wave dies out very quickly, that's why not the whole of spaghetti bends. After watching slowed videos of impact I noticed that approximately 3 cm of spaghetti (from the bottom of spaghetti) bend. Further propagation of bending wave does not take place because of energy loss as a result of plastic deformation in spaghetti. Thus, all the energy of bending wave is spent on deformation and, consequently breaking. After breaking there is almost no energy left. Therefore spaghetti usually breaks only 1 time and only in 1 point.
How can we find this point? Spaghetti breaks at the distance *l ≈ λ/4 ≈ **1,5 cm*** from the bottom because of maximum curvature exactly in this point. The length of broke off pieces of spaghetti was around 1,5 cm in all the experiments. It perfectly proves my theory about bending waves as the main cause of breaking of spaghetti.

Experiment

First of all, let's clarify the way of characterizing probability of breaking of spaghetti. Let it be *p* – frequency of breaking of spaghetti. *N* – number of spaghetti which broke, N_o – number of all falling spaghetti

$$p = \frac{N}{N_o} \cdot 100\%$$

Secondly, I will describe my experimental setup. It is simple: It is a vertical tube (its length is 30 cm), fixed in a tripod. Spaghetti falls through this tube without initial velocity.
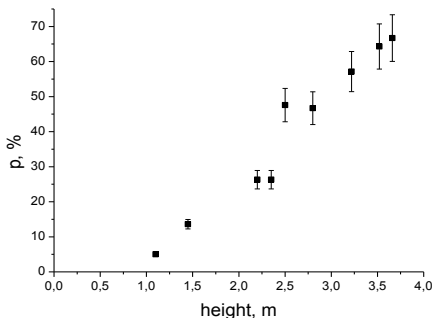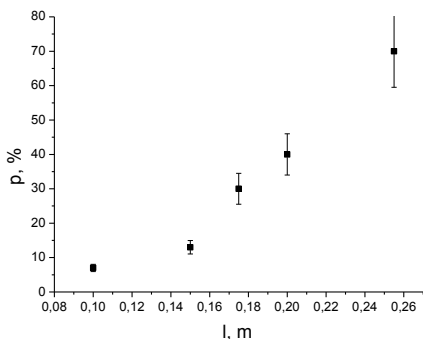

Figure 2: Frequency of breaking vs. height of falling

Thirdly, let's determine the most important factor what has influence on probability of breaking. We can say that this factor is quantity of energy what spaghetti has just before the impact with the surface. If we carry out experiments with the identical spaghettis, this quantity of energy depends only on the height of falling. We have run some experiments, so, you can see the experimental

dependence of frequency of breaking on height of falling (figure 2). So, the higher is the kinetic energy of spaghetti, the higher is possibility, that spaghetti bends very much and breaks.

But there are some other ways of changing kinetic energy: we can change mass of spaghetti by changing length of spaghettis, cutting them (certainly, not changing the diameter). You can see the experimental dependence of frequency of breaking on length of spaghetti (figure 3). We run this experiment keeping the

Figure 3: Frequency of breaking vs. length of spaghetti, height = 3,9 m

same height of falling. So, we change reaction force of surface by changing kinetic energy of spaghetti. But also we have the third way of changing kinetic energy of spaghetti. We can run 3 experiments with spaghettis with 3 different diameters and the same length. And what do we see on figure 4? Increasing kinetic energy by changing of spaghetti we do not increase frequency of breaking. But what is the reason of such a contradiction? Let's solve this ambiguity: we should notice that

when we increase diameter of spaghetti we increase not only mass. Increase diameter it becomes harder to bend spaghetti. It is just hard to believe that we need the same force to bend spaghettis with diameters of 1,45 and 2 mm. It goes without saying that there is some critical curvature for breaking for spaghetti of certain dimensions. Thus, changing of critical curvature is the most important cause of decreasing of frequency of breaking with increasing of diameter of spaghetti. Thus, there can be such a conclusion: it is easier to bend
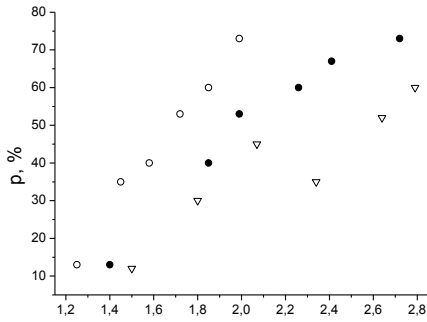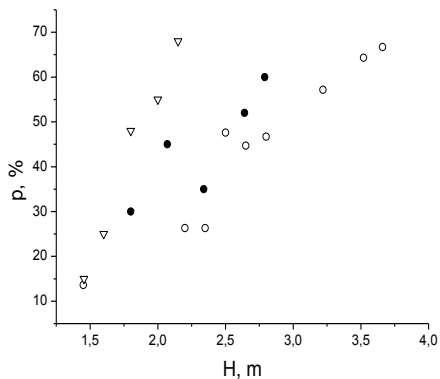
Figure 4: Frequency of breaking vs. height of falling: empty circles for d=1.4 mm, full – d=1.7 mm, triangles – d=2 mm

thin spaghettis than not thin one, that's why thinner spaghettis break with higher frequency falling from less height.

There are a lot of different interesting parameters what can have influence on frequency of breaking, but within the limits of IYPT report we cannot investigate all of them. Therefore, we must understand which parameters are the most relevant and which haven't so much physical meaning for us because of too much complicated mathematical formulation of certain parameter.

There are 3 the most relevant parameters: 1) height of falling,2) length of spaghetti, 3) diameter of spaghetti. These parameters influence kinetic energy of spaghetti to the utmost: All of these 3 parameters were investigated in my research.

Figure 5: Frequency of breaking vs. height of falling: empty circles for metal, full – granite, triangles – plastic

But there is one more parameter what I would like to investigate. It is nature of the surface. I run an experiment with 3 different surfaces (figure 5). It is rather surprising that frequency of breaking is higher when spaghetti hits plastic than granite or metal. It is really hard to explain it numerically because different surfaces have a lot of different properties. Nevertheless, during experiments I noticed that when spaghetti hits metal it jump up very high, when it hits granite – jumps up a bit lower, and when it hits plastic – spaghetti almost doesn't jump. Thus, I can make a conclusion that during the impact with metal great part of

kinetic energy lasts out and less quantity of energy spends on deformation. It is the simplest explanation of this surprising effect.

Conclusion

In summary, there is no exact answer of the question "find the conditions under which dry spaghetti falling on a hard floor does not break" because it is really hard to describe influence of all the parameters numerically. We can discuss only frequency of breaking in experimental research and quantity of energy required for breaking of ideal spaghetti in theoretical computation. (The energy needed to break a certain kind of spaghetti is the energy needed to curve spaghetti so much that it will be enough to tear its fibers. And this curvature will be the critical curvature.) But, summing up all the research, we can suppose that frequency of

breaking of an average spaghetti will be low if it falls from the low height (approximately lower than 1,5 m), has big diameter and has not very big length.

Influence of parameters

There is my summary of influence of parameters in this section:

1) Height: when height of falling increases, frequency of breaking also increases because velocity of spaghetti (consequently, it's kinetic energy) increases when height increases.

2) Length: when length of spaghetti increases, frequency of breaking also increases because mass of spaghetti (consequently, it's kinetic energy) increases when length increases, whereas diameter of spaghetti is the same (consequently, the energy required for breaking of spaghetti is also the same).

3) Diameter: when diameter of spaghetti increases, frequency of breaking also decreases because the energy required for breaking of spaghetti decreases.

4) Surface: when spaghetti hits plastic, frequency of breaking is higher than when spaghetti hits metal. The simplest explanation of it is that during the impact with metal great part of kinetic energy lasts out and less quantity of energy spends on deformation

References

[1] - N. F. Mott and E. H. Linfoot, Ministry of Supply Report No. AC3348 (1943), unpublished.
[2] - D. E. Grady and M. E. Kipp, Journal of Applied Physics 58, 1210 (1985).
[3] - R. Englman, J. Phys: Condens. Matter 3, 1019 (1991).
[4] - L. Oddershede, P. Dimon, and J. Bohr, Physical Review Letters 71, 3107 (1993).
[5] - E. S. C. Ching, S. L. Lui, and K.-Q. Xia, Physica A 287, 89 (2000).
[6] - J. R. Gladden, N. Z. Handzy, A. Belmonte, and E. Villermaux. Dynamic buckling and fragmentation in brittle rods. Phys. Rev. Lett. 94, 035503 (2005)
[7] - B. Audoly and S. Neukirch. Fragmentation of brittle rods: why spaghetti do not break in half. Phys. Rev. Lett. 95, 095505 (2005)
[8] - Ландау Л. Д., Лифшиц Е. М., Теория упругости, 3 изд., М., 1965 (Теоретич. физика, т. 7)

No. 4, Breaking spaghetti: Effect of material, impact velocity and orientation on the probability of fracture

Stanislav Krasulin [1]

[*] Team of Belarus, IYPT 2011

[1]*Belarusian State University, Belarus*

Corresponding author: s.krasulin@gmail.com (S. K.)

Introduction

This problem asks us about conditions, under which dry spaghetti falling on a hard floor will not break. Certainly, one of the main parameters of a strike is angle at which spaghetti hits the floor. There are three possibilities: spaghetti can fall prone, it can jump in the tin-soldier position, and also it can hit the floor at some angle between 0° and 90°.Because of the difficulty of the task and both size of the report and time for it's preparation being limited, we had focused our research on just one case: when spaghetti falls vertically (tin-soldier position).
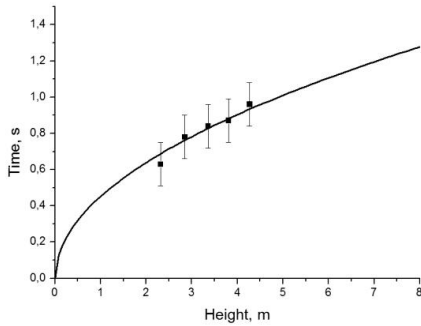
Figure 1. Time of falling depending on height. Line is theory, without taking drag into account; dots are experimental

Air drag influence

Another very important parameter is velocity spaghetti has right before the strike. However, velocity isn't very graphic value; everything is easier to understand if use height of fall instead. But vacuum is rather uncommon environment for spaghetti; so before connecting these two parameters, it is necessary to check if air drag should be taken into account:

$$F = \frac{1}{2} C_d \rho \upsilon^2 S;$$

where S isreference area (for long cylinder it is it's basement area), v isvelocity, ρis air density,C_d is drag coefficient (for long cylinder it is 0,82). Fortunately, it turned out that in our range of heights drag influenceis negligibly small (see fig.1).At the same time, this equation helped us to calculate the maximal velocity spaghetti can achieve falling in the Earth's
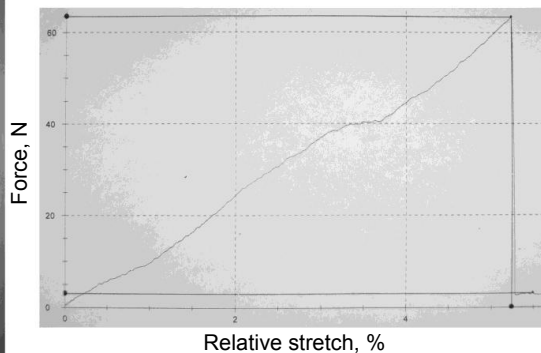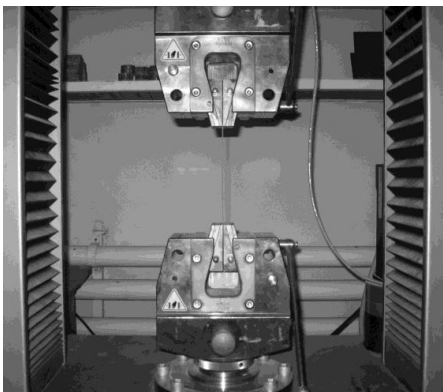
Figure 2. Spaghetti, mounted into Zwick Z100 tensile-testing machine and an example of it's output for *"pastaZARA"* spaghetti (horizontal axis is relative stretch, %; vertical is force, N)

atmosphere: about 60 m/s (for tin-soldier position). This is rather big value; at least big enough for us not to be able to achieve it in the lab. However, if spaghetti falls horizontally (prone) the maximal velocity is significantly lower(due to a bigger drag coefficient and reference area); it turns out to be 5.6 m/s. Experiments have shown that it is easy to throw spaghetti at even bigger velocity; but no spaghetti were broken during such an experiment: if spaghetti hits the floor prone, this velocity just isn't enough. That is why we can state, that if falling prone, spaghetti just can't achieve velocity required for breaking, due to air drag.

Spaghettis' mechanical properties

The research of deformation and possible destruction of an object requires knowing some mechanical properties of it's material, like Young's modulus and critical relative deformation. For obtaining these data we used Zwick Z100 tensile-testing machine (see fig.2). Output data can be seen in the Table 1.

Table 1. Results of testing of different spaghettis

Name	Diameter d, mm	Young's modulus E, GPa	Critical relative stretch ε_{crit}, %	Critical stress σ_{crit}, MPa
"pastaZARA" 1	1.45±0.03	0.59±0.02	5.25±0.05	31.0±0.5
"pastaZARA" 3	1.65±0.03	0.59±0.02	5.25±0.05	31.0±0.5
"pastaZARA" 5	2.05±0.05	0.59±0.02	5.25±0.05	31.0±0.5
"Monte Banato"	1.40±0.02	0.63±0.01	4.71±0.03	29.7±0.2
"Makfa"	1.40±0.03	0.92±0.05	2.63±0.06	24.2±0.4
"Borimak" 1	1.40±0.05	1.36±0.08	1.12±0.07	16.3±0.5
"Borimak" 2	1.70±0.05	1.36±0.08	1.12±0.07	16.3±0.5
"Borimak" 3	2.00±0.05	1.36±0.08	1.12±0.07	16.3±0.5

However, it is hard to believe that whole spaghetti during strike is stretched or compressed like in this machine; it is more likely to break because of curving. Certainly, it's also a combination of these deformations – some layers of spaghetti are stretched, some are compressed. And some are not deformed at all. Let's assume that the very central part of spaghetti isn't stretched whenever spaghetti is curved[1] and has length L_0. Then, if radius of curvature is R and diameter of spaghetti is d, relative stretch (ratio between absolute elongation and original length) of it'souter layer L_1can be easily calculated:

$$\varepsilon = \frac{L_1 - L_0}{L_0} \cdot 100\% = \frac{2\pi(R+d) - 2\pi(R+\frac{1}{2}d)}{2\pi(R+\frac{1}{2}d)} \cdot 100\% = \frac{d}{2R+d} \cdot 100\%$$

For spaghetti not to break, this value should be smaller than ε_{crit}; thereby, maximal radius of curvature:

$$R_{max} = \frac{100\% - \varepsilon_{crit}}{2\varepsilon_{crit}} \cdot d$$

Checking this dependence is rather complicated because we can't change values ε_{crit} and d.
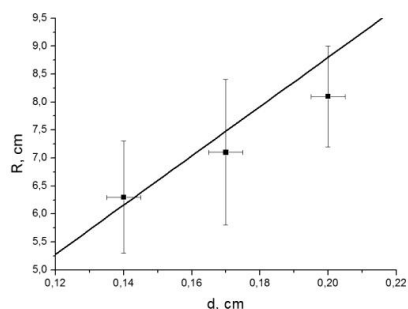
Figure 3. Critical radius of curvature vs. diameter of spaghetti (*"Borimak"*): points are experimental, line is theoretical

However, some manufacturers (*"pastaZARA"*, *"Borimak"*) do produce spaghettis of the different diameters, but same recipe. Unfortunately, number of such diameters is still strongly limited; that is why fig.3 has only three experimental points. We were curving spaghettis around a number of cylinders, which radiuses differed by 0.5 cm. Vertical error bars on the fig.3 depict the range of radiuses for which less than 100% but more than 0% of spaghettis broke. The point is set in the middle of the range.Within accuracy of our measurements even this very simple mathematical model gives results, close to real. It means, that there's no need in it's improvement: anyway we can't detect that it has come closer to the real value.
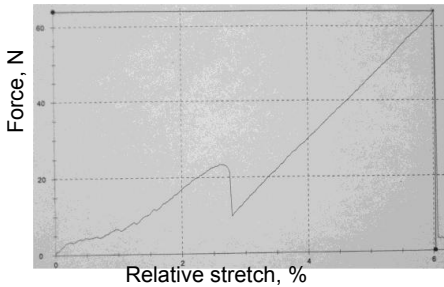
Figure 4. Another test of *"pastaZARA"* spaghetti. A random jump in the dependence significantly increases critical stretch

Stochasticity of the phenomenon

Also, it should be mentioned that not all experiments with tensile-testing machine were successful (fig.4). There you can see that at some point inner parts of spaghetti had moved relatively to each other; however, spaghetti hadn't fractured. Such results were marked as "mistake" and weren't included in the values given in the table. But same things can occur in the experiments with falling spaghetti, thus allowing it not to break under conditions it normally should. That is why we can't just set a range for each parameter, within which spaghetti will break; there will be only some certain frequency of breaking for each set of parameters. We defined the frequency of breaking as the ratio N/N_0, where N_0 is total number of spaghettis dropped, and N is number of spaghettis that were broken. Therefore, in our work we were researching this frequency of breaking depending on different parameters.

Gravity force

During discussions of this task there was often raised question about influence of gravity force during the impact.When spaghetti hits the floor it is reflected upwards, or, at least, stopped. It means that it's momentum changes at least by $m*v$, where m is spaghetti's mass. Through filming strike on a high-speed camera, it was found out, that it lasts less than $t=0.001$ of a
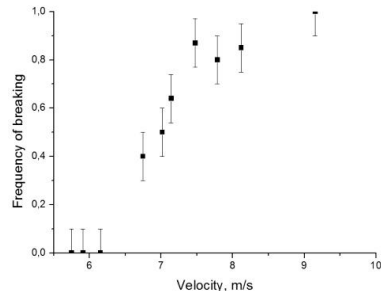
Figure 5. Frequency of breaking vs. velocity (*"Borimak" 1*)

second. Therefore, average force acting on the spaghetti during strike is:

$$F_s = \frac{m\upsilon}{t} \approx 5.67 \cdot 10^{-1}\ N$$

At the same time gravity force acting on this spaghetti is about $4.5*10^{-4}$ N – thousand times smaller. So, gravity force is negligible during strike.
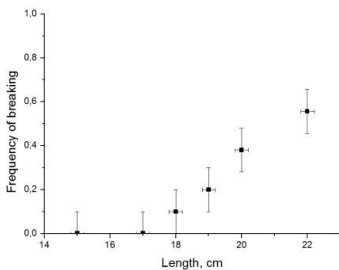
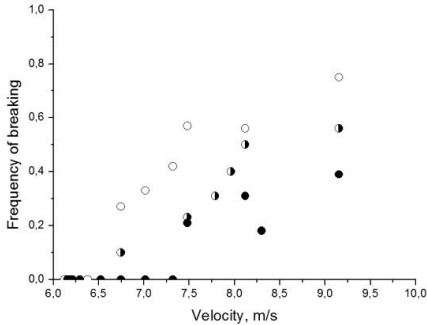**Figure 6.**Frequency of breaking depending on spaghettis' length for velocity 8 m/s (*"pastaZARA" 3*)

Different parameters

It was already mentioned; that one of the main parameters is velocity.Fig.5 shows dependence of frequency of breaking on the velocity spaghetti has right before the strike. There are velocities, for which this frequency is zero; but as velocity gets higher, frequency increases too. It is easy to explain: spaghetti breaks, if it reaches critical curvature; but this bending requires energy. So, the higher is the kinetic energy of spaghetti, the higher is possibility, that critical curvature will be reached.

But changing velocity isn't the only way of changing kinetic energy; mass of spaghetti also can be varied; for example, through varying it's length.Fig.6 shows that increase in length (and, respectively, mass) causes increase in frequency of breaking –additional kinetic energy gives higher possibility of reaching critical radius of curvature.
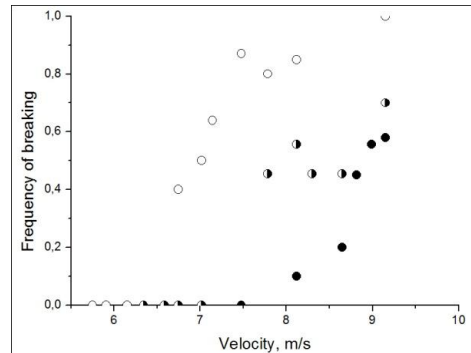
Figure 7. Empty circles are for d=1.45 mm, half-full – d=1.65 mm, full – d=2.05 mm. Average error of frequency is 0.12. (*"pastaZARA"*)

Changing of diameter also will cause changing of kinetic energy.However, fig.7 (dependence of frequency of breaking on velocity for different diameters) shows that here additional kinetic energy does not increase frequency: because of bigger diameter, it requires more energy to deform spaghetti to it's critical curvature (even though the critical curvature itself decreases). The plot shows that this increase in required energy overcomes gain in kinetic energy.

It is also interesting that there is a correlation between spaghettis' price and frequency of breaking: in general, cheaper spaghettis are easier to break (fig.8). It can be explained by differences in the chemical structure: expensive spaghettis (*"Monte Banato"*) have eggs as their ingredient. And in this situation eggs work as some kind of glue, increasing spaghettis' critical relative stretch, therefore increasing energy, required for breaking.

Figure 8. Empty circles are for cheap spaghettis (*"Borimak" 1*), half-full are for medium priced (*"Makfa"*), full are for expensive (*"Monte Banato"*). Average error of frequency is 0.11

Also, it should be noticed, that all such comparative experiments should be run within one day; otherwise there will be mistakes, because of the changes in the humidity of air; and humidity of air affects that of spaghettis. Water increases elastic properties of spaghettis and decreases their fragility. This is shown on the fig.9, where usual spaghettis are compared to the very dry ones.

Figure 9. Squares are for usual spaghettis, circles are for Spaghetti Extra Dry.Average error of frequency is 0.07. (*"pastaZARA" 5*)

Point of breaking

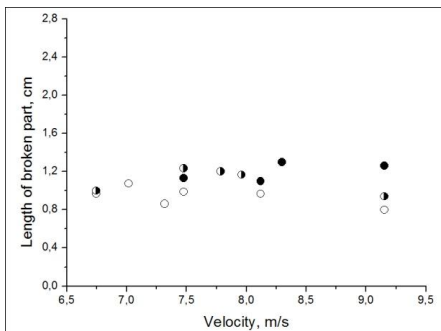During experiments we have noticed that spaghetti always breaks in the point, close to the hitting end.After we had measured lengths of broken parts in experiments with *"pastaZARA"* spaghettis, it turned out that spaghettis were breaking in the point approximately 1 cm away from the hitting end; and it hadn't depended on the length (fig.10) or diameter (fig.11) of spaghetti. We decided that probably something in the way spaghettis are produced causes this point to be the weakest; however, when we had cutoff 1 cm long parts from both ends of spaghetti and then dropped it, once again length of broken part was 1 cm, proving that something in the process of breaking defines the point, not in the spaghetti initial structure.That led us to a conclusion that spaghetti breaks because of standing wave.
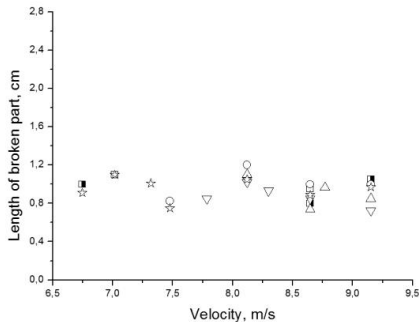
Figure 10. Length of broken part depending on velocity for different original length: empty square – 15 cm, half-full square – 17 cm, upwards triangle – 18 cm, circle – 19 cm, downwards triangle – 20 cm, star – 22 cm.Average error of length is 0.20 cm. (*"pastaZARA"* 3)

Standing wave

When spaghetti hits the floor a bending wave occurs. And if the wave reaches opposite end of spaghetti it is being reflected and summed with itself, producing standing bending wave. Now, spaghetti should break in the point of first antinode[2] (since second one will be smaller due to losses). And we know, that hitting end of spaghetti is the place of first node. So, distance between the end of spaghetti and breaking point should be a quarter of wavelength; therefore, wavelength λ=4*x, where x=1cm was found experimentally. At the same time,spreading rate of the wave can't be higherthan spreading rate of the sound wave, travelling in spaghetti:

$$c = \sqrt{\frac{E}{\rho}} = 0.87 \; km\!\!\Big/\!\!s \; ;$$

Figure 11. Length of broken part vs. velocity. Circles show same diameters, as on fig.7.Average error of length is 0.18 cm. (*"pastaZARA"*)

where ρ is spaghetti's density. Thereby, frequency of the bending wave is less than:

$$\nu_{max} = \frac{c}{\lambda} = 21.75 \, kHz$$

At the same time, we can say that whole strike lasts for a half of the bending wave's period: this time is enough for spaghetti to bend to it's maximal curvature and return into it's initial shape, thus forcing it to jump upwards. And it has already been found through experiments that impact lasts for less than 0.001 s. So, period of wave is less than 0.002 s; and frequency of bending wave is higher than ν_{min}=0.5 kHz.

Different angles

Talking about possibility of spaghetti to fall on the floor at some angle between 0° and 90°, we can say that there are two different cases: the hitting end of spaghetti may remain fixed during the impact (it generally happens if spaghetti falls in position close to vertical, or if hitting end gets stuck because of some small obstacles on the surface of the floor); also it can slide to the side. The first situation is very close to the one described in our solution; it's highly possible that all is need is to take into account that smaller part of original kinetic energy of spaghetti is transferred into energy of bending wave.

The second case is more complicated;first bending caused by friction force and normal reaction force occurs, and then a bending wave starts. Spaghetti can be broken both by just bending and by bending wave.

We have run an experiment to compare frequency of breaking in two situations. To resemble the second case we were dropping spaghetti on the sheet of acrylic resin. To resemble the first case we were dropping spaghetti on the sheet of the same acrylic resin, but with a number of scratches put with intervals of 1 cm; hitting end of spaghetti was caught on this scratches and, therefore, remained fixed during the strike.

Experiment has proven that frequency of breaking is higher if hitting end is fixed.

Conclusions

If spaghetti falls prone in Earth's atmosphere it can't reach velocity required for breaking.If spaghetti falls in tin-soldier position, it will be broken in the first antinode of standing wave, which is situated 1 cm away from hitting end. Frequency of this wave is between 0.5 kHz and 21.75 kHz. But breaking will occur only if spaghetti's kinetic energy is higher, than energy required to bend spaghetti to it's critical curvature. So, for spaghetti not to break, kinetic energy should be decreased; for example by decreasing velocity or mass (by decreasing length). However, if mass is decreased through changing diameter required energy decreases either. Other way of changing energy, required for breaking is changing chemical structure: adding water or eggs increases critical relative stretch, thereby requiring more energy for spaghetti to break.

However, in all this situations we can discuss only energy, required for breaking of ideal spaghetti. In real life, we can say only about increasing in breaking frequency, when close to described values.

References

[1] D. Sivuhin, "General Course of Physics", vol.1 "Mechanics", MIPT publishing, 2005;
[2] J.R. Gladden, N.Z. Handzy, A. Belmonte, E. Villermaux, "Dynamic Buckling and Fragmentation in Brittle Rods", Physical Review Letters**94**, 2005.

No. 4, Breaking spaghetti: Analysis and measurement of fracture as a function of impact velocities and angles

Hamid Ghaednia[1] and Hossein Azizinaghsh[2]
[*] Team of Iran, IYPT 2011
[1]*Amirkabir University of Technology, Iran*
[2]*Sharif University of Technology, Iran*
Corresponding authors: ghaednia.hamid@gmail.com, hossein.azizi@gmail.com

Abstract

Simulating the fracture of brittle materials with hard surfaces due to the collision of brittle materials with hard surfaces can be effective in different engineering applications. Investigating the deformation of a brittle rod in collision with a rigid body can be done using various algorithms. In this article we present a new simple algorithm using numerical methods to find and the fracture criterion of the collision in brittle material. Spaghettis a brittle material shows a great deformation in respond to collision is used in our experimental setups. The contact of the spaghetti with rigid surface causes stresses to propagate along the spaghetti and hence the spaghetti deforms. Three different kinds of stresses have been considered, shearing stress, pressure (normal stresses) and tension caused by bending. By studying these stresses and considering the effect of them all together, the fracture criterion of brittle materials in collision with rigid surfaces has been investigated.

Introduction

The collision contact time when a brittle material hits a rigid surface is small (near .005 s), therefore the velocity of stress propagation caused by collision cannot be considered as infinite. Thus when the collision starts, there is concentration of stresses in the region near the collision point. However, the other regions of the spaghetti have not been affected by the collision yet because of low velocity of stress propagation.

The collision results into three kinds of stresses: shear stress, pressure and tension in some regions of spaghetti, which is caused by bending. Although, for each of these stresses there is a critical point in certain distances from the contact point, these three stresses should be considered all together in order to find the fracture point.

We divided the spaghetti in several elements using numerical method to find the deformation and stress distribution along the length of the spaghetti during collision then by defining a fracture unit, which finds the effect of all stresses together, the fracture point can be found.

The problem can be broken down into four parts, first the deformation of the first element will be found, second by having this deformation, the forces applied to the next element of the spaghetti can be found, third by having the stress distribution and using the fracture unit, the break point will be found and finally the angle of the crack in the breaking cross section of the spaghetti will be define in order to satisfy theoretical considerations.

Several experiments have been designed in order to find mechanical properties of spaghetti. The conditions, under which the spaghetti breaks, are also investigated experimentally.

Finally, we will discuss the reason and nature of fracture in different angles of

contact and evaluate the theory by investigating the angle of crack.

Theory

Theoretical analysis of the problem is based upon some assumptions:
- Ground is rigid, which means that we have not considered any deformation for surface.
- Spaghetti is a brittle material, which will be proved in further experiments
- The velocity of stress propagation is constant[7]
- Spaghetti is homogenous and uniform

We consider the length of the elements as formula bellow, thus each element will be one step underdeveloped from the last element.

$$l_{Element} = v_{propagation} \times dt \tag{1}$$

$$v_{propagation} = \sqrt{\frac{E}{\rho}} \tag{2}$$

Where E is modulus of elasticity and ρ is the density of material in use.

Deformation of the first element

Because the surface was assumed as rigid the contact point remains on its first position but the other end of the element will continue to fall (Fig.1), this will result in deformation of the first element (Formula.3)[8].Using this deformation the force applied to the first element can be found(Fig.2).
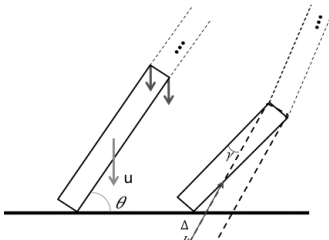
Figure 1: deformation of the first element
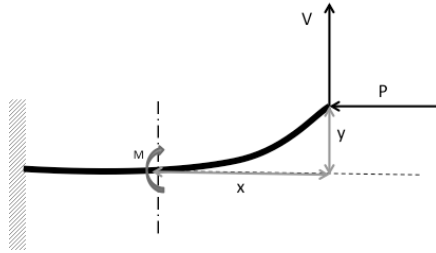
Figure 2: deformation of the first element

$$M = Px + Vy, \quad \frac{M}{EI} = \frac{y''}{(1+y'^2)^{3/2}}$$

$$y = \frac{LV}{P}\sin(\frac{P}{EI}x) + \frac{V}{P}x \tag{3}$$

Stress distribution

In the first time step, the deformation and thus the forces applied to the first element can be found. Second element has not noticed the collision yet. In the second time step the deformation of the first element is developed again and the second element notices the forces resulted from the deformations of the first time step. By continuing this process until the spaghetti is stopped or broken, stress distribution during collision on the length of the spaghetti can be found.

Fracture unit

A fracture unit has to be defined in order to merge the effect of different stresses together and predict the break point:[8]

$$F = (\frac{\sigma}{\sigma_u})^2 + (\frac{\tau}{\tau_u})^2 < 1 \tag{4}$$

Where σ_u is the ultimate normal stress, τ_u is the ultimate shear stress, σ is the normal stress applied to the cross section and τ is the shear stress applied to the cross section. When the fracture unit is higher than one the section will break.

Crack investigation

Finding the angle of crack helps us to find out whether or not the prediction about amount of shear and normal stresses was correct. Formula 5 presents the angle of crack based on the amount of shear and normal stress in a cross section [8]:

$$\tan(2\theta) = \frac{\tau}{\sigma} \tag{5}$$

Experiments

We designed some experiments to find mechanical properties of the spaghetti such as modulus of elasticity, ultimate shear stress and ultimate normal stress, and in the next part the fracture criterion has been found which will be discussed in the following section.

Measuring coefficients

a) Modulus of Elasticity
A force is applied at the end of the spaghetti, while the other end is fixed. Δ was measured while the force was applied (Fig. 3). By using the following equation [8], modulus of elasticity was measured (Fig. 5).

$$\Delta = \frac{PL^3}{3EI} \tag{6}$$

$$E = 4.57 \times 10^9 \, {N}/{m^2}$$

Figure3: Δ was measured while increasing the force applied to the end of the spaghetti
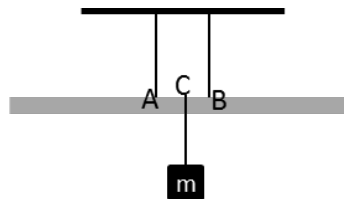
Figure 4: The force was applied between two fixed points and ultimate shear load was measured

b) Maximum tension stress
Force is applied to one spaghettis end while other end is fixed (Fig. 3), by finding the spaghetti failure load for different length, the ultimate tension can be found using bellow equation [8](Fig.6).

$$p = \frac{\sigma I}{LR} \tag{7}$$

$$\sigma_u = 2.9 \pm 0.1 \times 10^8 \, {}^N/_{m^2}$$

Figure 5: modulus of elasticity
This diagram also proves that spaghetti is a brittle material.
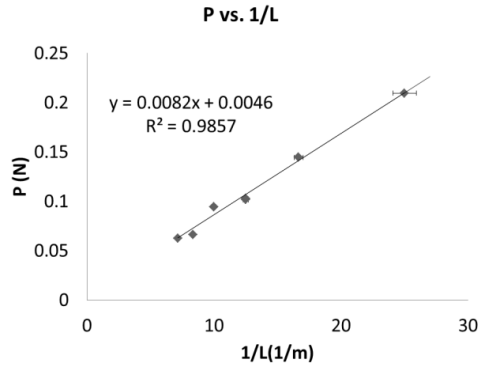
Figure 6: ultimate tension stress

c) Maximum shearing stress
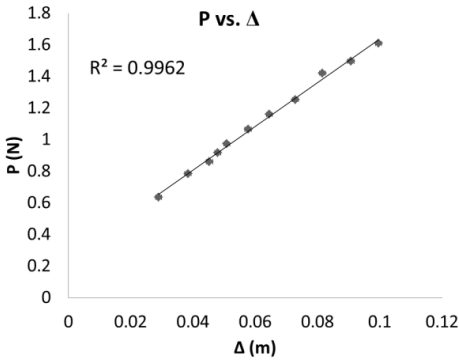The amount of shear stress under which the spaghetti will break was measured. Spaghetti is fixed at points A and B, the force is applied at point C, between A and B, (Fig. 4) when AB is small enough, bending can be neglected and shear stress will break the spaghetti.

Experiments analysis

A high speed camera (1000 frame/sec) was used to capture the collision of spaghettis. By processing the videos the velocity of spaghettis at the time of contact and the angle of contact were found. The fracture criterion of collision was predicted based on the measured coefficients. Diagram bellow is consisted of more than 600 points resulted from the experiments and the fracture criterion, which is resulted from the theory (Fig.7).
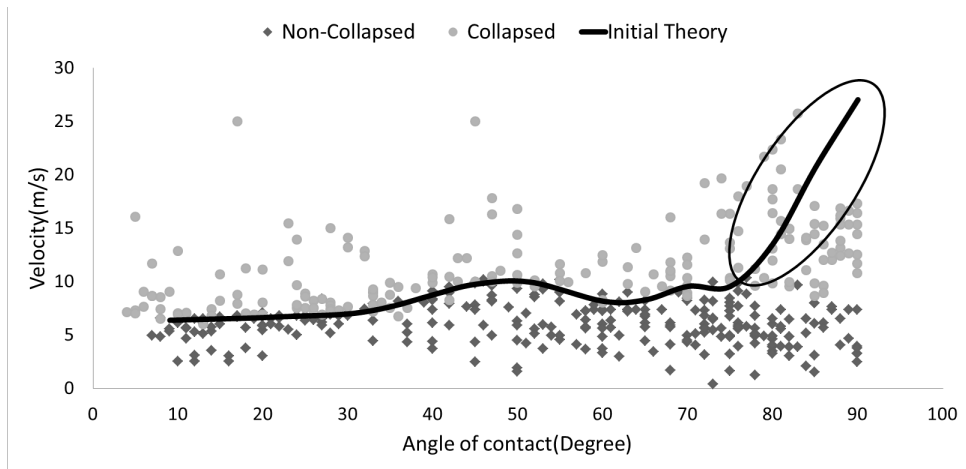
Figure 7: fracture criterion (initial theory)

It can be seen in (Fig.7) that there is no good agreement between theory and experimental results, thus the theory must be revised.
Considering the effect of buckling in angles near 90 degrees, the new result is as Fig.8.
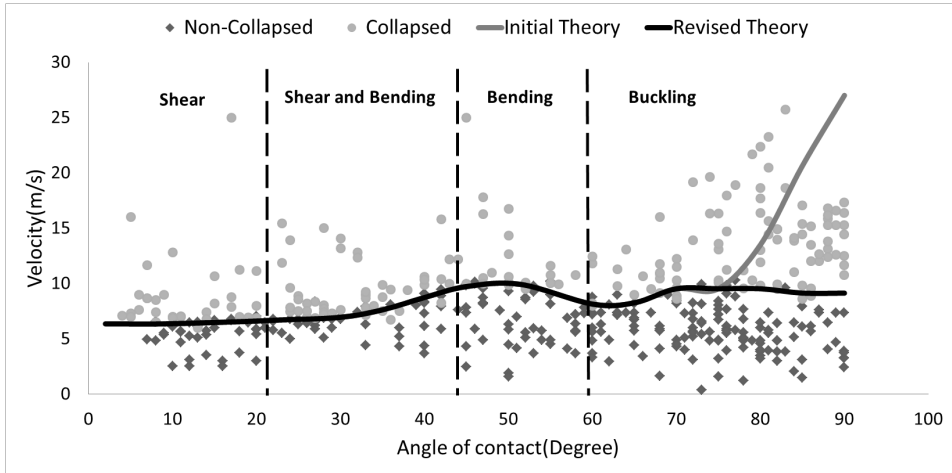
Figure 8: fracture criterion (revised theory)

Shear region

Based on the theoretical model, in this region ($0 < \theta < 20$), shear stress is the only type of effective stress. Thus based on formula 5, the angle of crack must be near 45 degree. This prediction is verified experimentally, for $\theta = 20$ amount of effect of stresses predicted by the theory are as bellow, and the angle of crack is as shown (Fig.9)
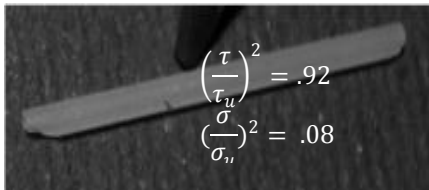
Figure 9: angle of crack when $\theta = 20$
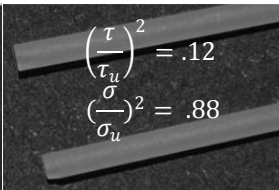
Figure 10: the angle of crack when $\theta = 60$
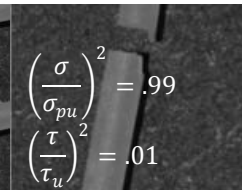
Figure 11: the angle of crack when $\theta = 85$

Bending region

By doing same process done for shear region:
For $\theta = 60$ amount of effect of stresses are as mentioned above, and the angle of crack is as shown (Fig.10)

Buckling region

In buckling region the reason of fracture is normal stress thus based on formula 5 the angle of crack must be near zero, for example:

For $\theta = 85$ amount of stresses effect are as mentioned above and the angle of crack is as shown (Fig.11).

References

[1] Audoly B and Neukirch S (2004). Fragmentation of rods by cascading cracks:
Why spaghetti does not break in half. Physical Review Letters, 95 (No. 9), 95505
    (Dec 22) (http://www.lmm.jussieu.fr/spaghetti/index.html)
[Their website also contains several videos of spaghetti breaking]
[2] Belmonte A (2005). How spaghetti breaks.
      http://www.math.psu.edu/belmonte/spaghetti.html
      http://www.math.psu.edu/belmonte/PaperFile/PRL_pasta.pdf
[3]D'Andrea C and Gomez E (2006). The broken spaghetti noodle. American
Mathematical Monthly, June-July.
      http://www.maa.org/pubs/monthly_jun_jul06_toc.html
[4] Feynman R. See video of Feynman breaking spaghetti at
http://heelspurs.com/feynman.html
[5]Nickalls O.J. and Nickalls R.W.D. (1995).
Linear spaghetti. New Scientist, 145, 18th February, p. 52. [Letter]
http://www.science-frontiers.com/sf099/sf099p15.htm
[6] Nickalls O.J. and Nickalls R.W.D. (1998).
Pasta puzzle: Why does spaghetti break into three pieces?
In: THE LAST WORD, New Scientist, 160, 12th December, p. 101.
[7] K.SankaraRao 2007,3[rd]ed, Numerical methods for scientists and engineers, Prentice hall of India
[8] Ferdinand P.Beer, E.Russel Johnson, Jr., Jhn T. DeWolf, 4[th]ed, Mechanics of materials, ISBN 0-07-298090-7

No. 4, Breaking spaghetti: A theoretical insight into the probability of fracture

Matej Večerík, [1] Tomáš Kulich, [2] and Michal Hledík [3]
[*] Team of Slovakia, IYPT 2011 and Team of Slovakia, AYPT 2011
[1] *School for Exceptionally Gifted Children and Grammar School, Bratislava, Slovakia*
[2] *Comenius University, Slovakia*
[3] *Gymnázium Juraja Hronca, Bratislava, Slovakia*
Corresponding author: matejvecerik@gmail.com (M. V.)

Problem

Find the conditions under which dry spaghetti falling on a hard floor does not break.

Introduction

So far a lot of research has been done in this area, considering mostly the bending waves and their interference. The accepted solution is that spaghetti is more probable to break in a point where these bending waves constructively interfere because stresses constructively interfere as well. These waves are well described by so-called Kirchhoff's equation. However, solving similar tasks analytically is quite hard and as far as we know, it is possible only for very specific scenarios [1]. In the given problem we encounter several difficulties such as non-trivial boundary conditions and wave reflections.

Therefore, for the given problem, we have written a computer simulation. It basically simulates Kirchhoff's equation by midpoint method [2] on discrete 20 points. Furthermore, for obtaining more precise results, we include term that describes two different kinds of friction.

Theoretical model:

We used numerical model, that is motivated by Kirchhoff's equation for our simulation and we introduced new terms into our motion equations due to damping. We therefore assume following forces applied at each element: bending stiffness for a thin rod with nonuniform, non-zero equilibrium bending, bending damping, longitudinal stiffness, normal force from the surface, and friction force from the surface. Since spaghetti cannot be considered as a straight thin rod because of irregularities we considered the equilibrium bending of each point of the spaghetti to be non-zero.

$$\mathbf{F_i} = k_l \hat{\mathbf{d}}_i (x_0 - |\mathbf{d_i}|)$$

Longitudinal spring force:

Where $\mathbf{d}_i$ is the vector between i-th and $i+1$-th part of the spaghetti, x_0 is the equilibrium distance between two points and k_l is longitudinal spring constant.

Bending spring force:

We assumed that for a large curvature radius the torque restoring the equilibrium bending is proportional to the difference between equilibrium bending and current bending. As $sin\ x = x$ for small x, we set the force to be proportional to the difference between equilibrium bending and sine of current bending:

$$|\mathbf{F_i}| = k_b (\hat{\mathbf{d}}_i \times \hat{\mathbf{d}}_{i+1} - b_i)$$

$$\hat{\mathbf{F}}_i = k_b (-\hat{\mathbf{d}}_{i+1} \times (\hat{\mathbf{d}}_{i+1} \times \hat{\mathbf{d}}_{i+2} - \hat{\mathbf{b}}_{i+1}) + \hat{\mathbf{d}}_{i+1} \times (\hat{\mathbf{d}}_i \times \hat{\mathbf{d}}_{i+1} - \hat{\mathbf{b}}_i) \\ + \hat{\mathbf{d}}_i \times (\hat{\mathbf{d}}_i \times \hat{\mathbf{d}}_{i+1} - \hat{\mathbf{b}}_i) - \hat{\mathbf{d}}_i \times (\hat{\mathbf{d}}_{i-1} \times \hat{\mathbf{d}}_i - \hat{\mathbf{b}}_{i-1}))$$

Where k_b is bending stiffness constant for our spaghetti and b_i is the equilibrium bend. This force is created by every triple of subsequent points and their relative bend. From it we can derive the total force exerted on single point:
Bending damping force:

$$\hat{\mathbf{F}}_i = k_d \frac{d}{dt}(-\hat{\mathbf{d}}_{i+1} \times (\hat{\mathbf{d}}_{i+1} \times \hat{\mathbf{d}}_{i+2} - \hat{\mathbf{b}}_{i+1}) + \hat{\mathbf{d}}_{i+1} \times (\hat{\mathbf{d}}_i \times \hat{\mathbf{d}}_{i+1} - \hat{\mathbf{b}}_i)$$
$$+ \hat{\mathbf{d}}_i \times (\hat{\mathbf{d}}_i \times \hat{\mathbf{d}}_{i+1} - \hat{\mathbf{b}}_i) - \hat{\mathbf{d}}_i \times (\hat{\mathbf{d}}_{i-1} \times \hat{\mathbf{d}}_i - \hat{\mathbf{b}}_{i-1}))$$

where k_d is bending damping constant for our spaghetti.
Last thing in our numerical model was friction from surface which acts as a horizontal force on points touching the surface and trying to move. This force is proportional to normal force and coefficient of friction. This constitutes a complete numerical model which we simulated.

Parameters for theory

Longitudinal spring force constant was estimated from Young's modulus of elasticity. Given the equation for simple harmonic motion we wanted to get the same result from our simulation and theory:

$$\ddot{x} = -x k_l = -\frac{x}{L_{piece}} \cdot \frac{E\pi r^2}{m_{piece}}$$
$$k_l = \frac{Es}{L_{piece} m_{piece}} = \frac{E\pi r^2 n^2}{L_{whole} m_{whole}}$$

where E is Young's modulus of elasticity, L is length of spaghetti, m is mass of spaghetti, s is cross section of spaghetti, r is radius of spaghetti and n is number of points in the model (20 in our case).
We have found out that if this parameter is correct in its order, then no higher precision is necessary as changing this constant by a factor of 10 in either direction way has almost no influence on final results.
Bending stiffness was chosen so that after holding the spaghetti horizontally on one end, the ratio of the relative vertical displacement to the spaghetti length was the same. For our spaghetti the relative vertical displacement to length was approximately 0.06.
Bending damping was measured from video using our own video analyzing software. We took a video of a few periods of the spaghetti such that one end was attached to table while the other one was displaced and let to oscillate. Then we chose the damping parameter such that the ratios of amplitudes of periods would be the same in simulation and experiment.
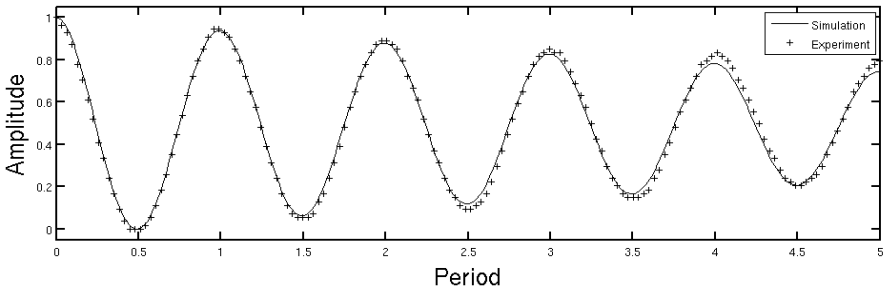
Figure 1: Fitting the bending damping value of spaghetti

Experiment

To prove that our simulation is correct we decided to predict a dependency of probability of spaghetti breaking on angle under which it hits the floor and calculate from our theory the minimal curvature radius during the bending.
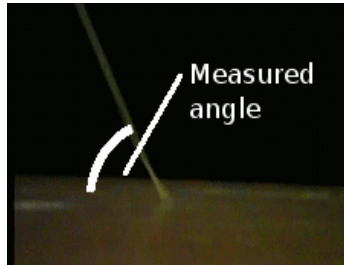

We cannot predict probability from computer model as this probability is dependent on inner spaghetti structure which is not known. We also cannot measure the minimal curvature radius from experiment as this would require very precise and accurate measurement of spaghetti shape during the whole process which is impossible in our conditions. This is not a big shortcoming though as there proved to be a strong correlation between minimal curvature radius and breaking probability. This proves our simulation to be valid.

In our experiment we let spaghetti fall from the height of 2m at a random angle and we were taking a video of the hitting process. We then determined the angle under which it hit the floor from the video by measuring the vertical length of spaghetti and comparing it to the known length of spaghetti. From this we could get the angle as *arcos* of this ratio.
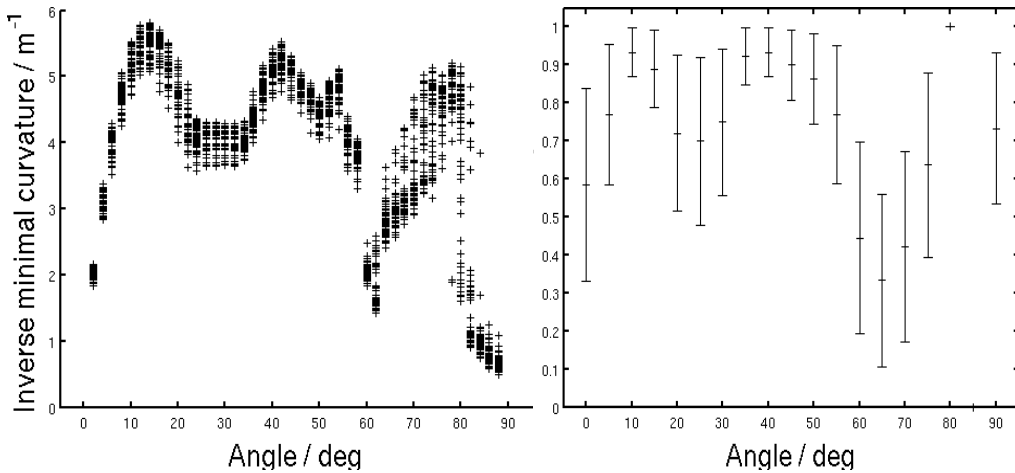
Figure 2: Comparison of simulated inverse minimal curvature(left) which for every simulated angle generated 50 different sets of equilibrium bending of spaghetti and experiment(right) in which we let spaghetti fall and then recorded the angle of hit and whether it broke

Conclusion

We can see that the shape of these dependencies is very similar, so our assumption about their strong correlation proved to be true. We can see a disagreement for very high and low

angles. For very low angles our theoretical model is that spaghetti hits the floor and lays still. We suspect though that thickness of spaghetti is not negligible in this case for real spaghetti, since the speed is perpendicular to length. On the other hand, for very high angles where we can see that a very small piece of spaghetti (usually about 2-5mm) is ejected with relatively high velocity and angular velocity in the experiment. This cannot be explained by our theoretical model as this phenomenon is strongly caused by longitudinal compression which does not appear in our chart.

For better understanding of the phenomenon we introduce the following chart where we again show the dependency of inverse minimal curvature, but this time dependent on both the angle of hitting the floor and the impact velocity:
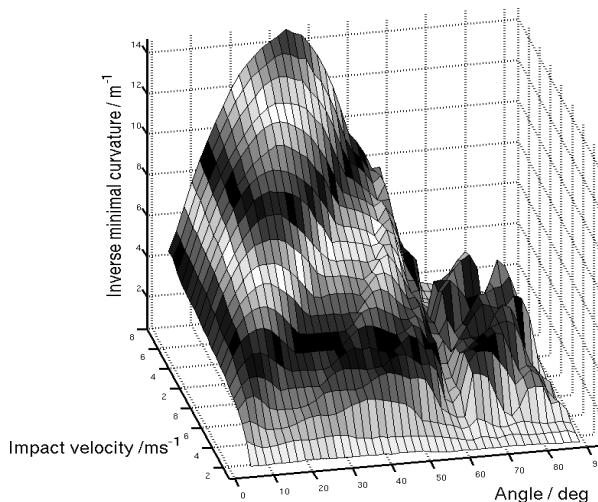
Figure 3: Simulation output for the dependency of inverse minimal curvature on impact velocity and angle of hit. Each value is an average of 5 different sets of equilibrium bending. We can see that for higher velocities we get higher Inverse minimal curvatures – higher probabilities of spaghetti break. There is also a node at approximately 60° which is caused by slipping of spaghetti

This chart has three interesting regions. One is from 0° to 60° and it represents almost horizontally falling spaghetti. The relative error here is small and can be well described. In these cases spaghetti hits the floor, slips and then there is a bending wave coming across the spaghetti as the spaghetti is sticking to the floor. This bending wave causes maximal bending to appear at the end of spaghetti. We can see a node at approximately 60°, which is the critical angle for slipping in our system. If spaghetti hits the floor at this angle, it slips, but most of its energy is dissipated in this process. Therefore only a small part of its energy is left to cause bending. Processes where the angle of hit is higher than 60° are very chaotic as we can see from the figure. Spaghetti tends to bounce from its ends even several times before resting on ground.

From this we can conclude our solution to this task which is that spaghetti is least likely to break when its hitting angle is close to the critical slipping angle.

References

1) B. Audoly, S. Neukirch, Phys. Rev. Lett. 2005, 95, 095 505.
2) W. H. Press, S. A. Teukolsky, W. T. Vetterling, and B. P. Flannery, Numerical Recipes (Cambridge University Press, Cambridge, 1992).

No. 5, Car: Effect of nozzles, wheels, and balloon elastic properties on the range of a balloon powered car

Stanislav Krasulin [1]
* Team of Belarus, IYPT 2011
[1]*Belarusian State University, Belarus*
Corresponding author: s.krasulin@gmail.com (S. K.)

Introduction

In this task we were asked to "build model car powered by an engine, using an elastic air-filled toy-balloon as the energy source". Then two main questions were raised: dependences of distance, travelled by such a car, on relevant parameters and maximizing efficiency of the car.

Obviously, we had to start from the first part of the task, building a model car. Since we had to increase distance travelled by car, we tried to reduce all friction forces; respectively, model had also to be as light as possible.

The balloon we had chosen for the car was a spherical rubber balloon, capable of stretching up to the volume of 40 liters. Spherical shape had been chosen because it made all calculations easier, and had no drawbacks compared to other shapes (it will be proven later in the article, that air drag is negligibly small).

Another major part of the car was engine; the very first idea was just to attach a nozzle to a balloon, creating a rocket-type car. We had also tried several concepts for using air stream to produce a rotational motion of the car's wheels. However, high number of moving partscaused additional losses of energy on friction, making all those prototypes ineffective, compared to a simple propulsion engine.

Figure 1. Scheme of the car.
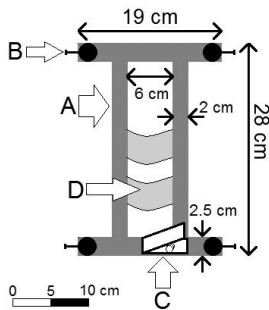
Car

Fig.1 shows our final version of the car. Its body (A) was cut out of sheet of balsa (6 mm thick). Length and width of the body were chosen through a series of tests, where car's stability had been checked (we tried to make car as small as possible; however, too small models tended to turn over; also, balloon could touch the wheels).

For reducing friction in the axes we had used bearings (B) (inner diameter 3 mm, outer 7 mm), to which we could attach different wheels. Bearings were placed on the small metal rods; other end of the rods was put into small pieces of balsa. These pieces of balsa were attached to the car's body with needles. By changing angle between forward and rear wheels it was possible to set car for circle trajectory (since finding a long enough even surface wasn't always possible).
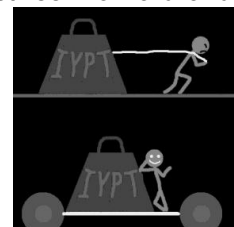
A clothespin (C) had been used for holding the nozzle, attached to the balloon. Small pieces of adhesive tape (D) prevented deflated balloon from falling down and touching the ground.

Figure 2. Smile makes everything obvious

Efficiency

To describe efficiency of the car we used efficiency coefficient:

$$\eta = \frac{A}{E} \cdot 100\% \, ;$$

where A is useful work, and E is full energy of the system. For our car full energy is the energy stored in the balloon. But what is useful work for our system? What is main purpose of the car? Why do we use it? To understand it I've painted fig.2. And it became obvious: car is used to overcome friction. If energy from the balloon was used to overcome friction, it means that car has moved something forward, and, therefore, done something useful. And if energy was spent on the turbulence in the nozzle or on air drag, then it was wasted.

Energy in the balloon

The energy source for the car is balloon, so we have to determine how much energy it stores. Note, that energy hides itself in two places: in pressurized air inside balloon and in the balloon itself – as energy of the stretched rubber.

Let's assume that balloon now has volume V_1 and pressure of air is P_1. The maximum energy from this air can be gained if it expands adiabatically, as there are no losses through heat. Air would expand until its pressure is equal to atmospheric pressure P_{atm}. Through equation of adiabatic process volume of the air after expansion can be found:
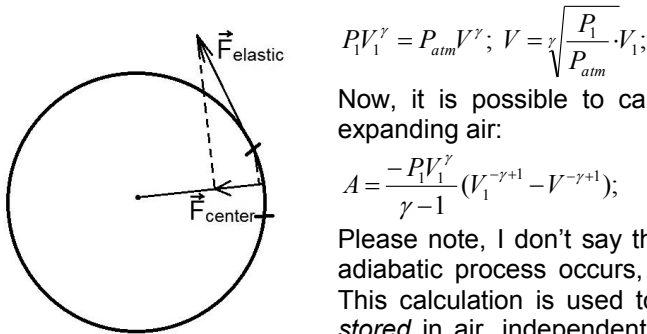
$$P_1 V_1^\gamma = P_{atm} V^\gamma; \ V = \sqrt[\gamma]{\frac{P_1}{P_{atm}}} \cdot V_1;$$

Now, it is possible to calculate work, done by the expanding air:

$$A = \frac{-P_1 V_1^\gamma}{\gamma - 1}(V_1^{-\gamma+1} - V^{-\gamma+1});$$

Please note, I don't say that anywhere in the car an adiabatic process occurs, or that I want it to occur. This calculation is used to find the energy which is *stored* in air, independently of any processes in the car.

However, to use this formula we need to know pressure in the balloon and its volume. They can be connected through the mechanical stress in the

Figure 3. Elastic force, acting on a small piece of shell, and its component, directed towards center

balloon's shell. On one hand, relative increase of area of some small part of the shell can be found as:

$$\frac{\Delta S}{S} = 2 \cdot (1 - \mu)\frac{\sigma}{E};$$

Where E is Young's modulus, μ is Poisson's ratio, σ is mechanical stress. Relative increase of area of the whole surface of the balloon will be the same, and as soon as our balloon is a sphere, it will be 3/2 of relative increase of balloon's volume.

On the other hand, if we consider elastic force acting on a small part of the balloon's shell, because of the curve of surface it will have some projection towards balloon's center (as shown on fig.3). This small force

Figure 4. Line is plot of theoretical formula, while dots are experimental. Average error of volume measurements is 0.0008 m³

should be equal to the pressure force acting on this part of shell, so difference between pressure inside the balloon and atmospheric pressure is:

$$\Delta P = P_1 - P_{atm} = \frac{2\sigma d}{R};$$

whered is width of the shell, R is balloon's radius. Now, if two equations are combined:

$$\Delta P = \frac{2}{3} \frac{V - V_0}{V_0 \dfrac{(1-\mu)\sqrt[3]{\dfrac{3V}{4\pi}}}{Ed}};$$

where V_0 is original volume of the balloon. This formula is checked in the fig.4, wheredependence of extra pressure ΔP on the total volume of balloon is shown. Certainly, we also had to know rubber's properties for plotting formula. Our measurements had shown 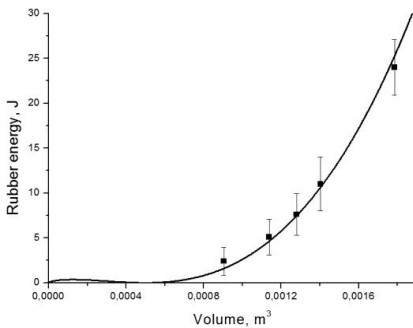that rubber's Young's modulus E was equal to (0.47±0.03) MPa, Poisson's ratio μ= (0.46±0.02); also width of the balloon shell d was (0.23±0.01) mm.

For volumes less than 1.8 liters results calculated through the formula are correct; however, at volume of 1.8 liters rubber reaches its proportionality limit and for bigger volumes it doesn't behave according to Hooke's law anymore. Since in this area even very small increase in stretching force will cause a significant deformation, we approximated that after volume of 1.8 liters pressure will remain constant.

Energy of rubber

Rubber itself also stores energy. Knowing mechanical stress in the shell, energy density can be calculated as:

$$W = \frac{\sigma^2}{E}(1-\mu);$$

Therefore, energy in the shell is:

$$U = W \cdot Sd = \pi \frac{\Delta P^2 R^4}{Ed}(1-\mu)$$

Figure 5. Dependence of the rubber energy on the volume. Line shows theoretical prediction, dots are experimental data

Certainly, the formula should be checked. So how can be energy stored in rubber measured? Well, we can easily find work done by the pump, when we are inflating balloon (for example, we can put a weight on the pump – change of weight's potential energy will be equal to the work done by the pump). So, this difference in potential energy of the weight ΔE_p will turn into energy of pressurized air E_{air1}, energy of rubber E_R and energy of losses E_L(due to friction in the pump and heating of the air):

$$\Delta E_p = E_{air1} + E_R + E_L$$

How can we find these losses? The answer is: let's inflate something else, with shell which can't be stretched; for example, a plastic bag. Now, work of the pump will turn into energy of the air and energy of losses:

$$\Delta E_p = E_{air2} + E_L$$

Since change in weight's potential energy and energy of losses are same in both cases:

$$E_{air1} + E_R + E_L = E_{air2} + E_L;$$
$$E_R = E_{air2} - E_{air1};$$

E_{air1} and E_{air2} can be calculated through volume and pressure of air in the balloon and plastic bag.Results of thesemanipulations are shown on fig.5. Again, at the

volume of 1.8 liters rubber reachesits proportionality limit; therefore energy density will remain constant, and rubber energy will increase because of the increase of the volume of the shell itself.

It also should be noted, that for volumes less than 0.0005 m^3 formula, in fact, tries to predict energy of the compressed balloon's shell and, therefore, this area of plot shouldn't be considered.

Efficiency

In the car, energy losses occur in the nozzle and also some energy is used to overcome air drag. However, air drag had been very small. To prove it, an experiment was made: we had put a sheet of cardboard on our car; first time – horizontally (for small drag),second time – vertically (for increased drag). Then we pushedthe car forward manually and plotted law of its movement (fig.6). The difference between forces, which were stopping the car in two cases is less than 5%. Therefore, air drag can be ignored.
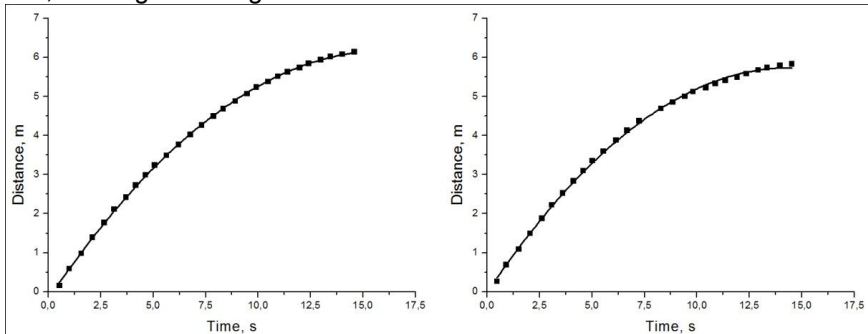
Figure 6. Left plot shows travel when a sheet of cardboard was placed horizontally, right – when vertically. Both are fitted by square parabola

Unlike air drag, losses in nozzle are significant. There are three reasons of losing energy in nozzle: turbulence, viscous drag and scattering of the jet, after it exits nozzle. Amount of energy, lost in any of this ways, strongly depends on the length and width of the nozzle. It is difficult to describe this dependence even for just one of the effects; describing all three effects at once is almost impossible. Therefore, we tried to research dependence of the efficiency coefficient on the nozzle parameters experimentally. We had inflated balloon to the same volume for all launches; respectively, full energies were equal. We also kept car's mass the same, so friction forces were the same either. Therefore, the only thing changed with changing of efficiency coefficient was distance, travelled by car:
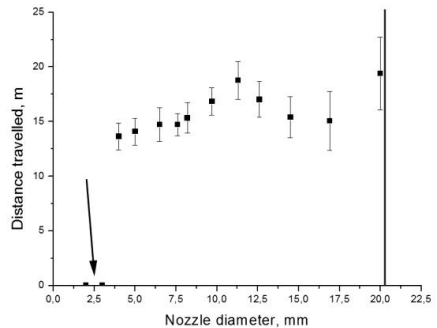
Figure 7. Arrow points at the dots, where car hasn't moved at all. Black line shows nozzle diameter, after which car becomes unstable

$$\eta = 100\% \cdot \frac{F_{fr}}{E} \cdot L;$$

whereF$_{fr}$ is total friction force acting on the car and L is distance travelled by car. That is why instead of plotting efficiency coefficient against nozzle diameter, we

plotted L against nozzle diameter (fig.7) – anyway, efficiency coefficient plot will look all the same, just multiplied by a constant value.

Let's take a closer look at the plot. With too small diameter car just can'tmove forward (first two dots). Then we have a local maximum of efficiency, and in the end dependence is growing. Unfortunately, with nozzle diameters bigger than 20 mm car is incapable of holding stable trajectory. But we can predict, that there will be another local maximum, after which dependence will fall to 0. It is easy to prove: if we take our balloon and stick adhesive tape over its equator, and then pierce it. The side, which we've pierced, will explode and let the air out; adhesive tape will prevent the other side from tearing apart. So we will achieve nozzle diameter equal to the diameter of the balloon. But when we had performed such experiment, our car travelled only 5 cm. Knowing all this, we can say that for maximal efficiency coefficient we should use the nozzle diameter from the first local maximum.

Unfortunately, for the length of the nozzle even experimental dependence wasn't found: dots were jumping randomly.

Travelled distance

It is very interesting, thateven if efficiency coefficient remains the same, travelled distance still can be varied through varying friction force.

In fact, there are two friction forces, acting in our system:rolling friction force (F_1) and static friction in the axes (F_2). These forces will be calculated as:

$$F_1 = k\frac{N}{R};\ N = Mg + n\sigma\pi R^2;\ F_2 = \mu Mg;$$

where R is wheels radius, M is car's body mass, n is number of wheels, σ is surface density of wheel's material, k and μ are static and rolling friction coefficients respectively. If car has travelled distance L, then work of rolling friction will be F_1*L; however, work of static friction will be $F_2*L*(r/R)$, where r is radius of the axis; it is so because static friction force is applied closer to wheel's center, where smaller distance will be covered. In total work of friction forces is equal:

$$A = g\frac{M(k + \mu r) + nk\sigma\pi R^2}{R}\cdot L = g\cdot X(R)\cdot L;$$

Since we want for L to be maximal, we have to make X(R) minimal; to find its minimum we can take its derivative and put it equal to 0:

$$X'_R = nk\sigma\pi - \frac{M(k + \mu r)}{R^2} = 0;$$

After solving these equations, a formula for optimal wheel radius is achieved:

$$R = \sqrt{\frac{M(k + \mu r)}{nk\sigma\pi}}$$

It is interesting to note,that total mass of the wheels in this case is connected with car's body mass by this equation:

$$m_{wheels} = n\pi R^2\sigma = M\frac{\mu r + k}{k}$$

Experimental check

To check dependence of the distance travelled on wheels' radius it was necessary to find friction coefficients for
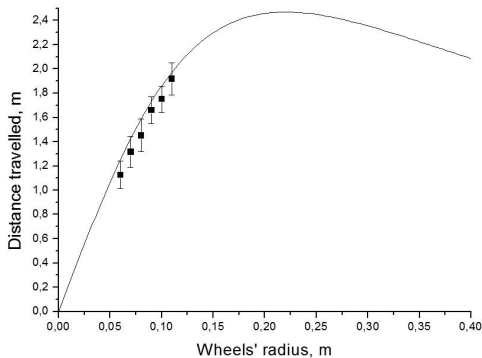
Figure 8. Dots show experimental data, line is theoretical dependence

our model. For finding static friction coefficient in the axis we had removed metal rod with bearing and wheel from the car and mounted it into a support. Then we painted a small dot on the edge of the wheel, and rotated it, filming everything on the high-speed camera. From the video, we had plotted angular velocity of the wheel depending on time. This dependence was linear; therefore, proving that we really can consider friction in the bearing as static. Then through angular coefficient of the line we had calculated static friction force and static friction coefficient. For finding rolling friction force we had performed same operation as for finding air drag: we had pushed car forward and plotted its motion; through this plot we found total friction force, acting on the car. Also we could already calculate static friction force; the difference between total friction force and static friction force was equal to rolling friction force. Through the rolling friction force we could calculate rolling friction coefficient.

Putting these friction coefficients into theoretical formula we plotted theoretical line, as seen on fig.7. Now we had to make experimental points. Since we had constant efficiency coefficient, constant amount of energy was used for overcoming friction forces. So, to increase accuracy of measurements, we had decided to give this amount of energy not through inflated balloon, but through a pendulum: it was turned to same angle and then released.It was hitting car, and car was moving forward (fig.8), having same amount of energy each time. It should be noted, that we hadn't checked wheels with radius close to optimal value, because they were too big to fit the car. Well, just one wheel was size of the whole car.

Conclusions

Full energy stored in the balloon is a sum of energy of pressurized air and of stretched rubber. With help of the equation, which connects pressure and volume of the balloon, we can calculate both those energies.

All this energy goes into two places: some is used to overcome friction forces – that's useful work; other is wasted on the losses in the nozzle. Air drag for our car was negligibly low.

Efficiency coefficient depends on the nozzle length and diameter; however, it's impossible to describe these dependences theoretically. Experimentally we have found two peak values for the nozzle diameter; the first one should be used, because with second car became unstable.

Distance travelled by car depends mainly on the wheels' parameters. They all can be connected in order to calculate optimal radius; however, it appears to be too big to use.

No. 5, Car: A study of aerodynamic and general properties of a balloon powered car

Bárbara Cruvinel Santiago [1]
* Team of Brazil, IYPT 2011
[1]*ColégioObjetivo, Santos, Brazil*
Corresponding author: barbaracruvinel_santiago@yahoo.com.br (B. C. S.)

Abstract

This paper has the aim of solving one of the problems of IYPT 2011, called Car: "Build a model car powered by an engine using an elastic air-filled toy-balloon as the energy source. Determine how the distance travelled by the car depends on relevant parameters and maximize the efficiency of the car." Throughout this paper, there are presented definitions and the experimental data acquired by a series of experiments related to the solution of this problem. The results are treated qualitatively because of some limitations that are going to be explained later. Also, the results about the design of the car showed to agree with the theory.

1. Limitations to the solution

The most important limitation to this solution is the measurement of the efficiency of the car, basically because of the need of specific equipment and the variable pressure inside the balloon during the movement. But as the problem just asks to "maximize the efficiency", that could be done by indirect ways of measuring it, not being strictly necessary to measure the efficiency itself. Other limitations are related to the locking of parameters for different experiments, like changing the balloon stiffness without changing its shape or changing the chassis without changing the wheels.

2. Definitions

Car will be treated as any object which moves over wheels without getting off of the floor or overturning, just using an internal source of energy that, in this case, is the air inside the balloon. This definition is used because it fits the objective proposed by the problem, as an "elastic air-filled toy-balloon" is to be the "energy source" and if the car overturns or get off of the floor, it would be impossible to measure the travelled distance and find its dependence on relevant parameters.

Efficiency[1] is a dimensionless ratio between the energy used in the motion (not dispersed) and the energy that has been given to the system.

$$\eta = \frac{E_{out}}{E_{in}} = \frac{P_{out}}{P_{in}} \tag{1}$$

In this equation, E_{in} is the internal energy, E_{out} is the useful energy, P_{in} is the internal pressure and P_{out} is the outside pressure.

As it would be difficult to measure this ratio empirically, we are going to use the travelled distance per a determined quantity of air (combustible) as the definition for "vehicle autonomy". This last one will be used as an indirect

measurement of the efficiency. It could be done because the larger the travelled distance for a determined amount of combustible, the lower the loss of energy.

3. Forces acting over the car

The air is pushed backwards with a force F, pushing the car forwards with a thrust T, forces with the same magnitude and opposite directions.
Since then, we start to have other forces acting on the car. These forces are: a thrust [2] force T, the air drag force and the friction force (fig.1). We also have weight and the normal forces.
In order to maximize the efficiency of the car, we must increase the driving force and decrease the resisting ones.
When the air inside the balloon is finished, the propulsion force ceases to exist. So, the other forces continue to act over the car till its velocity reaches zero (fig.1).
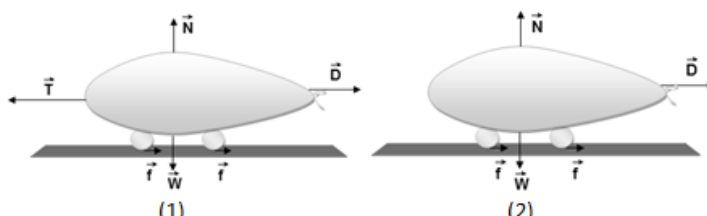
Figure 1: (1) initial forces over the car and (2) forces after the end of the gas propulsion

4. Gas propulsion force

We must consider that this force is variable because of the variable pressure, mass and volume inside the balloon.
Temperature and molar mass (that depends on the used gas) will influence the pressure, influencing the propulsion force.

5. Drag force (resistance of the air)

The drag force can be calculated by the following formula[3]:

$$D = \frac{1}{2}\rho C_x A V^2 \tag{2}$$

In this case, D is the drag force, ρ is the fluid density, C_x is the drag coefficient (that depends on the shape), A is the transversal section area and V is the relative velocity between fluid and car.

6. Friction force

We have a car propelled by the air inside the balloon and there is no force producing torque directly over the wheels, just a propulsion force acting all over the car, producing a translational motion (of the body and of the wheels). In this situation the tendency of slipping is in the same direction of the motion, so the friction is contrary to the movement.

7. Rolling between wheel and axis

The friction existent in the rolling between wheel and axis must also be considered. This friction must be decreased in order to improve the rolling.

8. Propeller nozzle shape

Depending on the shape that we have in the car nozzle, we have a determined type of flow. This is going to depend on the shape of the balloon nozzle: square, rectangular, circular etc. In this problem we will consider two kinds of flow: laminar (characterized by its parallel fluid lines and overlapping layers) and turbulent (characterized by the chaotic state of the fluid), remarking that there is a region of transition between both.

In the case of the balloon car, it will be more efficient whether the fluid is laminar. We have some differences between car's shapes because of the break of the boundary layer by a gradient of pressure [4].

9. Elastic properties of the balloon

If the balloon is stiffer, the pressure inside it is higher. So, the propulsion force would be higher too. There isa maximum number of times that one can use the same balloon to get similar results.The most used mechanism to quantify the elasticity of a body is the Hooke's Law, which can be used just for a strip of the balloon in this case.

$$F = kx \qquad (3)$$

In which, F is the elastic force, k isthe spring constant, x is the deformation.

10. Experiment 1: aerodynamic test

Solids made of cardboard and Styrofoam with the same transversal section area are put in the end of the wind tunnel (next to the fan). The lower the velocity of the solid that is pushed by the air to get out of the tunnel, the lower the drag force, so the better the aerodynamics.
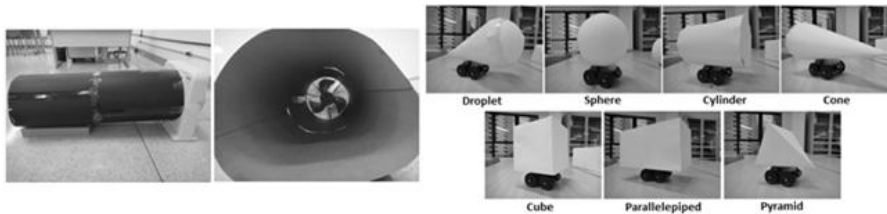
Figure 2: Wind tunnel (left) and used solids (right)
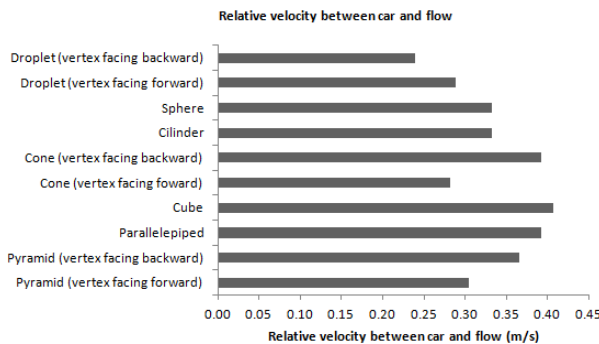
Figure 3: Chart of velocities of different solid's shapes

As it is possible to notice, the droplet shape has had the best aerodynamic (lower velocity), as predicted by the theory. The lag time due to the chronometer use (≅0.4s) is a possible source of errors.

11. Experiment 2: nozzle test

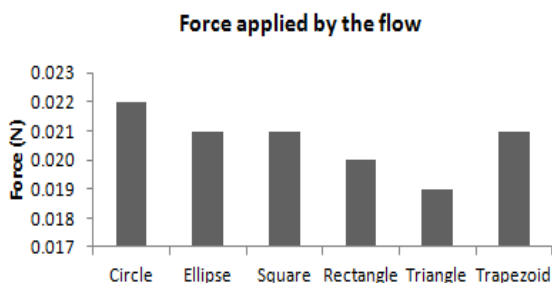The air exit shape of a hair dryer is varied (with same area) and put from a standard height of 5cm in relation to the scale. The mass registered is converted to force according to the scale calibration.

Figure 4: Chart of forces for different nozzle's shapes

The circle showed to be slightly better (no regional turbulence), although all the shapes showed similar results. Distance between dryer and scale (precision of the caliper rule: ±0.05mm) and precision of the scale (±0.1g) are possible source of errors.

12. Experiment 3: test of a straw as the nozzle

A test track was made to make the distance measurements easier. The same amount of air was used in all the experiments, with an air pump.

Table 1: Distance (measured in m) travelled with and without a straw as the nozzle

	Without a straw	With a straw
	2.49	3.38
	2.12	4.05
	2.02	3.15
Average	2.21	3.53
Standard deviation	0.25	0.47

The paper straw directed the flow, so the car could travel a larger distance for the same amount of combustible. The precision of the measuring tape (±0.05cm) is a possible source of errors.

13. Experiment 4: chassis test

Two different chassis (wedge and rectangular prism shapes) are tested in the same test track of the last experiment, using the pump to apply the same amount of air.

Table 2: Distance (measured in m) travelled for different chassis' shapes

	Rectangular prism	Wedge
	2.39	0.41
	1.89	0.35
	2.01	0.39
Average	2.10	0.38
Standard deviation	0.26	0.03

Even though the wedge shape was more aerodynamic, the chassis in rectangular prism had less rolling friction in its wheels, so it showed to be better. The precision of the measuring tape ($\pm$0.05cm) is a source of errors again.

## 14. Experiment 5: surface test

The test track and the same amount of gas (using an air pump) are used again. Both surfaces are made basically of the same material, but the first has slots and the second do not.

Table 3: Distance (measured in m) travelled over different surfaces.

	With slots on the floor	Without slots
	2.39	2.49
	1.89	2.12
	2.01	2.02
Average	2.10	2.21
Standard deviation	0.26	0.25

Considering the standard deviation, there is no difference between the surfaces.But it is known, theoretically, that the more uniform the surface is, the larger the distance travelled by the car. The precision of the measuring tape is, again, a source of errors.

15. Experiment 6: elasticity test
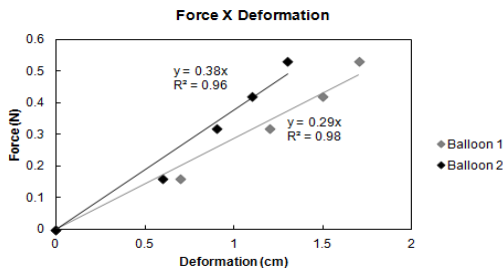
Figure 5: chart of the applied force versus deformation of the balloon strip

Strips with the same dimensions of both used balloons are tested in order to take its spring constant. Marbles are used to apply the force. Then, the distance travelled for the same amount of gas, in the test track, for both balloons were measured.

- Balloon 1: k = 0.29N/cm
- Balloon 2: k = 0.38N/cm

The precision of the caliper rule ($\pm$0.05mm) is a possible source of errors.

Table 4: Distance (measured in m) travelled with balloons of different elasticities

	Balloon 1 (k=0.29N/cm)	Balloon 2 (k=0.38N/cm)
	2.49	2.06
	2.12	2.11
	2.02	1.89
Average	2.21	2.02
Standard deviation	0.25	0.12

The balloon 1 was more aerodynamic and its car travelled a larger distance because of it, even being less stiff. The precision of the measuring tape ($\pm$0.05cm) is a possible source of errors again.

16. Conclusion

Basically, the efficiency is improved when the driving force (air propulsion) is increased over the resisting ones (drag and friction forces).For it to happen, the car must be built presenting, essentially, the following characteristics (got empirically): droplet shape, circular nozzle, a straw as the nozzle itself and wheels that produce less friction.These features were applied in the final model of the car (fig.6), which travelled the longest distance with the same amount of air (average of 3.53 m). This shows that the necessary characteristics to maximize the efficiency are also the relevant parameters for the distance travelled by the car.

Figure 6: Built car based on tested parameters

References

[1] http://www.epa.gov/chp/basic/methods.html

[2] http://www.grc.nasa.gov/WWW/K-12/airplane/thrust1.html

[3] http://www.portalsaofrancisco.com.br/alfa/resistencia-do-ar/resistencia-do-ar.php

[4] WHITE, Frank M. *Fluid Mechanics*. Forth Edition.Ed. WCB McGraw-Hill.pp. 250, 429.

No. 5, Car: Behaviour of the balloon in a moving rocket-type car

NivesBohačić[1]
[*] Team of Croatia, IYPT 2011
[1]*University of Zagreb, Croatia*
Corresponding author: nives.bonacic@hotmail.com (N. B.)

Abstract

This paper focuses on building a rocket-type car powered by an engine using an elastic air-filled toyballoonas the energy source, determining how distance travelled by thecar and efficiency depend on relevant parameters and maximizing them.
Balloon observations were done using a piston inflation/deflation model to calculate energy input, output and rubber stretching losses. Car motion was observed and initial condition parameters (volume and pressure), different jet diameters and nozzle angles were taken into consideration.

Piston model

As the balloon deflates pressure, volume and the number of molecules in it change. Therefore, imagine a piston containing all air later used for inflation to which the balloon is attached to. Moving the piston slowly inflates the balloon and releasing it results in spontaneous balloon deflation.

Initial system state is$p_0(V_{10} + V_{20}) = nRT$, $p_0$being the atmospheric pressure, V_{10} balloon volume before inflation and V_{20} piston volume.
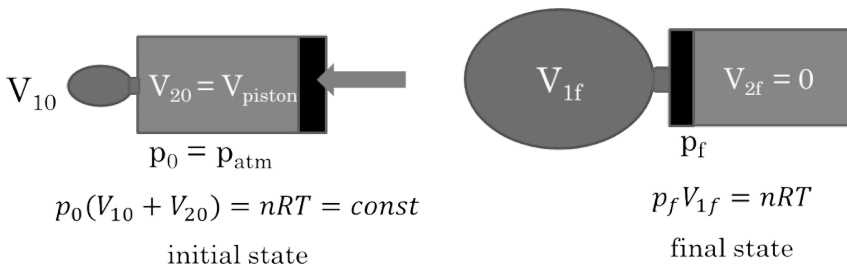
Ideal gas law equation states that at every moment$p(V_1 + V_2) = nRT$where$V_1$is the changing balloon volume and V_2 the piston volume, $R$is the gas constant.

Final state is $p_f V_{1f} = nRT$ where p_f is the final balloon pressure and V_{1f} the final volume (figure 1).

Integrating initial to final state of $dW = -(p - p_0)dV$ gives both inflation and deflation work as the same equations are valid. Energy needed for inflation and gained from deflation is:

$$W = \int_{p_0}^{p_f} p dV_1 + p_f V_f (\ln \frac{p_f}{p_0} - 1) + p_0 V_{10}$$

Where $p_f V_f (\ln \frac{p_f}{p_0} - 1) + p_0 V_{10}$are the known conditions and $\int_{p_0}^{p_f} p dV$ $_1$is determined experimentally for both processes separately.

V_{10} $\quad$ $V_{20} = V_{piston}$ $\qquad$ V_{1f} $\quad$ $V_{2f} = 0$

$p_0 = p_{atm}$ $\qquad\qquad\qquad$ p_f

$$p_0(V_{10} + V_{20}) = nRT = const \qquad p_f V_{1f} = nRT$$

initial state $\qquad\qquad\qquad$ final state

Figure 1: Piston model at initial and final state for inflation, valid also for deflation with inverted markings (left and right) provides a way to evaluate initial input energy and rubber losses.

Balloon inflation/deflation

Pressure was measured using a digital pressure sensor (resolution$0.05\ kPa$, possible calibration) at different volumes. Balloon volume was indirectly calculated

by taking photos) at known pressures, marking the balloon edge coordinates to find a shape (radius/height) function and numerically integrating this function (using shape rotation). These data give us the overpressure/volume relation shown in figure 2, where the deflation curve is under the inflation curve as expected due to energy losses from rubber deformation and elastic rubber hysteresis is observable.

This experimental results can be explained by balloon elastic energy where $\lambda = \frac{r}{r_0}$ is relative strain and κ is a rubber property.
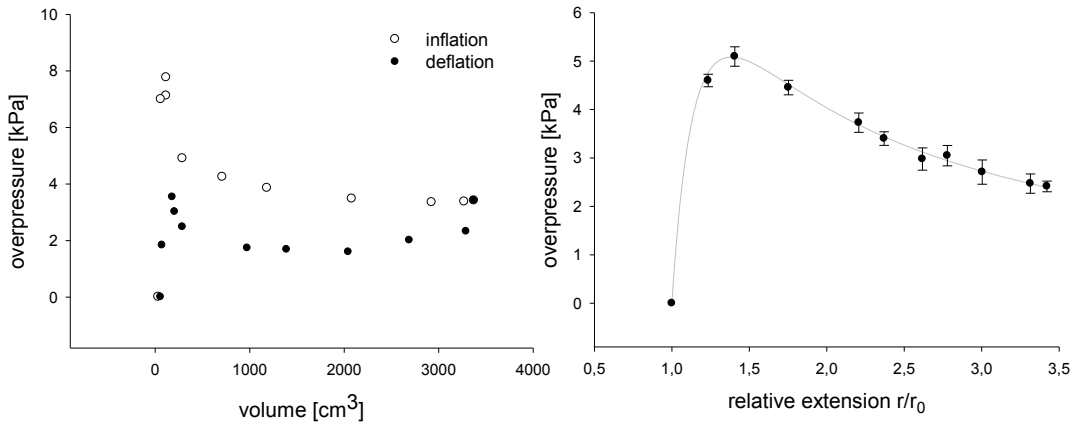
$$U = 4\pi r_0^2 \kappa RT \left(2\lambda^2 + \frac{1}{\lambda^4} - 3 \right) [1]$$

Work needed to increase radius from *r* to *r+dr* under pressure difference ΔP (being overpressure) is:

$$dW = \Delta P dV = \Delta P 4\pi r^2 dr = \left(\frac{dU}{dr} \right) dr = 16\pi\kappa RT \left(r - \frac{r_0^6}{r^5} \right) dr$$

$$\Delta P = \frac{4\kappa RT}{r_0} \left(\frac{1}{\lambda} - \frac{1}{\lambda^7} \right)$$

These equations were used to plot a regression, explain and confirm the obtained overpressure/strain curve (figure 2).

Figure 2: Left graph shows the elastic hysteresis of rubber. Gradual inflation and deflation curve differ and the energy is partly dissipated due to material plasticity. Right graph is a fit of elastic energy theoretical model to the experimental results which explains the initial maximum and gradual overpressure drop as the volume continues to increase

Surface under the volume/pressure curve enlarges with greater initial volume and so do the input and output energy. Efficiency of the balloon is the ratio between deflation energy (work that can be later used to power the car) and inflation energy. Both of them are according to the piston model energies of the initial and final conditions plus surfaces under the curves of these processes.

Maximising travelled distance is having the greatest possible energy after deflation (input energy), and maximizing the efficiency of the balloon is a comparison of remaining energy after deflation and total input energy for inflation (figure 3).
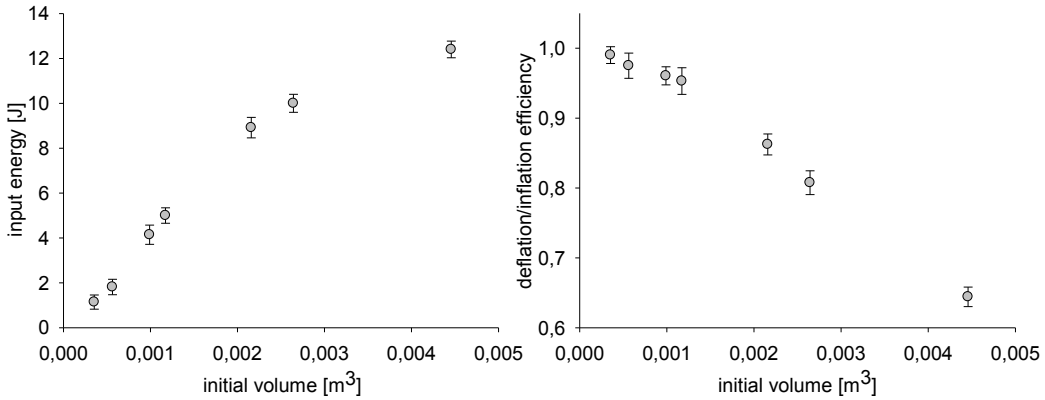
Figure 3: Left graph shows the increase of total energy with volume increase and the right graph showing the decrease of efficiency with volume increase (more rubber losses)

Construction and motion observation

Car consists of a plastic cart (length ~ 12cm), styrofoam base for a plastic tube (d = 2,9 cm) and metal jets / cardboard nozzles, attached at the tube end (figure 4). Car mass is ~120g. This car was placed on metal rails with distance scale to enable us its position determination and keep the movement straight.

A car with filled air-balloon was placed on the rails and a video of its motion was taken with a 120 fps camera. This video was later analysed to find distance/time coordinates and create a graph.

A computer program which analyses these coordinates with a 5 data points frame was created. This program fits a linear or cubic polynomial on the first 5 data points, derives this function and returns the value for the middle point. Frame than moves to the second point taking 2nd to 6th coordinate and repeats the procedure. The result of it is a velocity/time graph on which the initial accelerated motion caused by deflation is easily distinguished from the deceleration part when the car moves due to maximal velocity reached in deflation (figure 4).

Travelled distance is $s = s_0 + s_1$, s_0 being the acceleration path distance in which the maximal velocity v_{max} is reached (determined from the video) and $s_1 = \frac{v_{max}^2}{2a}$ being the deceleration path. The deceleration path was simply calculated with the presented equation in which both v_{max} and a are read from the graph (the latter as the linear coefficient from deceleration).
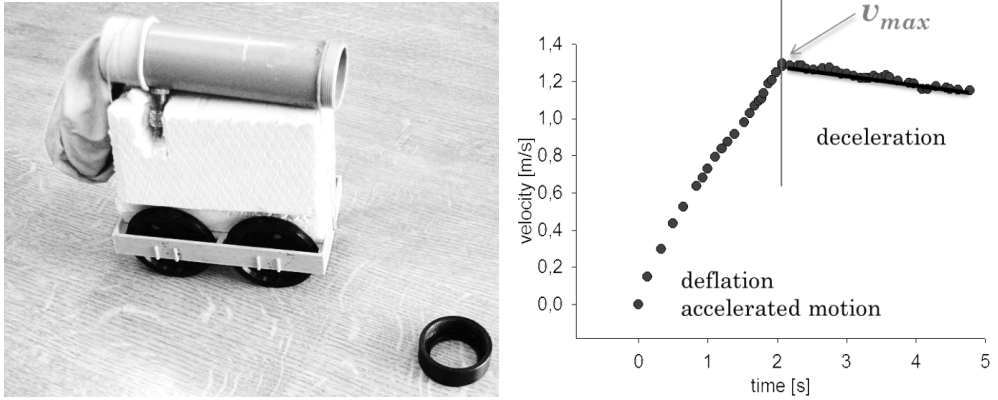
Figure 4: Final car model photo on the right and a velocity/time graph on the left. After the video analysis, distance/time coordinates were obtained and derived using a program especially created for this purpose

Motion description equations

Input energy defined previously is used for inflatio and it is transformed into kinetic energy of the air molecules during deflation.Lossesfirstly occur due to resistance to movement (mutual collisions).

Momentum conservation states $d(m_a v_a) - F_{fr} dt = m_c dv_c$, m_a and v_a being the air mass and velocity respectively, F_{fr} being the total friction force (air resistance, rolling friction) and m_c and v_c being the car mass and velocity respectively.

Simplified model describes the air behavior taking the mass inside the balloonas $m_a = \bar{p}V\frac{M}{RT}$, $\bar{p}$ being the average pressure evaluated from graphs, V balloon volume, M air relative atomic mass. Flow at the tube end is here aproximately described according to Bernoulli's principle, neglecting the fluid viscosity in that part so the air velocity is $v_a = \sqrt{\frac{2\bar{p}}{\rho}}$, ρ being air density. Friction force's F_{fr} main source is air drag due to car shape $F_{fr} = \frac{1}{2}C\rho S v_c^2 \sim V^{\frac{2}{3}} v_c^2$ and its duration is given from flow rate/volume relation as $t \sim \frac{v}{v_a}$.Momentum conservation equation is simplified to $m_a v_a - F_{fr} t = m_c v_c$.
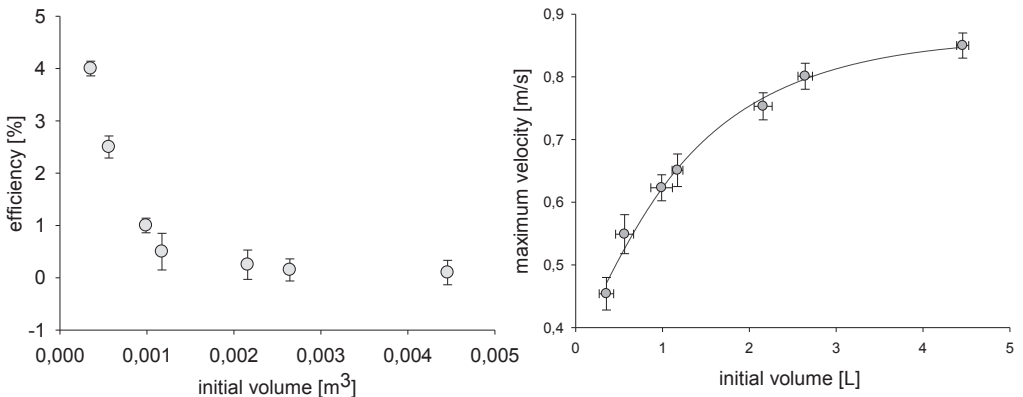

Figure 5: Left graph is the representation of the maximum velocity achievable at a certain volume. Regression expression for Initial volume/maximal velocity relation is obtained using presented equations.Right graph is the total efficiency initial volume relation. It is defined with ratio of final kinetic energy$\frac{mv_{max}^2}{2}$ and total input energy (as in the piston model)

Jets and nozzles

Jets are metal circular tube openings which vary the diameter of the tube end. Jet diameter changes how much is the air directed, time needed for deflation, air drag force duration and the amount of resistance air molecules endure in mutual collisions. Flow inside the tube is turbulent with the estimated Reynolds number at the order of magnitude 10^5. Experiment was conducted for different diameters to find the maximum v_{max} value as both traveled distance and efficiency depend on v_{max}^2.

Nozzles are cardboard cone shaped extensions attached to the tube end to increase the effective velocity, horizontal component of rapid molecules movement. Different nozzles have different angles, changing how much is the air directed but also different tube length as one cone end has a fixed (tube) diameter and thus the amount of losses due to friction changes. Analogous to the jet diameter – maximal velocity relation, the best cone angle also depends on v_{max} as it was earlier explained.

Best jet diameter and nozzle angle were found to be from 1.2cm to 1.4cm and from 15° to 20° respectively for this tube and conditions (figure 6).
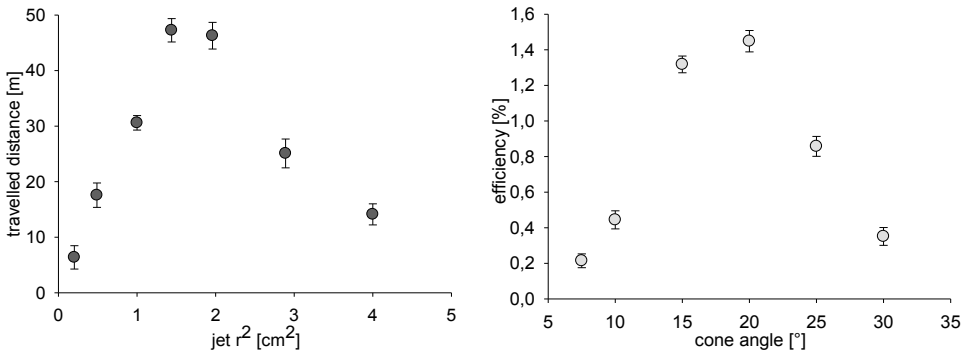
Figure 6: Left graph shows that the travelled distance/jet diameter curve has a maximum which is same for the efficiency as both of these sizes depend on v_{max}^2. Analogous to it the right graph has a maximal value too, also valid for travelled distance due to v_{max} relation

Discussion and conclusion

These experiments were conducted on a single car design, neglecting the possible influence of a more aerodynamic shape though the friction force as defined in motion description depends on the balloon size creating the air drag. Rolling friction is negligible in comparison to air drag friction and thus other wheels or moving mechanisms are not observed. Nozzle angle optimisation is also presented for a single nozzle shape (cone) and other shapes were not taken into consideration. These possible parameters have been in the initial experiments shown to be of less relevance than the balloon observation.

Balloon was described with a piston inflation/deflation model which was verified by comparing the theory for stretching losses with an experimental curve. The basic working principle was explained and maximum conditions for jets and nozles are found. Longest travelled distance optimised with all parameters (maximal volume before breakage 4.5dm^3, best jet and nozzle) is 70m and the highest efficiency (minimal volume to start 1.5dm^3, best jet and nozzle) is 6.4%.

References

[1] Y. Levin, F. L. da Silveira, Two rubber balloons: Phase diagram of air transfer, PHYS. REV.E (2004), Volume 69, Issue 5

No. 5, Car: Energy losses and efficiency in a balloon powered car

Parham Zendedel Nobari[1], Reza Montazeri Namin[2], Hossein Azizinaghsh[3]

[*] Team of Iran, IYPT 2011

[1]*Mofid Gheytarie High School, Tehran, I. R. Iran.*
[2]*School of Mechanical Engineering, Sharif University of Technology, I. R. Iran.*
[3]*School of Computer Engineering, Sharif University of Technology, I. R. Iran.*

Corresponding authors: pzn1995@gmail.com (P. Z. N.), namin@mech.sharif.edu (R. M. N.),
hossein.azizi@gmail.com (H. A.)

Abstract

The present paper is an investigation of the efficiency of a car, powered by an air-filled toy balloon in which the deflating balloon produces jet propulsion. The causes of energy loss have been investigated theoretically and several precise experiments have been made to determine the amount of energy loss that occurs for different causes. Experiments were done using image processing techniques, measuring the volume of the balloon and its changes in several cases and leading to energy analysis. It will be shown that about 50% of the energy will be lost as a result of the Moulin's effect, and a variable amount will be lost as a result of the head loss.

Introduction

The main design we will emphasize in this paper on, is the installation of a filled balloon on the car, with its end pointing towards the back of the car, deflating and causing propulsion (rocket type car). In this case, because of the momentum of the outgoing air jet, a force will be exerted to the car, forcing it to move. There are other designs which couldutilize a balloon as a source of energy to mobilize the car as used in the Balloon Car Contest at NASA's Jet Propulsion Laboratory [1], many of which do not fill the balloon with air but use it as a rubber band instead(and since our task is to investigate air filled balloon cars, this approach was not a subject of our investigation). Another design is to chronically release the outgoing air jet into a turbine-like structure and use the energy to rotate the wheels. This way, the efficiency may increase due to head loss decrease resulted by the velocity decrease.This method has not been used elsewhere before, and we also did not investigate it. However, further investigations are suggested on this method.
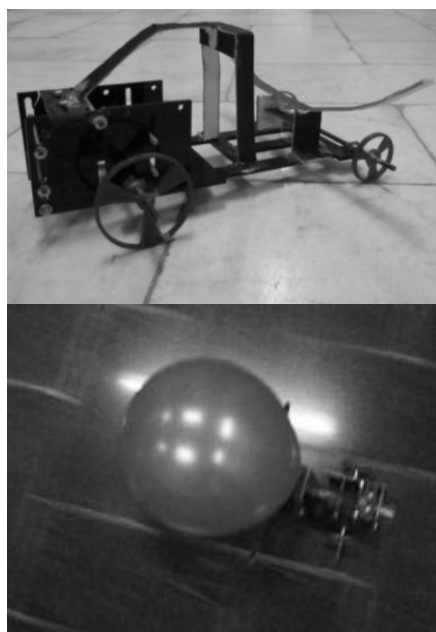
Figure 1: The Model Car

In our case, the balloon is attached to a cylindrical nozzle and deflates through it (Figure 1). A cylindrical nozzle with diameter of 4cm and length of 10cm was used in our experiments. In this case three forces are exerted to the car; the motivational force which is exerted to the balloon due to the momentum of the outgoing air flow, and two resistive forces which are: Aerodynamic drag force and the friction forces applied to the car. Regarding the conservation of momentum, the motivational force could be calculated as a function of the relative velocity of the outgoing air flow.

According to the Work and Energy Theorem, the total work done by all the external forces exerted to the car must be equal to its alterations of kinetic energy. Since the initial and final kinetic energies of the car are of zero value (initial and final velocities are zero), the total work done by all the forces exerted to the car must be zero. Thus the amount of work done by the motivational force equals to the work done by the resistive forces. It is desired to maximize the work done by the motivational force, since our definition of efficiency is the ratio of the work done on the car by the motivational force to the energy needed to fill the balloon.

In view of the motivational force to be much greater than the resistive forces (since it functions in a much shorter time and does the same amount of work) the work done by the motivational force is independent from the resistive forces. The energy released by the balloon air flow will be divided into two main compartments; the energy which moves the car and the energy which moves the air. The input energy given to the car would mainly waste in two ways (other than the kinetic energy of the air). Initially, a fraction of the energy will be lost during the inflation process due to the balloon's plastic deformation. This phenomenon is entitled as the "Moulin's Effect" [2]. Note that a filled and emptied balloon will be larger than the initial balloon. This means that a part of the energy given to a balloon while inflation will be used to deform the rubber material, which is not given back when it deflates.

The second form of energy loss occurs when the fluid is in rapid motion during deflation. This energy loss is widely known as "Head Loss", and has two main factors: Head Loss caused by the viscous friction forces with the inner membrane of the balloon, and the head loss resulted by the turbulent motion which arises from the high velocity. Both of these factors are proportional to the velocity square and the proportions are functions of the system's size and geometrical properties (in our case, the head loss coefficient alters during time and cannot be considered as a constant.)

In the following, we will determine the amount of these energy losses.

Several factors were to be experimented physically, mainly to measure the constants in the system and the amount of energy losses in different steps. The physical experiments would also approve the theoretical assumptions. During the experiments, each balloon was used only once to avoid changes in the results because of the Moulin's Effect. About 200 balloons were experimented totally.

Initial Energy and Moulin's Effect

The first set of experiments was designed to measure the amount of energy needed to fill the balloon and the amount of the restorable energy. To do so, our method was to find the relation between the internal pressure of the balloon and its volume.

To find the Pressure-Volume relation in emptying and filling stages, the balloon was attached to a leak-proof valve-pipe system, which could simultaneously fill the balloon with an air pump with a known small flow rate and demonstrate the internal pressure (Figure 2). A manometer gauge filled with inked water, was used to signify the internal pressure and two valves were attached in that the pressure alteration during deflation or inflation would visually materialize. The process was filmed by a camera far enough to minimize the effect of the perspective view subsequently, both the volume of the balloon and the pressure were calculated in each frame by a program using MATLAB™ image-processing. The balloon volume was calculated assuming axial symmetry about the z-axis (As demonstrated in Figure 2), and the internal pressure was calculated measuring the difference of water elevation in the two sides of the manometer gauge (Figure 2). In order to provide $P - V$ diagrams in the case of inflation (Figure 3), the experiment was reversely accomplished so that both valves were initially open and the balloon's inflation was recorded along with the changes in internal pressure and was ultimately analysed by the program. Using these techniques, the Pressure-Volume diagrams could be achieved.
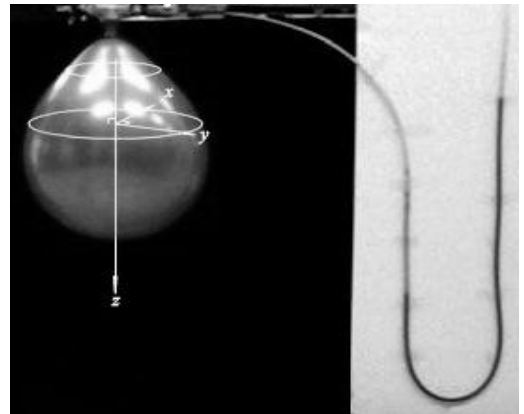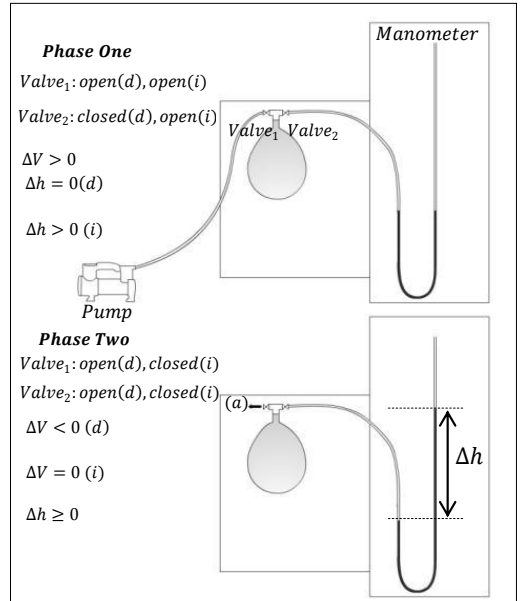
Figure 2: The $P - V$ Experiment Setup illustration (i) indicates the inflation setup and (d) indicates the deflation setup.(Note: in the deflation setup $h \not< 0$ thus flow rate (a) was dramatically minimized.)

While measuring the Pressure, there were some errors caused by the dynamic motion of the water in the tube, particularly in the inflation process, which the discharge could not be smaller than a specific amount. Therefore, at the beginning of the inflation process, where there is no maximum point for the pressure, the dynamic behaviour of the water would not seem to be crucial, since it is the integration of the $P - V$ diagram which will be used later, and this oscillation does not have a significant effect.
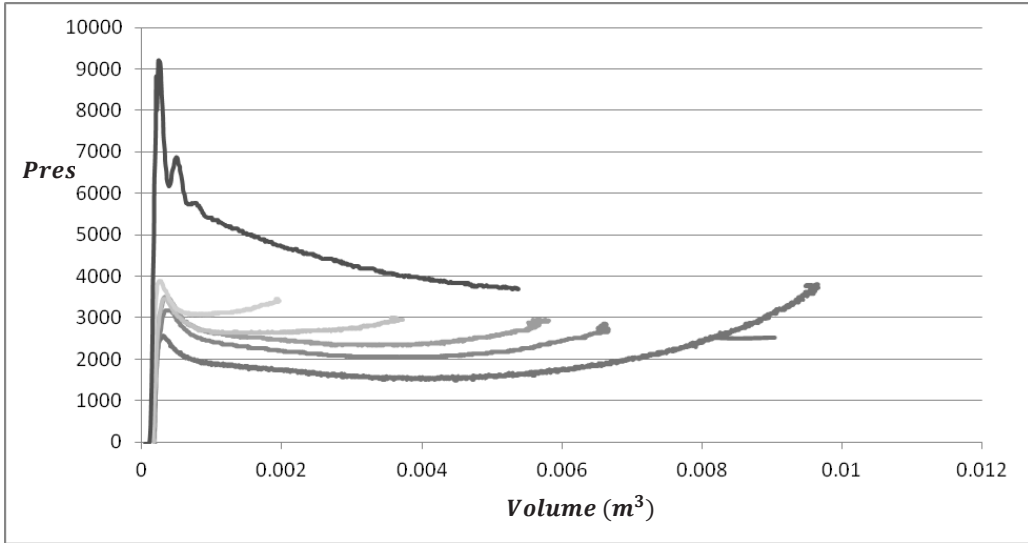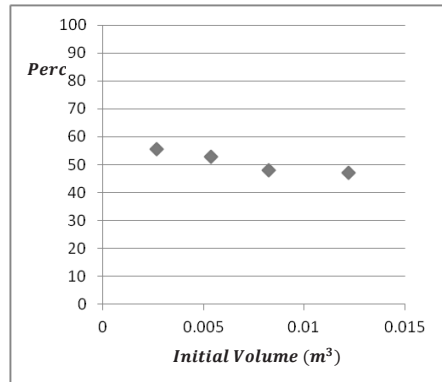
Figure 3: The P-V Diagram for Several Deflation Cases and an Inflation case (the Top Curve) Each Curve is consisted of about 1000 Points outputted from the Image Processing

Having the $P - V$ graphs for inflation and deflation from different initial volumes, the energy was to be calculated. To inject an infinitesimal volume dV of a gas to a container with a pressure of P, the energy required is PdV. Thus, the energy to fill the balloon is the integration of pressure that is a function of volume:

$$E = \int_{V_0}^{V} P(V)dV \qquad (1)$$

The same occurs for the deflation process. Hence, the energy needed to fill the balloon was calculated by numerical integration. Moreover, the restorable energy was calculated by integrating the relation for the deflation case.

Figure 4: The Ratio of the Restorable Energy to the Total Given Energy
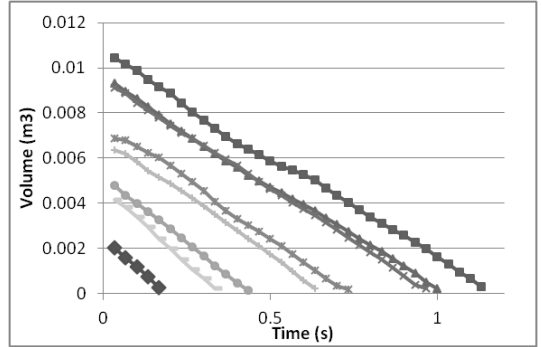
Our results illustrate that about half of the work required to fill a balloon is not restorable, (Figure 4) in other words; 50% of the energy is used to cause the plastic deformations among the rubber-like material.

Fast Deflation Process and Head Loss

The entire energy loss is not limited to the Moulin's effect. Some energy will be lost due to the dynamic of the outgoing fluid during the fast deflation, e.g. the viscous force between the fluid layers will do some negative work, converting the mechanical energy to heat. Flow turbulence also wastes some energy [3]. We must determine the amount of the energy lost during the deflation process, which is of course a function of the volume, varying the deflation velocity and deflation time. In order to investigate the reproduced energy by the balloon, we attach the balloon to a cylindrical nozzle (similar to the ones used on the car) and let it deflate. A high speed video was captured from the deflating balloon, and again using image processing, the volume of the balloon was found as a function of time (Figure 5). This was done for several initial volumes, and the experiment reproducibility was also checked by repeating the experiments.

It was observed that the rate of volume change (flow discharge) remains slightly constant during the emptying time. The discharge is plotted against the initial volume, and a decreasing behaviour is observed (Figure 6). This behaviour is acceptable, since the average internal pressure of the balloon also has a decreasing behaviour regarding the initial volume.Note that the discharge was interpolated to be used for countless un-experimented points in that specific range. The interpolation was made by fitting a logarithmic trend to the data, and the only reason of using a logarithmic function (and not a linear curve for instance) was that it could give a better prediction for un-experimented points. Using the discharge, the emptying velocity and time can also be calculated for a known initial volume.

Figure 5: Some Emptying Diagrams

$y = -0.005\ln(x) - 0.0062$
$R^2 = 0.9799$
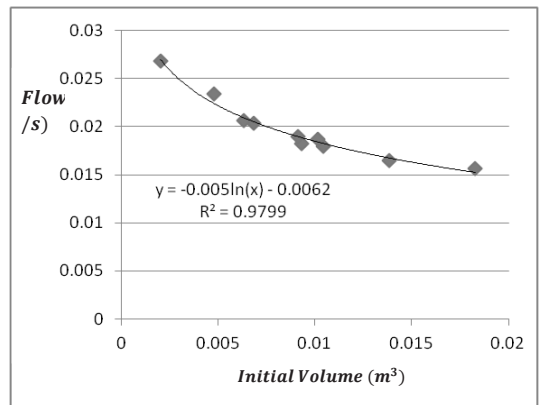
Figure 6: Flow Discharge
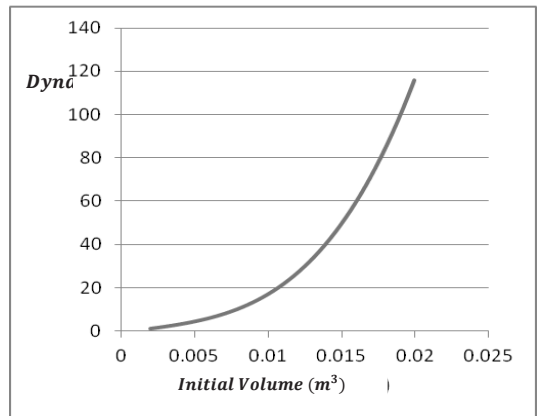
Figure 7: Dynamic Energy Loss

In this case, the energy released by the balloon is equal to the sum of the kinetic energy of the outgoing air. By calculating the mass and velocity of the outgoing air, the following equation would be achieved:

$$E_{released} = \frac{1}{2}(\rho A v \Delta t)v^2 = \frac{1}{2}\rho A v^3 \Delta t \ (2)$$

Where v is the relative velocity of the air flow. Using the experimental data, the amount of energy loss resulted by fluid flow was calculated in different initial volumes of the balloon. (Figure 7)

Car Motion Investigation

Until this point, the total energy released by the balloon has been investigated, as well as the discharge of the outgoing flow. Now it must be specified what portion of this energy is transferred to the car as kinetic energy, and the overall car motion must be investigated. According to the momentum conservation for the Car-Air system, the force exerted to the car can be calculated regarding the velocity of the outgoing flow:

$$F = \rho A v^2 \qquad (3)$$

Experimentally, we built a car and attached the balloon to its end, the balloon was filled using an air pump with a known discharge and filling time, consequently, the initial volume of the balloon was calculated. The car was set on the floor which its textures made it possible to find the distance travelled by the car. Videos were captured with a camera chasing the car from the top, and the motion diagrams were obtained (Figure 8).Furthermore, the total distance travelled was measured (Figure 10).
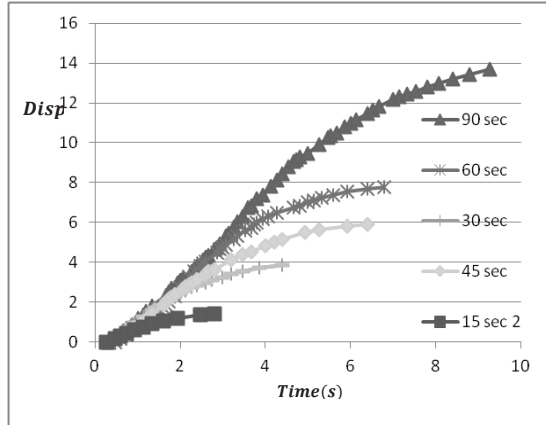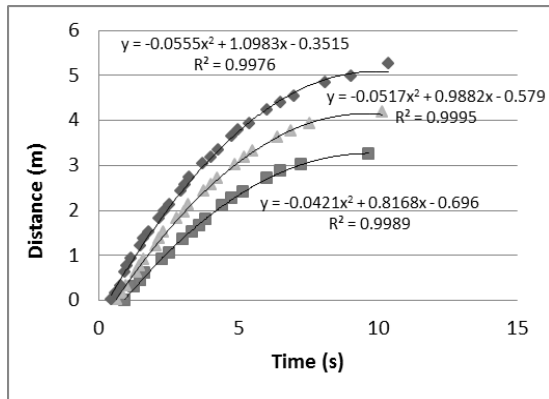

Figure 8: Motion of the Car

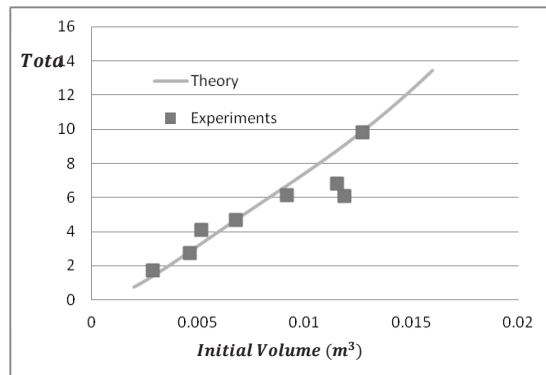**Figure 9:** Friction Measurement

Figure 10: Distance Travelled by the Car, Theory and Experiments

To find the friction forces, the car was pushed and released forward with varying velocities and its acceleration was measured (Figure 9).

Since the outgoing velocity and duration of deflation is known as a function of the initial volume (Figure 5 and Figure 6), the motivational force can be calculated usingformula 3 and since the resistive force is experimentally measured (Figure 9), the total force applied to the car in each phase of motion (increasing velocity and decreasing velocity) is known and the acceleration can be calculated as F / m, so theoretically the motion of the car can be predicted. The total displacement of the car, predicted by the theory, was compared with the experiments; evincing an acceptable concurrence (Figure 10).

Using the theory discussed above, it could be shown that the amount of the released energy which will be the kinetic energy of the car, obeys this equation:

$$\frac{E_{Car}}{E_{released}} = \frac{\rho A v \Delta t}{m} \tag{4}$$

Where m is the car mass and Δt is the emptying time.

Conclusion

In this investigation we tried to determine the sources of energy loss and describe the behaviour of each cause. We suggested three sources of energy loss: One caused by the plastic deformation of the rubber material, known as the Moulin's effect, and the energy loss caused by the dynamic fluid as a result of viscosity and turbulence which is known as head loss, and at last a small portion of the remaining energy will be used to move the car, and the rest will be transferred to the air.

Note that the plots and numbers can only be applied to our specific model and materials. As if the balloon changes, the $P-V$ diagrams will change since it is a function of the shape and material of the balloon.

By measuring the Pressure and Volume in the inflating and deflating balloon using image processing (Figure 3) and integration, to find the energy needed to fill the balloon and the reproducible energy, the ratio of the energy lost as a result of the Moulin's effect was calculated (Figure 4). The results suggest that about 50% of the energy needed to fill the balloon will be lost as a result of this effect.

Next the amount of energy lost by head loss was to be estimated. The discharge rate of the balloon was measured using the same image processing technique, and it was used to calculate the kinetic energy released by the balloon. As shown in Figure 5, the discharge decreases as the initial volume increases, and this is because of the decrease of the mean internal pressure of the balloon as in Figure 3. The difference between the total reproducible energy and the kinetic energy produced during the deflation and the energy loss, as a result of head loss was found as in figure 7.

The flow discharge, as a function of initial velocity, as interpolated in figure 6, was then used to compute the motion of the car theoretically. So after estimating the friction force (Figure 9), the total distance travelled by the car as a function of the initial volume of the balloon was measured experimentally and was compared with theoretical predictions (Figure 10).

In conclusion, the overall efficiency of the car system as a function of the initial volume of the balloon could be calculated. As evinced in figure 11, there is a specific initial volume of the balloon which has the maximum efficiency overall. However, according to Figure 10, there is no maximum for the total distance travelled by the car, unless a maximum possible volume for the balloon exists.
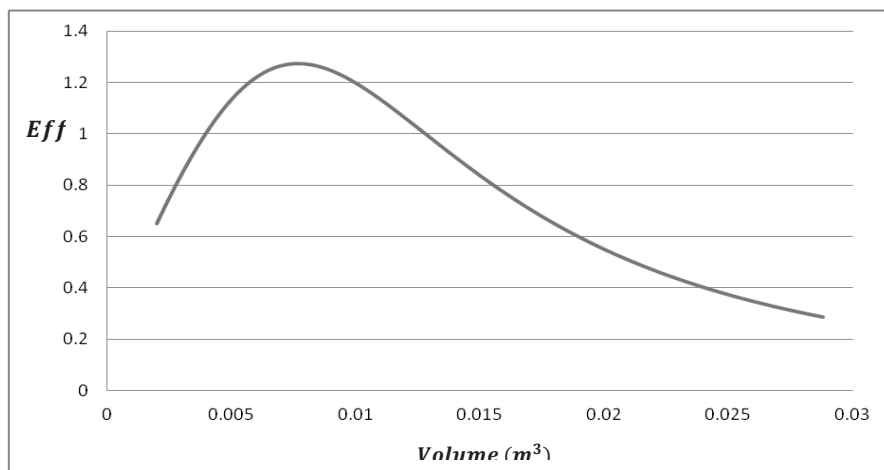
Figure 11: The Overall Efficiency of the Car

References

[1] Balloon Car Contest at NASA's Jet Propulsion Laboratory,http://balloonhq.com/balloon_car/balloon_car.html
[2] Treloar L R G 2005 The Physics of Rubber Elasticity, *Oxford University Press.*
[3] Shames I H 2003 Mechanics of Fluids, *McGraw-Hill.*

No. 8, Domino amplifier: A numerical analysis of the motion in a chain of dominoes

Alireza Tahmaseb Zadeh[1]
* Team of Iran, IYPT 2011
[1] School of Electrical and Computer Engineering, University of Tehran, I.R Iran
Corresponding author: info@tami-co.com (A. T. Z.)

Abstract

This paper presents an investigation on the motion of a falling row of dominoes with different dimensions. Motion is described in means of Falling and Collision. Dominoes are assumed not to slip on the surface. The equations are solved numerically and a comprehensive simulation program is developed by the means of angle specification of dominoes as a function of time. The program works for any given arrangement of dominoes with different heights and distances. Video processing is used to measure the angle of dominoes in real experiments. Precise agreement between experimental results and simulation verifies the theory. In each collision, some percentage of the energy remains, some is transferred and the other part is wasted. These percentages are compared for different height increase rates and are used to designate limitations.

Theory

Motion is divided to Falling and Collision. The former refers to the falling of *n* dominoes lying on each other before reaching *n+1*. The latter is related to the collision procedure of *n* and *n+1*.

A) Falling

Forces applied to one of the dominoes are: *1)* Normal force *k-1* and *k2)* Friction force *k-1* and *k3)* Normal force *k* and *k+14)* Friction force *k* and *k+15)* Weight *6)* Normal force from surface *7)* Friction force between domino and the surface.

Referring to the third law of Newton, the forces that *k* applies to *k+1* (normal force and friction force) is equal to the force that *k+1* applies to *k*. Angular acceleration of dominoes could be found using the torques applied to them.

$$I\ddot{\theta}(k) = \text{Torque}\big(F(k-1),\ \mu F(k-1),\ F(k),\ \mu F(k), \text{weight}\big)$$
(1)

More precisely:

$$I(k)\ddot{\theta}(k) = -F(k-1) \times \left\{\left[\left(l(k-1) - \frac{d(k)}{\sin(\theta(k))}\right)^2 + \big(h(k-1)\big)^2 - 2h(k-1)\left(l(k-1) - \frac{d(k)}{\sin(\theta(k))}\right)\cos\big(\theta(k-1)\big)\right]^{0.5} - d(k)\cot\big(\theta(k)\big)\right\} + \mu F(k-1)d(k) + F(k)h(k)\cos\big(\theta(k+1) - \theta(k)\big) + \mu F(k)h(k)\sin\big(\theta(k+1) - \theta(k)\big) - m(k)g\frac{\sqrt{h(k)^2 + d(k)^2}}{2}\cos(\theta(k) + \text{atan}(\frac{d(k)}{h(k)}))$$
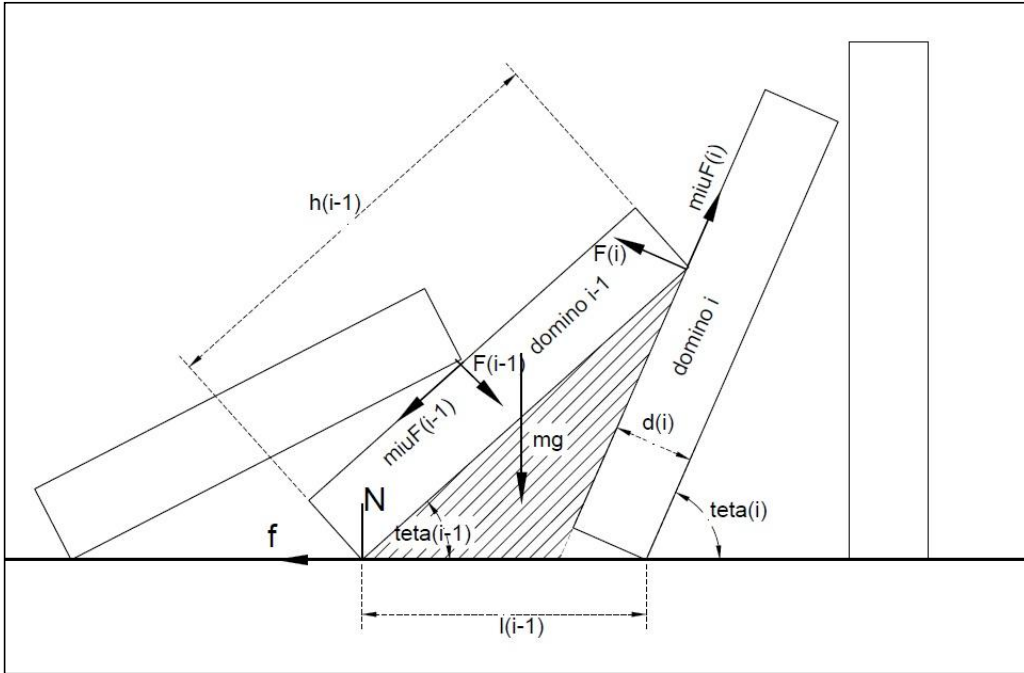(2)

Figure 1: Forces applied to the domino

Dominoes always remain in contact. This results in an equation between height$h(k)$, distance between right sides of *k* and *k+1*,$l(k)$, width $d(k)$ and angle with surface $\theta(k)$.(Using the sinusoids law in the hatched triangle in Figure 1)

$$\frac{h(k-1)}{sin\theta(k)} = \frac{l(k-1) - \frac{d(k)}{sin\theta(k)}}{sin(\theta(k) - \theta(k-1))} \tag{3}$$

Second derivative of this equation gives an equation between angular accelerations of *k* and *k-1*.

$$\ddot{\theta}(k-1) + \ddot{\theta}(k)[-1 + \frac{l(k-1)\cos(\theta(k))}{h(k-1)\sin(\theta(k)-\theta(k-1))}] = \frac{l(k-1)\dot{\theta^2}(k)}{h(k-1)\cos(\theta(k)-\theta(k-1))^2}[\sin(\theta(k))\cos(\theta(k) -$$

$$\theta(k-1))^2 - \frac{\cos(\theta(k))^2\sin(\theta(k)-\theta(k-1))}{h(k-1)}] \tag{4}$$

In better words, two equations are available for each of *n* dominoes.

$$C1(k)F(k-1) + C2(k)F(k) = C3(k) \tag{5}$$

$$P1(k)\ddot{\theta}(k-1) + P2(k)\ddot{\theta}(k) = P3(k) \tag{6}$$

where C1(k), C2(k), C3(k), P1(k), P2(k), P3(k) are known constants (These constants could be calculated using equations (2), (4)).

There are *n* dominoes and 2 equations for each, making *2n* equations totally. Also there happens to be *2n* unknown parameters which are $F(k)$ and $\ddot{\theta}(k)$ for all *n* dominoes. This system of *2n* equations and *2n* unknowns could be solved numerically.

Collision

Based on high speed videos, the following procedure is observed: As *n* hits *n+1,* some energy is wasted. Angular velocity of *n* and consequently preceding dominoes decrease. *n+1* obtains an angular velocity greater than the angular velocity of *n* after collision; therefore *n* and *n+1* separate. The large mass of the first *n* dominoes causes *n* to reach *n+1* soon again. *n* lies on *n+1* and the set of *n+1* dominoes continue to fall. Collision is immediate and the friction force between the domino and the surface is rather minor, hence conservation of momentum in horizontal direction is available. Restitution coefficient gives the relation between velocity before and after the collision.

$$\sum_1^n m(k)v(k) = \sum_1^n m(k)v'(k) + m(n+1)u \tag{7}$$

This equation could be exactly expressed.

$$\sum_1^n m(k)h(k)|\dot{\theta}(k)|\sin(\theta(k)) = \sum_1^n m(k)h(k)|\dot{\theta}'(k)|\sin(\theta(k)) + m(n+1)h(n+1)|\dot{\theta}(n+1)| \tag{8}$$

First derivative of the geometric constraint against time gives the relation between angular velocities of any neighbor dominoes:

$$\dot{\theta}(k-1) = \dot{\theta}(k)[1 - \frac{l(k-1)\cos(\theta(k))}{h(k-1)\cos(\theta(k)-\theta(k-1))}] \qquad 0 < k \le n \tag{9}$$

This equation indicates that if $\dot{\theta}(k)$ decreases by coefficient α after the collision, $\dot{\theta}(k-1)$ will also decrease by the same coefficient. Therefore, if $\dot{\theta}'(n) = \alpha\dot{\theta}(n)$, it could be inferred that $\dot{\theta}'(k) = \alpha\dot{\theta}(k)$ for $0 < k \le n$

Re-writing equation (7) we get:

$$\sum_1^n m(k)h(k)|\dot{\theta}(k)|\sin(\theta(k)) = \alpha\sum_1^n m(k)h(k)|\dot{\theta}(i)|\sin(\theta(k)) + m(n+1)h(n+1)|\dot{\theta}(n+1)| \tag{10}$$

For simplification we call S=$\sum_1^n m(i)h(i)|\dot{\theta}(i)|\sin(\theta(i))$. Equation (9) gives

$$S(1-\alpha) = m(n+1)h(n+1)|\dot{\theta}(n+1)| \tag{11}$$

The other equation is the restitution coefficient. The relative velocities of *n* and *(n+1)* becomes –e times (e<1) after the collision.

$$v'(rel) = -ev(rel) \tag{12}$$

Which is:

$$-e(h(n)|\dot{\theta}(n)|\sin(\theta(n)) - 0) = h(n)|\dot{\theta}(n)|\sin(\theta(n)) - h(n+1)\dot{\theta}(n+1) \tag{13}$$

The coefficient *e*, is calibrated in experiments. Solving equations (10) and (12), two unknowns of **α** and $\dot{\theta}(n+1)$ are calculated.

Simulation Program

Using MATLAB®,a program is developed to fully simulate the motion. The angle and angular velocity of the first domino and properties of dominoes namely: height, width, distance, density and friction coefficient are inputs. In each of the iterations, angular accelerations of dominoes are calculated solving the system of *2n* equations and 2n unknowns discussed above. Next, angular velocities and angles are updated by following equations:

$$\dot{\theta}(k)(t + dt) = \dot{\theta}(k)(t) + \ddot{\theta}(k)dt \tag{14}$$

$$\theta(k)(t + dt) = \theta(k)(t) + \dot{\theta}(i)dt \tag{15}$$

The program continuously checks if domino *n* has reached *n+1*. In case that it has reached, it solves equations (10) and (12) to find velocities after collision. Then it uses equation (8) to find angular velocities of preceding dominoes. Here is the phase that dominoes are separated for a short period. The program resumes the falling motion of first *n* dominoes and *n+1* separately until *n* reaches *n+1*again. The program assumes *n+1* to be in contact with *n* in the rest of the motion and upgrades the system to *n+1*in contact dominoes. This process continues until the last domino reaches the surface. Finally a movie from this motion is made.


Figure 2: The movie simulating the motion

Experiments

Dominoes were made of Plexiglas in different heights and widths. Experiments were done on an abrasive to provide the non-slipping condition which was assumed in the theory. A screw was used to firmly tilt first domino to ensure free falling for the first domino with no initial angular velocity (Figure 3).

Videos with 1000 frames per second were recorded. The dominoes, along with the background, were colored in black and a thin white line was drawn on dominoes. Analyzing videos by MATLAB, white lines were detected and traced to measure the angle of dominoes. The time between initiation of the motion and first collision was used to calculate the initial angle. Giving this angle and zero value for initial velocity as inputs, the simulation program plotted the angle of each of dominoes vs. time graph. The same graph was plotted using video processed data. Precise agreement between simulated and experimental graphs demonstrated accuracy of the theory. Three chief experiments are presented.
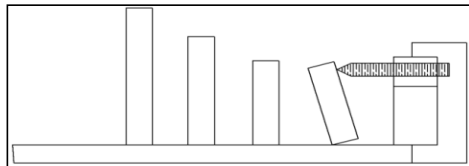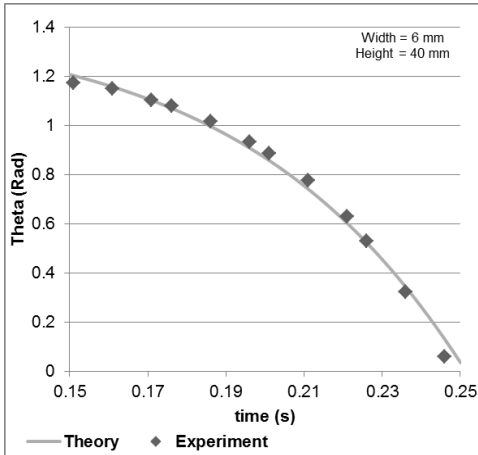

Figure 3: Setup Scheme
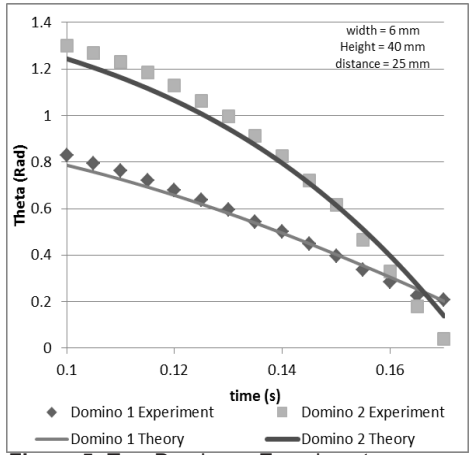
Figure 4: One Domino Experiment

Figure 5: Two Dominoes Experiment

A) One Domino: This experiment was done using one domino to check the falling procedure of the program (Figure 4).

B) Two Dominoes: Two identical dominoes were located. Falling time of the second domino was used to find the restitution coefficient. The great match verified equations of the collision (Figure 5).

C) Increasing Height Dominoes: Eight dominoes with different heights were placed in a row. The dominoes were each increased by 4 mm in height. The agreement between simulation program and video processing results in this experiment verifies theory's reliability (Figure 6).
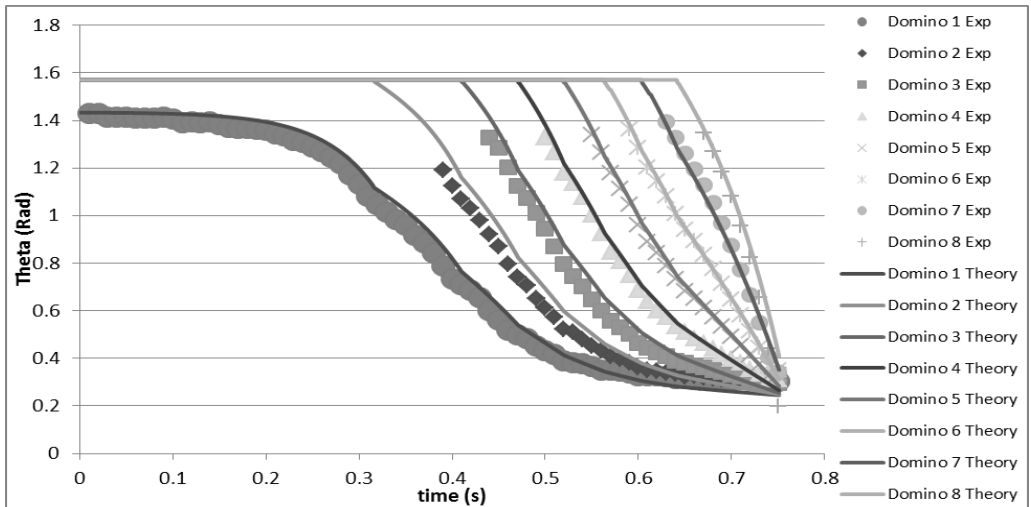

Figure 6: Increasing Height Dominoes Experiment

Discussion

Considering the high agreement between experiments and the theory, the simulation program was used to demonstrate energies and limitations. An increasing height arrangement was studied. Dominoes, all with a constant width, were located in a fixed distance from each other. The height of dominoes were increased by a constant *rate*(i.e h(i)=h(i-1)+*rate*). In order to illustrate height increase effect, four situations were analyzed: identical height and increasing height rates of 2, 6 and 10 mm by each domino.

The initial gravitational potential energy transforms into kinetic energy (Figure 7). Since dominoes are assumed to be stable on the surface, the kinetic energy is only rotational kinetic energy. In each collision, some energy is wasted. Using experiments, the restitution coefficient was calculated to be $\varepsilon = 0.2$ for our set of materials.
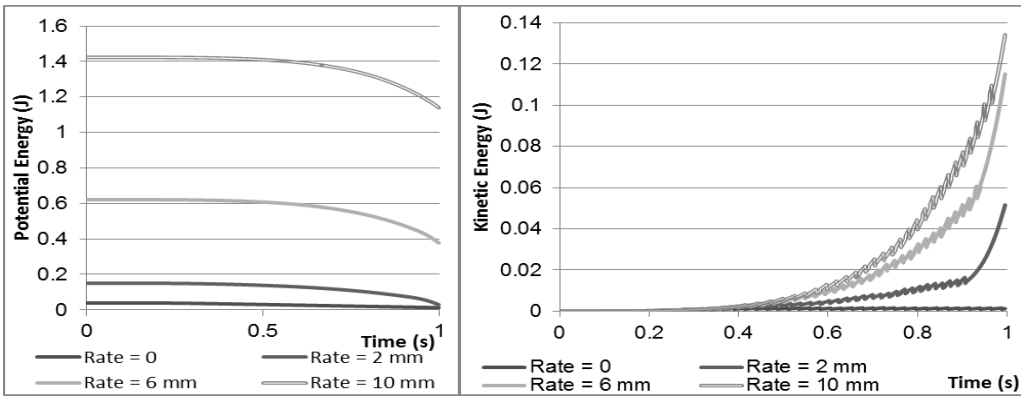

Figure 7: Potential Energy transforms into Kinetic Energy

Considering the collision of *n* and *n+1*, some part of the total kinetic energy remains in the first *n* dominoes, some transfers to *n+1* and the rest is wasted. Figures 8 and 9 illustrate this concept (*e.g.* In the collision of dominoes 20 and 21, in a 6 mm rate, 17 percent of the sum of kinetic energies before collision, will be transferred to 21[st]domino)

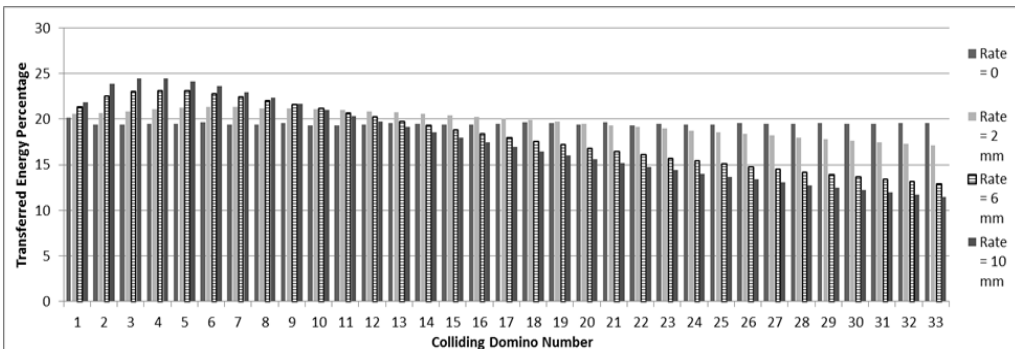In case of identical dominoes, after approximately 5 collisions, the energy that the

Figure 8: Transferred Energy Percentage at all collisions for 4 rates

system gains due to the transformation of potential energy becomes equal to the energy loss in the collision. Moreover, the time between collisions converges to a constant. Therefore a wave of falling dominoes which moves with a constant velocity is observed.
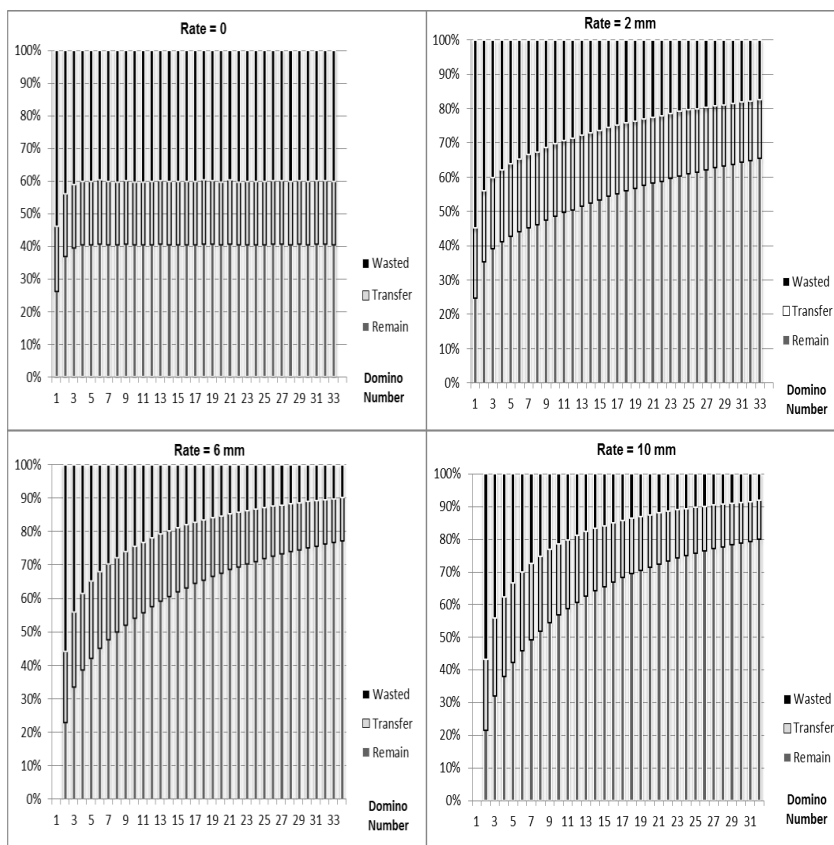
Figure 9: Remained, Transferred and wasted energy Percentages

Limitation

The situation in which a domino withstands when it is hit could be defined as a limitation. Considering the potential energy of a domino (Figure 10), it requires an initial energy to be toppled. This energy is required because the height of its center of mass should be increased when tilting the domino. This energy is supplied by transferred energy. Hence, transferred energy should be greater than the initial potential energy. Such kinds of limitations are acquirable using the simulation program. If width of the domino exceeds a critical amount, the motion will cease. As the width increases, the motion stops sooner. For instance, figure 11 shows the limiting domino number against width for a particular set of dominoes. (*e.g.* if width is between 3.21 cm to 4.01 cm, the motion will stop in the 3rd domino)
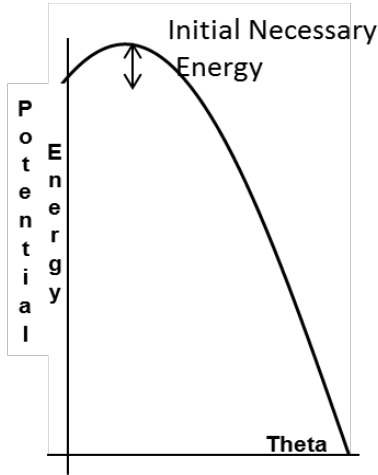
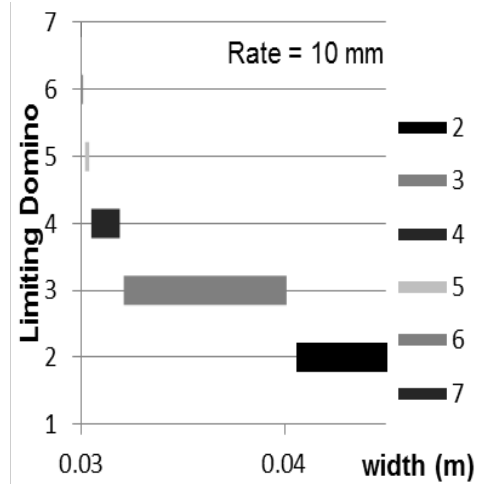**Figure 10**: Potential Energy of the domino

Figure 11: a) Potential Energy of a domino b) Limiting Domino against width

Conclusion

The theory has been several times modified to present the best model. The program works as well in every arrangement and height functions of dominoes and reports all parameters including transfer rate, energies, collision times and etc.In this paper, there was more attention on the effect of height increase rate. The simulation program is capable of recognizing any motion failure and limitations.

References

[1] J. M. J. van Leeuwen. *The domino effect*. Am. J. Phys. 78, 7, 721-727 (2010), arXiv:physics/0401018v1 [physics.gen-ph

[2] Steve Koellhoffer, ChanaKuhns, Karen Tsang, and Mike Zeitz. *Falling dominoes* (University of Delaware, December 9, 2005), http://www.math.udel.edu/~rossi/Math512/2005/Team3.pdf

[3] Robert B. Banks, Towing Icebergs, *Falling Dominoes and other adventures in Applied Mechanics*,   Princeton University Press, 1998.

No. 11, Fingerprints: Frustrated total internal reflection on the walls of a glass of water

Katja Kustura [1]
[*] Team of Croatia, IYPT 2011
[1]*University of Zagreb, Croatia*
Corresponding author: katja_kustura@hotmail.com (K. K.)

Introduction

A glass is filled with liquid and held with hand. If looked from above at the inner walls of the glass, sometimes the only thing visible through the walls is a very bright and clear image of patterns on fingertips.In this paper, this interesting phenomenon was studied and explained. [1] The secret of such bright and clear image of a fingerprint lies in finger's relief structure. Fingers do not have smooth, even surface – they consist of ridges

Figure 1. Enlarged fingerprint section

and grooves (fig.1). Grooves have the order of magnitude 10^{-4} m, which is much greater than the wavelength of light (10^{-7} m) [2]. Therefore, when pressing the glass with fingers, we only touch the glass with our ridges, while the gaps between grooves and glass are filled with air. The simplified model was made using small pieces of paper glued with adhesive tape (fig.2). Adhesive tape had the role of ridges (due to big

Figure 2. Fingerprint model

adhesion with the surface) and the paper had the role of grooves (smaller adhesion → less attached to the glass).When seeing fingerprints, on this model only adhesive tape can be observed (fig.3a). If we see the whole finger, not just the fingerprint pattern, on this model we see both adhesive tape and the paper (fig.3b). The model was used for easier measurements and parametrization of the problem.
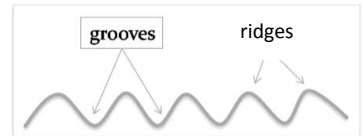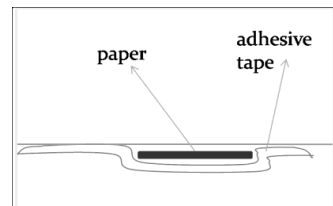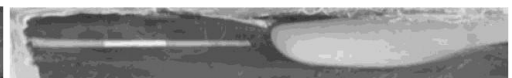

Figure 3a. Fingerprint visible

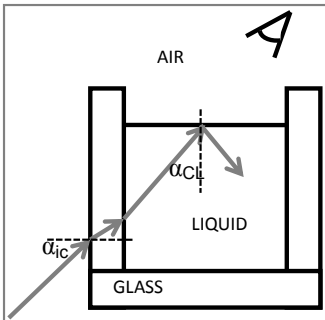**Figure 3b.** Fingerprint not visible

There is a critical angle that separates two different images. For smaller angles, we see blurred image of a whole finger and its surrounding. For greater angles, only clear image of a fingerprint can be observed. The existence of a critical angle related this phenomenon to total reflection, which became our main idea in explaining it. Another two properties of light were important: refraction of light and optical tunneling. The phenomenon of optical tunneling distinguishes the ridges and the grooves of a fingerprint, since they do not affect the light in the same way. It was also investigated

how the image and its intensity changes over some angle interval around the critical angle.

Two main questions were studied in this paper: Why nothing outside the glass is visible? And why such clear image of a fingerprint is visible? The main goal of this paper was to answer these questions and to give a good understanding of the phenomenon.

Theory

If a light ray comes outside of the glass, it can be totally reflected from the surface of the liquid, which means it will not get to the observer's eye (fig.4). We used Snell's law ($n_i sin\alpha_i = n_t sin\alpha_t$, where *i* stands for "incident", and *t* for "transmitted") for air-glass and glass-liquidinterface and the law of total reflection for liquid-air interface ($sin\alpha_{CL} = \frac{1}{n_L}$ where α_{CL} is the critical angle at which total reflection occurs on a liquid-air interface, and n_L is the index of refraction of liquid). With little trigonometry we obtained theexpression $sin\alpha_{ic} = \sqrt{n_L^2 - 1}$. Angle α_{ic} is the critical incident angle at whichtotal reflection occurs. For every incident angle smaller than this one, the light will get totally reflected and the observer will not see the light ray. In this case, since the whole ray is reflected, there is not any energy loss. For angles greater thanα_{ic}, light ray will be refracted at the liquid-air interface and will get to the observer's eye. When the light is refracted and goes to another medium, there is always some percentage of light that gets reflected. Due to conservation of energy, intensity of a light ray that leaves the water will be smaller than the intensity of the incident ray.

Figure 4. Light ray from outside not coming to the observer's eye

When we observe the fingerprint pattern, the distance *d* between the ridges and the glass is very small, almost negligible (d ≈λ, wavelength of light).This causes the phenomenon of optical tunneling.[3] [4] [5]Light travels in optically densermedium and reaches less dense medium at the angle greater than the angle of total reflection. In the normal conditions of only two media, the light is totally reflected back to the first medium. But, if the third medium is put very closely to the first two media, (d≈ 10^{-7}m), the light will not get totally reflected, but will manage to pass to the second and the third medium. This is because, at the end of every medium, an exponentially decayed light wave exists. If there is the third medium put very close, electric and magnetic oscillations will pass to the third medium before they exponentially disappear in the second medium. Lightthat incidents glass-air interface(Fig.5a) will not get totally reflected if there is a ridge very close to the glass. In this case light passes through and gets absorbed and scattered by the ridge. It comes to the observer's eye with smaller intensity, same as the light rays from surrounding behind the glass, explained above. The distance between grooves and the glass is much bigger, thus optical tunneling does not appear because exponential wave in the air decays much before it would reach the groove.Light totally reflects and comes to the observer with the full intensity. Thus, fingerprints are visible if the light incidents the glass-air interface with the angle

greater than the critical angle for total reflection (for glass n_G=1.5, $\sin \alpha_{CG} = \frac{1}{n_G} \rightarrow$ α=42°). By using this law and general Snell's law ($n_L \sin\beta = n_G \sin\alpha$),we can theoretically determine critical *observing* angle α_0: $\cos\alpha_0 = \sqrt{n_L^2 - 1}$ (fig.5a). For every angle greater than α_0, fingerprint pattern will be observed. We see that the only relevant parameter for the occurrence of this phenomenon is index of refraction of a liquid. With more geometrical approach, we can determine the expression for *D*, the distance at which the light ray leaves the water:
$D = (h - dtg\alpha_{CG})tg\beta$ which is then used for the experimental determination of the
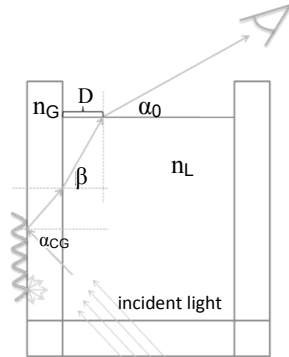
Figure 5a. Deriving expression for the critical angle
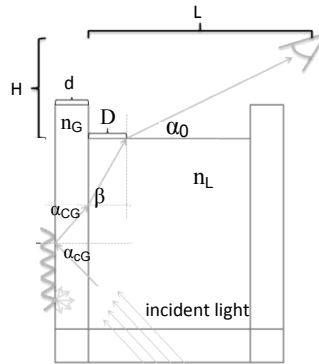
Figure 5b. Experimental determination of the critical angle

observing angle: $tg\alpha_0 = \frac{H}{L-D}$ (fig.5b), where H is the height of observer's eye and L is the observer's distance from the pattern. By doing measurements it was possible to compare the results with the theoretical expression. The problem with this phenomenon is that it is NOT binary. When light travels between two media of different indices of refraction, both reflection and refraction occur at the interface of the media. The ratio of intensities of reflected and refracted light depends on the incident angle and it can be predicted using Fresnel's equation [6]:

$$r = \frac{1}{2}\left(\frac{n_i \cos\theta_i - n_t \cos\theta_t}{n_i \cos\theta_i + n_t \cos\theta_t}\right)^2 + \frac{1}{2}\left(\frac{n_i \cos\theta_t - n_t \cos\theta_i}{n_i \cos\theta_t + n_t \cos\theta_i}\right)^2$$

r – reflectance (ratio of reflected and total light intensity)

t – transmittance (ratio of transmitted and total light intenstiy)

index i – incident angle, first medium

index t – transmitted angle, second medium

and $t = 1 - r$

From this equation, the angle of total internal reflection can be calculated for any two given media → the reflectance in that case is 1 (all light is reflected). We now see that the critical angle can only be approximately determined, because the intensity of the image (the finger) changes from maximum to minimum value over some interval of angles.
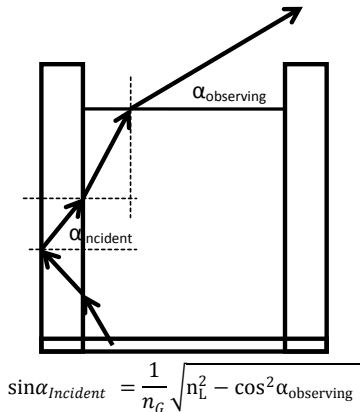
$$\sin\alpha_{Incident} = \frac{1}{n_G}\sqrt{n_L^2 - \cos^2\alpha_{observing}}$$

Figur 7. Conection between incident and observing angle
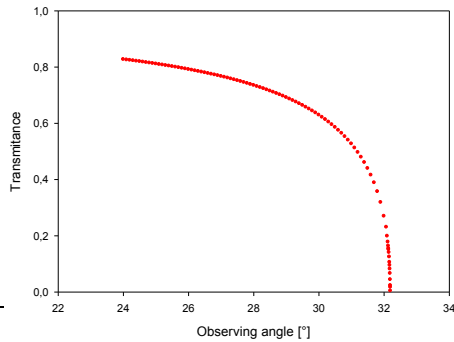
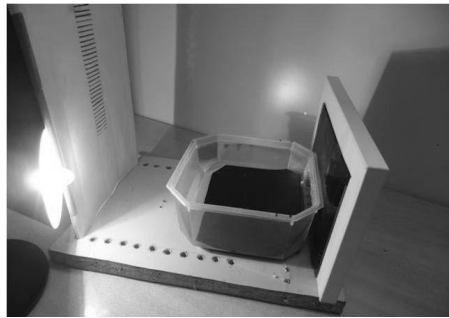**Graph 1.** Transmitance in dependance on observing angle (theoretical)

The angle of incidence and the observing angle are connected. Thus, using the above equation, a theoretical graph can be obtained, showing the dependence of transmittance of light through the glass (i.e. visibility) in dependence on the observing angle. This graph was later compared to experimental results to prove the non-binary shift from the whole finger image to fingerprint image.

Experiment

The experiment consisted of a few parts: measuring indices of refraction for 4 liquids (water with different concentrations of sugar), determining critical observing angle, and determining the intensity of light for different observing angles.

Indices of refraction were determined using a semi-circular vessel in which the liquid was put. With three needles one light ray was defined, and by measuring the incident and transmitted angle, one could determine the index of refraction. For determining critical observing angle, experimental setup was made. Rectangular

Figure 8. Experimental setup

vessel with water had one glass side for observing the patterns. This setup was observed through "windows" which enabled us to control the height of observing. For every height, the distance from the pattern was determined (for critical observing angle). From the height-distance graph, observing angle was determined. This was done for

every measured index and compared to the theoretical result. To show experimentally that the phenomenon was not binary, a photo of an image was taken and analyzed in a computer program. The graph showing the intensity of light in dependence on the depth of observed image was obtained. Dependence of depth on the observing angle can easily be derived using a little geometry and trigonometry → by transforming depthaxis to observing angle axis, we got the graph that was compared to theoretical graph that we got using Fresnel's equations.
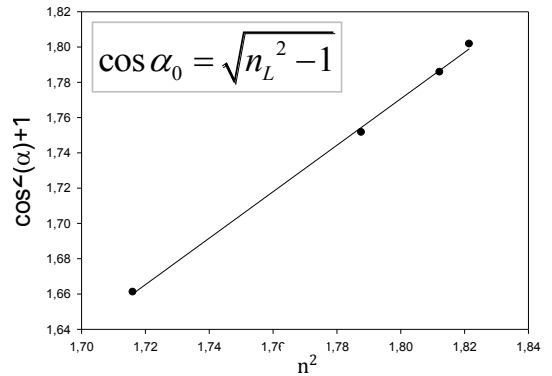
Results

4 indices of refraction were determined. For every index, the critical angle was determined experimentally and then compared to the theoretical value.

Table 1. Indices of refraction

Indices of refraction
$n_1 = 1,310 \pm 0,020$ (pure water)
$n_2 = 1,340 \pm 0,010$
$n_3 = 1,346 \pm 0,014$
$n_4 = 1,350 \pm 0,030$

$$\operatorname{tg}\alpha_0 = \frac{H}{L-D}(slope)$$
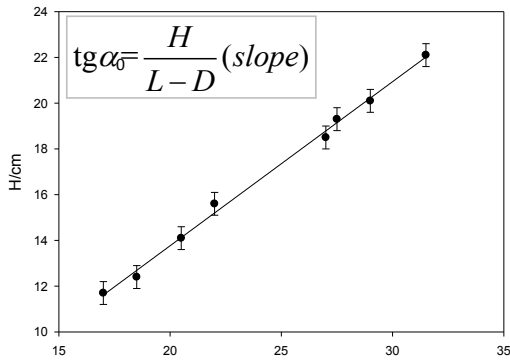
Graph 2. Height-distance dependence


$$\cos\alpha_0 = \sqrt{n_L^2 - 1}$$

Graph 3. Critical angle-index of refraction dependence

From the first graph we obtained critical angle as a slope of the graph. For $n_1=1,31$ the theoretical value of critical observing angle is 32°, while measurements give the value of 35°. The agreement is satisfactory. On the second graph we can see the relation between critical angle (little transformed expression) and the index of refraction. From theory, we expected the slope to be 1, but we got the experimental slope 1,3.

Intensity measurement was done for a bigger piece of paper – that way we could observe the effect for different angles at the same time and compare how transmittance changed with depth→observing angle.

We got the intensity in dependance on depth of the pattern. By transforming the depth into observing angle, the graph was obtained that could be compared to theoretical graph. We got the dependance of intensity (transmittance) on the observing angle. We can see that the phenomenon really is not binary and that intensity change from the whole finger to only fingerprint pattern happens in interval of 3°.
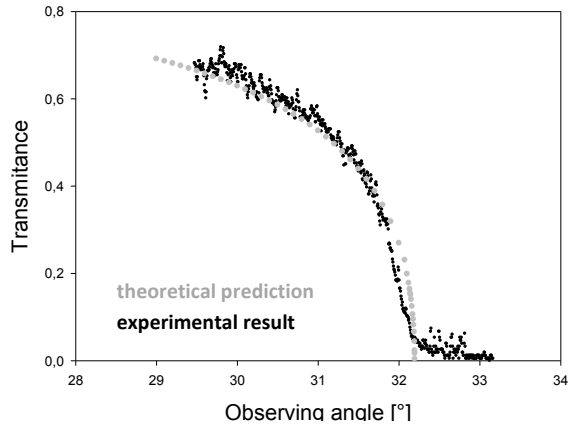
Graph 4. Intensity of light coming from the outside of the glass – grey: theoretical curve, black: experimental curve

These 3° goes into our estimated error in determining critical angle. That is why, although transmitivity change exists, we can not actually percieve it with our own eye successfully and for us the phenomenon seems binary, although it is not.

Conclusion

In this paper the phenomenon of clear image of fingerprints on a glass of water was studied and explained. The main reasons for this effect to occur are total reflection and optical tunneling. When the angle is greater than the critical angle of total reflection, on the ridges light will tunnel and be absorbed and then scattered by the finger surface. This we see as light with lower intensity and in skin colour. On the grooves, light will only get totally reflected and will come to the observer with the whole intensity. That we do not see as skin colour, but as the reflected light from the bottom of the glass (from the light's direction). Nothing outside of the glass is visible because of total internal reflection on the water surface. The light that manage to pass through and get to the observer's eye has a very low intensity due to lots of refractions and energy losses. The phenomenon was described using formulas which were then validate by experimental measurements. The error exists, but it is not big and experimental results can be compared to theoretical predictions. The change in image intensity was also studied and it was shown that transmittance of the light from outside of the glass (from the finger) changes from maximum to minumum value over a few degrees near the critical angle.

References

[1]Martchenko, I. (2011). "Preparation to the Young Physicists' Tournaments' 2011". (http://ilyam.org/Draft_2011_IYPT_Reference_kit_IM.pdf)
[2] Gorb, S. N. (2007). "Visualisation of Native Surfaces by Two-Step Molding". Microscopy Today, March 2007, pp. 44-46.
[3] Han, J. Y. (2005). "Low-cost multi-touch sensing through frustrated total internal reflection." Proceedings of the 18th annual ACM symposium on User interface software and technology UIST 05, p, 115. ACM Press.(http://www.cs.ucf.edu/courses/cap6105/fall2010/readings/Multi-TouchInterface_FTIR.pdf)
[4] Vörös, Z., and Johnsen, R. (2008). "A simple demonstration of frustrated total internal reflection". American Journal of Physics, Vol. 76, Issue 8, pp. 746-749.

[5] You, Y., Wang, X., Wang, S., Pan, Y., Zhou, J. (2008). "A new method to demonstrate frustrated total internal reflectionin the visible band". American Journal of Physics, Vol. 76, Issue 3, pp. 224-228.
[6] Fresnel's equations – http://en.wikipedia.org/wiki/Fresnel_equations

No. 12, Levitating spinner: Motion and stability of Levitron, simulation and time resolved experiments

AlirezaTahmaseb Zadeh[1]
Reza MontazeriNamin[2]
[*] Team of Iran, IYPT 2011
[1]*School of Electrical and Computer Engineering, University of Tehran, I.R Iran*
[2]*School of Mechanical Engineering, Sharif University of Technology, I.R Iran*
Corresponding authors: info@tami-co.com (A. T. Z.), namin@mech.sharif.edu (R. M. N.)

Abstract

A levitating spinner system is a toy consisted of a spinning magnetic top which levitates above a magnetic base for several minutes without being in touch with an external object. In the present paper the authors have developed a numerical solution which is able to fully simulate the motion of the top according to the basic principles. The magnets have been modeled as electric current loops. Next, physical experiments have been developed in terms of magnetic field, force and top's motion. Image processing has been made to get quantitative data of the motion of the top. Based on the acceptable agreement between the experiments and numerical results, the simulation program is used to demonstrate all the limitations of the levitating systems.

Introduction

The Levitron™ is a toy consisted of a magnetic spinning top and a magnetic base (usually a tube or box magnet). The equilibrium of the system in the vertical direction is a result of the equality of the weight and magnetic force in opposite directions. According to Earnshaw's theorem of 1842 [1], the stability of such a system cannot be explained if the rotation axis of the top remains vertical. The stability against the flipping and direction change of the top is a result of the top's rotation as a gyroscopic motion; however position stability in the vertical and horizontal directions cannot be obtained easily. As proposed by Simon et al.[2], this stability must be a result of the orientationchanges of the top, so this phenomenon must be investigated dynamically.As reported by the manufacturers[3], there is a very precise and narrow range of top's mass and base dimensions to cause the stable motion. We will investigate the effect of the mass, the upper and lower spin limits and initial perturbations in radial and vertical directions. Our experiments and investigation was based on Levitron® Platinum Prowhich's properties could be found at [3].

Force Evaluation

There are two magnets present in this system and we must be able to find the force and torques that they exert to each other. The magnets were modeled as electric current loops. Every small length of one current causes a magnetic field on every point on the other magnet as mentioned by the Biot-Savart law:

$$\vec{B} = \frac{\mu_0}{4\pi} \int i \; \frac{\vec{dl} \times \vec{r}}{|\vec{r}|^3} \qquad (1)$$

Integrating all the fields caused by every small length on the bottom magnet, the magnetic field on every top magnet's points would be computed. Now at the top magnet, since there is a current in the presence of the magnetic field, magnetic force occurs, known as the Lorenz Force:

$$\vec{F} = \int i' \overrightarrow{dl'} \times \vec{B} \qquad\qquad (2)$$

A single current loop simulates a simple cylindrical magnet. To simulate a Tube magnet, we assumed it to be two current loops in each other one with a smaller radius; cancelling the magnetizationof the inner area; the outer loop causes a positive magnetization in the entire aria, while the inner loop cancels the magnetization with the same current but opposite direction. The radios of the outer and inner loops were physically measured to 12 cm and 9 cm respectively.These current loops should be considered to be distributed in the width of the tube,
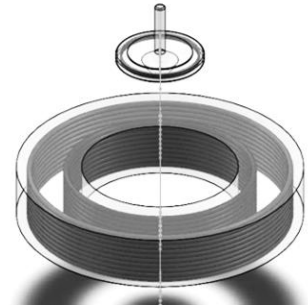
Figure 1: Modeling

therefore *n=10* current loops were assumed to get precise results (Figure 1).

A C++ program was developed to do the calculations. The input parameters were r_i and r_o, the inner and outer radius of the bottom magnet, *d* the thickness of the bottom magnet, r_t and d_t the radius and thickness of the top magnet;**r** vector and **orientation** vector; parameters describing the position and orientation of the top magnet despite the bottom magnet.*I*, the current intensity was also given to the program as a parameter that describes the magnet strength and was to be calibrated later in experiments.

Next numerical force evaluation was confirmed experimentally. Orientation of the magnetic field was measured experimentally using a needle compass and compared tonumerical results (Figure 2) in 13 different points which showed an acceptable match (Figure 3a). Next, to measure the magnetic force in different heights,a scale with the precession of 0.001g was used. The base magnet was put on the scale, the top magnet was positioned in several distances (*d*) in the symmetric axis, and the force on the scale illustrated the magnetic force.This experiment also showed a good match (Figure 3b).
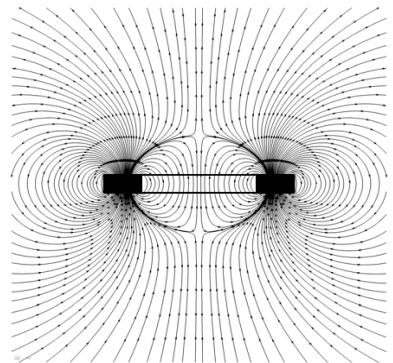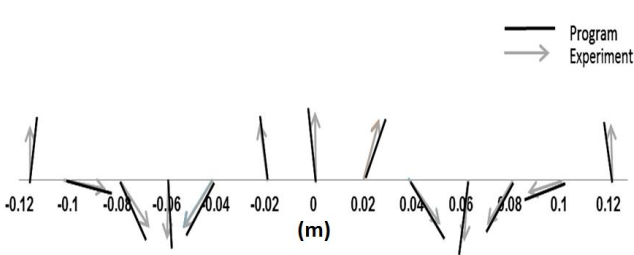

Figure 2: Field Orientation

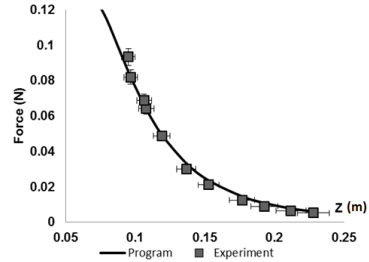**Figure 3a:** Field Orientation Experiment

Figure 3b: Force Experiment

Stability

As a result of the previous section, we had a function that could output the forces and momentum on the spinning top based on its position and orientation. The top's height must be justified to equalize the magnetic repulsion and weight. As it is illustrated by figure 5a, there are two possible points in vertical plane allowing the equilibrium. As figure 5b shows, equilibriumexists in radial direction in all heights. But equilibrium is not enough, the stability must also be considered. It must be satisfied that after when the conditions defer than the equilibrium condition, the top gets back to equilibrium point (*i.e.* the partial deviation of force despite displacement must be negative in every direction).

Figure 4: Video Analysis

The force simulation results showed that in the case when the top's orientation remains vertical, the stability cannot exist in both directions (This could be proven analytically as well[2]).In the case when the top is free to orient itself parallel to the field lines in its location, there will appear a small range of height where stability occurs in both directions (Figures 5c and 5d).The equilibrium condition relates the height of levitation to the top mass. Considering this point, the mass range in which levitation is possible is calculated in every levitating system. This range happens to be 20.3*g* to 21.1 *g* for our set of magnets.
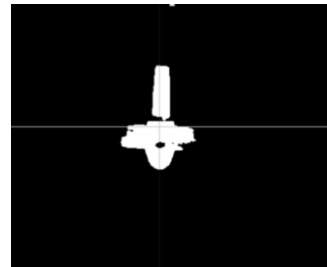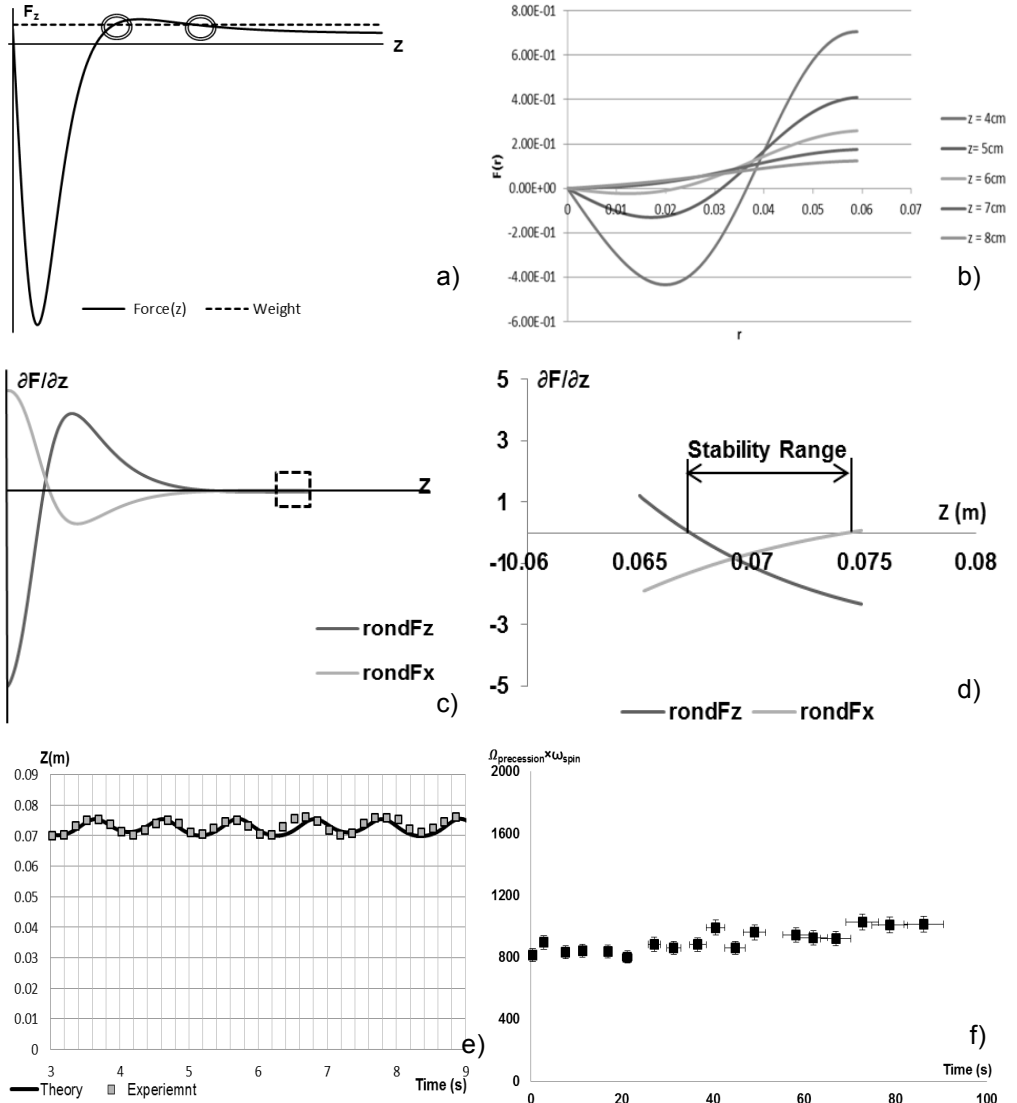
Figure 5: a) Force in vertical direction; equality of magnetic force and weight in two points b) Force in horizontal direction; Equilibrium at different heights c) Partial derivatives of force in vertical and radial direction; the dashed box is zoomed next graph d) Small range of stability e) Motion in vertical direction experiment; high agreement between video analyzed data and simulation program f) Multiplication spin frequency and precession frequency versus time; constant line confirming theory

Simulation Program

To get more information about the levitation and find out the dynamic conditions in which levitation is possible, the motion of the spinning top was to be fully simulated. The governing equations include the equations of linear motion and an equation regarding the angular momentum and torque:

$$\frac{d\vec{r}}{dt} = \vec{v} \tag{3}$$

$$m\frac{d\vec{v}}{dt} = \vec{F} \tag{4}$$

$$\frac{d\vec{L}}{dt} = \vec{\tau} \tag{5}$$

We assumed the top to have a high enough angular velocity so that the orientation of the angular momentum is the same as the orientation of the magnetic moment. We used the second order Runge-Kutta numerical method to solve the equations above. The simulations need the angular velocity and initial conditions as inputs, as well as all the parameters needed to find the force and torque.

Discussion

The motion could be analyzed in vertical and horizontal plane.

A) **Vertical Plane:**The top is in a stable equilibrium in vertical direction. Therefore a small perturbation in that direction leads to an oscillation. The oscillation is obvious in simulation program motion graphs (Figure 6a). To experiment this motion physically, high speed videos of 1000 Frames per Second were recorded. An image processing program was developed using MATLAB®, which could convert these motion videos to graphs (Figure 4). The results did show a great agreement between the theory and experiments, assuring that the numerical theory is functioning correct (Figure 5e). This oscillation happens only if the initial perturbation in vertical direction is less than a critical amount (Figure 6c). This shows the maximum initial velocity for the motion.For our set of magnets, the amount of critical initial velocity was found to be $\dot{z}$=8.5 mm/s.

*B)***Horizontal Plane:**The top gains a precession spin in addition to its spin frequency which is a result of gyroscopic action.The results of the numerical simulation also illustratethis motion (Figure 6b). Simulation program results also suggest that precession frequency is inversely proportional to the spin frequency. This was checked experimentally using high speed videos, again showing a good match between the theory and the experiments (Figure 5f).

It was observed that the top would have a curved motion back to the initial position when gained a velocity in the radial direction.If this initial velocity is more than a critical amount, the top will be thrown away (Figure 6g). The amount of critical initial velocity was found to be $\dot{r}$=12 mm/s using the simulation program.
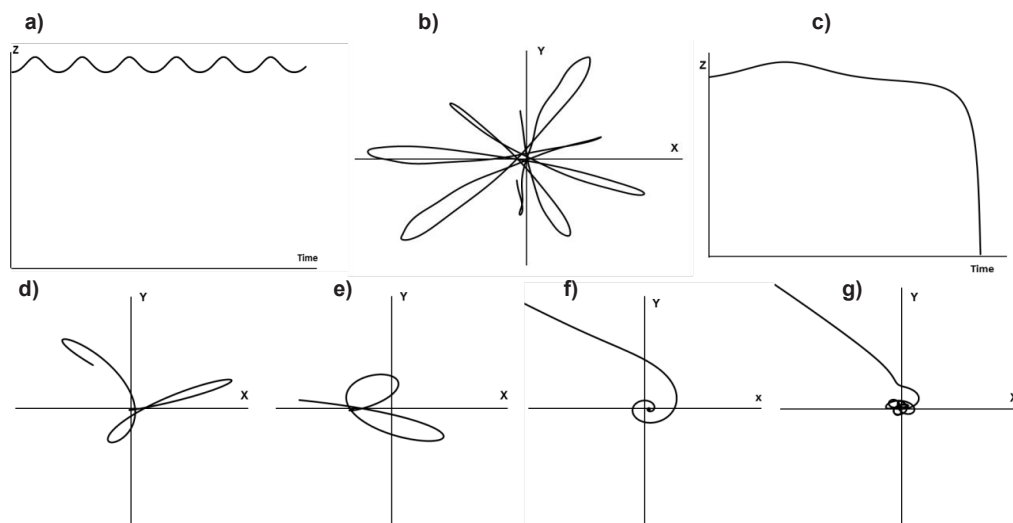
Figure 6: a) Oscillatory motion in vertical plane b) Curved returning motion in horizontal plane c) Out of range initial vertical velocity 10 mm/s; the top is pulled to the base d) Returning curve in spin frequency 180 Rad/s e) Returning Curve in spin frequency 280 Rad/s; bigger curves in comparison with previous graph f) Out of range spin frequency 330 Rad/s; passing the upper spin limit g) Out of range initial radial velocity 15 mm/s; the top is thrown away

While the increase of the angular velocity causes more stability against flipping, the axis of the top becomes too rigid; where the top cannot orient quickly enough with the field lines.This leads to an upper spin limit for the top which is ω_{upper}=311 Rad/s for our system (Figures 6d, 6e and 6f). If the top is spun too slowly, then the top becomes unstable against rotations. The top will then flip over and will be pulled quickly to the base. This is the instability that is well known from classical top physics. This amount was found experimentally using a tachometer detecting one point on the top. For our levitating system, it was ω_{lower}=118±5 Rad/s.

Conclusion

The theory and modeling of the magnets was applied to a simulation program to demonstrate the motion of the top. The simulation, works as well, in every other shapes and dimensions of magnets to calculate the motion of the top as a function of time. Using this program, the optimum dimensions of magnets to provide greater levitation heights or higher stability, could be found to design better levitating spinner systems.

References

[1] S. Earnshaw, Trans. *Cambridge Philos*. Soc. 7, 97-112

[2] Martin D. Simon, Lee O Heflinger, Torrance CA, SLRidgway 1997 Spin Stabilized Magnetic Levitation, Am J. Physc. 65 (4)

[3] *Levitron Physics*. (n.d.). Retrieved from Levitron Official Website: http://www.levitron.com/physics.html

[4] Roger F Gans, Thomas B Jones, Masao Washizu 1997, Dynamics of the Levitron, J. Phys. D: Appl. Phys. **31**

[5] S. Gov, S. Shtrikman, H. Thomas 1998, On the Dynamical Stability of The Hovering Magnetic Top

No. 13, Light bulb: Efficiency measurement via a calorimetric technique

Katja Kustura [1]
[*] Team of Croatia, IYPT 2011
[1] *University of Zagreb, Croatia*
Corresponding author: katja_kustura@hotmail.com (K. K.)

Introduction

Determining efficiency of a light bulb is a very useful task, since light bulb is a very present and widely used object in everyday life. This was our task in this year's IYPT problem – the goal was to determine the ratio between the thermal energy and the light energy emitted from a small electric bulb depending on the voltage applied to the bulb. Our first and main plan was to distinguish useful part of emitted energy (light) from the energy losses (heat).

We approached this problem in two different ways. First, calorimetric method was used to experimentally separate light and thermal energy and to determine the ratio. Besides this method, theoretical method was proposed and developed, by using Planck's law of radiation and approximating the light bulb as a grey body.

The light bulb

The light bulb filament is a resistor. Electrical current causes heating. When heated to the temperatures high enough, the filament emits light. The law of conservation of energy for a light bulb is: electrical energy → thermal energy + light. The energy is transferred in three ways:
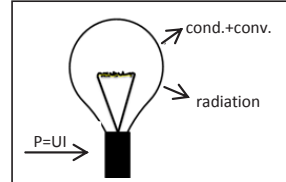
Figure 1. Transfer of energy

conduction, convection and radiation (fig.1) [1]. Conduction is heat transfer by direct contact (wires, glass). Convection is heat transfer by gases, caused by buoyancy (warmer gas is lighter and thus moves upwards, transfering the energy). By conduction and convection, the electrical energy is converted to thermal energy. Since the main purpose of a light bulb is producing light, conduction and convection are the causes of energy loss. The third way of energy transfer is radiation. All bodies with temperature T>0K emit continuous electromagnetic spectrum. They radiate waves of all wavelengths, which means ultraviolet, visible, infrared, microwaves… Planck's law of radiation explains the radiation and gives a connection between intensity of emitted light and the wavelengths, for a given temperature (fig.2). On higher temperatures, the

$$I(\lambda, T) = \frac{2hc^2}{\lambda^5} \frac{1}{e^{\frac{hc}{\lambda kT}} - 1}$$
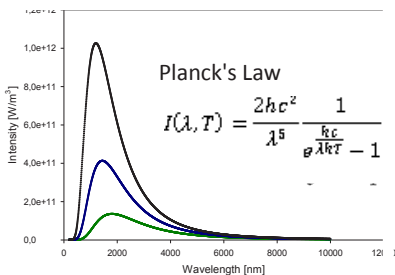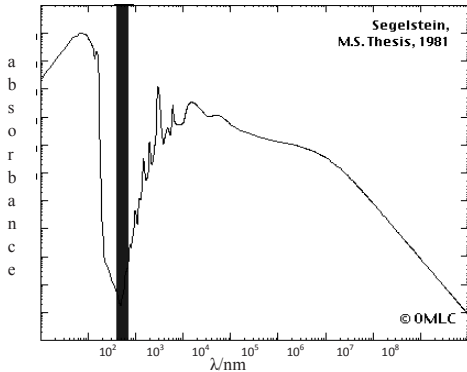
Figure 2. Black body radiation for 3 different temperatures

total intensity is higher. A little part of the spectrum (390 – 750 nm) is visible. Human eye can only detect light at higher temperatures (because of the greater intensity). This is why the light bulb is heated in the first place – for the light to be detected.

We defined efficiency of a light bulb as a ratio between visible energy (useful) and electrical energy (total) $\eta = \frac{P_{visible}}{UI}$.

Calorimetry method

The idea of this experiment was to separate infrared and visible part of the spectrum. The bulb mostly radiates in the infrared part of the spectrum, which means that the most of its radiation energy goes to thermal energy. Separating the little part of light energy may seem as a difficult task. For this purpose, a very precise experimental setup was made to detect the light. The most famous and the most affordable visible light filter is water. It has a very high absorbance factor for all the spectrum, except for that little part of visible light [2] (fig.3). The only flaw of this filter is that it does not absorb the radiation 300 – 900 nm. This interval is a little greater than the interval of visible light, so a little amount of infrared and ultraviolet radiation is not absorbed, which caused small error in experiment. But, the results were still valid since they were comparable with the already obtained values (from the literature).

The light bulb was put in the glass vessel with water and turned on. Due to water absorbance factor for each wavelength, only visible light passed through the vessel (fig.4a). The rest of the spectrum stayed in the vessel and heated the water. The water temperature was measured with the precision of $10^{-4}K$. Graph showing the change of temperature in time was obtained (graph 1). The measurement was repeated, but this time *carbon* was put inside the water, which made it black, not transparent for visible light (fig.4b). All the energy produced by the light bulb stayed in the water and heated it.

Figure 3. Absorbance factor of water [3]

We obtained another temperature-time graph. By comparing heating rates we
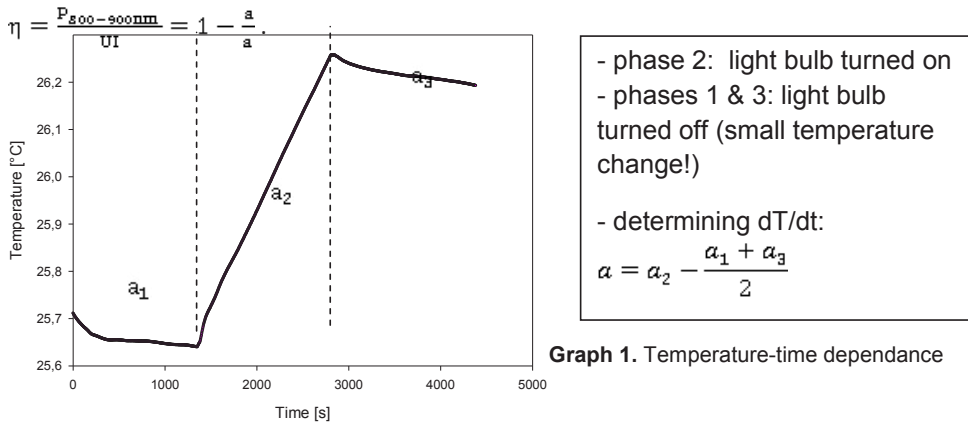

Figure 4a. Light passing through

Figure 4b. Light not passing through

measured the ratio between visible and total energy (efficiency of a light bulb). Power heating the water in the first case: $P_1 = UI - P_{300-900nm} = C\left(\frac{dT}{dt}\right)_1 = Ca$. Power heating the water in the second case: $P_2 = UI = C\left(\frac{dT}{dt}\right)_2 = Ca'$. Here C is heat capacity of the system, and a, a' are heating rates – slopes in T-t diagrams. Efficiency of a light bulb is

$$\eta = \frac{P_{300-900nm}}{UI} = 1 - \frac{a}{a'}.$$

- phase 2: light bulb turned on
- phases 1 & 3: light bulb turned off (small temperature change!)

- determining dT/dt:

$$\alpha = \alpha_2 - \frac{\alpha_1 + \alpha_3}{2}$$

Graph 1. Temperature-time dependance
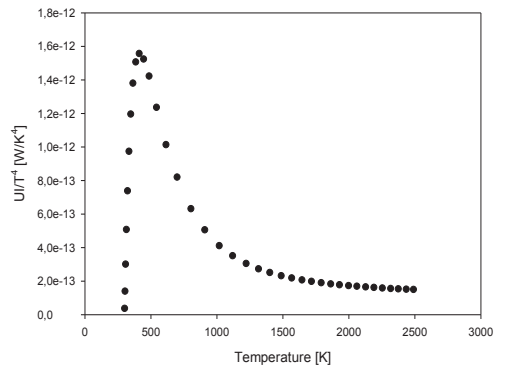
Black body method

Light bulb was considered a grey body. It behaves as a non ideal black body – it radiates electromagnetic spectrum with the intensity dependant on temperature, but with emissivity factor ε (constant over all wavelengths and temperatures). Stefan-Boltzman law: $\sigma S \varepsilon T^4 = P_{visible} + P_{IR}$ where S is the surface of the body, and T its temperature (here we neglected all the other parts of the spectrum, ultraviolet, microwaves… because these energies are much smaller than in infrared and visible spectrum). If we relate this law to law of conservation of energy, we can derive the ratio $\frac{P_{IR}}{P_V}$ as a function of temperature, i.e. $\frac{P_{IR}}{P_V} = f(T)$. The final formula is $\eta = \frac{\sigma S \varepsilon T^4}{UI\left(\frac{P_{IR}}{P_V}+1\right)}$.

Thus, for calculating the efficiency we need to know the temperature of a filament as a function of voltage, value of $\sigma S \varepsilon$ constant and ratio of powers P_{IR}/P_V as a function of voltage.

From the literature, we knew the connection between filament resistivity and temperature [4]. Measuring U-I characteristics of a bulb, we determined resistance (in dependence on voltage). By knowing the resistance at the room temperature, with little transformations we got final graph showing the dependence of temperature of a filament on a voltage applied (graph 2).
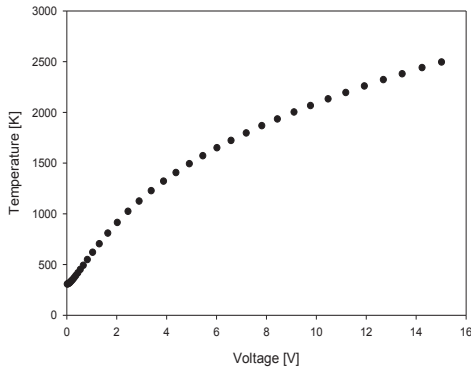
Graph 2. Temperature – voltage dependance   **Graph 3.** UI/T^4 – temeprature dependance

We rewrite the law of conservation of energy: $UI = \alpha(T - T_0) + \sigma S \varepsilon (T^4 - T_0^4)$, where the first member is due to conduction and convection, and the second is from radiation. We can write this as $\frac{UI}{T^4 - T_0^4} = \frac{\alpha(T - T_0)}{T^4 - T_0^4} + \sigma S \varepsilon$. It is obvious that for $T \gg T_0$ value UI/T equals $\sigma S \varepsilon$. From this graph the constant $\sigma S \varepsilon$ was determined (graph 3) [5].

The program was created in C programming language to determine the ratio P_{IR}/P_v as a function of temperature. In this program the only input was the temperature. The program then plotted Planck's curve and numerically integrated the visible part of the spectrum (the limits were 300 – 900 nm) and then the ratio of visible and total energy was calculated. This result was compared with the result obtained in the calorimetry method.

Final results

By calorimetry method, efficiency of light bulb (ratio P_{IR}/P_v) was determined for 4 different voltages. Using black body method, we got theoretical predictions for a light bulb for a greater interval of voltages. The results were put on the same graph to compare the methods. In the experimental setup, light of wavelengths 300 – 900 nm was considered visible light (because water did not absorb that part of the spectrum and we were able to separate it from the rest of the spectrum). In our theoretical calculation, limits were the same, because the goal was to compare these two methods for their validation.

From the graph it can be seen that both methods have similar results (graph 4). Theoretical prediction for 300 – 900 nm limits matches the experimental results. Although in our limits we took 300 – 900 nm instead of a smaller interval of visible part of the spectrum, from this results we see that the theory is valid, which means that it can be used to determine the real efficiency of a light bulb (limits 390 -750 nm). Finally, since the initial task was to determine the ratio between the thermal energy and the light energy, that is what we did in our last graph (graph 5). The efficiency was

defined as $\eta = \frac{P_V}{UI} = \frac{P_V}{P_V + P_{IR}}$. Transformations of the expression lead to formula $\frac{P_{IR}}{P_V} = \frac{1}{\eta} - 1$.
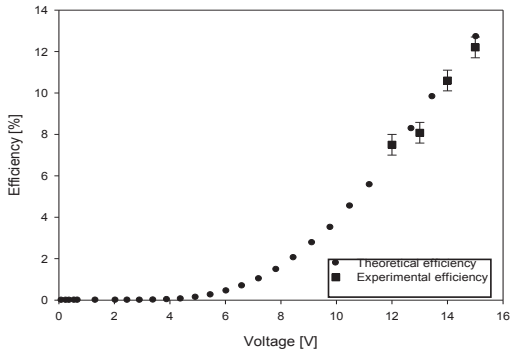
Graph 4. Efficiency – voltage dependance
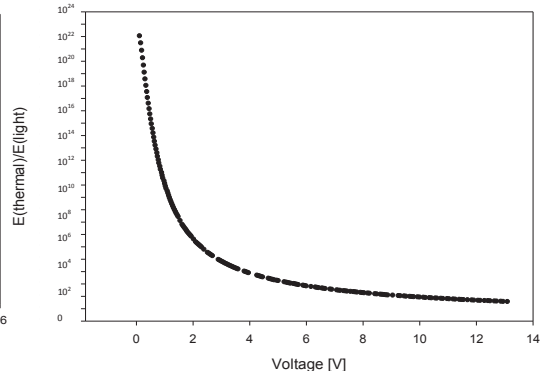
Graph 5. Ratio P_{IR}/P_V – voltage dependance (real light limits)

Conclusion

In this paper the efficiency of a light bulb was studied and determined. Two methods were proposed. We experimentally determined efficiency using calorimetry method. In this experiment we assumed that the visible part of the electromagnetic spectrum was 300 – 900 nm, because these are the limits in which water does not absorb the radiation. This property of water was used to separate the light energy from the thermal energy. The results were then compared with the expected results that we got using our theoretical method. In this method we created a program that calculated P_{IR}/P_V ratio for each temperature, in wanted limits. For limits 300 – 900 nm, the theoretical results were compared with our experimental values. Two approaches showed a good agreement. Once we confirmed our theoretical method, we changed the limits in the program to 390 – 750 nm and obtained the final results and the dependance of the ratio of the thermal and visible energy on voltage applied to the bulb.

References
[1] Martchenko, I. (2011). "Preparation to the Young Physicists' Tournaments' 2011". (http://ilyam.org/Draft_2011_IYPT_Reference_kit_IM.pdf)
[2] Hale, G.M., and Querry, M.R. (1973). "Optical constants of water in the 200 nm to 200 μm wavelength region". Applied Optics, Vol. 12, Issue 3, pp. 555-563.
[3] Segelstein, D. (1981). "The Complex Refractive Index of Water". M.S.Thesis, University of Missouri, Kansas City (http://people.seas.harvard.edu/~jones/es151/gallery/images/absorp_water.html)
[4] Jones, H.A., (1926). "A temperature scale for tungsten". Physical review, Vol. 28, pp. 202-207.
[5] de Izarra, C., and Gitton, J.M. (2010). '' Calibration and temperature profile of a tungsten filament lamp". European Journal of Physics, Vol. 31, Issue 4, pp. 933.

No. 13, Light bulb: Numerical and experimental evaluation of the efficiency

Reza MontazeriNamin[1] and AlirezaTahmasebZadeh[2]
[*] Team of Iran, IYPT 2011
[1]*School of Mechanical Engineering, Sharif University of Technology, I. R. Iran.*
[2]*School of Electrical and Computer Engineering, University of Tehran, I. R. Iran*
Corresponding authors: namin@mech.sharif.edu (R. M. N.), info@tami-co.com (A. T. Z.)

Abstract

The present paper is a theoretical and experimental investigation on the efficiency of incandescent light as a function of applied voltage. Theoretically, radiation is modeled in means of the Planck function, and heat is modeled considering convection and conduction. Experimentally, the luminous power is measured using an Integral Sphere, where luminous efficiency is considered, to estimate the radiation.Heat flux is measured in means of the changes of surrounding water temperature in the designed setup. The precise agreement between the theoretical predictions and experimental results proves the theory, which leads to a final conclusion on the efficiency of the bulb as a function of applied voltage.

Introduction

An incandescent light bulb is consisted of three main parts; tungsten filament, inert gas and glass mount.When electric current passes through the filament, it raises the temperature. This heated filament emits energy in two ways; one is Electromagnetic radiation and the other is heat flux. In the steady state, where the temperature of all the parts remains constant, all the given electrical power transforms into these two kinds.

$$P = IV = P(\text{rad}) + P(\text{heat}) \tag{1}$$

Heat flux happens in two levels. First is the convection in the inert gas, transferring the heat energy from the filament to the inner layer of the glass mount. Second is the conduction in the glass surface.
Electromagnetic radiation is either in the visible and invisible spectrum. However, only the visible part is used for illumination. In addition, illumination of different wavelengths in the visible spectrum is also different. This difference is described in means of luminosity function. This function, demonstrates a coefficient between zero and one for every wavelength, describing the sensitivity of human eye to the specific wavelength.
Efficiency is normally defined as the ratio between efficient work and given energy. For lamps, which are aimed for illumination, the efficiency could be defined more precisely. In this research, it is defined as the ratio between the energy of the part of the radiation that is used for illumination and all the given electrical power.

$$Ra = \frac{P_{\text{illumination}}}{P_{\text{total}}} \tag{2}$$

Theory

- **Heat Flux**

Since the heat transfer is a sum of the transfers by convection and conduction, and both convection and conduction have anenergy transfer rate proportional to the temperature difference, the total energy transfer is proportional to the differences of temperature of the filament surface and the temperature of the environment far from the light bulb. The coefficient must be determined experimentally.

$$P(heat) = K(T - Tout) \tag{3}$$

- **Electromagnetic Radiation**

The tungsten filament could be considered as a twisted cylinder, similar to a spring. Assuming R as the radius and L as the length of this cylinder, all the radiation power is found using Stephen-Boltzmann law for a gray body.

$$P(rad) = (2\pi RL)\varepsilon\sigma T^4 = cT^4 \tag{4}$$

ε is the emissivity of the material and c would be determined experimentally.

Some part of this electromagnetic radiation is visible and the other part is invisible. Using Planck Function, power of each of the wavelengths could be found. Planck's law describes the energy emitted at a certain wavelength for different temperatures:

$$J(\lambda, T) = \frac{2hc^2}{\lambda^5} \frac{1}{e^{\frac{hc}{\lambda kT}} - 1} \tag{5}$$

Human eye does not respond equally to different wavelengths. This means that illuminations of different wavelengths are different. Luminosity Function describes the average visual sensitivity of the human eye to light of different wavelengths. This function attributes a coefficient between 0 and 1 for each of the wavelengths in visible spectrum. The amount of this coefficient is absolutely zero for wavelengths in invisible spectrum.
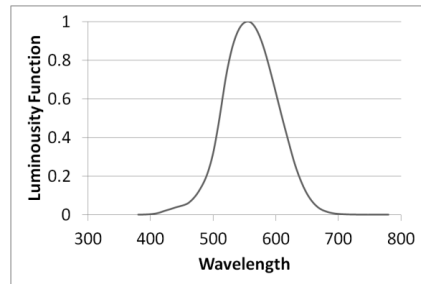

Figure 1: CIE PhotopicV(λ) modified by Judd (1951) and Vos (1978) [also known as CIE V$_M$(λ)]
Ref: http://www.cvrl.org/lumindex.htm

Considering the Luminosity Function, Luminous Efficiency could be defined. This describes the ratio between the amount of electromagnetic radiation which is used for illumination(considering the coefficient of luminosity function) and all the electromagnetic radiation.

$$\text{Luminous Efficiency:} = \frac{\text{Illuminating Radiation}}{\text{Electromagnetic Radiat ion}} := \frac{\int_{\lambda=0}^{\infty} J(\lambda,T)y(\lambda)d\lambda}{\int_{\lambda=0}^{\infty} J(\lambda,T)d\lambda} \tag{6}$$

In which, $J(\lambda, T)$ is Planck Function and $y(\lambda)$ is Luminosity Function.
The calculation of this amount was done using a C++ numerical solution program. This program integrated the terms above to calculate the luminous efficiency using the luminosity function and plank functions.

Luminous Efficiency is found as a function of filament temperature. In case there exists a relation between Voltage and temperature of the filament, the illuminating part of all the given energy could be found (Equation 1).

The amount of special resistivity of tungsten was found using a material Handbook. Measuring the resistivity of our lamp in 300 K, (Bulb is switched off) the resistivity is found as a function of temperature.

$$R(T) = R_0 \left(\frac{T}{T_0}\right)^{1.2048} \tag{7}$$

Where T = 1K leads to R = 0.0692 Ω. Finally, using equation (1) and the resistance function, the equation relating voltage and temperature is found:

$$\frac{V^2}{R(T)} = cT^4 + K(T - Tout) \tag{8}$$

Figure 3: Filament Resistance; Calculated using the resistivity of tungsten and resistance at 300K

Conducting two different Heat and illumination experiments temperature is found in means of Voltage. Therefore, heat and radiation are calculated as a function of Voltage. This results in calculation of efficiency as a function of voltage.
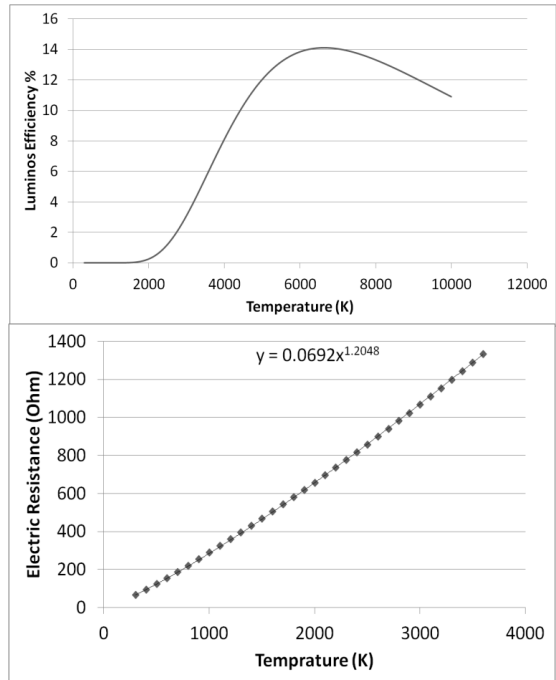
Experiments

Two experiments have been done in order to verify the theory and measure the constants; Heat Experiment and Illumination Experiment.

- **Heat Experiment**

Initially, the temperature of the filament at each voltage is measured in means of the resistance of the filament. The resistance is calculated knowing the current pass and voltage, and resistance as a function of temperature has already been explored.

According to equation (3), theory has predicted that heat flux power is proportional to the temperature difference between the filament and outside air far from the lamp. In these series of experiments, heat flux is measured for difference temperatures and result shows that these amounts are in a linear trend. General idea is to warm up some amount of water using the sample lamp.

A two-layered box was made using Plexiglas. A 20x20cm cubic square was placed in a 25x25cm one and there was air in between. Lamp, digital thermometer were placed in water. When the lamp is switched on, chronometer starts. The difference of temperature of water with its initial temperature is plotted vs. time. Using the data, the heat constant of the theory was found:

$$K = 1.2 \mp 0.2 \text{ mW/K} \qquad (9)$$

Figure 4: The thermal experimental setup

To minimize the heat loss from the container to the environment, in addition to using a two-layered container, the experiments were conducted in a range of 20° difference in temperature. Also the leakage of heat from the box was measured by doing another experiment; turning off the bulb and plotting temperature of water vs. time while it is decreasing. Using the gradient of the mentioned graph, the heat loss was calculated and added to the main graphs. The water may absorb some of the radiation, and show it as heat as an error. Using the Beer-Lambert law, using the absorption coefficientsfor water, glass and Plexiglas less than 5% of the radiation will be reported as heat in the experiments.

Figure 5: the integral sphere used in the illumination experiments, at University of Tehran

- **Illumination Experiment**

The luminous flux of a lamp could be measured using Integral Sphere. This instruments, measures the amount of luminous flux. The given relation for the amount that integral sphere measures follow:

$$\text{Luminous Flux} = F =$$
$$683.002 \frac{\text{lm}}{\text{W}} \int_0^\infty y(\lambda)J(\lambda)d\lambda \qquad (10)$$

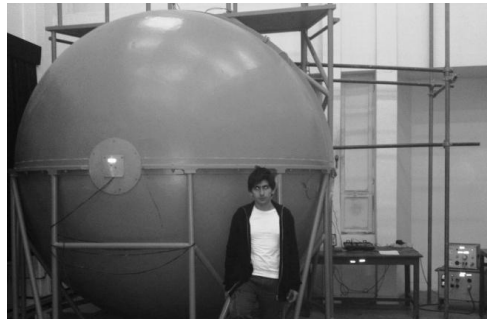**Figure 6:** Analyzed result of the illumination experiments

Using relation (6) and this equation, radiation power is found as a function of temperature of filament. The radiation power vs. T4 was plotted. This graph was linear that shows that our theory and special resistivity are precise. The amount of c was found using this graph:

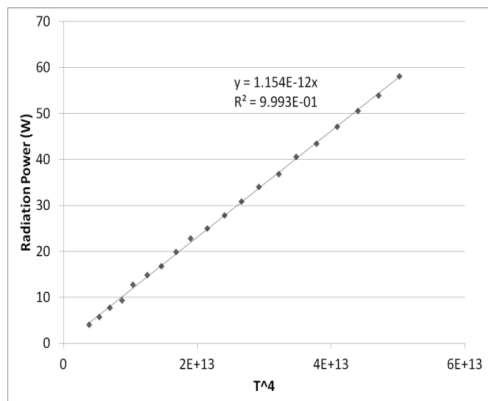$$c = 1.15 \mp 0.02 \times 10^{-12} \text{ W/K}^4 \qquad (11)$$

Results and discussion

Having the amounts of C and K from the experiments, equation (8) was solved numerically to obtain the temperature as a function of voltage. Having the temperature, all the other parameters could be found and results were compared with the theory.

The theoretical predictions match the experimental results very well in various cases, confirming the basic theoretical assumptions and the numerical method validity. So we were allowed to use the numerical solution to describe the efficiency of the light bulb in different voltages. As it is shown in figure 10, the efficiency increases when voltage increases. This increasing has two major reasons as discussed: with voltage increase, the total radiation power increases as in figure 8, and more important, with the increasing voltage, the temperature of the filament increases (as in figure 9) causing the luminous efficiency to increase (figure 2). This means that in higher voltages, a greater part of the electromagnetic radiation is consisted of the visible light.
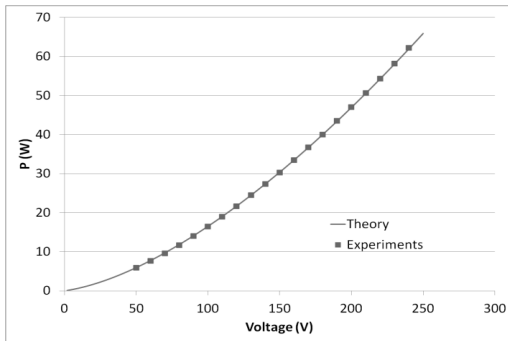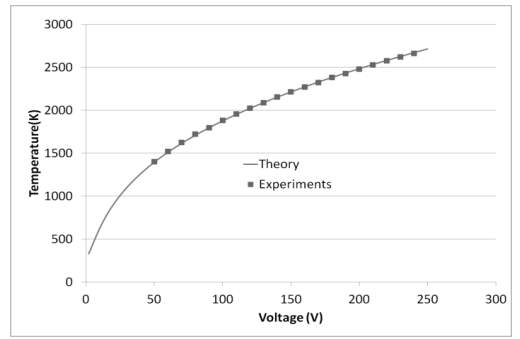

Figure 7: Theory-Experiment comparison, Total Power as a function of voltage
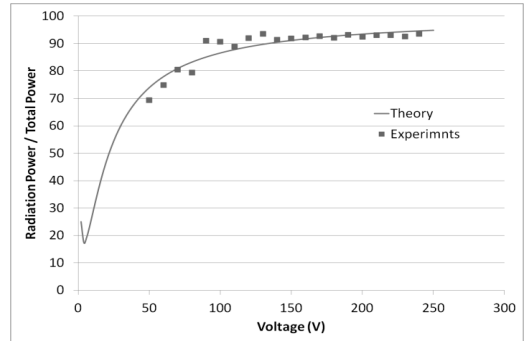
Figure 8: Theory-Experiment comparison, Radiation Percentage
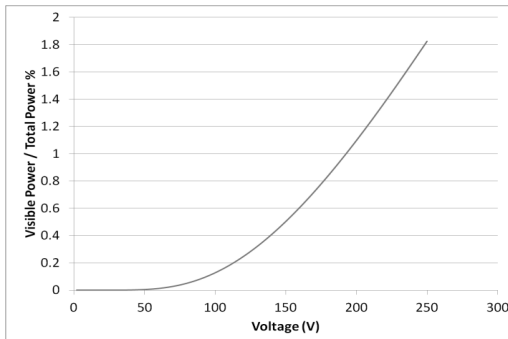
Figure 9: Theory-Experiment comparison, Filament temperature as a function of Voltage

Figure 10: The final result, percentage of the visible power to the total power as a function of voltage

No. 13, Light bulb: Probing the effect of orientation to determine the ratio between the thermal and the light energy

Alexey Krotov [1]

[*] Team of Russia, IYPT 2011

[1]*Lyceum 130, Ekaterinburg, Russia*

Corresponding author: bronze.eye@gmail.com (A. K.)

Introduction

An incandescent light bulb in the most known form was invented at the end of 1870s. The line production of such bulbs with tungsten filament has begun in 1906. That means the different properties of light bulbs have already been thoroughly investigated, and a humble school research can't possibly add something to existing knowledge. Despite that, the major part of it wasn't based on any prepared and structured plan and that may add a note of individuality into the whole work performed.

My research was based on the problem statement which was formulated as follows: *What is the ratio between the thermal energy and light energy emitted from a small electric bulb depending on the voltage applied to a bulb?*

First of all I needed to analyze rough plan of demanded work. It's said that the we're to measure light energy and thermal energy. So, I had to figure out how to do it and what devices I would use. The research was planned to consist firstly of experimental part where all needed parameters would be measured. And the next step had to be the theoretical model of phenomenon resulting insome quantitative estimation, which in turn had to be compared to experimental results.

Analysis

For a moment imagine a usual light bulb with rated power about 60W for the voltage 220V. It glows dimly when there're some troubles with the electricity in your room and voltage is lower than rated (That is quite an often thing to happen in many countries particularly in Russia). And if the voltage is about for instance 40V, the bulb doesn't glow at all; at least, we can't see it. In the meantime the current passes through a filament and warms it. Thus it was assumed: while the voltage rises, the required ratio does it too.

Most of the people relate energy and radiation with either light or radioactivity, as they are familiar to everybody. However only a few can also relate the heat with the energy radiated from all the bodies. The same is right for the bulb. The whole radiation is represented by infinite wavelength spectrum, only small part of which is perceived by human eye. Let's define light energy as the energy of radiation in range from 400 to 800 nm. In the meanwhile the heat is perceived from the entire spectrum. So let's presumably define demanded light and heat ratio as the ratio between light energy and full energy, which is defined
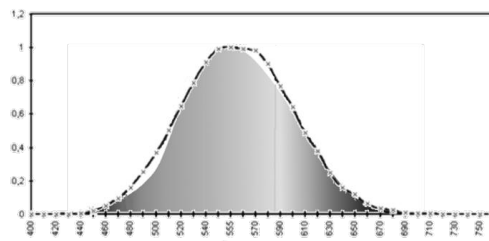
Figure 1. The illustrative diagram of spectral sensitivity. The eye characteristic[1] is shown as filled area; Thecharacteristic of used luxmeter[2] is shown as red line

as P=U·I.

It was decided to use luxmeter to perform raw measurements of luminosity of light bulb. This decision was based on the rela⁺ively easy way to get the device, as contrasted to bolometer. Besides, the chara teristics of the luxmeter and biological sources have shown that the curve of spectr sensitivity of light (Fig.1) is almost the same for both luxmeter and human eye (the ght" term applied to a bulb means light that people can perceive).

Experiment

Definetely, the most interesting part of research is the practice of experiment. As mentioned before, a luxmeter was used to measure luminocity. Two bulbs were investigated – one of rated 0.125W power for the pocket torch, and the other one usual 60W 220V bulb. As we saw later, the first bulb gave results which could be called chaotic, so it's decided to concentrate on the standard one. An autotransformer with output voltage 0..250V was used as power supply. We also cut a reference resistor in a circuit in order to measure current stregth indirectly. The sensor of luxmeter was set at a known distance from the bulb. It was totally about 20 series of measurements performed each including 10 readings and each with different power applied. Those samples of luminocity were to be derived into the power samples. First approximation performed was to consider light bulb as point light source, however it was got over later. A luminocity is defined as luminous flux per square of area being illuminated. The flux is luminous intensity in the solid angle. As we consider that bulb emits flux all around itself, we finaly represent luminous intensity as 1/683 of luminous power and get to the derivation below:

$$E = \frac{\Phi}{S} = \frac{I\Omega}{S} = \frac{1}{683}\frac{P}{S};$$

$$P_{light} = \frac{E}{683} \cdot 4\pi l^2$$

where E is illumination and L is a distance between a bulb and luxmeter sensor. Thus we get desired result in Watts.

The problem with point source approximation was solved as follows: different positions of bulb relative to sensor (Fig.2)were considered and comparative results are illustrated on a chart. A result with the greatest amount was chosen for further investigation.
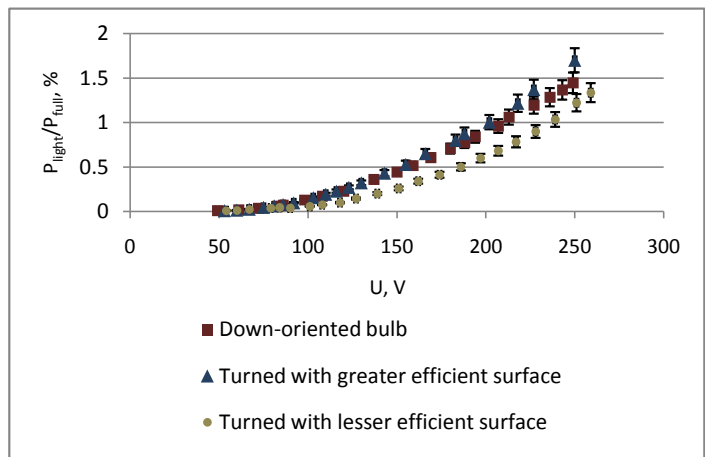
Figure 2. The ratio between light energy and full energy emitted from bulb against voltage applied for different bulb orientations
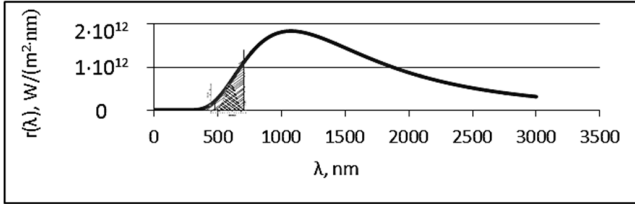
Figure 3. The radiant emission perceived by human eye (shown as intensively shaded area), the visible part of radiation (shown as faintly shaded area) and the total radiant emission for a blackbody warmed to 2600K, approximate temperature of

However usually bulb is down-oriented as we see it in any room, and respective results are very close to the greatest.

On a graph one can see the demanded dependence. It confirms the initial prediction. The ratio rises and dependence is non-linear. For the rated voltage of 220V the ratio is 1,22 per cent. Such a small amount may be explained by the graph (Fig.3) showing the part of light perceived by either human eyes or luxmeter in comparison with full radiation spectrum. As we can see, the "effective" part of radiation is very small comparing with the whole radiation. Now let's try to create a theoretical model of light emission of the bulb.

Theory

Inherently, the idea is that bulb glows because of the electromagnetic radiation of it. This idea is scientifically based on such definitions as radiant emission R, which shows the energy radiated per time per surface area. And when one is considering spectral density of radiant emittance r (dependant on temperature and either wavelength or frequency), the part of radiation represented at the given wavelength is shown.

Our theoretical model bases on the grey-body model. One should also add a few words about blackbody model itself. Any body absorbs the radiation and emits it simultaneously, however efficiency of both absorption and radiation strongly depends on the color of the body and other paremetres. The blackbody has coefficients of 1 for emissivity and absorption ability. Considering the first ablility, the respective coefficient is called emissivity. It's brought into play when it comes to Stefan-Boltzmanns Law, which defines the dependence between total radiant emission and the temperature of body-radiator: $R=\sigma T^4$. If one consider so called grey body, its emissivity is taken into formula: $R=\varepsilon\sigma T^4$. However, most of the real bodies are neither black nor grey: their emissivity depends on the temperature and wavelength.

The spectral density of radiant emittance depends on a wavelength under the law revealed by Plank (Fig. 4). It's also possible to derive Stefan-Boltzmann's Law as infinite integral from spectral density by wavelength increment. Let's try to turn to the part of radiation perceived by light. It would be derived as an integral of the same function
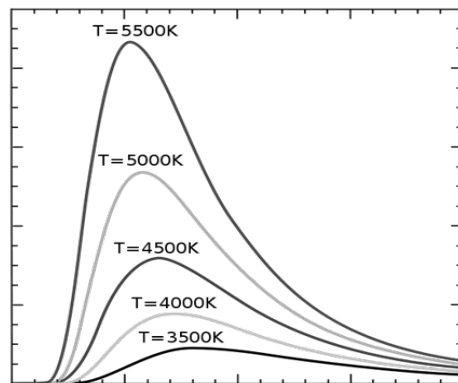
Figure 4. Diagram plotting Planck's Law[3] for blackbody of different temperature. Plot: spectral density of radiant emission against a wavelength

by wavelength increment in a range from 400 to 800 nm. And while dealing with a real body of given temperature, the emissivity has also to be accounted:

$$R_{light} = \int_{400}^{800} r(\lambda, T) \cdot \varepsilon(\lambda, T) \cdot d\lambda$$

In the usual light bulb there's a wolfram filament. We assumed that it's emissivity characteristics are negligibly different from which are given in physical thesaurus "Fizitcheskie velitchiny"[4]. The change of emissivity for "light" radiation within 400 and 800 nm is negligible (Fig. 5) and is approximately equal to 0.45. This amount has been taken into further estimation.

In order to achieve the dependence of $r_{\lambda, T}$ on the temperature of filament we had to find out the remperature. As the only parameter known from experiment was power we had to relate it with the temperature. From experiment the power applied and the resistance of filament were found and respective dependence was plotted and approximated to power function: $R=255.87 \cdot P^{0.268}$. It's perfectly known that resistivity of conductors is dependant on temperature. From the same thesaurus took we that dependence and considered the reversed one also approximated it to power function $T=3.1 \cdot 10^8 \cdot r^{0.831}$.
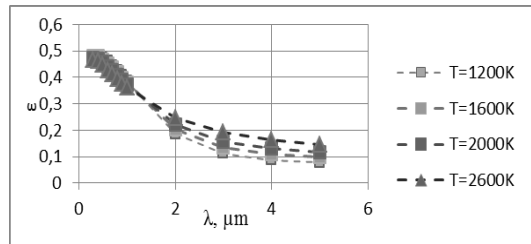
Figure 5. Diagram plotting emissivity of tungsten against wavelength for different temperature

The next step to perform was to derive the resistivity from the given resistance. To fulfil that we'd to find the length and diameter of coil of filament. At first we tried to estimate those quantitatives using zoomed photo, but the error was too big, so we took the coil itself and managed to strighten it. The diameter found was 15µm±2µm and the length was 25.4cm±0.05cm. Thus we could derive both area of cross-section and surfae area which was needed to go turn from radiant emittance of "light" radiation to the light power.

Finalizing

It was time to unite all the parts of algorithm which had to be programmed. The first step was to evaluate the resistance from power given, then through a trivial formula it was converted to resistivity of coil, on which the temperature was dependant.Then the temperature was substituted into integral of spectral density of radiant emittance by 400-800nm wavelength. Finally the integral was multiplied by emitting surface area and the light power agaínts full electric power got as a result. Then there was little derivation to be done: convert the power given into a voltage using resistance for each power value found from the experiment.
After supeimposing the experimental and theoretical plot (Fig.6) we've got an intersection,fortunately, right in the point of rated 220V, the ratio for which is 1.22%.

The little mismatch of the whole lines is easy to explain as we negliged error in emissivity and coil sizes estimation.

Neglections and predictions

In the very beginning it was mentioned that thermal conductivity is negligible comparing with heating radiation**.** That can be proved if mention that heat transferred through conductivity depends on the first power of temperature, while radiation depends on the fourth power of it, thus considering high temperatures thermal conductivity may also be neglected.

It's definitely right that heated filament warms the envelope of bulb too and also warms itself, due to the fact that part of coil surface is directed inside the spiral. But finally all this energy is emitted to the ambience, because thermal equilibrium is to be mainained inside bulb-envelope system. As we can see, bulb doesn't warming infinitely, so the energy of self-warming and energy of envelope is also radiated outside.

A glass of which the bulb shell is made absorbs some part of radiation. However there's mostly ultraviolet light which is being filtered, and it almost brings no change
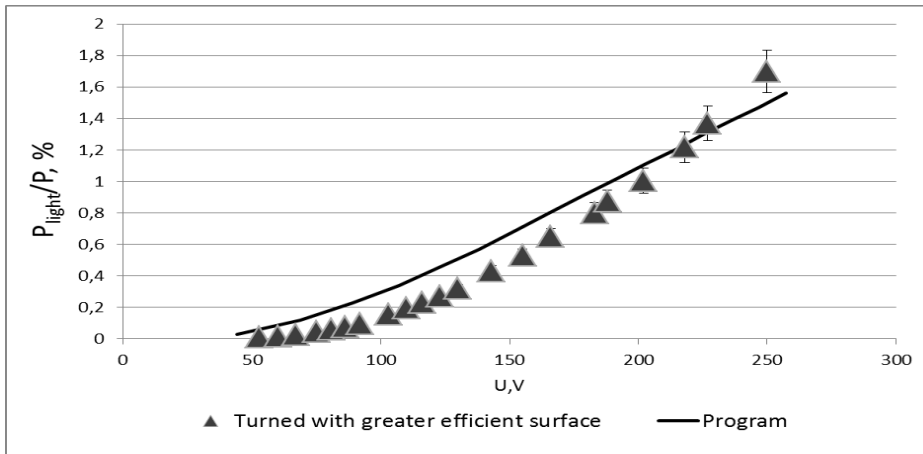

Figure 6. Comparison between theoretical and experimental plot

to the light perceived. And as for the heat, almost all energy absorbed is then being radiated outside.

As for the kind of the light energy part depending on the voltage here's an attempt to explain and predict that. Let's return to the diagram of Planck's Law and presume that wolfram has infinite melting point. When the voltage is small, the temperature is low and the maximum of emittance goes to the long wavelengthes. While the temperature rises so does the portion of visible light, and as expected it reaches its maximum when temperature equals 5600K. As the temperature continies to rise the portion of light slowly decreasing as the maximum radiation point is being displaced to lower wavelengthes.Thus considering the basic light/thermal ratio against power either voltage, we'd have got a curve with a maximum of power/voltage matching to a temperature of 5600K. But unfortunately it's impossible, so we can only hope for such refractory materials to be discovered.

References
(1)A   function   of   color   sensitivity   of   human   eye   depending   on   wavelength
http://en.wikipedia.org/wiki/File:Eyesensitivity.png

(2)Spectral characteristic of silicon photodiode used in luxmeters (particularly TKA-PKM used by me)
http://www.led-e.ru/articles/measuring/2010_3_26.php
(3)Wien's displacement law for Plank's law curve
http://ru.wikipedia.org/wiki/%D0%A4%D0%B0%D0%B9%D0%BB:Wiens_law.svg
(4)Fizicheskie Velichiny: Spravochnik/Babichev, Babushkina, Bratkovskiy etc. Energoatomizdat, 1991 p. 447,781

No. 15, Slow descent: Minimizing the descent time of a paper-made device

Hossein Azizinaghsh[1], Reza M. Namin[2]
[*] Team of Iran, IYPT 2011
[1]*Sharif University of Technology, School of Computer Engineering, I. R. Iran*
[2]*Sharif University of Technology, School of Mechanical Engineering, I. R. Iran*
Corresponding authors: hossein.azizi@gmail.com (H. A.), namin@mech.sharif.edu (R. M. N.)

Abstract

The ultimate goal in this article is to design a device, using one sheet of A4, 80 g/m^2 paper that takes the longest possible time to fall to the ground from a specific height. A large number of varied devices have been made. These observations, as a starting point,led us to find some of the specifications of the most appropriate device. A general numerical model of a falling rigid paper device was developed in order to optimize the device. The validity of numerical modelling was then verified by precisely capturing the motion of falling devices. Ultimately the ideal device was designed using the predictions of verified numerical model. This articleis based on the solution of team of Iran for the 15th problem of IYPT 2011.

Introduction

For us, there is no certainty in finding the best possible device. Because a theoretical method to predict the best possible device is undeniably unreachable as both mediums; air as a fluid and paper as a flexible material are too complicated to be modelled comprehensively and there is an infinite number of totally different devices to be considered. Therefore the most effective method to find an answer for this problem seems to be observation. A large number of observations can lead us to approach to the answer. However this method requires a broad range of varied paper-made devices and a high level of creativity in the matter of designing.

In order to maximize the efficiency of this method, this stage of problem was investigated from different points of view and varied devices were made by different individuals. A great number of diverse paper devices were made during a period of four months. Rotating and non-rotating devices, stable and unstable devices, devices inspired by airplanes, helicopters and even birds were designed. Based on these observations some deductions were made.
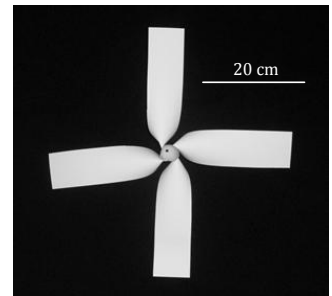
In different falling devices, generally two main types of motion were observed: Rotating motion and non-rotating motion. However the rotating motion is not necessarily a rotation about a specific axis, the rotation is usually observed without any primary rotation axis. The motion of devices was classified in three main categories: 1) rotating without a primary axis (e.g. a sheet of paper), 2) rotating with a primary axis (e.g. paper whirligig), 3) non-rotating (e.g. paper airplane)

A statistical analysis of data led us to find our ideal category. This analysis was based on the average time of fall and the variance of time of fall in each category. The result of this analysis is as follows:

- Rotating devices without a primary rotation axis (e.g. a sheet of paper):the variance of time of fall for these devices was considerably high (about 0.5 second in 10

measurements) and average time of fall was usually low (about 2.5 seconds). However in some test cases the time of fall was significantly high.Without any exceptions the reproduction of these numbers was not easily possible.Equivalently the motion of these devices is too unstable to be reliable. Due to the instability and random-like motion of these devices, there is no well-defined time of fall, thus our ideal device is not included in this category.
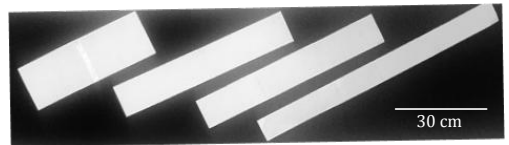
- Rotating devices with a primary rotation axis (e.g. figure 1): in this category due to the high stability of the motion of devices the variance of time of fall was relatively low (about 0.1 seconds). This stability is because of the large angular momentum, which critically increases the stability of motion. Therefore the time of fall can be defined as the average time of fall.

Figure 1: helicopter model

- Non-rotating devices: in this category the variance of time of fall was relatively low. In most cases, the rotating motion was diminished either because of large amount of rotational inertia or aerodynamic shape (e.g. paper airplane). However the average time of fallwas lowercompared to rotating devices (about 3 seconds).

Based on this classification, further investigations are specific torotating devices with primary rotation axis.
Two major types of motion were observed: rotation about a horizontal axis and rotation about a vertical axis.

Figure 2: rectangular rotating devices, rotation axis is parallel to the length

For devices with a horizontal rotation axis a rectangular device was designed (Figure 2). The rotation of this device not only increases the stability of motion, but also critically increases the time of fall. Since the ratio of width and length is the only influential parameter, based on adequate experimental data, optimization is easily possible (Figure 3).
For devices with a vertical rotation axis, a model inspired by helicopters was designed (Figure 1). The blades were firmly attached to a conic shaped center. The whole device could be considered rigid and deformations were negligible.
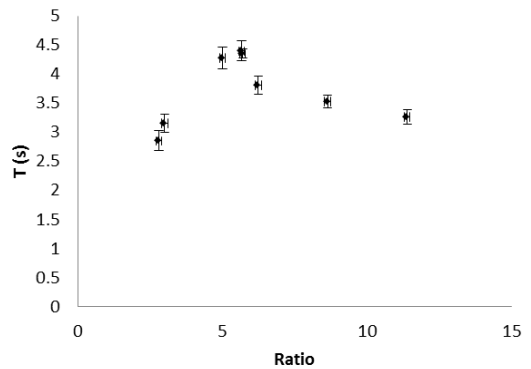
Figure 3: time of fall vs. the ratio of width and length of the rectangular rotating device

Since due to the variety of influential parameters, experimental optimization is not easily possible, a comprehensive numerical model was developed in order to optimize this device.

Theoretical Analysis
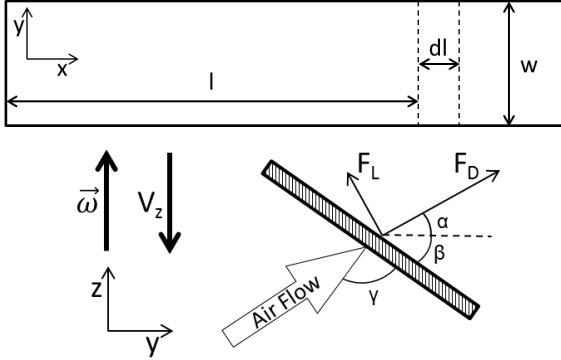
Figure 4: Declaration of parameters.
The upper rectangle is the blade of the helicopter. An infinitesimal element is indicated by two dashed lines. The lower image indicates the parameters related to an infinitesimal element.

In order to simulate the motion of the helicopter, the total force and total torque applied to the helicopter during the descent should be known.

Since the helicopter is rotating, the velocity of each element is determined by this formula:

$$\vec{V} = \vec{V}_{cm} + \vec{\Omega} \times \vec{R}$$

Air drag force is proportional to the velocity, thus, according to the above formula, the force applied to each part of the helicopter is different. We consider infinitesimal elements along the length of the helicopter and calculate the force and torque applied to that part. By summing up these infinitesimal forces, the total force and total torque applied to the falling and rotating helicopter can be found.

$$dF_D = \frac{1}{2}C_D\rho(dA)\left(l^2\omega^2 + V_z^2\right) \tag{1}$$

$$dF_L = \frac{1}{2}C_L\rho(dA)\left(l^2\omega^2 + V_z^2\right) \tag{2}$$

$$d\tau = dF_D \cos\alpha - dF_L \sin\alpha \tag{3}$$

In formulae (1) and (2) C_D and C_L are respectivley drag and lift coefficients. For an infintesimal element indicited in figure 4, we assume that this coefficient is constant. Drag and lift coefficients are dependant on the angle of attack of the flow. Air is assumed to be stationary in far enough from the device, thus the relative velocity of the flow and infinitesimal element and angle of attack would be:

$$\vec{V}_{rel} = 0 - \vec{V}_{cm} + \vec{\Omega} \times \vec{R} = V_z\hat{z} - \omega l\hat{y}$$

$$\gamma = \tan^{-1}(-\frac{\omega l}{V_z}) + \left(\frac{\pi}{2} - \beta\right) \tag{4}$$

Where β is the angle of blades with horizon, V_z is velocity of center of mass, and ω is angular velocity of the helicopter (Figure 4).

The total force and torque applied to the helicopter is the integration of infinitesimal forces, according to formulae (1), (2) and (3):

$$F_z = ma_{vertical} = n\int_0^L \frac{1}{2}\rho(l^2\omega^2 + V_z{}^2)(C_D\sin\alpha + C_L\cos\alpha)(w\cdot dl) - mg \qquad (5)$$

$$\tau_z = Ia_{angular} = n\int_0^L \frac{1}{2}\rho l(l^2\omega^2 + V_z{}^2)(C_D\cos\alpha - C_L\sin\alpha)(w\cdot dl) \qquad (6)$$

Where n is the number of the blades, L is the length of the blades, $\alpha = \frac{\pi}{2} - \tan^{-1}(-\frac{\omega l}{V_z})$ (Figure 4).

C_L and C_D are functions of angle of attack (Formula (4)), which is dependant on the radial distance of the element from the center (l in figure 4). Thus, each infinitesimal element has a different coefficient.

To find the drag and lift coefficients, we simulated the flow motion around a 2D flat plate using the Computational Fluid Dynamics Solver Fluent ®. Assuming the reynolds number to be $\frac{\rho V d}{\mu}$, it would have a maximum amount of about 10^5, so we shall have a fully turbulent motion around the wings in most of the parts [1]. For this reason, the flow could not be assumed laminar, and we used the K-Epsilon viscousity model in our CFD simulation to model turbulence [2]. We used an unsteady model in which the velocity direction changes slowly with time, covering the range between 0 to 90 degrees with 0.5 degree steps. The changes were made using a user defined function. The time-steps would proceed if all the residuals (including continuity, momentum, k and epsilon) would be less than 0.005. As a results, the amount of drag and lift forces were computed, and were used to find the drag and lift coefficients. (Figure 5)

Numerical solution

Fomulae (5) and (6) present the main equations of motion. C_L and C_D are not analytical functions. But their numerical valuesare obtained from FLUENT solver, for different angles of attack (Formula 4, Figure 5). A c++ program was developed to calculate the force and torque integration during the descent. Explicit Euler method with the time-step
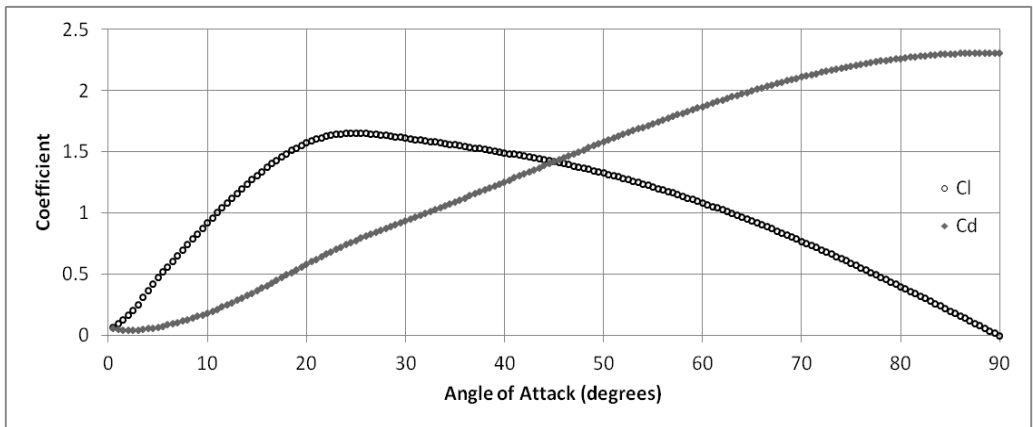
Figure 5: The Results of the CFD Simulation, Showing the Drag and Lift Coefficients

Figure 6: Torque-angular velocity correlation
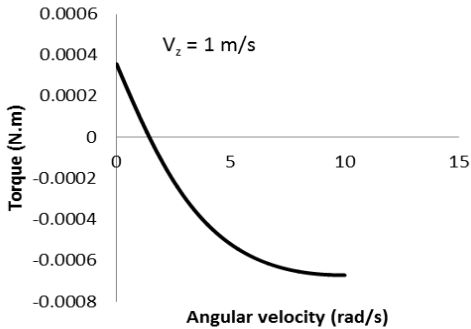
of 10^{-3} seconds was used to simulate the motion (see online supproting material: source code).
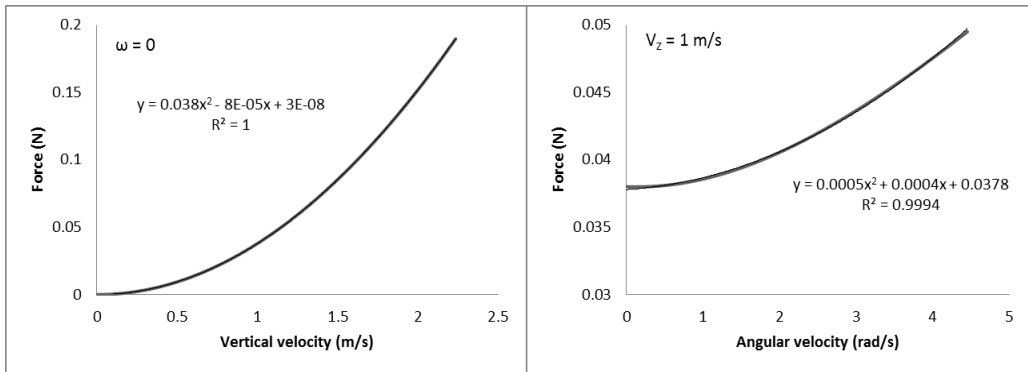

Figure 7: Force-velocity correlations resulted from the numerical integration of formulae (5) and (6).

Experiments

The vertical motion of a falling helicopter was recorded using a high-speed camera in 1000 FPS. Using image processing techniques, the location of the lower point of the helicopter was found in each frame. Velocity as a function of time was then derived from these data and was compared to the prediction of the numerical theory (see online supporting material: processed video of a falling helicopter).In order to minimize the error, ratio of the distance of camera and the height of fall was about 5. The behaviour of velocity vs. time graph presented in figure 8 is predictable. Initially gravity accelerates the helicopter, according to figure 7, the drag force increases until it completely cancels the gravity; this is the maximum point in figure 8. At this point velocity starts to decrease but air drag force (which is proportional to velocity) increases even more. This is because of rotation. Angular velocity is still increasing (Figure 6, torque is positive) and according to figure 7, air drag force increases. Without rotation, velocity wouldn't have had a maximum.
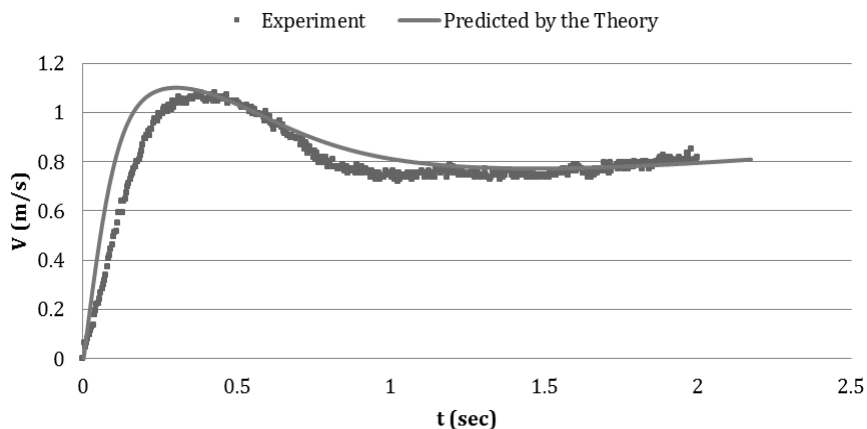
Figure 8: Predicted velocity as a function of time vs. measured velocity resulted from image processing
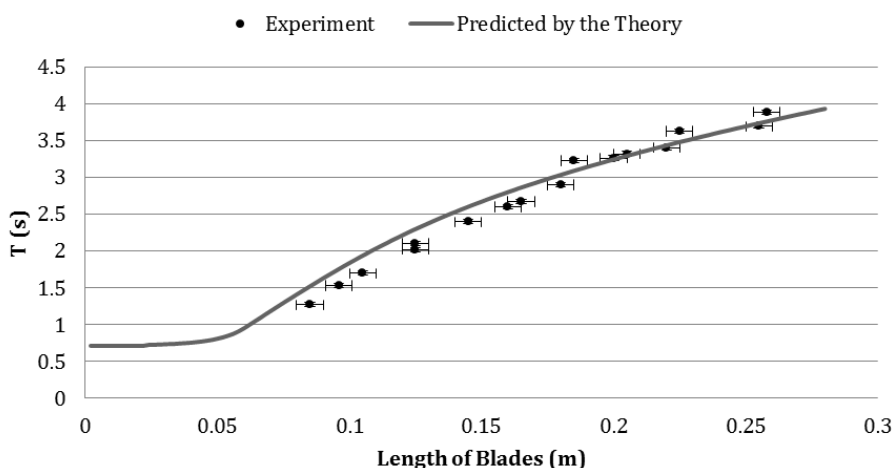
Figure 9: Predicted time of fall vs. length of the blades, the width of blades is fixed

Numerous helicopters were made with different lengths and fixed widths of wings. The time of fall was measured for each device. By increasing the number of measurements the error of each number was minimized.The time of fall as a function of the length of blades was then compared to the prediction of the numerical theory(Figure 9).
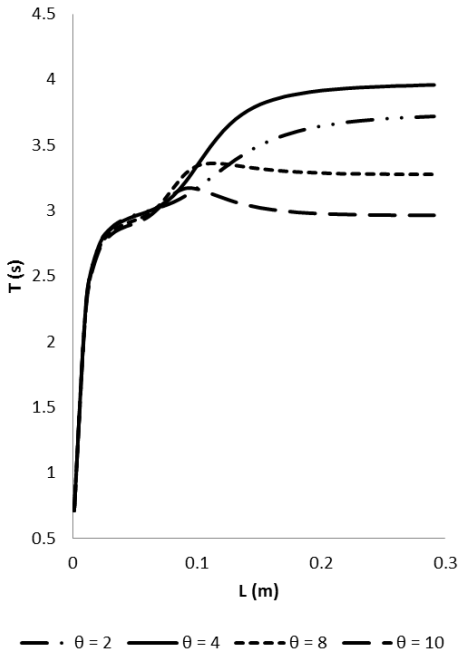
Discussion

Validity of the theory is approved with the experiments. The motion of a helicopter device with a set of specifications (number of blades, length of the blades, etc.) is completely simulated. The optimal specifications of the helicopter can be easily
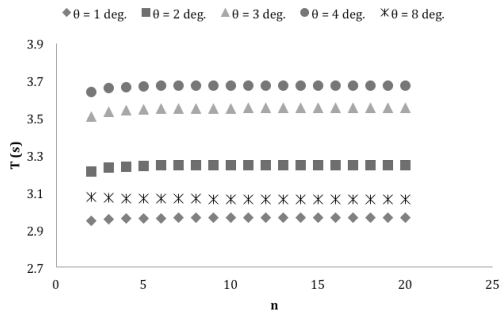
identified based on the prediction of the theory. Three diagrams were obtained from the theory in order to optimize the helicopter device.
The total area of the A4 paper is fixed, thus:
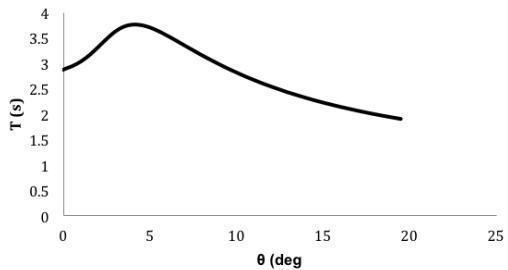
$$A = n \cdot w \cdot L = const.$$

Where L is the length of the blades, W is the width of the blades and n is the number of the blades. These parameters are not independent. If we change one of these parameters, one of the other two must also change.

Figure 11: Time of fall vs. number of the blades. Length is fixed. Width and number of blades vary

Figure 12: Time of fall vs. angle of blades with horizon. β in figure 4

Figure 10: Time of fall vs. length of the blades. Number of the blades is fixed. Width and length vary

Figure 10 demonstrates the time of fall as a function of length of blades. Number of the blades is fixed, therefore by increasing the length, the width of the blades decreases. It is implied by figure 10, that no optimum length for the blades exists. The length of blades should be large enough (more than 23 cm). Designing the helicopter with paper has some limitations. For example the length of the blades cannot be too long. Because the thin blades will loose and they wouldn't function as wings. But since 25 cm is an optimal length for the blades, and it is easily achievable, this limitation is not an obstacle.

Figure 11 demonstrates the time of fall as a function of number of the blades, the length of the blades is fixed. Number of the blades and width of the blades vary. The time of fall is not highly dependent on the number of the blades. This result is predictable. According to formulae 5 and 6, the force and torque are proportional to $n \cdot w$ which remains unchanged. It is implied that the number of blades is not a determinant.

Figure 12 demonstrates the time of fall as a function of angle of blades with horizon. A maximum amount for the time fall is expected. When angle of blades is zero (they are parallel to the ground), the device will not rotate and time of fall would be low, when angle of blades is 90 degrees (they are perpendicular to the ground), the device will not rotate and reference are is zero and the time of would be low. Thus,between zero and 90 degrees there must a maximum point.

Based on these three diagrams, optimal specifications of the helicopter are determined.

	Length of Blades (L)	Width of Blades (w)	θ	Number of Blades	Time of Fall
Actual	28 cm	7 cm	6 deg.	3	3.95±0.02 s
Predicted	24 <	A/nL	5 deg.	----	4.0 s

Figure 13: Specifications of the optimized helicopter based on diagrams resulted from the theory

Conclusion

The chief task of this investigation is achieved through three stages:

- Making numerous paper-made devices and analysing the results. The method used in this part of investigation was trial and error and it was based on the creativity in the matter of designing. The motion of paper made devices was categorized and the most appropriate category was identified.

- The helicopter device was chosen as the ideal device. In order to maximize the time of fall, a numerical theory was developed to simulate the motion of this device. Drag and lift coefficients, corresponding to infinitesimal elements along the blade of the helicopter were found by simulating the air flow around 2D surface using FLUENT. These coefficients were used to find the total force and torque applied to the helicopter during the descent. This way, the motion of the helicopter was simulated.

- The motion of the helicopter device was tracked using image-processing technique and it was compared with the prediction of the theory. In another experiment, numerous helicopters were made with different lengths of blades. Time of fall of each device was compared to the prediction of the theory. This way the simulation was verified and its reliability was proved. The optimal specifications of the device were identified by the theory and finally it was designed.
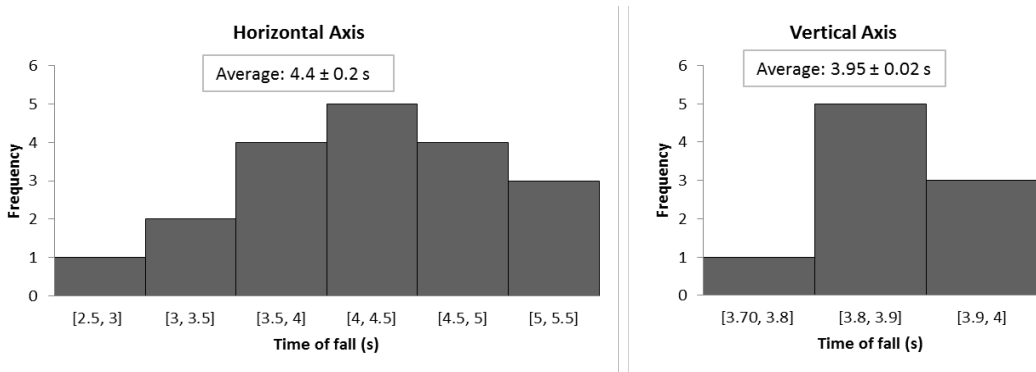
Figure 14: Histogram of falling time of best devices. Left histogram is for the rectangular device and right histogram is for the helicopter device. The relative stability of helicopter device is evident

According to the results of measurements, both rotating devices can be considered the best device (Figure 14). For the vertical axis device, due to the rotation and high angular momentum, the motion is highly stable compared to other devices, this fact is implied by figure 14. For the horizontal axis device, it may fall within a longer time but due to instability it is not reliable. Both time of fall and variance of time of fall are significant parameters.

Online supporting materials
Source code of the simulation program:
http://archive.iypt.org/iypt_book/2011_15_Slow_descent_Iran_HA_RMN_motion_simulation_source_code.txt
Processed video of a falling helicopter:
http://archive.iypt.org/iypt_book/2011_15_Slow_descent_Iran_HA_RMN_Falling_Helicopter_Theory_vs_Experiment.mp4
The red line indicates the predicted location of the helicopter, and the white line indicates the measured location of the helicopter.
Contours of static pressure:
http://archive.iypt.org/iypt_book/2011_15_Slow_descent_Iran_HA_RMN_Contours_of_static_pressure.mp4
Video resulted from CFD solution regarding the contours of static pressure in different angles of attack.

References
[1] Shames I 2002 *Mechanics of Fluids* McGraw-Hill
[2] Garde R J 2010 *Turbulent Flow* New Age Science